

DESIGN AND ANALYSIS OF THE FEDERAL AVIATION ADMINISTRATION
NEXT GENERATION FIRE TEST BURNER

by

ROBERT IAN OCHS

A dissertation submitted to the
Graduate School-New Brunswick
Rutgers, The State University of New Jersey

In partial fulfillment of the requirements

For the degree of

Doctor of Philosophy

Graduate Program in Mechanical and Aerospace Engineering

Written under the direction of

Professor Fransisco Javier Diez

And approved by

New Brunswick, New Jersey

October 2013

ABSTRACT OF THE DISSERTATION

Design and Analysis of the Federal Aviation Administration Next Generation Fire Test
Burner

By ROBERT IAN OCHS

Dissertation Director:

Professor Fransisco Javier Diez

The United States Federal Aviation Administration makes use of threat-based fire test methods for the certification of aircraft cabin materials to enhance the level of safety in the event of an in-flight or post-crash fire on a transport airplane. The global nature of the aviation industry results in these test methods being performed at hundreds of laboratories around the world; in some cases testing identical materials at multiple labs but yielding different results. Maintenance of this standard for an elevated level of safety requires that the test methods be as well defined as possible, necessitating a comprehensive understanding of critical test method parameters. The tests have evolved from simple Bunsen burner material tests to larger, more complicated apparatuses, requiring greater understanding of the device for proper application. The FAA specifies a modified home heating oil burner to simulate the effects of large, intense fires for testing of aircraft seat cushions, cargo compartment liners, power plant components, and thermal

acoustic insulation. Recently, the FAA has developed a Next Generation (NexGen) Fire Test burner to replace the original oil burner that has become commercially unavailable. The NexGen burner design is based on the original oil burner but with more precise control of the air and fuel flow rates with the addition of a sonic nozzle and a pressurized fuel system. Knowledge of the fundamental flow properties created by various burner configurations is desired to develop an updated and standardized burner configuration for use around the world for aircraft materials fire testing and airplane certification. To that end, the NexGen fire test burner was analyzed with Particle Image Velocimetry (PIV) to resolve the non-reacting exit flow field and determine the influence of the configuration of burner components. The correlation between the measured flow fields and the standard burner performance metrics of flame temperature and burnthrough time was studied. Potential design improvements were also evaluated that could simplify burner set up and operation.

\

ACKNOWLEDGEMENT

I would like to thank my advisor Professor Javier Diez for his guidance and direction over the years. His practical approach to experimental measurements and knowledge of applied physics has been extremely useful in developing this research. I would also like to thank Professor Polymeropoulos and Professor Jaluria for being on my dissertation committee.

I am grateful for the wealth of knowledge I have been exposed to since 2001 at the Fire Safety Branch of the FAA Technical Center. Dick Hill, Gus Sarkos, Tim Marker, Rich Lyon, Steve Summer, Harry Webster, and many others have been instrumental in learning all there is to know about aircraft fire safety research and development. This work could not have been performed without the incredible support of the skilled and talented engineering technicians, machinists, and IT personnel in Fire Safety – Paul Scrofani, Tom Carmen, Wayne Eichner, Frank Hahn, among others.

I would like to thank my family for the encouragement and support over these several years. I may not have made it through if it weren't for their constant reminders that the dissertation wasn't going to write itself. And of course I would like to thank my wife Betsey, whom I did not know when I started this journey, and might not have made it through if not for her love and support.

TABLE OF CONTENTS

ABSTRACT OF THE DISSERTATION	ii
ACKNOWLEDGEMENT	iv
TABLE OF CONTENTS.....	v
LIST OF FIGURES	vii
LIST OF TABLES.....	xxii
1 Introduction	1
1.1 Background.....	1
1.1.1 FAA Fire Safety Research and Development	1
1.1.2 FAA Fire Test Oil Burner	8
1.1.3 Development of the Next Generation Fire Test Burner	12
1.2 Measurement Techniques for NexGen Burner Analysis	18
1.3 Review of Literature	19
1.4 Dissertation Outline	28
2 Experimental Apparatus	47
2.1 Flow Visualization Laboratory	47
2.2 NexGen Burner – Seat Cushion Test Apparatus and Procedures	55
2.3 NexGen Burner – Insulation Burnthrough Apparatus and Procedures	56
2.4 Error Associated with Flame Temperature Measurements	60
3 Analysis of Burner Parameters	87
3.1 Internal Burner Flow	88
3.1.1 Airflow	88
3.1.2 Fuel Spray	96
3.2 External Burner Flow	100
3.2.1 Cone Exit Flow	100
3.2.2 Flow Field External to Burner Cone	104
3.3 Chapter 3 Summary	106
4 Analysis of Potential Design Improvements	152

4.1	Internal Burner Flow Improvements.....	152
4.1.1	Symmetric Stator	152
4.1.2	Flame Retention Heads	161
4.1.3	Correlation of Burnthrough Data with Velocity Data.....	165
4.1.4	Fuel Spray	165
4.2	External Burner Improvement	168
4.2.1	Reinforced Cone	168
4.3	Summary.....	171
5	Concluding Remarks	208
6	References	212

LIST OF FIGURES

- Figure 1.1 Photograph of the original FAA fire test methods, the horizontal Bunsen burner (left) and the vertical Bunsen burner (right). 30
- Figure 1.2. Examples of post-crash fire accidents: ONA Flight 032 at JFK airport, New York, 1975 (top) and Continental Flight 603 at LAX, Los Angeles, 1978. The accidents are considered survivable in that the passengers are fully capable of exiting the aircraft, though the effects of the external fire on the cabin materials significantly reduce survivability time. 31
- Figure 1.3. Full scale post-crash fire test photographs. Top: An external fire is positioned adjacent to a fuselage opening. Bottom: Interior view. The cabin interior is mocked up with aircraft-grade furnishings including sidewalls, stowbins, and seats. The cabin is instrumented with cameras, temperature measurement, and gas sampling. Test progression at 60 seconds (a), 90 seconds (b), 100 seconds (c), and 105 seconds (d). 32
- Figure 1.4. Post-accident photograph of Saudi Arabian Airlines Flight 163 at Riyadh, Saudi Arabia, August 19, 1980. A fire originating in a class D cargo compartment breached the cargo lining materials, allowing oxygen to fuel the fire and flames to spread to the passenger cabin. The plane successfully landed but flashover occurred before evacuation was initiated. All 301 persons aboard perished. 33
- Figure 1.5. Post-accident photograph of United Airlines Flight 227 at Salt Lake City, Utah, November 11, 1965. An excessive sink rate on approach to SLC led to

touchdown 335 feet short of the runway, shearing off the main landing gear, rupturing fuel lines and generator power cables, causing a large external fuel fire. Cabin materials quickly caught fire, incapacitating 43 of the 85 passengers aboard. Subsequent analysis indicated that the accident was completely survivable, as all victims perished not from impact forces but from the effects of fire..... 34

Figure 1.6. Improved Laboratory Scale Test Methods: rate of heat release of cabin interior materials (a), smoke density of cabin interior materials (b), seat cushion flammability (c), flame propagation for thermal acoustic insulation (d). 35

Figure 1.7. FAA oil burner test methods: powerplant components (a), cargo liner burnthrough (b), seat cushion flammability (c), thermal acoustic insulation burnthrough (d). 36

Figure 1.8. Park DPL3400 oil burner (a) and internal components stator (b), fuel nozzle (c), and turbulator (d). 37

Figure 1.9. Discrepancies amongst Park DPL3400 burners: draft tube length (a), different burner castings have either flanged (left) or socket (right) draft tube connections (b), fuel spray nozzles with same flow rating and spray pattern with different internal components (c). 38

Figure 1.10. Results from a worldwide comparative test series of the Park DPL3400 for thermal acoustic insulation burnthrough testing in 2005. A material fails the test if burnthrough is observed before 240 seconds. In this case, one lab would pass all samples, one lab would fail all samples, and two labs pass some and fail some.... 39

Figure 1.11. Exploded view of a 3D model of the final design of the NexGen burner.

This exploded view shows the burner housing and internal components: stator, turbulator, fuel pipe, fuel nozzle, and igniters and external components: air pressure regulator, sonic choke, muffler, and cone..... 40

Figure 1.12. Air mass flow rate, in standard cubic foot per minute, as a function of sonic nozzle inlet pressure for the NexGen burner. Comparison of theoretical calibration with the mass flow rate measured with a vortex shedding type mass flow meter. Slight deviation at higher mass flow rates occurs due to the range limitation of the mass flow meter calibration. 41

Figure 1.13. Comparison of original and re-engineered stator and turbulator. The original stator and turbulator (a and c, respectively) were cast from a mold, while the updated stator and turbulator (b and d, respectively) were modeled in 3D CAD software from the original stator, corrected to be symmetric, and CNC machined..... 42

Figure 1.14. Photographs of the original stator (a,b) and turbulator (c-e). The stator is nominally 101.6 mm in diameter, but some castings are not to specification (a). The stator is also asymmetric about the center hole (a,b). The turbulator opening should be centrally located, but is cut off-axis, resulting in a skewed exit plane (c, d). The turbulator profile view in (e) shows the off-axis direction of the exit plane.. 43

Figure 1.15. Photographs of the updated stator (a,b) and turbulator (c-e). The diameter of the new stator is closer to the nominal value of 101.6 mm (a) and is now symmetric about the central hole axis (a, b). The turbulator opening has been

corrected to be centrally located (c, d) and the exit plane is seen to be straight in the profile view (e).....	44
Figure 1.16. Worldwide NexGen burner comparative test results. Burnthrough time in seconds vs. material type for each laboratory-burner combination. The labs were Federal Aviation Administration, Centre D’Essais Aeronautique Toulouse, and Boeing.....	45
Figure 1.17. Worldwide NexGen burner comparative test series repeatability. Relative standard deviation vs. material type for each laboratory-burner combination. The labs were Federal Aviation Administration, Centre D’Essais Aeronautique Toulouse, and Boeing.....	46
Figure 2.1. PIV test chamber in test cell 2 of Aircraft Components Fire Test Facility showing location of the test chamber, laser, camera, traverse, burner, and seed inlet.	64
Figure 2.2. Schematic of the single-camera 2D PIV measurement setup (a) and dual-camera stereoscopic 3D PIV measurement setup (b), showing relative locations of the enclosure, NexGen burner, laser head, measurement plane, and cameras.....	65
Figure 2.3. Schematic of the seed generation system and connection to the NexGen burner showing the seeder pressure vessel, pressure regulator, DC voltage regulator, and burner seed inlet.....	67
Figure 2.4. Schematic of the coflowing turbulent jet validation measurement experimental setup in the PIV enclosure showing the NexGen burner and fuel pipe as the coflow and jet nozzle, respectively. The four measurement planes and locations are indicated, as well as the relative position of the laser head.....	68

Figure 2.5. Contour plot of normalized mean axial velocity field at $x/d=20-70$ downstream of the jet exit.....	69
Figure 2.6. Contour plot of normalized mean radial velocity field at $x/d=20-70$ downstream of the jet exit.....	70
Figure 2.7. Contour plot of normalized axial velocity fluctuations at $x/d=20-70$ downstream of the jet exit.....	71
Figure 2.8. Contour plot of normalized radial velocity fluctuations at $x/d=20-70$ downstream of the jet exit.....	72
Figure 2.9. Contour plot of normalized Reynolds stress contour plot at $x/d=20-70$ downstream of the jet exit.....	73
Figure 2.10. Normalized mean axial velocity profile at $x/d=30-70$ downstream of the jet exit. The mean velocity profiles at various downstream locations converge to a single profile when normalized by U_c and r/x . The present data agrees well with curve fits extracted from experimental data from Fig. 4 of [31], Fig. 7 of [25], Fig. 3 of [33], and DNS calculations from Fig. 8 of [32].....	74
Figure 2.11. Streamwise variation of the initial jet velocity normalized by the local excess centerline velocity for the current measurement at $x/d=40, 50, 60, 70$ and curve fit line. Comparison with the coflowing jet results of Fig. 2 of [33], Fig. 3 of [29], and Figs. 6,7 of [30].	75
Figure 2.12. Normalized mean radial velocity profile at $x/d=30-70$ downstream of the jet exit compared with experimental data extracted from Fukushima 2000 with approximated data scatter from Fig. 5 from [31].	76

Figure 2.13. Normalized axial velocity fluctuations at $x/d=30-70$ downstream of the jet exit compared with experimental data extracted from Fukushima 2000 with approximated data scatter from Fig. 6 from [31] comparison with DNS calculations from Boersma 1998 Fig. 9 from [32].	77
Figure 2.14. Normalized Reynolds stress profile at $x/d=30-70$ downstream of the jet exit compared with experimental data extracted from Fukushima 2000 with approximated data scatter from Fig. 8 [31] and comparison with DNS calculations from Boersma 1998 Fig. 13 [32].	78
Figure 2.15. Photograph of the FAA next generation fire test burner seat cushion flammability apparatus.	80
Figure 2.16. Location of thermocouples relative to burner cone exit plane, insulation burnthrough burner. The relative placement of the thermocouples is identical for both the seat burner and insulation burner.	81
Figure 2.17. Photograph of the FAA next generation fire test burner thermal acoustic insulation burnthrough apparatus.	82
Figure 2.18. Photographs of the picture frame sample holder.	83
Figure 2.19. Typical test progression of PAN material on picture frame sample holder as observed from the material backside. The material slowly degrades, allowing light from the flame to pass through. Initially the material is completely opaque (a), the light gets progressively brighter (b, c), cracks begin to form (c), and eventually burnthrough occurs (d).	84

Figure 2.20. Close-up photograph of the polyacrylonitrile (PAN) sample materials used to measure burner performance.	85
Figure 2.21. Baseline burnthrough times for PAN-8579 (a) and PAN-8611 (b) samples. The individual sample identification numbers are listed on the horizontal axis with the overall average. The material burnthrough time, in seconds, is displayed on the vertical axis. The average, standard deviation, and relative standard deviation (%) are displayed on the plot.	86
Figure 3.1. Burner configurations for empty tube baseline tests. The measurement plane is aligned with the vertical axis of the draft tube. The standard coordinate axes for this work are shown in the measurement plane. Straight configuration (top) and 90° elbow configuration (bottom).	110
Figure 3.2. Contour and vector plot showing measured mean in-plane velocity field exiting the empty draft tube from $x/d=0-1.8$. Comparison of the straight air inlet configuration (top) and the 90-degree inlet configuration (bottom).	111
Figure 3.3. Velocity profiles at the draft tube exit ($x/d=0.2$). Comparison of two different upstream muffler configurations shows asymmetry about the burner axis and nearly similar velocity profile shapes for both configurations.	112
Figure 3.4. Schematic of the fuel pipe in the burner tube and PIV measurement plane.	113
Figure 3.5. Contour and vector plot showing measured mean in-plane velocity field exiting the draft tube from $x/d=0-1.8$. The fuel pipe was installed in the burner and is aligned with the burner axis.	114

Figure 3.6. Velocity profiles at the draft tube exit. Comparison of two different upstream muffler configurations and the effect of the fuel pipe in the draft tube.	115
Figure 3.7. Schematic of the stator in the draft tube and PIV measurement plane. The holes on the stator were blocked with aluminum tape for these measurements.	116
Figure 3.8. Contour and vector plot showing measured mean in-plane velocity field exiting the draft tube from $x/d=0.1-1.8$. The stator was inserted into the draft tube and recessed 127 mm (a), 76.2 mm (b), and 25.4 mm (c) from the draft tube exit plane. The magnitude of the exit velocity and the jet growth are seen to vary with stator location in the draft tube.....	117
Figure 3.9. Comparison of measured mean velocity profiles for the three stator positions at $x/d=1$	118
Figure 3.10. Schematic of the turbulator on the end of the empty draft tube and PIV measurement plane.....	119
Figure 3.11. Contour and vector plot showing measured mean in-plane velocity field exiting the draft tube from $x/d=0.1-1.8$. The turbulator was installed on the end of the empty draft tube.	120
Figure 3.12. Measured mean axial velocity profiles at $x/d=1$, comparison between the empty draft tube configuration and the addition of the turbulator on the end of the draft tube.	121
Figure 3.13. Schematic of the fully configured NexGen burner and PIV measurement plane.	122

Figure 3.14. Contour and vector plot showing measured mean in-plane velocity field exiting the draft tube from $x/d=0.1-1.8$ for the fully configured NexGen burner.....	123
Figure 3.15. Front (a) and back (b) view of the turbulator with filled-in vanes.	124
Figure 3.16. Contour and vector plot showing measured mean in-plane velocity field exiting the draft tube from $x/d=0.1-1.8$. The turbulator vanes were filled in with putty to eliminate the effect of the vanes on the flow while still maintaining the exit plane area reduction of the turbulator; comparison to Figure 3.14 shows that the turbulator vanes limit jet growth and even out the flow, creating symmetry.	125
Figure 3.17. Front view of the turbulator exit plane showing the five measurement planes adjacent to the vertical centerline plane.....	126
Figure 3.18. Contour and vector plots showing measured mean in-plane velocity field exiting the draft tube from $x/d=0.1-1.8$, $z/d = -0.16d$ (a), $-0.08d$ (b), 0 (c), $0.08d$ (d), $0.16d$ (e).	128
Figure 3.19. Measured mean velocity profiles exiting the turbulator at 5 cross streamwise planes at $x/d=0.2$ (a), 0.5 (b), 1.0 (c), 1.5 (d), and 1.8 (e).	130
Figure 3.20. PIV measurement plane locations for stereoscopic measurements of unconfined swirling jet emerging from the turbulator exit.	131
Figure 3.21. Mean image of instantaneous raw data images for stereoscopic PIV measurements of the unconfined swirling jet emerging from the turbulator exit. The seed particles are seen to be concentrated in eight locations around the turbulator circumference, coincident with the location of the eight turbulator vanes.	132

Figure 3.22. Contour and vector plots showing measured three-component mean velocity field exiting the draft tube at $x/d=0.05$ (a), 0.1 (b), 0.25 (c), 0.5 (d), 0.75 (e), 1.0 (f), 1.25 (g), 1.5 (h), 1.75 (i), 2.0 (j), 2.5 (k), and 3.0 (l).....	136
Figure 3.23. Peak mean U -component velocity in each axial measurement plane from $x/d=0.05$ to 3 indicating the axial velocity decay as a function of the axial position.	137
Figure 3.24. Measurement plane location for spray nozzle PIV measurements.....	138
Figure 3.25. Contour and vector plots showing measured in-plane velocity field of the spray produced by Nozzle M, 2.25 gph-rated at 100 psig at 0° (a) and 180° (b) rotation.	139
Figure 3.26. Comparison of the mean axial velocity profiles at the spray nozzle exit ($x/d=0.37$) for nozzle M at 0° and 180°	140
Figure 3.27. Average measured flame temperature at seven thermocouple (TC) locations plotted against the nozzle rotation angle for nozzle M.....	141
Figure 3.28. Location of 9 cone exit flow measurement planes $0.25d$ apart from $-1d$ to $1d$	142
Figure 3.29. Measured mean in-plane velocity profiles exiting the burner cone at 9 cross-streamwise planes from $-1 < z/d < 1$ at axial distance $x/d=3$ (a), $x/d=3.25$ (b), $x/d=3.5$ (c), $x/d=3.75$ (d), and $x/d=4.0$ (e) from the turbulator exit plane. The flame temperature measurement locations are indicated by the green points.....	144
Figure 3.30. Flame temperature thermocouples immediately after a measurement. Note the heavy soot coating on thermocouple #1. This thermocouple location coincides with the low velocity region found in the cone exit plane measurements.	145

Figure 3.31. Measurement plane locations at the burner cone exit plane for stereoscopic PIV measurements of the cone exit flow.....	146
Figure 3.32. Contour and vector plots showing measured three component velocity field at the burner cone exit plane formed by combining four individual measurement planes (a) and comparison with the unconfined swirling jet emerging from the turbulator (b).....	147
Figure 3.33. Location of the external cone flow field measurement plane.....	148
Figure 3.34. Typical raw PIV image of the cone centerline plane, external flow field. The blacked-out area is the top portion of the cone, which was masked out for analysis.....	149
Figure 3.35. Contour and vector plots showing measured in-plane velocity field (a) and calculated streamlines (b) of the burner cone external flow field.	150
Figure 3.36. Contour plots showing the scalar mean of the vorticity (a) and typical instantaneous vorticity (b) from the cone exit flow on the cone centerline.	151
Figure 4.1. Original stator (left) and symmetric stator (right) on the fuel pipe with fuel nozzle.	174
Figure 4.2. Ignition of the NexGen burner with a handheld propane torch. The use of an igniter-less stator requires an external ignition source.....	175
Figure 4.3. Schematic of the test configuration for the symmetric stator PIV measurements. The draft tube is cut away to show the internal components. The measurement plane is approximated by the green rectangle.....	176
Figure 4.4. Typical PIV image data for the symmetric stator tests.....	177

Figure 4.5. Contour and vector plots showing measured mean in-plane velocity field exiting the turbulator for the symmetric stator baseline configuration (a) and the original stator baseline configuration (b).	178
Figure 4.6. Comparison of mean axial velocity profiles at the turbulator exit, $x/d=0.3$ (a) and one diameter downstream $x/d=1$ (b), for the original stator (blue) and symmetric stator (red) configurations.	179
Figure 4.7. Contour and vector plots showing measured mean in-plane velocity field exiting the draft tube. All internal components except the symmetric stator were removed from the draft tube. The symmetric stator vertical centerline was aligned with the draft tube vertical centerline, and recessed 50.8 mm (a) 101.6 mm (b) from the draft tube exit plane.....	180
Figure 4.8. Measured mean velocity profiles for the two symmetric stator positions at $x/d=1$. Comparison with Figure 3.9 shows greater jet growth for the symmetric stator.....	181
Figure 4.9. Average measured flame temperatures at each thermocouple measurement location (TC) for the original stator baseline (blue) and the baseline symmetric stator (red).	182
Figure 4.10. Burnthrough times for PAN 8579 (a) and PAN-8611 (b) material. Comparison of original stator baseline (blue) vs. symmetric stator baseline (red)....	183
Figure 4.11. Average measured flame temperature for the symmetric stator at various axial and radial locations (a) and flame temperature spread (ΔT , blue) and overall	

average flame temperature (TC AVG, red), for the symmetric stator at various axial and radial locations (b).....	184
Figure 4.12. Average measured flame temperatures at each thermocouple location (TC) for the symmetric stator (blue) and the original stator baseline (red) at the baseline position (solid) and at 0° 50.8 millimeters (dashed).	185
Figure 4.13. Burnthrough times for PAN-8579 material (a) and PAN-8611 material (b). The average burnthrough time of baseline stator position (solid) is compared with the new stator position (dashed) for the original stator (blue) and the symmetric stator (red).	186
Figure 4.14. Contour and vector plots showing measured mean in-plane velocity field exiting the turbulator for the symmetric stator at 0° 50.8 millimeters (a) and the original stator at 0° 50.8 millimeters (b).	187
Figure 4.15. Comparison of mean axial velocity profiles at the turbulator exit for the original stator (blue) and symmetric stator (red) at 0° 50.8 millimeters at $x/d=0.3$ (a), and $x/d=1.0$ (b).....	188
Figure 4.16. Photograph of three flame retention heads tested in this work showing the locations of the center opening, primary slots, and secondary slots.	189
Figure 4.17. Average measured flame temperatures for the three flame retention heads, F12 (blue), F22 (red), and F31 (green).	191
Figure 4.18. Average burnthrough times for PAN-8579 and PAN-8611 materials for the three flame retention heads tested: F12 (blue), F22 (red), F31 (green), and original stator baseline (blue/white).....	192

Figure 4.19. Contour and vector plots showing measured mean in-plane velocity field exiting the flame retention heads for the F12 (a), F22 (b), and F31 (c).....	193
Figure 4.20. Comparison of the mean axial velocity profiles for each flame retention head at the draft tube exit $x/d=0.2$ (a) and $x/d=1.0$ (b).....	194
Figure 4.21. Average material burnthrough time as a function of measured peak axial velocity at $x/d=1$ for PAN-8579 (a) and PAN-8611 (b).....	195
Figure 4.22. Average material burnthrough time as a function of measured average flame temperature for PAN-8579 (a) and PAN-8611 (b).	196
Figure 4.23. Contour and vector plots showing measured in-plane velocity field of the spray produced by Nozzle D, 126 mL/min (2.0 gph)-rated at 6.87 bar (85 psig). The nozzle was rotated in 60-degree increments resulting in 6 nozzle rotations (a-f).198	198
Figure 4.24. Comparison of the mean axial velocity profiles at the spray nozzle exit ($x/d=0.37$) for nozzle D at 60° increments.	199
Figure 4.25. Average measured flame temperature at seven measurement locations plotted against the nozzle rotation angle for nozzle D.....	200
Figure 4.26. Average burnthrough times for PAN materials from nozzle M (blue) and nozzle D (red).....	201
Figure 4.27. Photograph of a reinforced burner cone.	202
Figure 4.28. Sample PIV image of the reinforced cone centerline plane, external flow field. The blacked-out area is the top portion of the cone, which was masked out for analysis.	203

Figure 4.29. Contour and vector plots showing measured in-plane velocity field (a) and calculated streamlines (b) of the reinforcement ring burner cone external flow field.	204
Figure 4.30. Contour plots showing the scalar mean of the vorticity (a) and typical instantaneous vorticity (b) from the reinforcement ring cone exit flow on the cone centerline.	205
Figure 4.31. Average measured flame temperatures for the standard cone (blue) and the ring cone (red).	206
Figure 4.32. Burnthrough times for PAN-8579 material (a) and PAN-8611 material (b). Comparison of the standard cone design (blue) and the reinforcement ring cone design (red).	207

LIST OF TABLES

Table 2.1. Flow conditions for the turbulent jet validation measurements.....	66
Table 2.2. General flow properties of the NexGen burners used in this work.	79
Table 4.1. Measured exit plane area for the flame retention heads compared to the turbulator.....	190

1 Introduction

1.1 Background

1.1.1 FAA Fire Safety Research and Development

The United States Federal Aviation Administration (FAA) is the sole authority for regulating commercial aviation safety in the United States. The FAA mission is “*to provide the safest, most efficient aerospace system in the world.*” Working to fulfill that mission is the FAA Fire Safety Branch, which supports the FAA’s aviation safety goal by developing technologies, procedures, test methods, and fire performance criteria that can prevent accidents caused by a variety of fire threats and improve occupant survivability.

Beginning in the 1940’s, the Civil Aeronautics Authority (predecessor to the FAA) mandated requirements for evaluating the flammability of airplane cabin materials, initially only if smoking was allowed on the flight, then eventually irrespective of smoking [1]. The flammability criteria were based upon the ignition of cabin materials by a small flame from matches or a cigarette. The initial requirements stated only that for each compartment to be used by the crew or passengers:

- a) The materials must be at least flash-resistant

- b) The wall and ceiling linings, and the covering of upholstery, floors, and furnishings must be at least flame resistant

Flash resistant was defined as not susceptible to burning violently when ignited, and *Flame resistant* defined as not susceptible to combustion to the point of propagating a flame, beyond safe limits, after the ignition source is removed [2]. A simple Bunsen burner apparatus, displayed in Figure 1.1 and adopted from Federal Specification CCC-T-191b method 5902, was recommended to show compliance with the regulations at the time [3]. The advent of the jumbo jet in the early 1970's resulted in a more stringent 60 second vertical Bunsen burner test as opposed to the standard 12 second with wider application throughout the cabin.

Despite the new flammability requirement, the next few decades saw several accidents that were considered survivable but had high fatality rates due to the ensuing post-crash fire and its effects on the cabin environment. Examples of post-crash fire accidents are displayed in Figure 1.2. FAA research was conducted to study these effects in a full-scale configuration of a wide-body fuselage adjacent to a large external jet fuel pan fire, simulating a survivable accident, as displayed in Figure 1.3 [4]. It was determined that though the effects of the fire itself were significant, the combustion of the cabin interior materials could potentially have the greatest impact on passenger survivability. It was found that intense flame radiation ignited the interior polymeric materials resulting in elevated cabin temperature, toxic combustion byproducts, and thick black smoke, which combined to significantly decrease the ability of passengers to escape the fuselage.

Moreover, as cabin materials were heated by flame radiation they underwent thermal decomposition, releasing flammable gases that collected in the upper portion of the fuselage and ignited in a flashover – the rapid combustion of the gases and consumption of cabin oxygen. The research indicated that the threat upon which the flammability requirements were based was grossly underestimated, and that the small-scale test method was not adequate in reflecting a material’s full hazard potential that could occur when exposed to intense thermal radiation from an external fuel fire. New test methods and material flammability standards would be required to ensure that the cabin materials would no longer be the primary detriment to post-crash survivability.

Two FAA public hearings in the late 1970’s on fire and explosion reduction and fire worthiness of compartment interior materials resulted in the formation of a Special Aviation Fire and Explosion Reduction (SAFER) advisory committee and a significant increase in worldwide cabin fire safety research and international cooperation [5]. One major recommendation of the committee was to increase the amount of full-scale fire testing to determine the contribution of the current in-service cabin materials in a post-crash fire to cabin survivability. Following this, the full-scale test results should be correlated down to realistic, fire threat-based, laboratory-scale test methods that are capable of discriminating between the good- and poor-performing cabin materials under similar conditions to the full scale fire test. The fire threats are divided into two main areas, in-flight fires and post-crash fires, each with unique mitigation strategies but one common goal – increase survivability. The fire threats are described below, each

exemplified by a significant aircraft accident resulting in loss of life and subsequent regulatory action.

An in-flight fire can occur in an area of the aircraft cabin that is not readily accessible to the crew or passengers, such as the below-floor cargo compartment, behind galleys or cabin sidewalls, in or behind lavatories, or in the overhead area. A significant amount of material is located in inaccessible areas, including ducts, insulation material, and electrical wiring, as well as the contents of a cargo compartment. The most catastrophic in-flight fire occurred in 1980 in Riyadh, Saudi Arabia aboard Saudi Arabian Airlines Flight 163, a Lockheed L1011 wide body transport tri-jet airplane, pictured in Figure 1.4 [6]. Seven minutes after take-off from Riyadh an alarm indicated smoke in the aft cargo compartment area. The flight engineer went back in to the cabin and confirmed smoke and fire in the passenger compartment. A decision was made to return to Riyadh where ground fire and rescue crews were notified. The aircraft was successfully landed, though the pilot did not initiate an emergency exit. Ground rescue crews surrounded the aircraft and watched helplessly as they observed flashover through the aircraft windows. The entire cabin was engulfed in flames and all 301 people aboard perished. The accident investigation was inconclusive in determining the exact source of the fire except that it did originate in the cargo compartment. The compartment was certified as a Class D cargo compartment, which is required to contain a fire by oxygen starvation due to low leakage rates and relatively small volume. This method of fire containment relies on the cargo lining materials to maintain integrity during a fire such that no oxygen can be

drawn in, which will extinguish or at least suppress the fire by oxygen starvation. On the L1011 the cargo liner material met the flammability requirements at the time, a 45-degree Bunsen burner material burnthrough test, where burnthrough is defined here as the point in time at which a flame penetrates a material. Subsequent full-scale tests simulating a cargo compartment fire indicated that the same material would easily burn through; allowing oxygen to enter and feed the fire while spreading flames outside the cargo compartment. These findings spurred FAA research to develop a more realistic and severe threat-based test utilizing a kerosene oil burner test apparatus to simulate a cargo fire impinging upon cargo lining materials, and new regulations requiring that cargo liner exhibit burn through resistance in the new test [7].

Post-crash fires result from unexpected failures on take-off or landing, including uncontained engine failures, bird strikes, tire bursts, or a multitude of other events. The fuselage remains largely intact, though a ruptured fuel tank or fuel line causes an external fire to impinge on the fuselage skin, melting the aluminum within approximately 60 seconds or less, subjecting the cabin materials to flames and cabin occupants to smoke and toxic gases. One of the earliest examples of a post-crash fire accident occurred in 1965 aboard United Airlines flight 227, a Boeing 727 narrow body tri-jet, at Salt Lake City, Utah, pictured in Figure 1.5 [6]. An excessive sink rate on final approach resulted in the aircraft touching down 335 short of the runway, shearing off the main landing gear and rupturing fuel lines beneath the floor and generator power leads, causing a fire that entered the cabin through the air return grills during the crash deceleration, quickly

igniting cabin materials causing extreme temperatures, thick black smoke, and toxic gases to fill the cabin. Of the 85 passengers aboard there were 43 fatalities. The accident investigation concluded that the accident was entirely survivable as no passengers died as a result of impact injuries; all were smoke and fire related. Had the cabin materials been more fire resistant, the fire would not have intensified as quickly as it did, allowing the passengers additional time to escape before flashover occurred. This accident was one of the earliest to highlight the critical role of burning cabin materials on post-crash fire survivability. Similar survivable accidents with loss of life attributable to burning interior materials led to significant FAA full-scale fire testing to determine methods of survivability enhancement during post-crash accidents. New certification requirements, based on this research, resulted in the development of more stringent, threat based requirements for cabin interior materials. Seat cushions, considered the largest fuel load in the cabin, were typically constructed from polyurethane foam and wool dress covers. The polyurethane foam is flammable, and ignites easily and spreads flames quickly. FAA research led to the development of fire resistant blocking layers - lightweight barriers that encapsulate the foam, protecting it from the fire. A threat-based test method employing a kerosene oil burner was developed to ensure that the fire blocking layer maintained integrity when exposed to a severe fire. The new requirement for seat cushions became effective in 1984, and mandated a fleet wide retrofit for all transport category airplanes over a three year period [8].

FAA research has led to significant, lifesaving flammability requirements for transport airplanes. The test methods that were developed over the years, displayed in Figure 1.6, have become more threat-based, replacing simple Bunsen burner tests with severe fires representative of those that could occur or have occurred in real accidents. Transport airplane and materials manufacturers have worked over the years to develop materials and installations that comply with the regulations, requiring continuous fire testing during development and certification. Worldwide, there are hundreds of facilities that perform FAA fire tests, and the International Aircraft Materials Fire Test Working Group (IAMFTWG) was formed in 1990 to bring together all those who must comply with the FAA requirements and those who perform the fire tests to address issues with testing and new test method development [9]. Through the working group, several worldwide comparative test series have been conducted to evaluate the reproducibility of the FAA fire test methods, where the FAA tests sample materials at its lab then sends out the same materials to other labs to test. Significant scatter was found in lab to lab reproducibility, indicating that although the materials were identical and all labs followed burner set up and operation guidelines in the test method, the test apparatuses themselves were providing different results. The kerosene oil burner, displayed in Figure 1.7, is the most widely used test apparatus, and though significant work has been done to eliminate variations in configuration and testing, reproducibility of the test method still needs improvement.

1.1.2 FAA Fire Test Oil Burner

The FAA adopted a modified household heating oil burner as a fire test apparatus beginning in the 1960's to simulate an aircraft jet engine fire to determine the fire resistance of components to be used on and around the powerplant, including pumps, firewalls, and liquid reservoirs, among others [10]. The characteristics of the kerosene flame were considered representative of an engine failure in which jet fuel flames may escape the engine case and impinge upon external components. The original burner was a Lennox 0B-32 residential oil burner, but equivalent burners could be used as long as the fuel flow rate, measured flame temperature and heat flux were matched. Since the FAA sought fire test equipment that more closely simulated the intensity of a real fire for certification of interior materials, the oil burner was chosen as the apparatus for fire testing of cargo compartment liners, seat cushions, and thermal/acoustic insulation.

The oil burner, pictured in Figure 1.8, consists of an electric motor that is connected by a shaft to a blower wheel and an oil pump. The blower wheel draws air from the room and directs it down the draft tube, a 101.6 mm inner diameter, 381 mm long tube. Inside the draft tube is a stator, or internal stationary air swirling device, that also holds two electrodes for ignition. The stator has 4 angled vanes that impart a swirling motion to the incoming air. A fuel pipe, aligned coaxially to the draft tube and 10.16 mm outer diameter, passes through the center hole of the stator and terminates at a fuel nozzle. The nozzle is a commercial off the shelf pressure-swirl atomizer that delivers fuel in a conical spray pattern out the end of the draft tube. The fuel is pressurized by a shaft-driven

mechanical oil pump powered by the electric motor. Located at the end of the draft tube is an area-reducing component called the turbulator which reduces the exit area by 68%. The turbulator has vanes on its inner surface angled in the opposite direction to those on the stator, intended to create high shear on the periphery of the swirling flow exiting the draft tube, thus mixing the atomized fuel droplets and the burner air for better combustion. An extension cone, 304.8 mm long with an initial circular cross-sectional area of 91 cm² blending to an elliptical cross-sectional area at the end 294.4 mm wide by 152.4 mm high with an exit plane area of 190 cm², is fastened to the end of the draft tube. It is constructed from 1.27 millimeter thick type 310 stainless steel, and is intended to direct the flame towards the test sample as well as re-shape the flame to the rough dimensions of the sample.

The exact configuration of the oil burner depends on the test being performed, as each test method was developed by considering the fire threat and the position of the component relative to the fire, as pictured in Figure 1.7. The cargo compartment liner test uses the oil burner to simulate a cargo fire, which would impinge directly on the ceiling of the cargo compartment and indirectly on the cargo compartment sidewalls. Therefore, the burner is oriented so that the draft tube and extension cone are vertical, impinging upon a cargo liner material 20.32 centimeters above and perpendicular to the direction of the flame. The seat cushion test uses the burner to simulate a post-crash fire entering the cabin through an opening in the fuselage, either an open door or a rupture. The burner is mounted horizontally, directing the flame toward a representative seat

cushion from the side, as would occur in the actual fire. The thermal/acoustic insulation test uses the burner to simulate the impingement of the post-crash fire on the exterior of the fuselage. Considering the curvature of the lower half of the fuselage and the angle of incidence of the fire on the fuselage, the burner is mounted 30° from the horizontal while the test sample frame is mounted 30° from the vertical, simulating the impingement that a post-crash fire would have on the lower fuselage.

Oil burner test procedures require measurement of the flame temperature and flame heat flux. The temperature is measured with a thermocouple “rake”, consisting of seven, 3.175 or 1.5875 millimeter diameter K-type stainless steel sheathed grounded junction thermocouples, arranged in a row spaced linearly at 25.4 millimeters apart. The temperature is acquired by immersing the thermocouple rake in the flame for one minute, and then recording the average temperature of each thermocouple over thirty seconds. Flame heat flux was initially measured with a heat transfer device consisting of a copper tube immersed in the flame with water of a specified flow rate flowing through the tube. The temperature rise was measured by thermocouples upstream and downstream from the flame. The heat flux, in BTU/hr, was calculated from the temperature rise of the water through the tube. Later, Gardon style heat flux gauges were used to measure heat flux density, as the measurement procedure was greatly simplified. The Gardon gauge is constructed from a thin circular Constantan foil bonded to a water-cooled copper slug [11]. A copper wire is attached to the center of the back side of the foil, while a second copper wire is connected to the perimeter of the circular foil. Since the gauge is water

cooled, the edge of the foil is at or near the cooling water temperature, while the center of the foil is at an elevated temperature. The foil becomes a thermopile, with two junctions measuring dissimilar temperatures. The temperature differential measured with a voltmeter and the radius of the foil are used to calculate the heat flux density in BTU/ft²s, which is calibrated against a NIST-traceable standard Gardon gauge [12].

Each test method specifies acceptable ranges for the measured flame temperature and heat flux. The initial test descriptions only required that the burner achieve the temperature and heat flux, regardless of other burner configurations. It was found that some laboratories would meet the temperature and heat flux requirements by drastically increasing burner air velocity; other labs might use flow deflecting “tabs” mounted on the turbulator to move the flame to the measurement location. Despite all labs having burners with similar measured temperature and heat flux, test results still showed wide variations in lab to lab reproducibility [13]. Other factors were determined to have more of an effect on burner performance besides flame temperature and heat flux. The development of the thermal acoustic insulation burnthrough test method in the early 2000’s revealed many of the inconsistencies of the test apparatuses worldwide. It was decided to mandate strict burner configuration requirements, including the exact make and model of the oil burner, the Park DPL 3400, and the location and orientation of the internal components and the air and fuel flow rates. Even still, when performing lab to lab comparative tests for insulation burnthrough, results still did not match adequately, as displayed in Figure 1.10 [14]. Only after comparing identically-branded oil burners from

two different labs was it realized that some burners were made of different components, despite having the same make and model number, as shown in Figure 1.9. Moreover, as the implementation of the final rule neared, the major airframe manufacturers contested the rule due to the lack of availability of the Park DPL 3400, as it was out of production and hard to locate. The FAA responded by delaying the rule implementation for two years while searching for an alternative burner apparatus [15].

1.1.3 Development of the Next Generation Fire Test Burner

The FAA sought a burner that could produce a flame similar to the Park oil burner, but would be more repeatable and reproducible, and more simple to set up and operate. The burner should also have tighter control of the burner inlet conditions, greatly reducing the reliance on flame temperature and heat flux measurements that do not necessarily indicate burner performance. Rather than choose another commercially produced home heating oil burner, a burner would be constructed from basic components that could be obtained anywhere in the world. In order to meet the timeline of the rule implementation, the burner was designed to utilize many of the same components of the Park oil burner, greatly reducing development time. The burner was called the Next Generation (NexGen) fire test burner, or the Sonic Burner, due to the use of a sonic nozzle as the air flow metering device. An exploded view of a 3D model of the NexGen burner is displayed in Figure 1.11 with all components labeled. A complete description of the NexGen burner, along with detailed drawings and comparative testing results, is available in [16] and will be summarized in this section.

The basic concept for the NexGen burner is to replace the electric motor and burner housing of the Park DPL3400, as worldwide electric supply differences result in varying fan speeds at different labs, and supply fluctuations have been found to create variability in burner performance. The air flow is supplied by compressed air regulated by an air pressure regulator and metered with a sonic nozzle. Sonic nozzles are a practical application of converging-diverging nozzle theory. They are used in industry and laboratories to accurately maintain stable gas flow rates in systems where precision is necessary. Air enters the diverging section of the nozzle, where it is accelerated due to the reduction in cross sectional area. At the throat, or the point of minimum cross sectional area, the flow reaches Mach 1 and a shock is established. Once this happens, the mass flow rate of air through the nozzle is fixed for a given inlet air pressure, and the mass flow rate is directly proportional to the inlet air pressure as long as the downstream pressure is less than 88% of the inlet pressure. The calibration chart for the nozzle used for the NexGen burner is displayed in Figure 1.12. A flow design point of 80 SCFM (0.04535 kg/s) was initially requested due to the measured inlet flow rate of the Park burner, however subsequent testing indicated that to achieve an equivalent draft tube exit flow rate, as measured by a vane anemometer, a lower flow rate around 66 SCFM (0.0384 kg/s) was required for the NexGen burner. The expansion of the air creates significant noise; therefore a muffler was added to the burner immediately downstream of the choke. The burner itself is constructed from mild seam steel tubing and is composed of three sections. The draft tube is 101.6 millimeters inside diameter, 107.95 millimeters

outside diameter and 381 millimeters in length. The back section is constructed from the same steel tubing, but is 152.4 millimeters in length. A coupling section, 107.95 millimeters inside diameter, 114.3 millimeters outside diameter, 101.6 millimeters in length, joins the back section and draft tube together. The back section is inserted into the coupling 25.4 millimeters, and the two are welded together. The draft tube is inserted 76.2 millimeters into the other end of the coupling, and set screws are used to hold it in place. This forms a single inside flow section of 101.6 millimeters in diameter by 533.4 millimeters in length. A back plate is welded to the back section, with a pipe nipple welded to the center for burner the airflow inlet and a hole 38.1 millimeters below the pipe nipple for the fuel inlet. The fuel is provided by a pressurized fuel tank filled with JP8 jet fuel or equivalent kerosene fuel. The tank is partially filled with fuel and a head pressure is applied with nitrogen gas. The tank is plumbed to the back of the burner where it connects to the burner fuel pipe, which is a 10.2 millimeter outside diameter, 5.461 millimeter inside diameter steel tube bent into a dogleg shape in order to allow the fuel inlet to be below the air inlet at the back of the burner but align both the fuel and air on the burner axis just downstream. A fuel nozzle and adapter are threaded on to the end of the fuel pipe, similar to the nozzles specified for the Park DPL3400.

The NexGen burner utilizes a similar but updated stator and turbulator as the Park oil burner. Manufacturing defects and asymmetry resulting from production of the components led to a variety of different shaped stators and turbulators, despite having the same model number. 3D models of the stator and turbulator were created using CAD

software, and the component irregularities were corrected. The models were sent to machine shops with CNC machining capabilities, and exact replicas of the 3D models were manufactured. The original and re-engineered components are displayed in Figure 1.13, while the flaws in the original parts are displayed in Figure 1.14 and the corrections in Figure 1.15. These CNC machined components are now preferred over the original cast stators and turbulators.

The burner inlet air and fuel temperatures are monitored at the burner inlet and are required to stay within a specified range to eliminate fluctuations in flow rates at various labs due to temperature effects. The simplest method to maintain constant temperatures is to use an ice bath or freezer as a heat exchanger for the air and fuel before entering the burner [17]. The air temperature is required to be within 4.4-15.5 °C and fuel within 0-11.1 °C for the duration of testing [18].

With more precise control over the NexGen burner inlet parameters and internal configuration, measurement of the flame temperature and heat flux is not as crucial; if the required temperature or heat flux cannot be achieved there are no changes that can be made to obtain the desired value that would not adversely affect test results. The likely source of inconsistency is the measurement device or method, not the burner flame. Flame temperature measurement with thermocouples, discussed in Section 2.4, has error due to the thermocouple junction not achieving the true flame temperature due to significant radiative losses. Errors arise in heat flux measurement with Gardon or

Schmidt-Boelter gauges in mixed-mode convective and radiative environments due to the purely radiative calibration method, and correction factors can be applied based on the heat transfer coefficient and the gauge body temperature relative to the surrounding wall [19]. An uncertainty analysis of heat flux measurements with Schmidt-Boelter heat flux gauges in JP-8 fuel pool fires determined a range of typical uncertainties from $\pm 23\%$ to $\pm 39\%$ arising from large convective contributions to the incident heat flux and the gauge sensitivity to radiation and convection is not equal [20]. Also, maintaining a calibrated gauge is difficult when using in a harsh environment as calibration is entirely dependent on the gauge surface emissivity and repainting and recalibration of gauges is costly and time consuming. It is for these reasons that the heat flux requirement was abandoned when using a NexGen burner. Flame temperature measurement is still required, but a broad range of $\pm 37.7^\circ\text{C}$ allows room for the uncertainty of the thermocouple measurement.

Before the NexGen burner design could be mandated for certification of thermal acoustic insulation, the design required validation testing before it could be considered equivalent to Park DPL3400 burners. Several NexGen burners were constructed and tested at the FAA Technical Center, and some were shipped to IAMFTWG members around the world to confirm that the burners provided similar results regardless of the location of the laboratory. A material sample holder called the picture frame sample holder was developed to simplify the test procedure for performing comparative burnthrough tests, and a specially manufactured material proven to provide consistent burnthrough results

was used for testing [16]. The worldwide comparative testing results, displayed in Figure 1.16, show that overall the NexGen burners performed similarly regardless of location. The relative standard deviation, or the sample set standard deviation normalized by the sample set average, is used to show repeatability for a test series. Good repeatability was also found at the various labs, displayed in Figure 1.17, with a maximum relative standard deviation of 5.25% across all lab-burner combinations tested.

Though it was proven that the NexGen burner could be considered equivalent to the Park burner for thermal acoustic insulation burnthrough testing, the development of the NexGen burner is not yet complete. Other test methods that rely on Park oil burners would benefit from the use of the NexGen burner as well, however the same burner settings for insulation burnthrough may not be appropriate for a seat cushion or cargo liner NexGen burner. Also, the measurement of the burner flame output has been found to not necessarily characterize the burner performance adequately. Other unknown parameters that better correlate to burner performance should be identified and regulated. Lastly, the NexGen design still relies on components from the Park burner, and further improvement can be made to update the NexGen design and to simplify the specification for set up and operation.

1.2 Measurement Techniques for NexGen Burner Analysis

The present investigation is focused on identifying burner parameters that influence burner performance. Since the burner flame is controlled by the burner airflow and fuel spray, fluid flow measurement techniques were considered the most advantageous method of acquiring data to identify flow patterns created by the burner components. Of the available methods for flow measurement, particle image velocimetry (PIV) was chosen for its whole field, non-intrusive velocity measurement capability, wide range of measurement resolution from zero to supersonic, and large data set acquisition for statistical analysis of flow properties. PIV relies on the illumination of a single plane in the cross section of a particle-seeded flow field by a high power, pulsed Nd:YAG laser through a series of lenses creating an instantaneous sheet of light, essentially freezing the motion of the particles as viewed by a triggered CCD camera. An image pair is created by capturing two images separated by a specified time interval, Δt . Each image is divided into small subsections called interrogation areas (IA). Each interrogation area contains particles that are assumed to shift with the flow from image 1 to image 2. The interrogation areas from image 1 and 2 are cross-correlated, producing a signal peak that identifies the common particle displacement in pixels. The local displacement vector is calculated by dividing the displacement of the particles in pixels by the time interval between images Δt . The magnification factor of the image, in pixels per millimeter, is used to obtain the local velocity vector in standard velocity units of meters per second [21].

PIV can also be used to resolve the out of plane velocity component with the use of an additional camera and proper alignment and calibration. The cameras are configured so they observe the light sheet plane from two different angles, resulting in slightly dissimilar two-component velocity vector fields from the same measurement plane. The difference between the two vector fields arises from the third, out of plane component. Proper camera mounts, called Scheimpflug mounts, are required to allow the whole light sheet plane to be clearly focused on the CCD by slightly misaligning the CCD sensor and the camera lens. A standard target is used to calibrate the cameras in the light sheet plane as well as just outside of the light sheet plane, giving the ability to resolve the out of plane component properly. Not only does PIV have the ability to resolve an entire three component velocity field, but due to its non-intrusive measurement technique it can also be used in harsh environments, including flames. Measurements on reacting flows require that the seed particles withstand the high flame temperatures. Also, for highly luminous flames, narrow-band camera lens filters are required to block all light except for that reflected off the particles from the 532 nanometer wavelength laser sheet. The versatility of PIV makes it extremely useful for measuring NexGen burner flow properties, both non-reacting and reacting, and can be used for other research and development applications by FAA Fire Safety.

1.3 Review of Literature

PIV is a versatile measurement technique that has been used for a wide variety of measurements from micro scale flows on blood flow in micro channels to full scale flows

around ships and airplanes. Analysis of the NexGen burner begins with developing comparisons between the flow conditions of the burner with those from previous experimental investigations with PIV of similar flows.

The Turbulent Jet. The flows created by the NexGen burner can be viewed as a turbulent jet – one of the most studied flows in fluid dynamics due to the simplified theoretical analysis and experimental measurement. Fluid emerging from a round nozzle into a quiescent medium interacts with fluid from the surroundings and forms a jet. A jet is considered free when not influenced by walls or boundaries. After separation from the solid surfaces of the interior jet nozzle the surfaces no longer influence the development of the jet. Free jets have different regions with unique characteristics and relations. The potential core is the region immediately downstream of the nozzle exit. The velocity and concentration within this region remains unchanged from when the flow was inside the pipe. The potential core typically extends for the first five to ten pipe diameters downstream of the jet exit. Outside the boundaries of the potential core lies the mixing region in which a free boundary layer develops and mass and momentum are transferred perpendicular to the direction of the flow. A transition region lies between the potential core and the fully developed flow region, typically ten diameters long. The fully developed region is self-similar, and general relationships can be used to describe the axial and radial velocity distributions as a function of the axial distance and radial position.

The axial velocity at any point on the jet axis downstream of the potential core is independent of the nozzle diameter if the distance is measured in terms of the nozzle diameter, x/d . The initial jet exit velocity u_0 , normalized by the centerline axial velocity, u_c , is proportional to the axial distance, x , normalized by the nozzle diameter d

$$\frac{u_0}{u_c} \propto \frac{x}{d} \quad (1.1)$$

And the jet spreads linearly according to

$$\delta(x) \propto x \quad (1.2)$$

Where $\delta(x)$ is the full jet width defined as the width of the Gaussian velocity profile at the point which the velocity has decreased to 5% of the centerline value. Self-similarity dictates that all velocity profiles will collapse onto one similar curve. At any axial distance x in the fully developed region the corresponding axial velocity u relative to the centerline velocity u_c at that axial distance is a function of the radial position r normalized by the axial distance x

$$\frac{u}{u_c} \propto e^{-k_u \left(\frac{r}{x}\right)^2} \quad (1.3)$$

For every axial position x , the velocity profiles $u(x)$ all collapse on to a single profile. The constant k_u is found to have values between 82 and 92 for turbulent jets [22]. The local Reynolds number in an axisymmetric jet will remain constant at all downstream axial distances x since the centerline velocity and jet width scale inversely and directly proportionally, respectively, with axial distance x [23]

$$Re_x = \frac{\delta(x)u_c}{\nu} \quad (1.4)$$

Fluid from the surroundings becomes entrained across the jet boundaries resulting from momentum exchange between the jet and the surrounding fluid. The friction between the jet and the surrounding fluid creates a shear layer where the velocity gradients are normal to the velocity direction. Fluid is entrained, but if no external forces are acting on the jet and there are no pressure gradients, the momentum flux is conserved. The momentum crossing a plane perpendicular to the jet axis remains constant downstream of the jet exit and equal to the jet exit momentum flux. As the jet entrains ambient fluid, the mass flux of the jet increases, the jet spreads radially, and the velocity must decrease in order for the momentum to be conserved. The total momentum flow per unit time in the axial direction is

$$J_0 = \int_A \rho_0 u_0^2 dA = \frac{\pi d^2}{4} \rho u_0^2 \quad (1.5)$$

Since no external forces act on the jet the momentum flux $J(x)$ at any axial location must remain constant and equal to the source momentum flux J_0 . In the self-similar portion of the flow the source momentum flux is the only integral invariant of the flow, so the jet width $\delta(x)$ and the local centerline velocity u_c can only depend on J_0 , x , and ambient fluid density ρ_∞ [24]. Measurements in jets with laser-doppler anemometry (LDA) [25] determined the relations to be

$$u_c(x) = 7.2(J_0/\rho)^{1/2}x^{-1} \quad (1.6)$$

$$\delta(x) = 0.36x \quad (1.7)$$

Jets in coflowing parallel streams will have different velocity gradients normal to the flowing direction compared with jets issuing into a quiescent environment. The turbulent

mixing is dependent on the velocity gradients; therefore the amount of mixing will change depending on the relative velocities of the jet and the coflow. As the coflow velocity is increased to match the jet velocity, the velocity gradients will decrease to a point of minimum mixing, and reducing the rate of jet spread and velocity decay. The potential core region will also extend throughout the flow field when the jet and coflow velocities are equal. When the velocity of the coflow is increased well beyond that of the jet, velocity gradients increase, resulting in increased mixing. Jets in coflows will have mean velocity values composed of the coflow velocity, U_∞ , and the excess velocity, U_0 . The excess mean velocity is found by subtracting the total measured velocity by the coflow velocity for better comparison with free axisymmetric jets.

Early experimental investigations in [26], [27], [28] failed to obtain self-preservation of the turbulence intensities. Linearized constant temperature hot-wires were used in [29] to make accurate measurements in the self-preserving jet by integrating over long time periods to obtain good statistical averages. These results have become the standard reference for the quantification of jet velocity and turbulence, and for validation of numerical simulations. Variations in the experimental configuration of the jet enclosure and measurement techniques have been found to influence data, as demonstrated in [30], recommending that the historical experimental data may not necessarily be trusted for validation of experimental results or numerical models.

The validation of the current PIV measurements required comparison of velocity measurements to published data. The round turbulent jet has been widely studied in experimental fluids with pitot tubes, hot wire anemometry, and laser diagnostics. Papanicolaou and List 1987 investigated round vertical turbulent buoyant jets with laser Doppler velocimetry (LDV), though they presented measurements from fully developed self-similar turbulent jets at around Reynolds number 11×10^3 for validation [25]. Fukushima et al. 2000 investigated the mixing process in an axisymmetric turbulent jet using PIV and PLIF, also providing data of the turbulent jet at Reynolds number 2×10^3 [31]. Boersma et al. performed direct numerical simulation (DNS) of spatially developing free round jets at Reynolds number 2.4×10^3 , which will be useful for comparison of measured velocity values with theoretically-derived DNS calculations [32]. Borean et al. studied the effect of a coflowing stream on the structure of an axisymmetric jet, and found that the streamwise variation of the excess mean velocity, jet expansion, and spanwise distribution of the longitudinal normal Reynolds stress are close to that observed on free jets [33]

PIV on Reacting Flows and Sprays. Though the non-reacting flow of the NexGen burner will be analyzed, insight can be gained from previous work on measurements of reacting flows with PIV. Fundamental aspects of PIV must be considered when attempting to measure a reacting flow, including high temperature seed material, flame luminosity, and optical access [21]. Metal oxide particles such as alumina or silica have been proven to be suitable flame seeding materials and are widely available. Flame

luminosity caused by broadband emission of strongly radiating soot particles will saturate the typically long-exposed second PIV frame, making peak detection difficult. Narrow-band lens filters can be used to eliminate all but the laser wavelength light, 532 nm for Nd:YAG lasers. Electromechanical or electro-optical external camera shutters can also be used if the filters are not adequate. Optical access for the light sheet and cameras to reacting flows can be limited due to measurements in high pressure combustion chambers or extreme temperatures near the region of interest [34]. Limited viewing angles can also limit the use of stereoscopic PIV for obtaining the out of plane component, requiring alternative methods such as combined PIV and Doppler global velocimetry (DGV) [35].

Analysis of a gun-type oil burner was conducted in [36] with stereoscopic PIV measurements on the reacting flow exiting the oil burner, focusing on the evaporation of the fuel spray droplets and the determination of droplet movement at the burner exit [36]. Sprays from a gun-type burner were analyzed in [37], developing a multi-intensity-layer PIV technique to detect velocity and droplet size simultaneously [37]. A comprehensive review of swirl flows in combustion was presented in [38] describing swirling flow characteristics for industrial burners. An experiment was designed to use PIV to analyze liquid fuel injectors for gas turbine burners by simulating high pressure combustor conditions with a high density fluid [39]. The authors describe the use of a standard PIV system to analyze the fuel spray in a simulated combustion chamber.

Simultaneous planar-laser induced fluorescence (PLIF) and PIV were used in [40] to investigate the stabilization region of turbulent lifted jet diffusion flames. The PLIF measurements acquire the scalar concentration fields while the PIV measurements acquire the velocity fields. Glycerol-water fog droplets are used to seed the flow field. Since the fog evaporates at 100°C the interface between high and low seed density on the acquired images indicates the flame front. In this case it was advantageous to use seed material that does not survive the high temperature flame to identify the location of the flame front and study the stabilization mechanisms of the turbulent lifted jet. Stereo PIV (SPIV) was used in [41] to study the non-reacting and reacting flow field created by a low swirl lean premixed prevaporized burner concept. Propylene glycol droplets were used to seed the non-reacting configuration while titanium dioxide particles were used to seed the reacting flow. The burner provided a lifted flame that allowed good optical access to the whole recirculation zone for both hot and cold flow.

Combined stereo SPIV-planar laser Rayleigh scattering (PLRS) was used in [42] to study the turbulence and temperature fields of turbulent lean methane/air flames from a Bunsen burner. The flame-generated turbulence was investigated by independently measuring the turbulence parameters of the burnt and unburnt gases. A threshold setting procedure was developed to separate the burnt and unburnt gases in the raw PIV images. The expansion of the reacting gases leads to a sharp density gradient between the burnt and unburnt regions. An image processing procedure is used to separate the burnt and

unburnt gases in the raw PIV images for independent analysis of the turbulence properties.

A droplet size classification technique was used to resolve the three-dimensional velocity field of the non-reacting spray flow emerging from a gun type burner in [43]. The size of the droplets was used to separate the raw PIV images into different layers by defining a scattered light distribution depending on the intensity of the particle images. For particles that are large relative to the wavelength of the reflected light, the intensity of the scattered light is proportional to the droplet square diameter [44]. The raw SPIV images were filtered into layers depending on the pixel intensity and sets of three size classified images were created for each image. The movement of the particles was then analyzed as a function of droplet size. It was found that the larger droplets have stronger penetration and do not follow the incoming airflow while small droplets follow the incoming airflow and entrain the recirculation zones.

The current investigation utilizes aspects of previous research with PIV on burners, sprays, and turbulent fluid flows to design an experiment capable of analyzing the NexGen burner flow field with PIV and determine the effect of individual parameter on the burner flow field, and to correlate these parameters with flame temperature measurements and material burnthrough times.

1.4 Dissertation Outline

This current investigation focuses on the analysis of the FAA NexGen fire test burner with particle image velocimetry. The intent is to correlate the measured flow fields with the standard burner performance metrics of flame temperature and burnthrough time that are performed when using the burner for certification of aircraft materials. A solid understanding of the fundamental flow properties created by various burner configurations is crucial to developing an updated standardized burner configuration for use around the world for aircraft materials fire testing and airplane certification. It is desired that the burner be simple to construct, calibrate, and use; therefore the configuration of the burner components should be simplified as much as possible in order to reduce errors during construction and set up.

Chapter 2 describes the test apparatuses and procedures used in this investigation including the PIV setup and NexGen oil burners. Chapter 3 presents results gathered from analysis of the burner components, isolated to determine individual and combined effects on flow fields. The non-reacting burner exit flow fields are resolved for the following configurations:

- Baseline flow field – empty draft tube
- Insertion of fuel pipe
- Stator – effects of axial position relative to draft tube exit
- Turbulator – effects of area reduction and turbulator vanes
- Fully configured NexGen burner exit airflow at multiple cross-streamwise planes

- Fully configured NexGen burner – visualization of non-reacting unconfined swirling jet flow with stereoscopic PIV
- Spray nozzle spray pattern – effect of nozzle rotation on spray pattern symmetry
- Burner cone exit flow field – measurement at multiple cross-streamwise planes and stereoscopic PIV measurement at the exit plane, correlation of non-reacting cone exit flow field with measured flame temperature profiles, comparison with unconfined swirling flow field in same volume
- External flow around burner cone – measurement of entrained ambient air into non-reacting cone exit flow, vorticity of cone exit flow

Chapter 4 describes measurements made on potential design improvements based on the results of Chapter 3. The draft tube exit velocity fields, flame temperatures, and material burnthrough times were measured for each configuration and compared to the baseline configuration. The design improvements include:

- Redesigned stator with no igniter holes (symmetric stator)
- Flame retention heads
- Fuel spray nozzle from different manufacturer
- Burner cone with reinforcement ring around exit plane

Chapter 5 summarizes the results obtained in this investigation and provides insight for design changes of the NexGen burner as well as recommendations for further research on the NexGen burner.



Figure 1.1 Photograph of the original FAA fire test methods, the horizontal Bunsen burner (left) and the vertical Bunsen burner (right).



Figure 1.2. Examples of post-crash fire accidents: ONA Flight 032 at JFK airport, New York, 1975 (top) and Continental Flight 603 at LAX, Los Angeles, 1978. The accidents are considered survivable in that the passengers are fully capable of exiting the aircraft, though the effects of the external fire on the cabin materials significantly reduce survivability time.

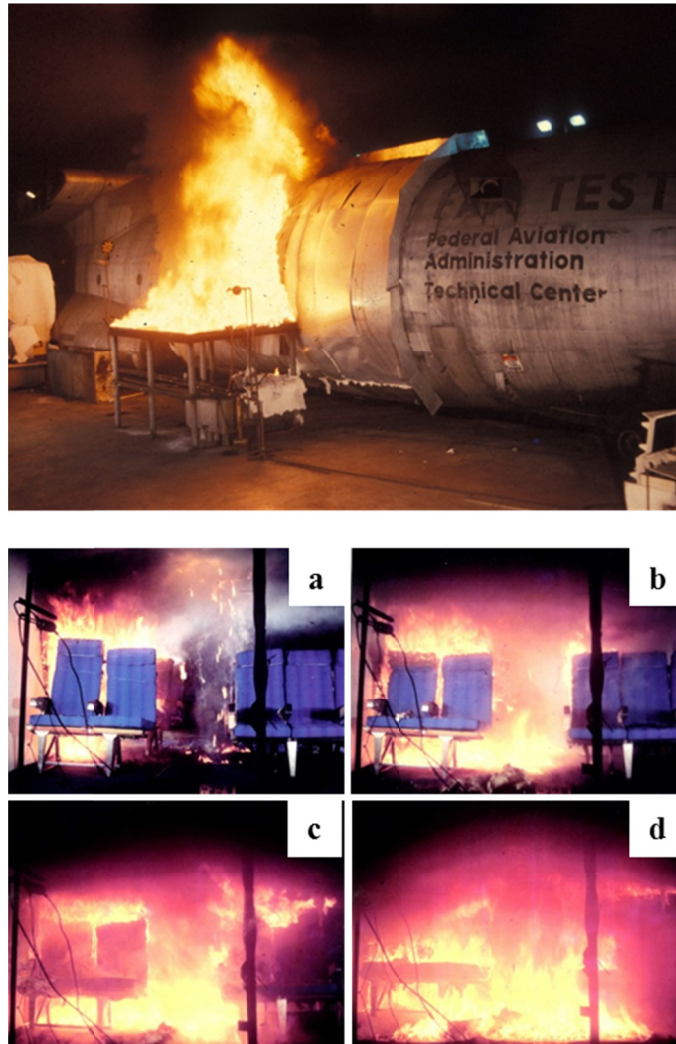


Figure 1.3. Full scale post-crash fire test photographs. Top: An external fire is positioned adjacent to a fuselage opening. Bottom: Interior view. The cabin interior is mocked up with aircraft-grade furnishings including sidewalls, stowbins, and seats. The cabin is instrumented with cameras, temperature measurement, and gas sampling. Test progression at 60 seconds (a), 90 seconds (b), 100 seconds (c), and 105 seconds (d).



Figure 1.4. Post-accident photograph of Saudi Arabian Airlines Flight 163 at Riyadh, Saudi Arabia, August 19, 1980. A fire originating in a class D cargo compartment breached the cargo lining materials, allowing oxygen to fuel the fire and flames to spread to the passenger cabin. The plane successfully landed but flashover occurred before evacuation was initiated. All 301 persons aboard perished.

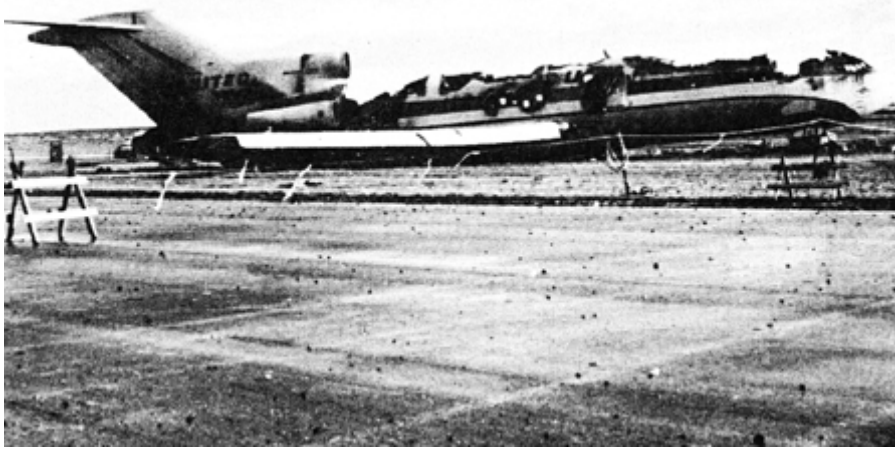


Figure 1.5. Post-accident photograph of United Airlines Flight 227 at Salt Lake City, Utah, November 11, 1965. An excessive sink rate on approach to SLC led to touchdown 335 feet short of the runway, shearing off the main landing gear, rupturing fuel lines and generator power cables, causing a large external fuel fire. Cabin materials quickly caught fire, incapacitating 43 of the 85 passengers aboard. Subsequent analysis indicated that the accident was completely survivable, as all victims perished not from impact forces but from the effects of fire.

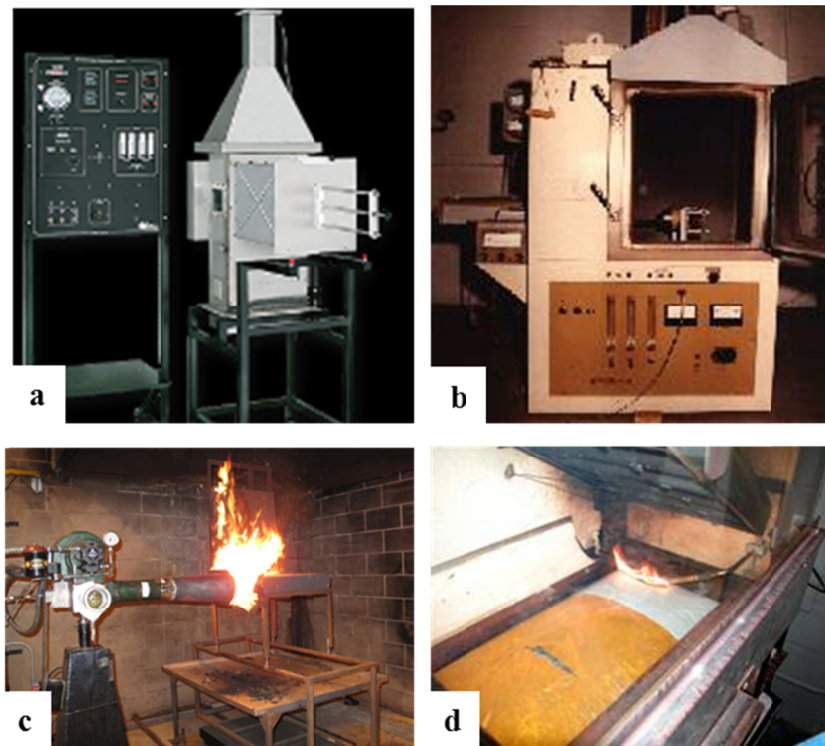


Figure 1.6. Improved Laboratory Scale Test Methods: rate of heat release of cabin interior materials (a), smoke density of cabin interior materials (b), seat cushion flammability (c), flame propagation for thermal acoustic insulation (d).

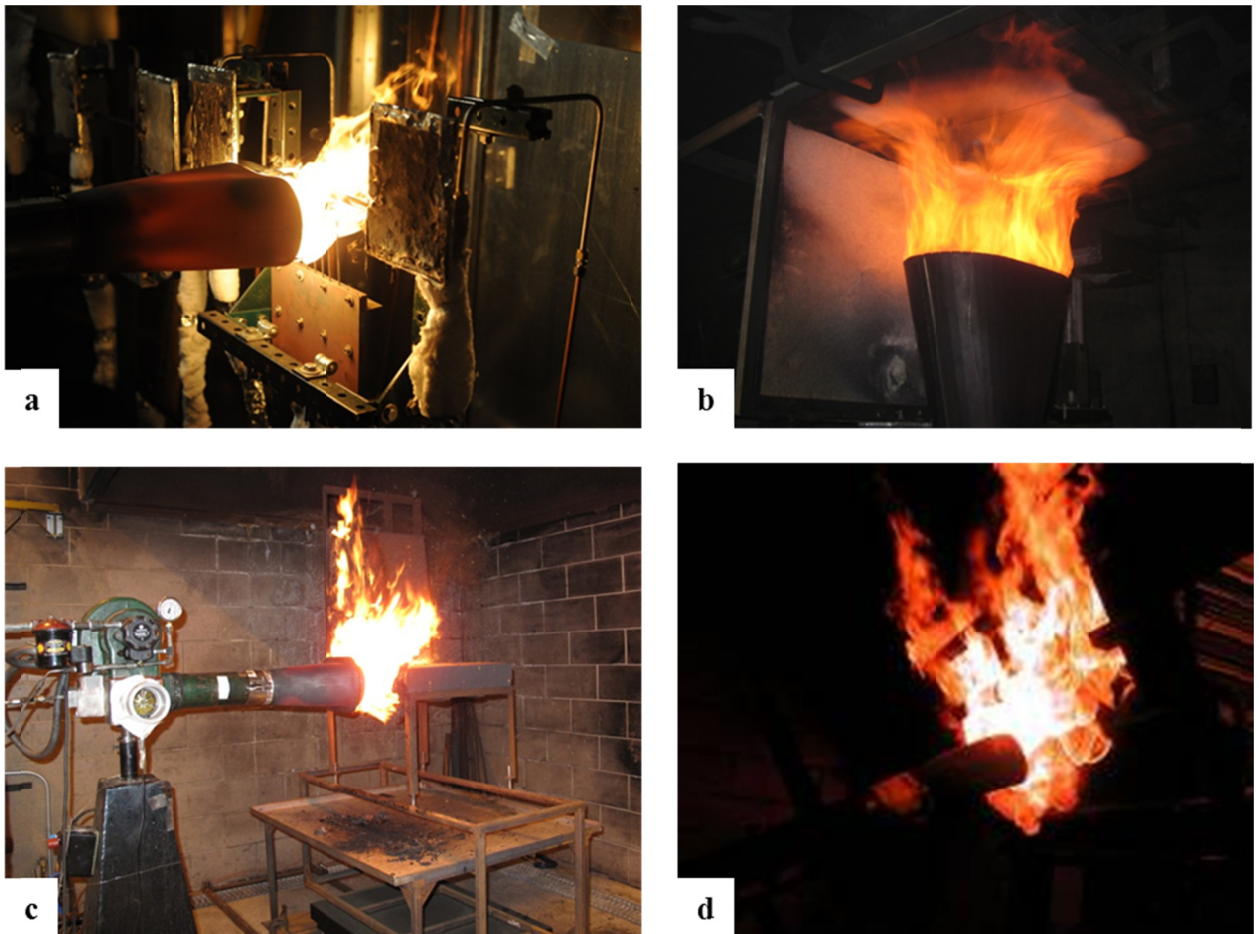


Figure 1.7. FAA oil burner test methods: powerplant components (a), cargo liner burnthrough (b), seat cushion flammability (c), thermal acoustic insulation burnthrough (d).



Figure 1.8. Park DPL3400 oil burner (a) and internal components stator (b), fuel nozzle (c), and turbulator (d).

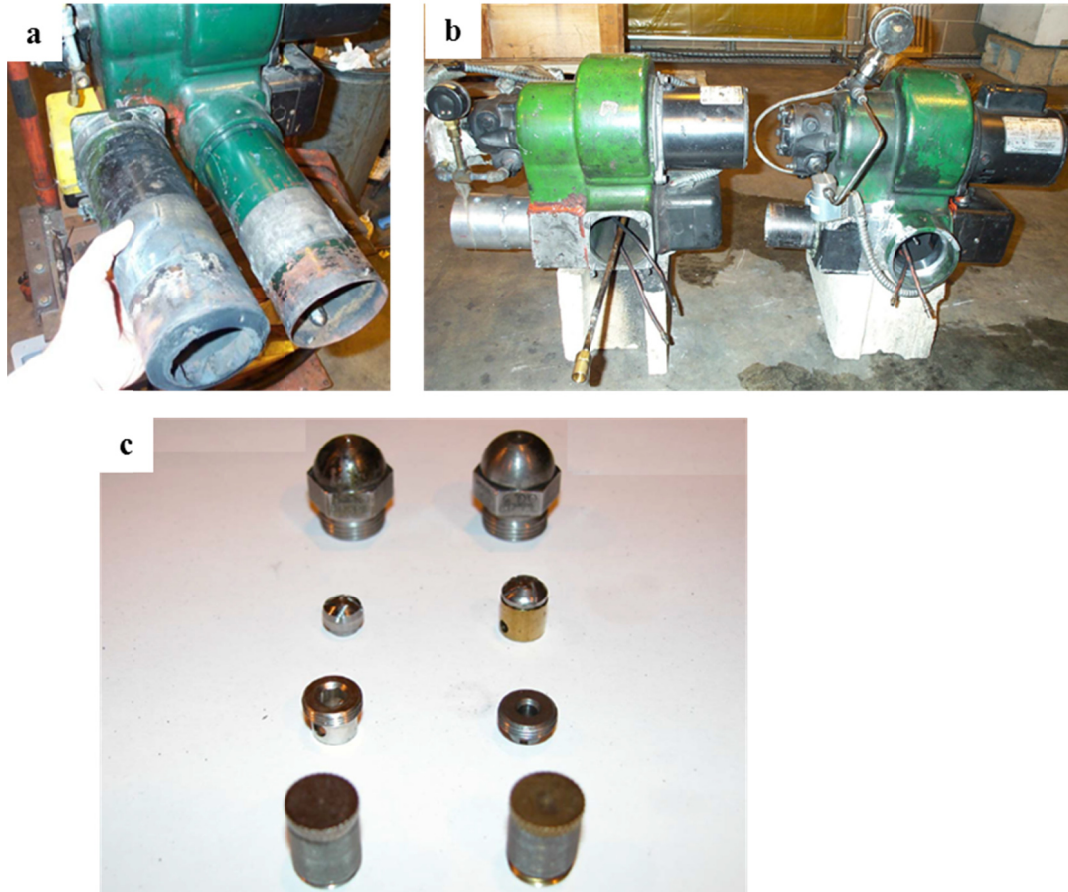


Figure 1.9. Discrepancies amongst Park DPL3400 burners: draft tube length (a), different burner castings have either flanged (left) or socket (right) draft tube connections (b), fuel spray nozzles with same flow rating and spray pattern with different internal components (c).

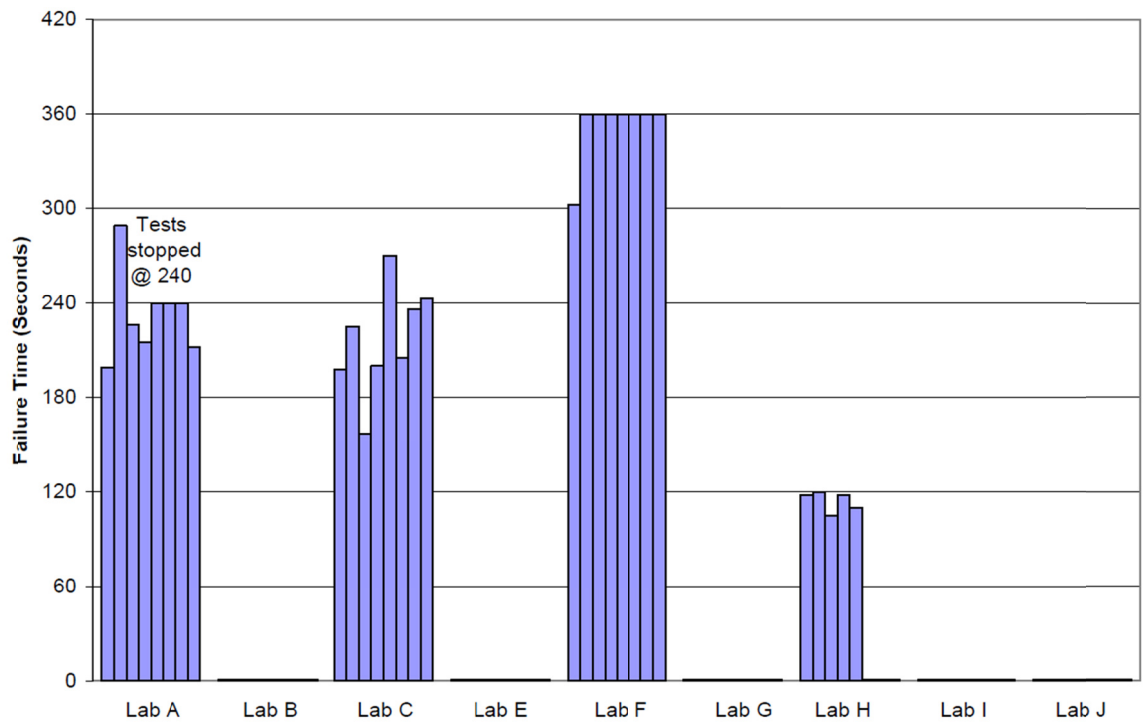


Figure 1.10. Results from a worldwide comparative test series of the Park DPL3400 for thermal acoustic insulation burnthrough testing in 2005. A material fails the test if burnthrough is observed before 240 seconds. In this case, one lab would pass all samples, one lab would fail all samples, and two labs pass some and fail some.

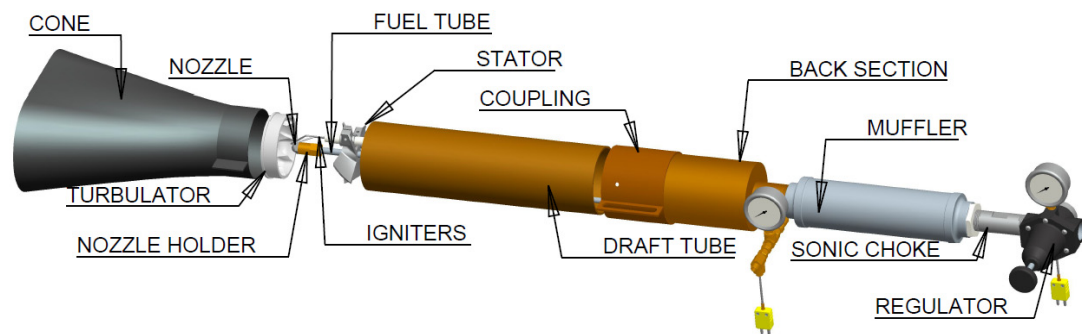


Figure 1.11. Exploded view of a 3D model of the final design of the NexGen burner. This exploded view shows the burner housing and internal components: stator, turbulator, fuel pipe, fuel nozzle, and igniters and external components: air pressure regulator, sonic choke, muffler, and cone.

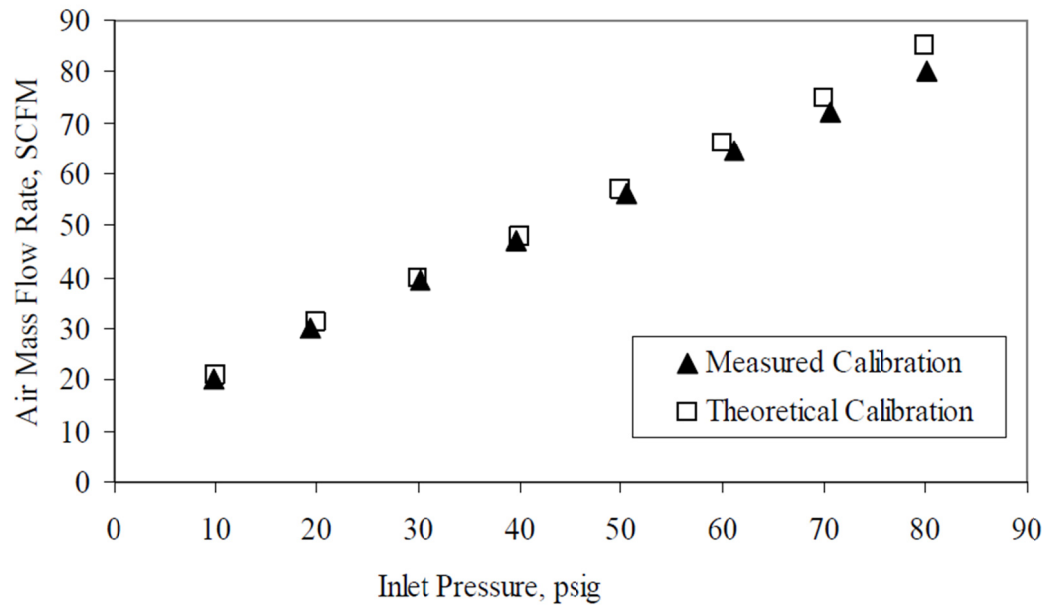


Figure 1.12. Air mass flow rate, in standard cubic foot per minute, as a function of sonic nozzle inlet pressure for the NexGen burner. Comparison of theoretical calibration with the mass flow rate measured with a vortex shedding type mass flow meter. Slight deviation at higher mass flow rates occurs due to the range limitation of the mass flow meter calibration.

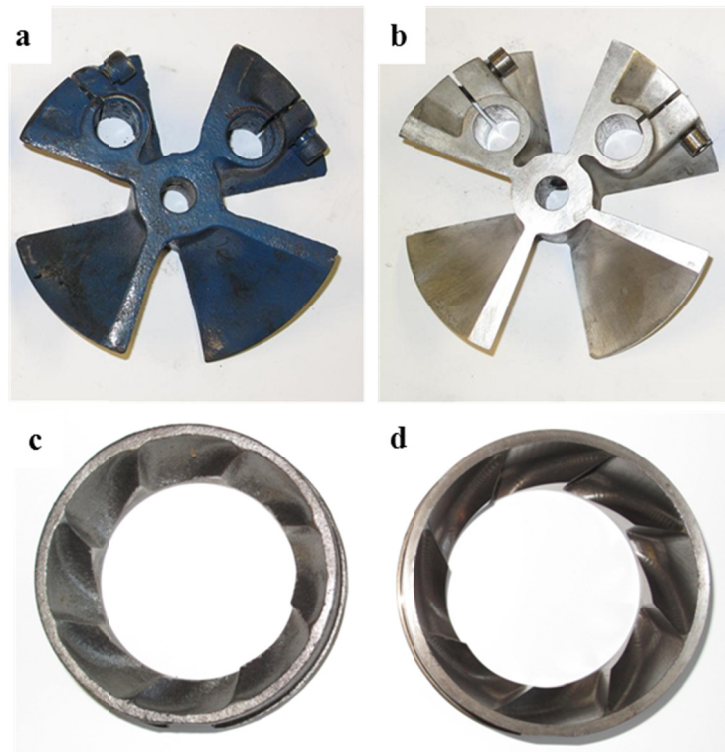


Figure 1.13. Comparison of original and re-engineered stator and turbulator. The original stator and turbulator (a and c, respectively) were cast from a mold, while the updated stator and turbulator (b and d, respectively) were modeled in 3D CAD software from the original stator, corrected to be symmetric, and CNC machined.



Figure 1.14. Photographs of the original stator (a,b) and turbulator (c-e). The stator is nominally 101.6 mm in diameter, but some castings are not to specification (a). The stator is also asymmetric about the center hole (a,b). The turbulator opening should be centrally located, but is cut off-axis, resulting in a skewed exit plane (c, d). The turbulator profile view in (e) shows the off-axis direction of the exit plane.

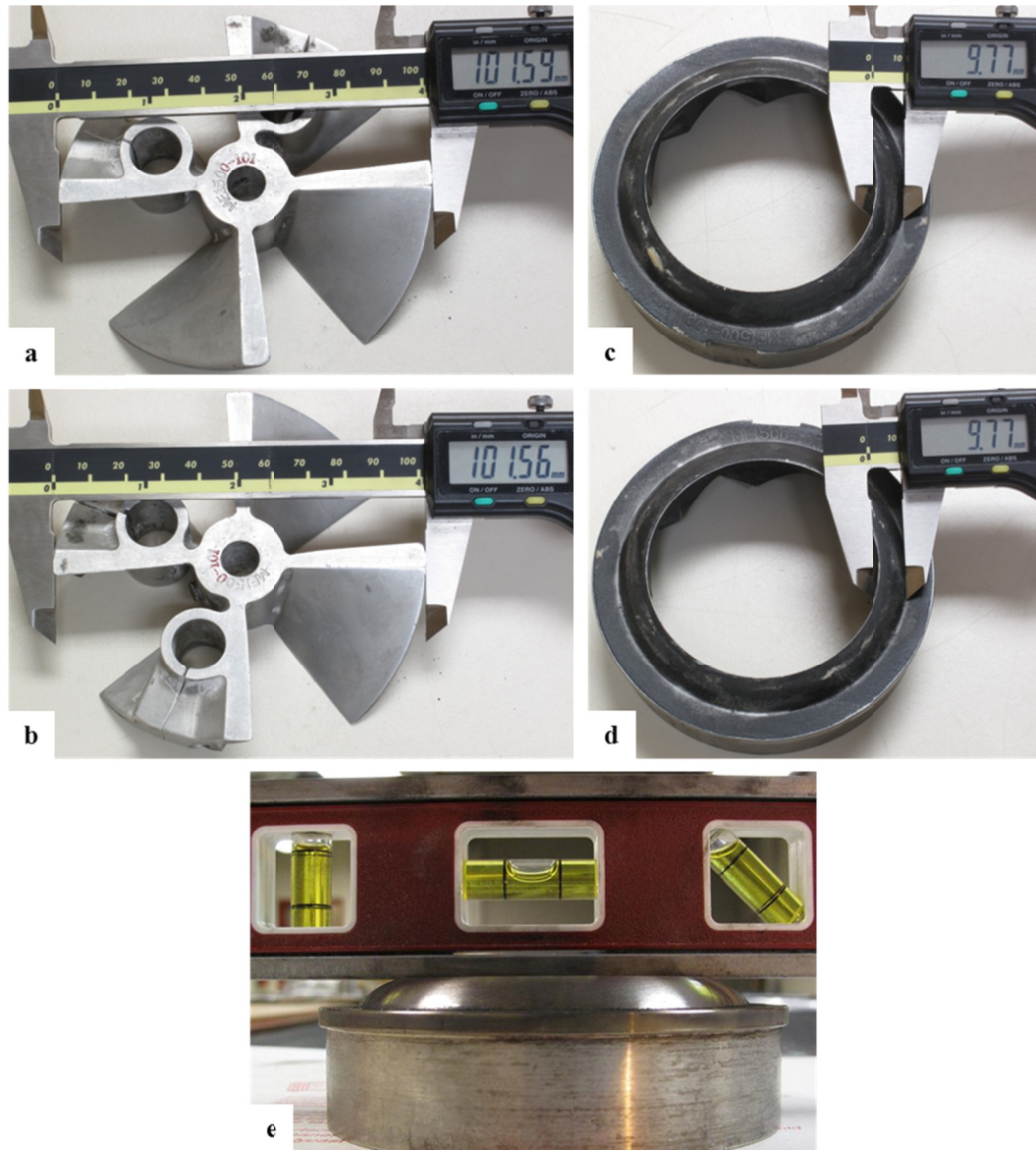


Figure 1.15. Photographs of the updated stator (a,b) and turbulator (c-e). The diameter of the new stator is closer to the nominal value of 101.6 mm (a) and is now symmetric about the central hole axis (a, b). The turbulator opening has been corrected to be centrally located (c, d) and the exit plane is seen to be straight in the profile view (e).

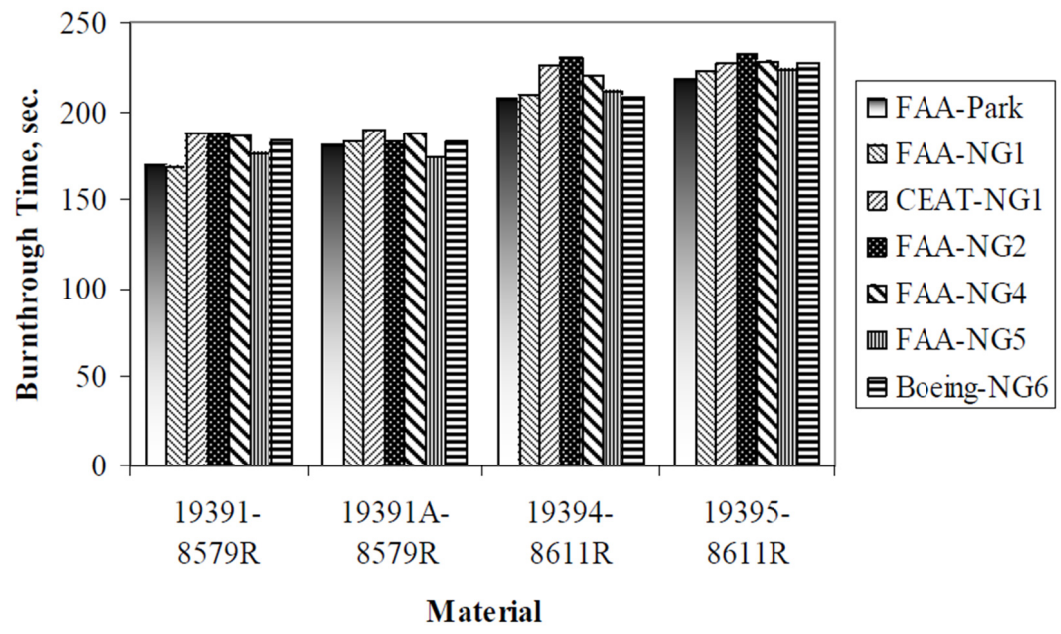


Figure 1.16. Worldwide NexGen burner comparative test results. Burnthrough time in seconds vs. material type for each laboratory-burner combination. The labs were Federal Aviation Administration, Centre D’Essais Aeronautique Toulouse, and Boeing.

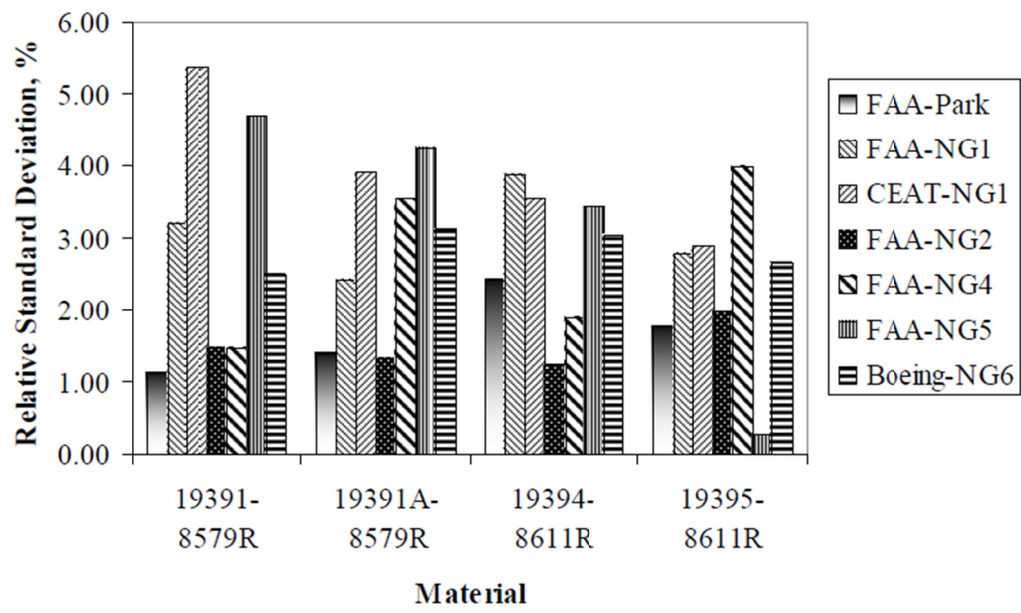


Figure 1.17. Worldwide NexGen burner comparative test series repeatability. Relative standard deviation vs. material type for each laboratory-burner combination. The labs were Federal Aviation Administration, Centre D'Essais Aeronautique Toulouse, and Boeing.

2 Experimental Apparatus

This chapter describes the equipment used to analyze the FAA next generation fire test burner. There were three setups used: Particle Image Velocimetry in the FAA Fire Safety Flow Visualization Lab, flame temperature measurements on the FAA next generation seat cushion fire test burner, and flame temperature measurements and material burnthrough tests on the FAA next generation thermal acoustic insulation fire test burner. Each apparatus will be described in the following sections.

2.1 Flow Visualization Laboratory

Particle Image Velocimetry (PIV) was chosen for this work due to its capability to analyze a whole flow field non-intrusively in rapid succession, allowing for collection of large amounts of data in relatively short periods of time. Since the Fire Safety Branch did not previously have a PIV system or experience with PIV, a large portion of this work was dedicated to specifying, purchasing, setting up, and learning PIV from the basics. A commercial system was desired, as all components would be packaged together with software for analysis, and basic training would be included with the purchase. A

commercial system was purchased from Dantec Dynamics, with capability for stereoscopic PIV. The system included a pulsed 120 mJ 532 nm laser with maximum pulse rate of 15 Hz. The light sheet optics were attached to an adapter that mounted directly to the laser aperture. A 90° attachment was included to make the laser head adaptable to various acquisition configurations. Two 1600 by 1200 pixel cameras were included, along with several camera lenses with variable focal lengths up to 180 millimeters for a variety of measurement plane sizes. A computer workstation with quad-core processor and 4 GB RAM was included for acquisition and analysis, complete with camera and synchronizer plug-in cards. A complete acquisition and analysis software package was pre-loaded on the PC.

The PIV system was set up in test cell #2 of the FAA Fire Safety Branch Aircraft Components Fire Test Facility. The room is 1600 ft² with 20 foot ceilings and a full-length rollup door. It is fully conditioned and maintains a year-round temperature between 60 and 70°F with low to moderate humidity. A PIV test chamber was constructed and placed in the test cell to create an experimental enclosure free of room drafts. The chamber, displayed in Figure 2.1, measures 1.2 meters wide by 1.2 meters high by 2.4 meters long, resulting in a total volume of 2.45 cubic meters. The frame was constructed from extruded aluminum T-slot framing with sheets of 6.35 millimeter thick acrylic enclosing the chamber allowing for optical access from all angles. The laser head was mounted to a custom-built traversing mechanism fixed above the top sheet of acrylic. The traversing mechanism allowed for the light sheet to be precisely moved in the x - w

plane relative to the standard coordinate axes. An internal traversing mechanism controlled from outside the chamber was constructed to allow for mounting of calibration targets and alignment with the light sheet. Two exhaust louvers with variable flow gates were mounted in the lower portion of the back acrylic panel to allow for exhausting of particles after testing. A sawdust extractor with a 1.5 horsepower, 1,200 cubic foot per minute motor and one micron filter was used to evacuate the chamber through two 10 centimeter diameter flexible hoses. A computer-controlled three-dimensional traversing mechanism was used to mount the cameras external to the experimental chamber. Figure 2.2 displays a schematic of the single-camera 2D measurement setup (a) and the dual-camera stereoscopic 3D PIV measurement setup (b) used in the current investigation.

A solid particle powder seeding generator was used to introduce seed particles into the airflow to be measured. The generator consisted of a pressure vessel with compressed air inlet and powder outlet. The inlet air pressure was controlled by a pressure regulator mounted upstream of the vessel. Inside the pressure vessel is a removable drum connected to a small DC motor controlled by a variable DC power supply. The drum contains the seed powder and disperses it through a hole on one side as it rotates. The powder that falls out of the drum is then mixed with the compressed inlet air and directed to the vessel outlet, which is then plumbed to the apparatus. The rotation rate of the drum is regulated by the DC voltage applied, and corresponds to the seeding rate of the system. Aluminum oxide powder, Al_2O_3 at 99.5% purity and 15 μm in size, was chosen as the seed particle. According to [45] the scattering of light by the particles is size-dependent.

The scattering cross section C_s defined as the ratio of the total scattered power P_s to the laser intensity I_0 incident on the particle:

$$C_s = \frac{P_s}{I_0} \quad (3.1)$$

The light scattering cross section for a particle of diameter 1 μm is approximately 10^{-12} m^2 , whereas for a particle of diameter 10 μm is approximately 10^{-9} m^2 . The alumina particles chosen for this work are found to scatter sufficient light for imaging and follow the large structures in the flow field. Though the present work focuses on non-reacting flows, a seed generator and particle type was chosen that was more universal in applications to non-reacting and reacting flow studies in the future.

PIV Analysis Routine. The PIV images were analyzed in the commercial software included with the system. An adaptive correlation technique, which is an iterative form of cross correlation, was used to calculate the velocity vectors from the images. Cross correlation compares pixel intensity from an interrogation area in image 1 to the pixel intensity in the same interrogation area in image two, the images separated in time by Δt . The information is transformed using Fast Fourier Transform and spatial cross-correlation to estimate displacement functions and the highest peak in the correlation plane, which corresponds to the average particle displacement in that interrogation area. Bad correlations resulting in bad vectors can occur if particles leave or enter the interrogation area. Adaptive correlation compensates for this by using multiple cross correlations starting with an initial guess of the particle displacement that is used to

estimate a shift in the second interrogation area. The interrogation areas get iteratively smaller, allowing for more precision in subsequent steps, while reducing loss of pairs by capturing particles that enter or leave the interrogation area. An adaptive correlation with a 64 x 64 pixel interrogation area size was used with 50% IA overlap in the horizontal and vertical directions. 3 adaptive refinement steps with 2 passes per step were used along with a central difference IA offset. A criterion for minimum peak to peak height relative to peak 2 was set at 1.2. Moving average validation was performed in a 3 by 3 neighborhood size with 0.1 acceptance factor and 3 iterations. The vector statistics were computed from the array of vector maps generated, giving mean velocity, standard deviation, variance, and correlation coefficient. Data was exported from the PIV software and post-processed and plotted in MATLAB.

Experimental Validation – The Turbulent Jet. In order to proceed with analysis of the NexGen burner with PIV, it was first necessary to determine the measurement accuracy of the PIV system's velocity measurements. A turbulent jet was chosen for the validation measurement as it has been the subject of numerous experimental fluid measurement studies and a large amount of published data is available to compare the current measurements to. The jet properties are displayed in Table 2.1. The NexGen burner fuel pipe, with an inside diameter of 5.4 millimeters, was used as the jet nozzle, while the flow exiting the draft tube was used as a coflow to seed the flow around the jet for better measurement accuracy near the jet-ambient boundary. A schematic of the experimental setup is displayed in Figure 2.4, showing the burner draft tube as the coflow, the fuel pipe

as the turbulent jet, the laser head mounted above the enclosure aligned with the vertical burner axis, and the measurement planes. The seeder was plumbed to both the jet tube and the draft tube for uniform seeding of both flows. The camera was mounted on the traverse in order to translate the measurement plane downstream to acquire a larger portion of the jet flow field. Four different acquisitions were run to obtain four total measurement planes with an overall measurement plane size of 50 diameters long by 14 diameters high centered on the jet axis, starting 19 diameters from the jet nozzle exit ending at 70 diameters downstream.

The mean jet velocity field at each measurement plane was obtained from 500 image pairs at a sample rate of 8 frames per second. Figure 2.5 displays the mean axial velocity field from $x/d=20-70$ downstream of the jet exit plotted against the axial and radial directions, both normalized by the nozzle inner diameter d . The axial velocity U is normalized by the jet centerline velocity u_c for comparison to results at different Reynolds number. The jet is seen to be symmetric about the nozzle axis and expands in the radial direction as it moves downstream. The measured axial velocity field agrees well with previous experimental work [46]. The mean radial velocity field is displayed on identical axes in Figure 2.6. The radial velocity is nearly symmetric about the nozzle axis, though more positive radial velocity is found on the top portion of the jet. This is due to a somewhat elevated temperature of the jet air compared to the coflow and chamber air, causing the jet to be slightly buoyant.

The axial and radial velocity fluctuations are displayed in Figure 2.7 and Figure 2.8, respectively. The fluctuations are normalized by the jet centerline velocity, u_c . Both sets of data can be seen to be symmetric about the nozzle axis with values below 27% of the centerline velocity and the axial fluctuations being greater in magnitude than the radial fluctuations. The Reynolds stress $\overline{u'v'}$ is plotted in Figure 2.9 normalized by the square of the jet centerline velocity. It can be seen to be antisymmetric about the nozzle axis, agreeing well with previous experimental work [46] [47].

For further validation of the current experimental setup, the normalized profiles of velocity, turbulence, and energy can be used to compare directly to previous experimental data. Figure 2.10 displays the excess mean axial velocity, normalized by the local jet centerline velocity $u_c(x)$, plotted against the normalized radial position $r/(x-x_0)$. Five downstream locations, $x/d=30, 40, 50, 60,$ and 70 , are plotted against the local axial position, $r/(x-x_0)$. The current results are compared to published data from previous experimental works measuring axisymmetric free jets with laser-Doppler anemometry and PIV [25] [31], coflowing axisymmetric jets with stationary hot wires [33], and DNS calculations [32]. The axial velocity profiles for all downstream locations collapse to a single profile due to normalization of the magnitude and position, and assume a Gaussian type curve. The current results compare well with the published data from [33] with a coflowing axisymmetric jet, and [31] [25] for free axisymmetric jets without coflow. Figure 2.11 displays the variation of the initial jet velocity, U_0 , normalized by the local excess centerline velocity $u_c(x)$ for the current measurement at $x/d=40, 50, 60, 70$. The

longitudinal variation of the ratio of the exit velocity to the local centerline velocity is seen to be linear, similar to the relations found in [33], [29], and [30].

The normalized mean radial velocity profiles are displayed in Figure 2.12 at five downstream locations, $x/d=30, 40, 50, 60,$ and 70 , plotted against the local axial position, $r/(x-x_0)$. The current measurements are compared with data extracted from [31] with error bars indicating the scatter in values at each radial position. Both results show high scatter due to the low absolute value of the radial velocity component and the PIV resolution, though the overall profile shape agrees with previous data.

The normalized axial RMS velocity fluctuation profiles at the same downstream locations are displayed in Figure 2.13. The current experimental results are again compared with data extracted from [31] and DNS calculations from [32]. The current measurements are found to be symmetric about the nozzle axis. The off-axis peaks of the axial velocity fluctuations can be seen in the current data, indicative of the location of shear production of kinematic energy typical of turbulent jets. The axial velocity fluctuation profile of the current work is seen to be slightly narrower than the published data due to the effect of the coflow limiting the radial growth rate of the jet. The results compare well, however, for the purposes of the current investigation. The normalized Reynolds stress profile $\overline{u'v'}$ is plotted in Figure 2.14 and compared with data extracted from [31] and DNS calculations from [32]. As was found earlier, the Reynolds stress is found to be antisymmetric about the nozzle axis with a range of about ± 0.02 . The current PIV

measurements were found to agree with published experimental data. These validation measurements give confidence in the PIV measurements made in the Flow Visualization Laboratory for the current investigation of the flow properties of the FAA next generation fire test burner.

2.2 NexGen Burner – Seat Cushion Test Apparatus and Procedures

A next generation fire test burner configured for seat cushion testing was utilized to make flame temperature measurements with 126 mL/min fuel nozzles that were later analyzed with PIV. The inlet mass flow rate of air, regulated by the sonic orifice, is 49 SCFM (0.028 kg/s). The burner is located under a smoke hood in Test Cell #1 of the FAA Fire Safety Branch Aircraft Components Fire Test Facility. It is a horizontally mounted burner, as pictured in Figure 2.15, and is set up to perform seat cushion flammability tests in a manner described in [48]. Table 2.2 displays the general flow properties for the NexGen burners.

Measurement of the flame temperature was done in the manner outlined in Chapter 7 of the FAA Aircraft Materials Fire Test Handbook [48]. Seven K-type, stainless steel sheathed, ceramic packed, grounded junction thermocouples, 1.6 millimeters in diameter, are used for the flame temperature measurement. The thermocouples are mounted in to a thermocouple holder that aligns them in the same plane, 25.4 millimeters apart, forming a thermocouple rake. The rake is mounted on to a rolling cart that can be pushed in front

of the flame and aligned with the burner cone exit plane, 101.6 millimeters from the cone exit plane and 25.4 millimeters above the horizontal cone centerline, with the center thermocouple aligned with the vertical burner cone axis. A schematic of the thermocouple measurement location is displayed in Figure 2.16. The thermocouples are connected to a data acquisition board via K-type thermocouple signal wire. The board is connected to a PC running custom data acquisition software that samples each thermocouple once per second. The following procedure is used to obtain flame temperature measurements. The burner is warmed up for two minutes with the thermocouple rake off to the side during warm-up. At two minutes the cart is rolled in to the flame positioning the thermocouple rake in the proper alignment with the burner cone. The thermocouples are heat soaked for one minute, at which point a thirty second measurement is made. The final flame temperature values are a thirty second average of each thermocouple channel. An overall flame temperature average is calculated by averaging the mean values from each of the seven thermocouples.

2.3 NexGen Burner – Insulation Burnthrough Apparatus and Procedures

A next generation fire test burner configured for thermal acoustic insulation testing was utilized to obtain flame temperature and material burnthrough data for the various burner configurations analyzed with PIV. The burner, pictured in Figure 2.17, is located under a smoke hood in Test Cell #1 of the FAA Fire Safety Branch Aircraft Components Fire

Test Facility. It is a six gallon per hour (378 mL/min) burner with a higher inlet air flow rate of 66 SCFM (0.0384 kg/s) compared to the seat cushion burner, though the overall construction and components are identical. It is mounted on a stand that orients it 30° from horizontal. Flame temperature measurements are made in an identical manner to the seat cushion burner, as displayed in Figure 2.16, though the thermocouple rake is mounted to a stand that orients it 30° from the vertical, making the thermocouples parallel to the burner cone exit plane. The rake is aligned at the same relative location, 101.6 millimeters from the cone exit plane, 25.4 millimeters above the horizontal cone centerline, and the center thermocouple is aligned with the vertical cone centerline. Average flame temperature measurements were acquired in an identical manner to the seat cushion measurements.

Material burnthrough data was obtained with this burner using a test frame and a specific material designed for measuring burner performance. The test frame, called the picture frame sample holder, is shown in Figure 2.18. It is constructed from 25.4 millimeter angle steel, 3.2 millimeters in thickness, and holds a sample material 457.2 by 812.8 millimeters in size. An inner frame, slightly smaller than the outer frame, is used to hold the material in the outer frame. Steel wires, 1 millimeter in diameter, are strung across the front face of the outer frame and the back face of the inner frame to lightly restrain the material during testing. The frame is mounted to a stand that orients the front face of the frame 30° from the vertical, making the frame face parallel to the burner cone exit plane. The test position of the frame aligns the horizontal and vertical centerlines of the

frame with those of the cone exit plane, and the sample plane is parallel to and 101.6 millimeters from the cone exit plane. The sample holder is attached to a rolling cart to enable translation of the sample from the warm up position to the test position in front of the burner.

The material used to measure burner performance was developed during initial insulation burnthrough test method development in the late 1990's and early 2000's. The FAA worked with a materials manufacturer to produce a sample material that would be a flexible material representative of actual aircraft insulation materials and exhibits burnthrough times near the maximum allowable burnthrough time specified in FAR 25.856b, four minutes. It was also desired that the material provide consistent burnthrough times with low fluctuation in burnthrough time from test to test. The manufacturing process was refined over several iterations in order to determine the optimal method of production, and the resulting materials are used in the current study. The test sample materials are composed of 100% oxidized polyacrylonitrile (PAN) fibers, 12.6 μm in diameter and 60 millimeter fiber cut length. Materials made from oxidized PAN fibers have excellent thermal and fire resistant properties as a result of the high temperature oxidation manufacturing process of the fibers. The sample materials, pictured in Figure 2.20, are woven from PAN fibers into a felt-like material that is flexible and can resist burnthrough for 3-6 minutes depending on the material density. Two different densities are typically tested in order to determine a range of burner performance around the 4-5 minute burnthrough time; PAN-8579 is $.33 \text{ kg/m}^2$ areal

weight while PAN-8611 is $.56 \text{ kg/m}^2$. The samples measure 812.8 millimeters wide by 457.2 millimeters high.

The following procedure is used to obtain material burnthrough data with the picture frame sample holder. The burner is warmed up for two minutes while the sample holder is in the standby position away from the flame. At two minutes, the sample is translated in front of the flame to the test position, at which point the test begins. The sample is observed from the back side, watching for flame penetration. A typical test progression is displayed in Figure 2.19. The burnthrough time is defined as the point in time at which the burner flame penetrates the back face of the material. The baseline burnthrough data sets for the current investigation are displayed in Figure 2.21 (a) for PAN-8579 and (b) for PAN-8611. The individual sample identification numbers are listed on the horizontal axis with the overall average. The material burnthrough time, in seconds, is displayed on the vertical axis. The average, standard deviation, and relative standard deviation (%) are displayed on the plot. Both materials are seen to exhibit excellent test to test repeatability. The relative standard deviation, or the standard deviation of the sample set divided by the average of the sample set, is a good measure of the overall repeatability of the test series. Both data sets have relative standard deviation of below 5%, indicating that both the material and the burner exhibit excellent repeatability.

2.4 Error Associated with Flame Temperature Measurements

The use of thermocouples to measure flame temperature in the oil burner flame is known to yield a flame temperature value significantly lower than the actual flame temperature. The thermocouple junction is formed by the joining of two dissimilar metal wires, creating a potential difference between the open ends proportional to the temperature of the junction. A bare-bead thermocouple is a small sphere created by the junction of the two wires; a sheathed thermocouple shrouds the junction in a high temperature metal, typically packed with ceramic insulation. The measurement of the thermocouple temperature is determined with accuracy; the issue is that the junction temperature is not necessarily equal to the temperature of the gas it is measuring [49], [50]. For steady-state conditions, the temperature difference between the gas and the junction arise from radiative heating or cooling, heat conduction along the wires, catalytic heating of the junction due to radical recombination reactions at the surface, and aerodynamic heating at high velocities. Radiative effects are the most significant for measuring temperatures in flames. Assuming a steady-state condition and only considering convective and radiative processes, the difference between the gas temperature (T_g) and the junction temperature (T_j) can be approximated as:

$$T_g - T_j = \frac{\sigma \varepsilon}{h_c} (T_j^4 - T_s^4) \quad (3.2)$$

where h_c is the convective heat transfer coefficient, ε is the junction emissivity, and σ is the Stefan-Boltzmann constant, and T_s is the temperature of the surroundings. The

convective heat transfer coefficient can be determined from correlations in terms of the Nusselt number (Nu):

$$Nu = \frac{h_c d}{k} \quad (3.3)$$

where d is the wire diameter and k is the gas conductivity. A common correlation for Nu is found in [51]:

$$Nu \left(\frac{T_m}{T_j} \right)^a = A + B Re^n = A + B \left(\frac{Ud}{\nu} \right)^n \quad (3.4)$$

where T_m is the film temperature defined as the absolute value of $0.5(T_g - T_j)$, Re is the Reynolds number as defined for the local gas flow velocity U and kinematic viscosity ν . A , B , and n are constants having values -0.17, 0.24, 0.56, and 0.45, respectively. Substituting equation (3.3) into (3.2) neglecting the small temperature dependence and assuming that U is sufficiently large that A can be ignored yields:

$$T_g - T_j \sim \frac{d^{0.55}}{U^{0.45}} (T_j^4 - T_s^4) \quad (3.5)$$

Equation (3.5) shows that the difference in the thermocouple junction temperature from the gas temperature is dependent upon the diameter of the thermocouple junction and the gas flow velocity. As the diameter of the junction increases, the difference between the gas and junction temperatures increases; as the gas velocity over the junction increases the error is reduced. Equation (3.5) provides two methods to reduce the error; one by using shielded, aspirated thermocouples to measure flame temperature, the other to

record temperatures with several bare-bead thermocouples having different diameters and extrapolate the results to zero diameter [52].

The measured value differs from the true gas value as a result of radiation heat transfer exchanges between the thermocouple bead and the flame, soot, and the surrounding environment [53]; the resulting measured value will be a net balance of heat input to the thermocouple minus heat loss by radiative exchange to the surroundings. The size of the thermocouple bead dictates the heat loss as well as radiation transfer is a function of surface area. Corrections are difficult to make as the surrounding temperature is difficult to assess, convection velocity and gas composition at the thermocouple is highly variable, and soot can accumulate on the bead, entirely changing the heat transfer of the thermocouple. According to a model developed in [53], a bare bead thermocouple with diameter 1 millimeter, emissivity 0.8, flame velocity 0.5 meters per second, and temperature of the surroundings at 300 Kelvin can have up to 20% temperature measurement error when immersed in a flame of actual temperature 1400 Kelvin. Stainless steel sheathed thermocouples can have even more error due to the larger surface area of the heated probe resulting in increased heat loss by radiation to the surroundings.

The flame temperatures presented in this work are the measured flame temperatures, and are known to be significantly less than the actual flame temperature. However, for a relative measurement and for burner-to-burner comparisons the measured flame

temperature values and profile shapes give insight to the effect of burner configurations on burner performance.

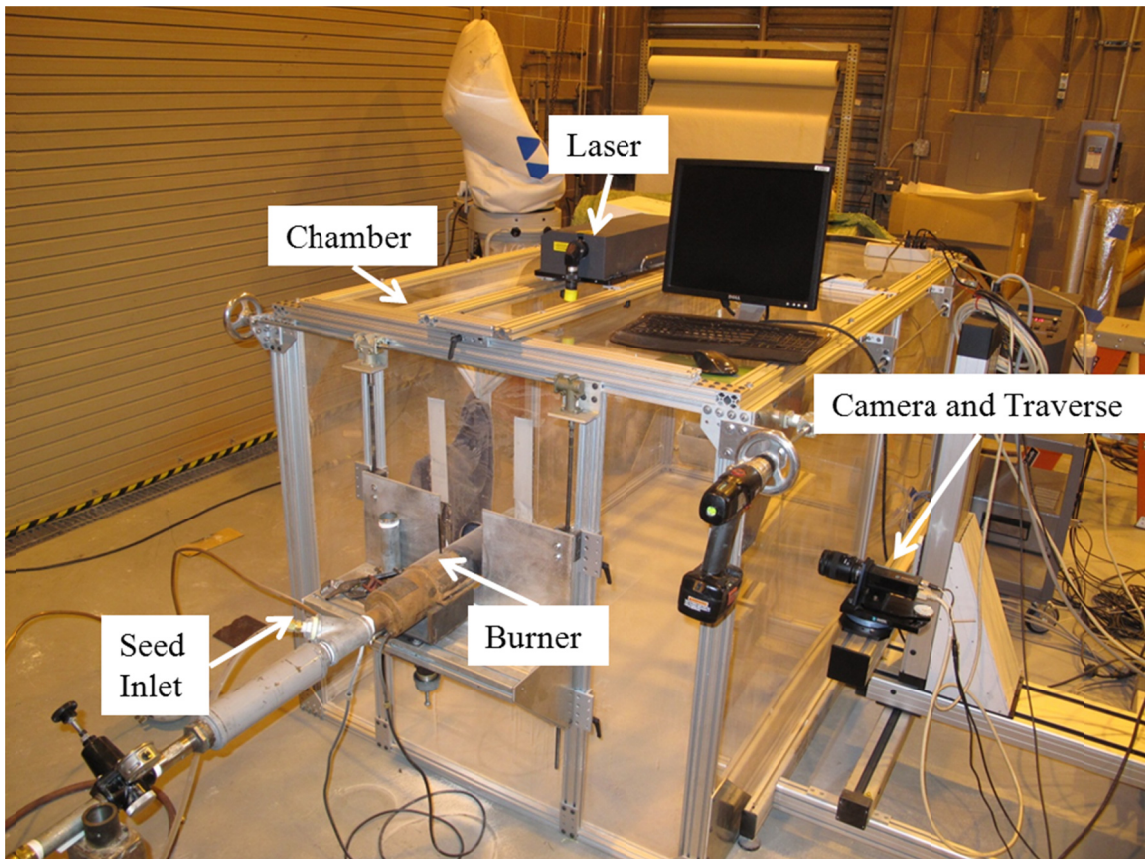


Figure 2.1. PIV test chamber in test cell 2 of Aircraft Components Fire Test Facility showing location of the test chamber, laser, camera, traverse, burner, and seed inlet.

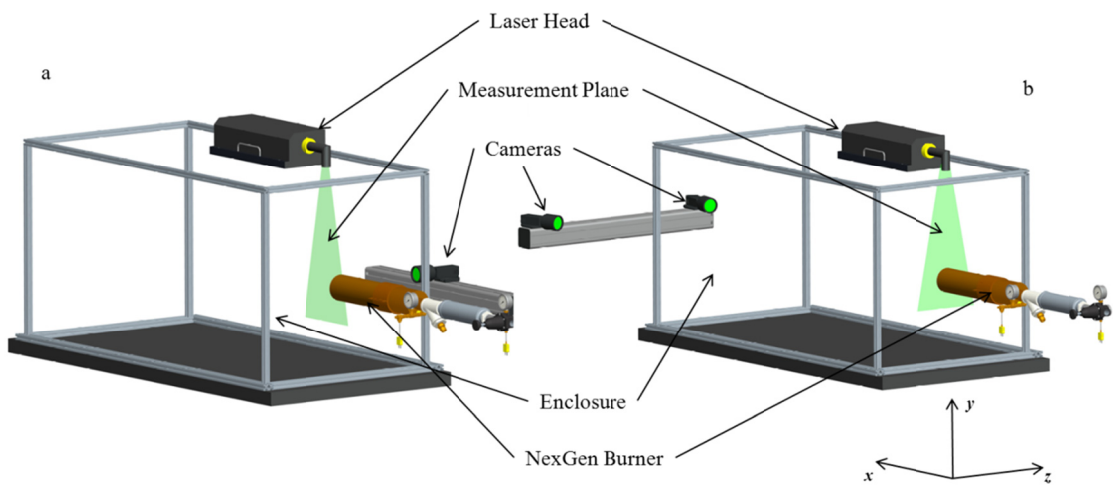


Figure 2.2. Schematic of the single-camera 2D PIV measurement setup (a) and dual-camera stereoscopic 3D PIV measurement setup (b), showing relative locations of the enclosure, NexGen burner, laser head, measurement plane, and cameras.

Parameter	Symbol	Unit	Value
Temperature	T	$^{\circ}\text{C}$	21
Kinematic Viscosity	ν	m^2/s	1.5203×10^{-5}
Density	ρ	kg/m^3	1.2006
Source Diameter	d	mm	5.4
Coflow Diameter	D	mm	101.6
Exit Velocity	U_0	m/s	59.25
Source Reynolds Number	Re_d	--	21045
Center of Observation Volume from Jet Exit	X	mm	241.2
Observation Volume Location Relative to Source Diameter	x/d	--	19
Local Jet Centerline Velocity	u_c	m/s	11.4
Coflow Velocity	U_{∞}	m/s	1.0

Table 2.1. Flow conditions for the turbulent jet validation measurements.

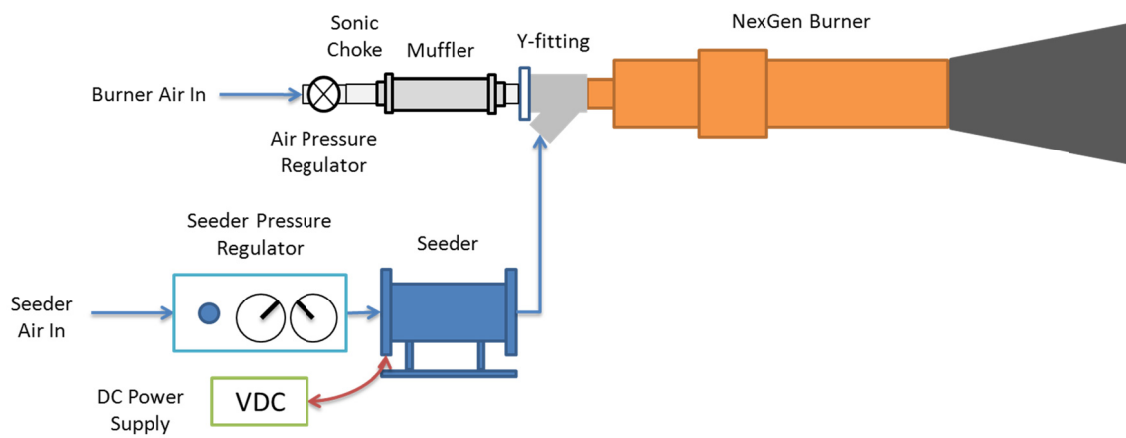


Figure 2.3. Schematic of the seed generation system and connection to the NexGen burner showing the seeder pressure vessel, pressure regulator, DC voltage regulator, and burner seed inlet.

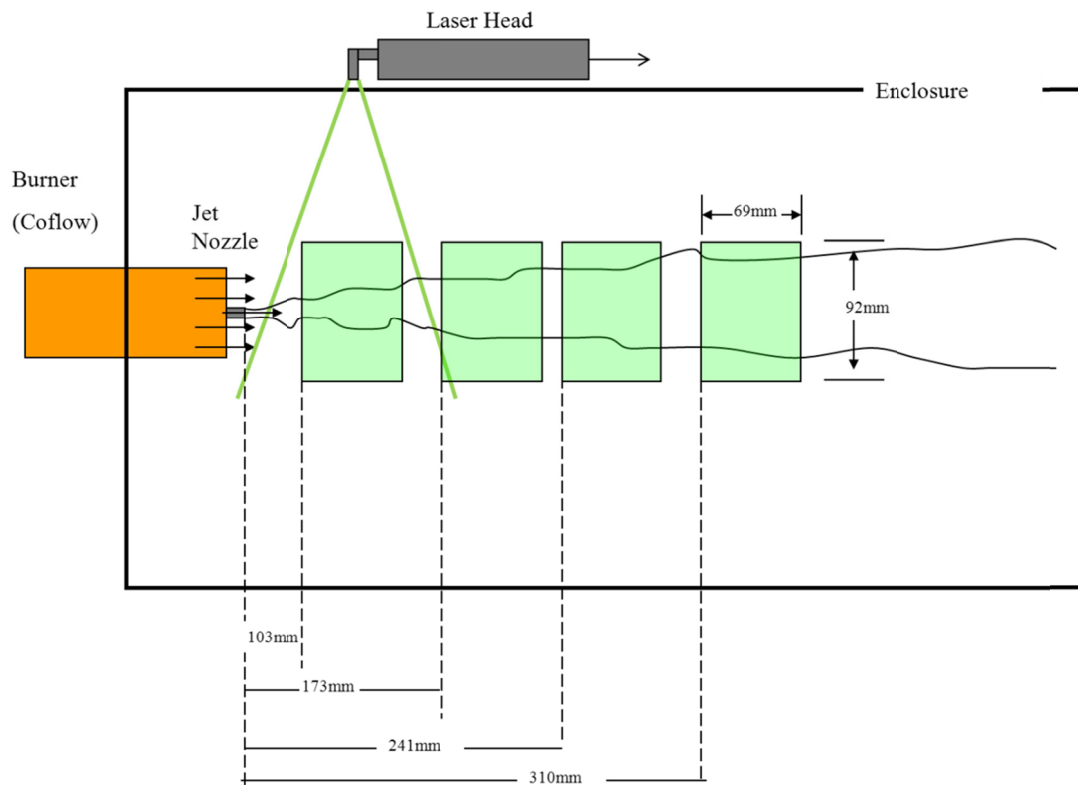


Figure 2.4. Schematic of the coflowing turbulent jet validation measurement experimental setup in the PIV enclosure showing the NexGen burner and fuel pipe as the coflow and jet nozzle, respectively. The four measurement planes and locations are indicated, as well as the relative position of the laser head.

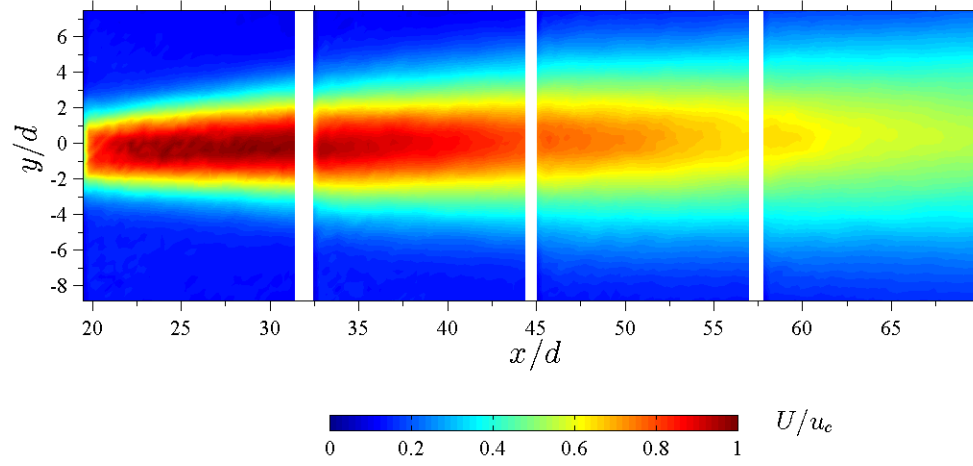


Figure 2.5. Contour plot of normalized mean axial velocity field at $x/d=20-70$ downstream of the jet exit.

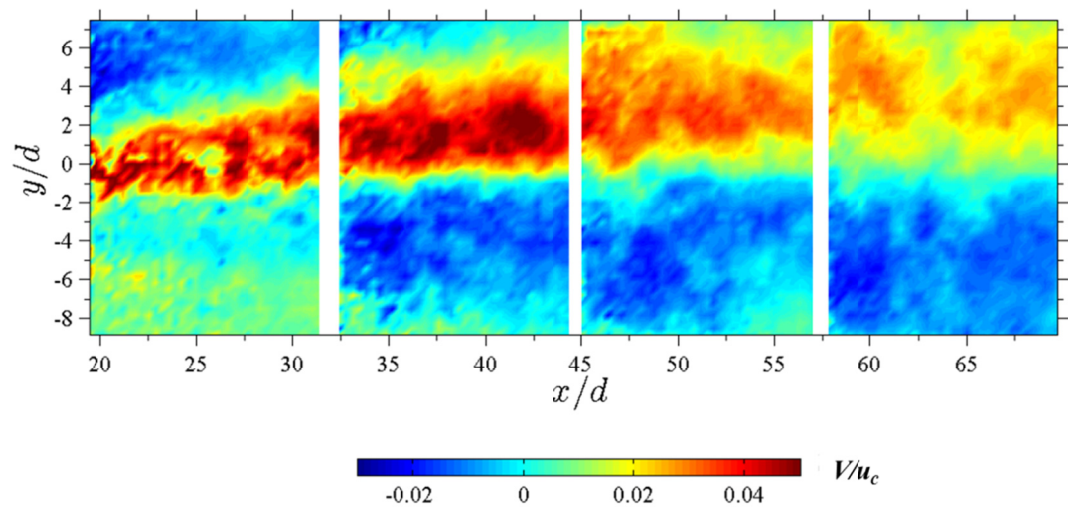


Figure 2.6. Contour plot of normalized mean radial velocity field at $x/d=20-70$ downstream of the jet exit.

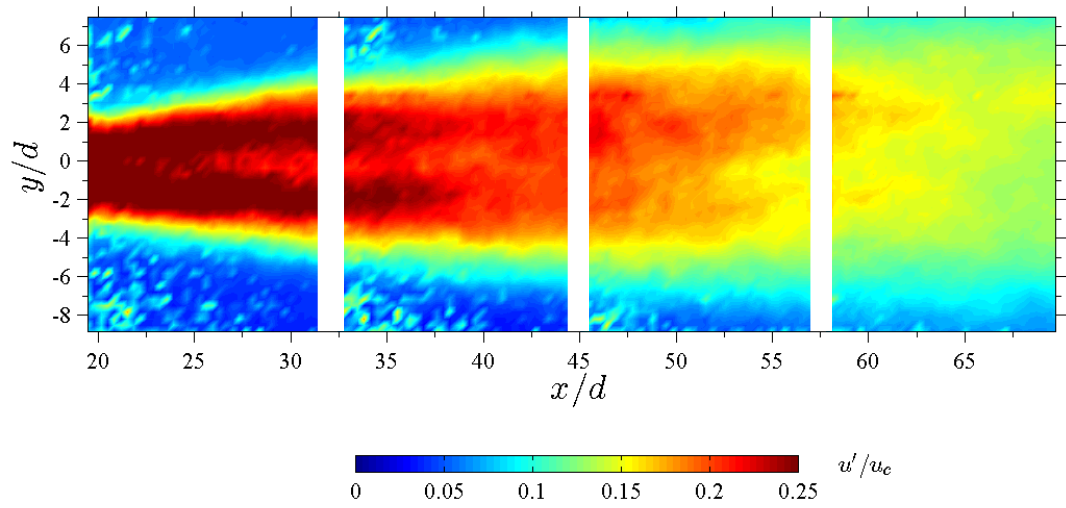


Figure 2.7. Contour plot of normalized axial velocity fluctuations at $x/d=20-70$ downstream of the jet exit.

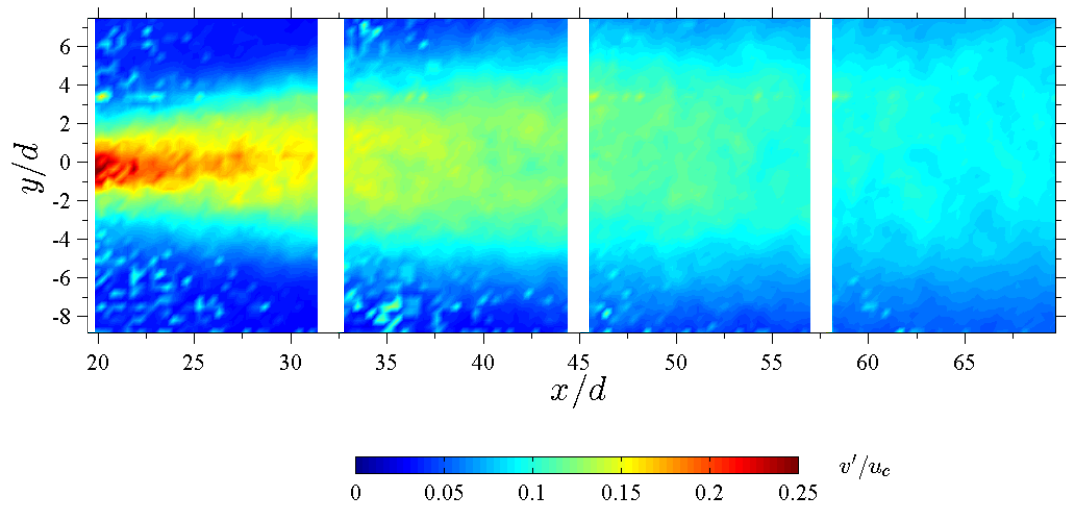


Figure 2.8. Contour plot of normalized radial velocity fluctuations at $x/d=20-70$ downstream of the jet exit.

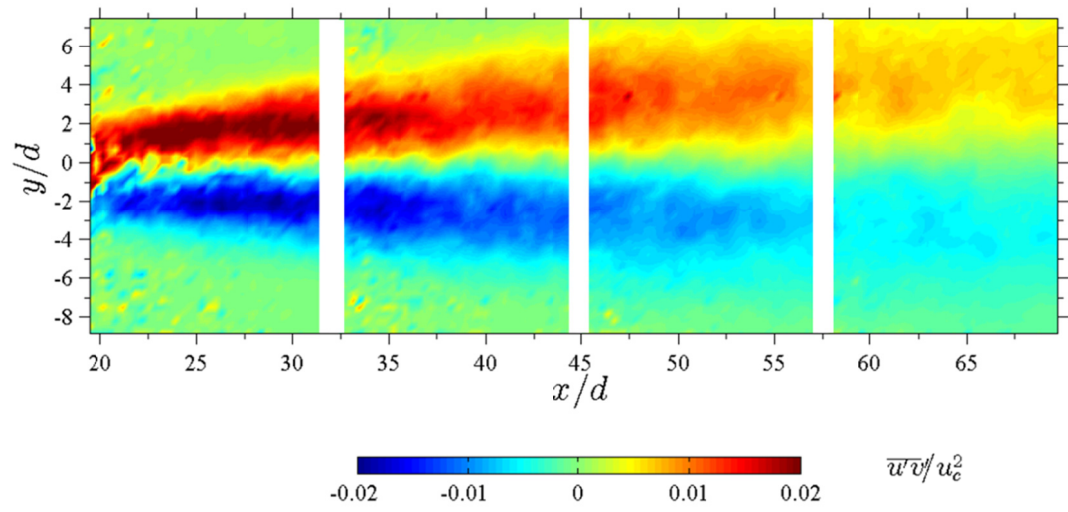


Figure 2.9. Contour plot of normalized Reynolds stress contour plot at $x/d=20-70$ downstream of the jet exit.

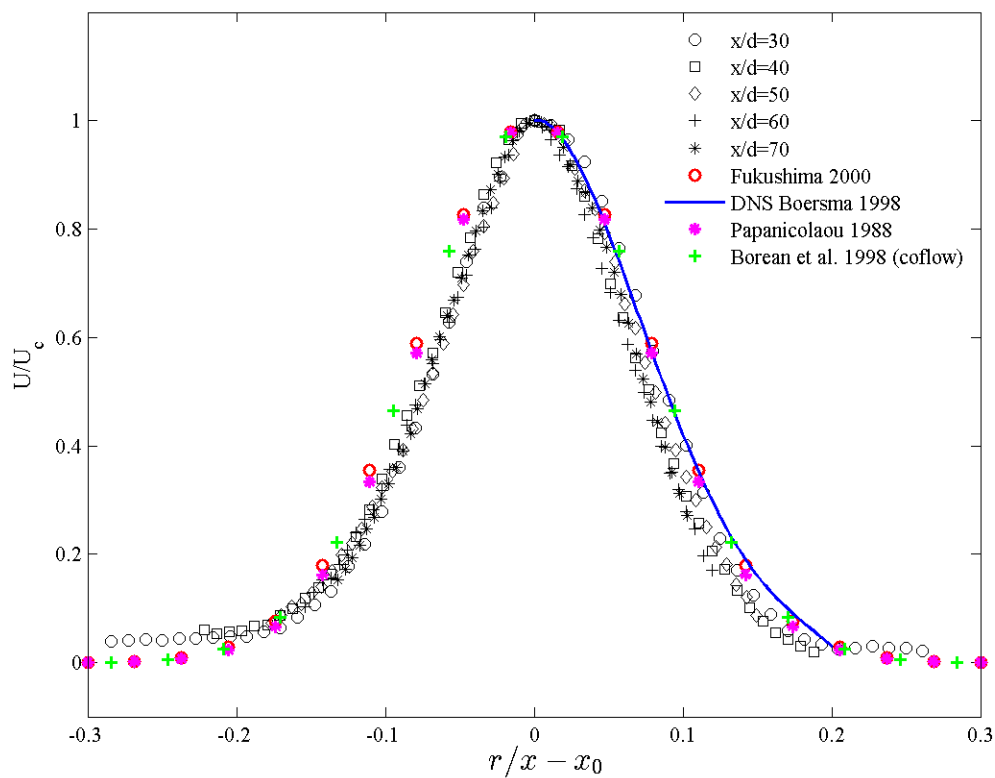


Figure 2.10. Normalized mean axial velocity profile at $x/d=30-70$ downstream of the jet exit. The mean velocity profiles at various downstream locations converge to a single profile when normalized by U_c and r/x . The present data agrees well with curve fits extracted from experimental data from Fig. 4 of [31], Fig. 7 of [25], Fig. 3 of [33], and DNS calculations from Fig. 8 of [32].

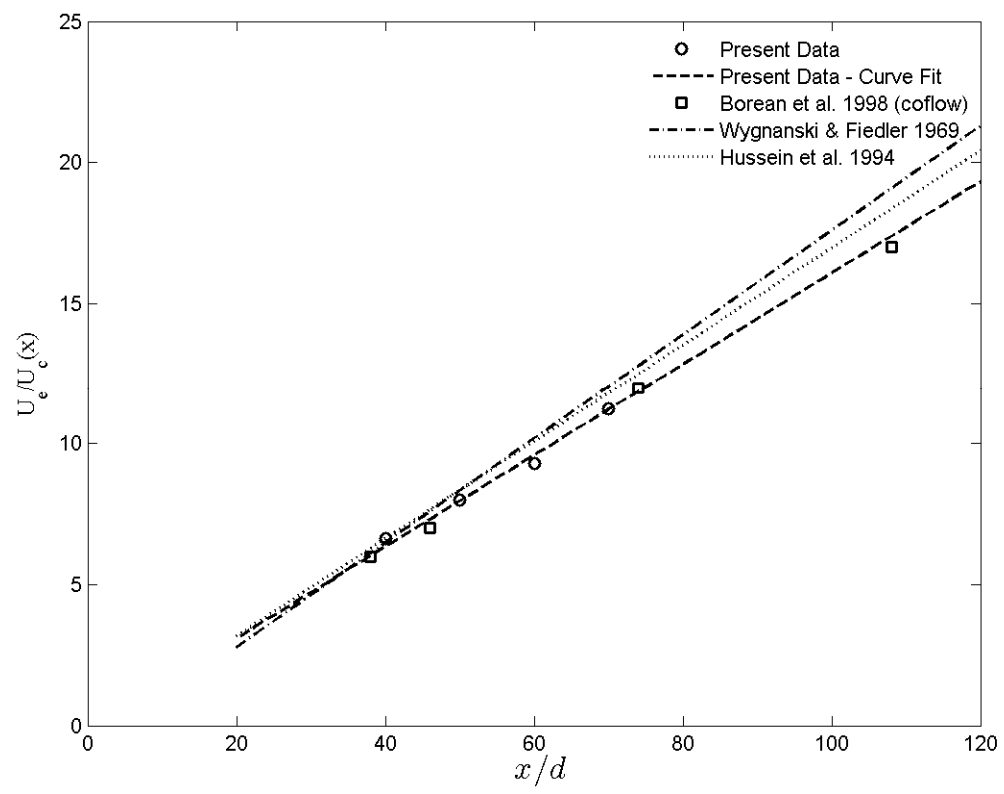


Figure 2.11. Streamwise variation of the initial jet velocity normalized by the local excess centerline velocity for the current measurement at $x/d=40, 50, 60, 70$ and curve fit line. Comparison with the coflowing jet results of Fig. 2 of [33], Fig. 3 of [29], and Figs. 6,7 of [30].

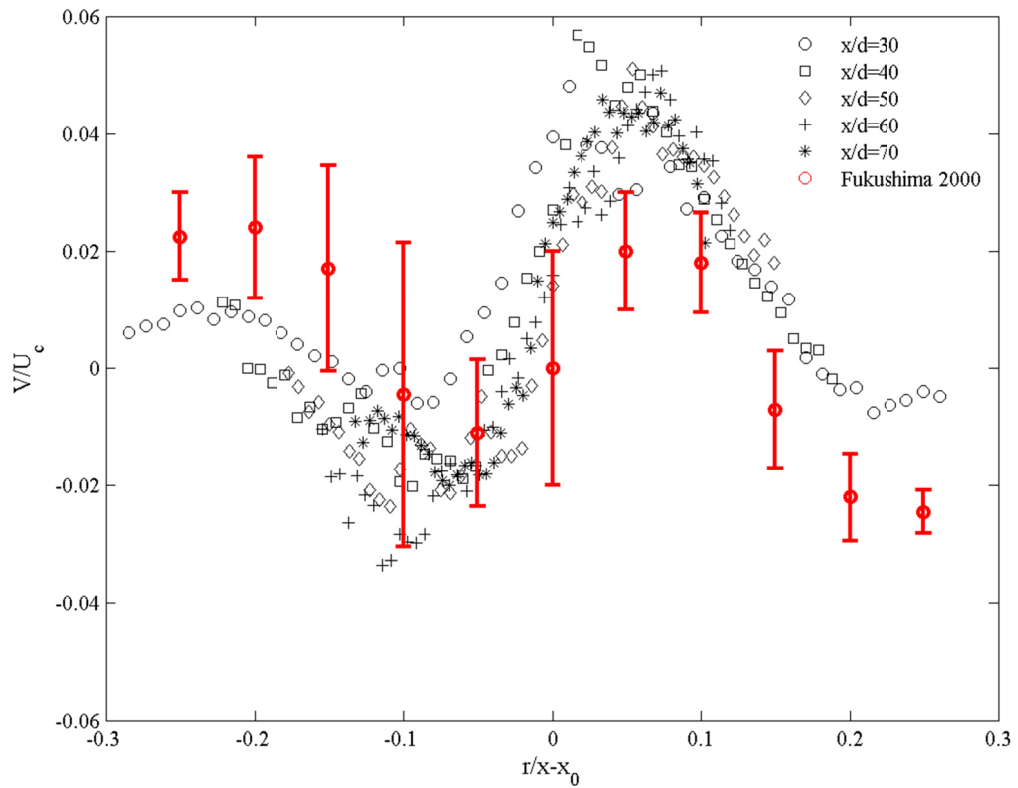


Figure 2.12. Normalized mean radial velocity profile at $x/d=30-70$ downstream of the jet exit compared with experimental data extracted from Fukushima 2000 with approximated data scatter from Fig. 5 from [31].

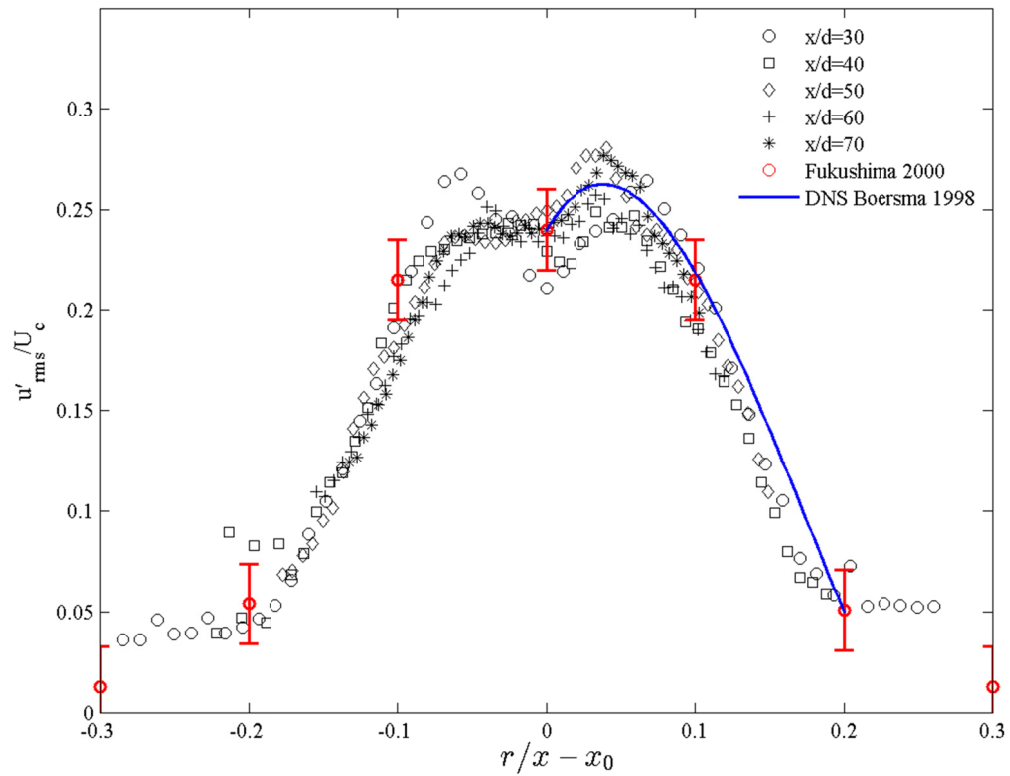


Figure 2.13. Normalized axial velocity fluctuations at $x/d=30-70$ downstream of the jet exit compared with experimental data extracted from Fukushima 2000 with approximated data scatter from Fig. 6 from [31] comparison with DNS calculations from Boersma 1998 Fig. 9 from [32].

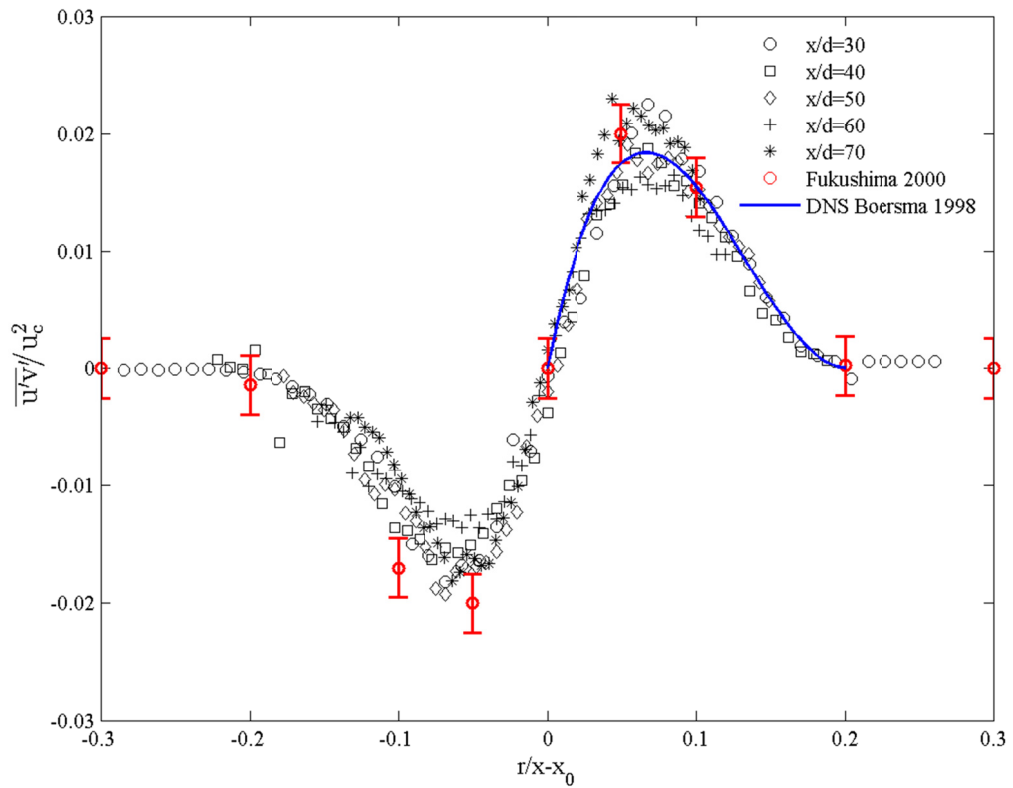


Figure 2.14. Normalized Reynolds stress profile at $x/d=30-70$ downstream of the jet exit compared with experimental data extracted from Fukushima 2000 with approximated data scatter from Fig. 8 [31] and comparison with DNS calculations from Boersma 1998 Fig. 13 [32].

Parameter	Symbol	Unit	Insulation Burner	Seat Burner
			Value	Value
Air Temperature	T	$^{\circ}\text{C}$	10	10
Air Pressure	P_a	bar	5.15	3.77
Air Mass Flow Rate	\dot{m}_a	kg/s	0.0384	0.0281
Kinematic Viscosity	ν	m^2/s	1.4207×10^{-5}	1.4207×10^{-5}
Density	ρ	kg/m^3	1.2474	1.2474
Mean Exit Velocity	U_0	m/s	8.24	6.26
Air Flow Reynolds Number	Re_a	--	40309	30623
Draft Tube Diameter	d	mm	101.6	101.6
Turbulator Exit Diameter	d_T	mm	69.5	69.5
Fuel Temperature	T_f	$^{\circ}\text{C}$	5.5	5.5
Fuel Pressure	P_f	bar	9.28	7.22-8.59
Fuel Flow Rate	Q_f	mL/min	378	126

Table 2.2. General flow properties of the NexGen burners used in this work.



Figure 2.15. Photograph of the FAA next generation fire test burner seat cushion flammability apparatus.

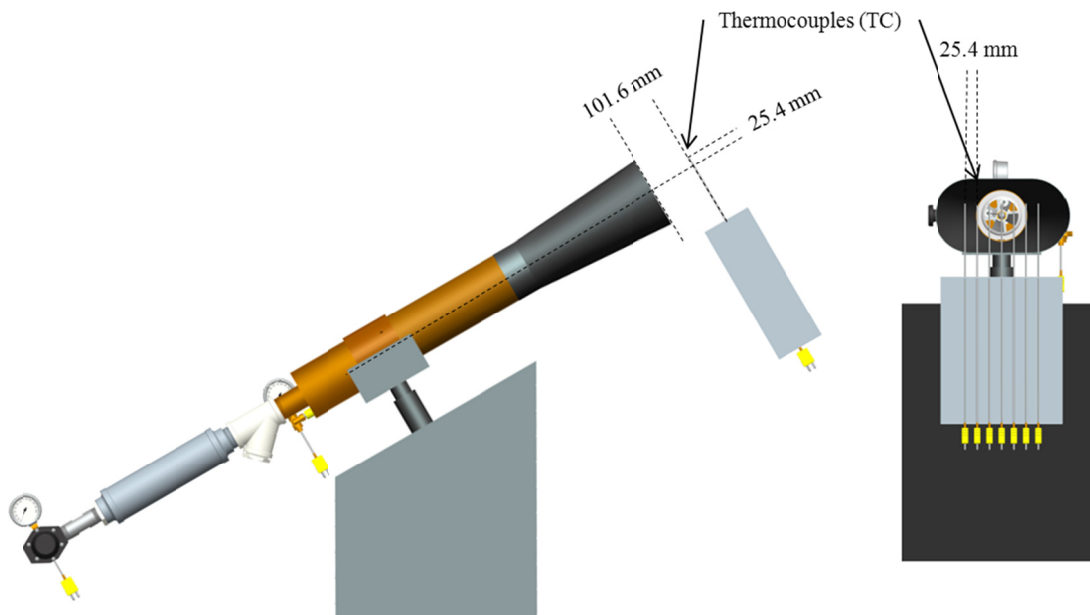


Figure 2.16. Location of thermocouples relative to burner cone exit plane, insulation burnthrough burner. The relative placement of the thermocouples is identical for both the seat burner and insulation burner.



Figure 2.17. Photograph of the FAA next generation fire test burner thermal acoustic insulation burnthrough apparatus.



Figure 2.18. Photographs of the picture frame sample holder.

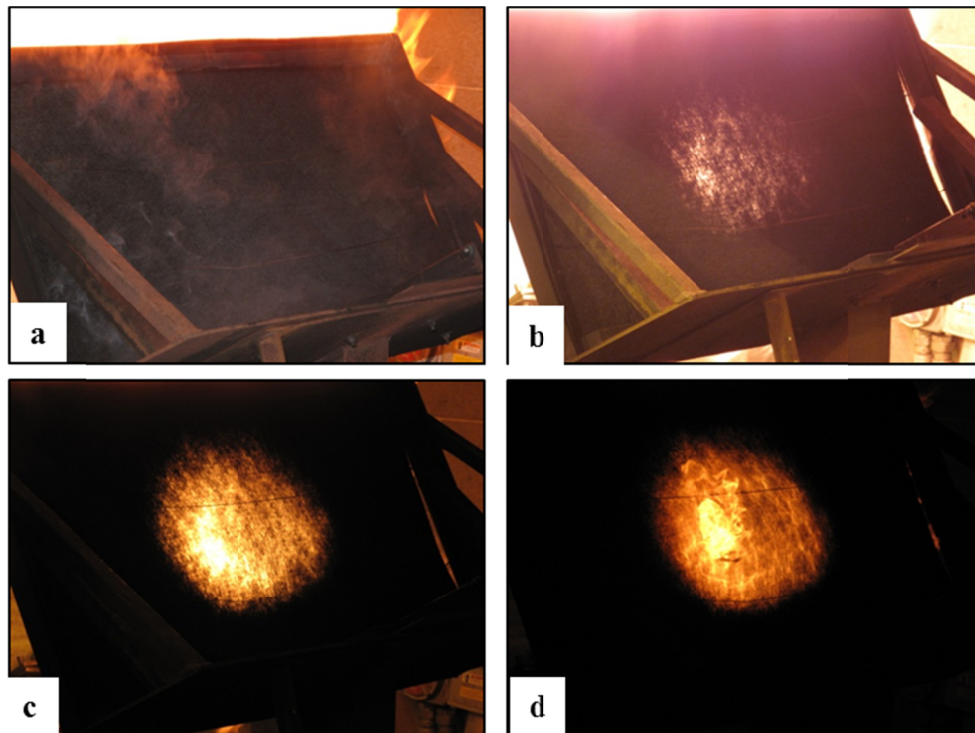


Figure 2.19. Typical test progression of PAN material on picture frame sample holder as observed from the material backside. The material slowly degrades, allowing light from the flame to pass through. Initially the material is completely opaque (a), the light gets progressively brighter (b, c), cracks begin to form (c), and eventually burnthrough occurs (d).

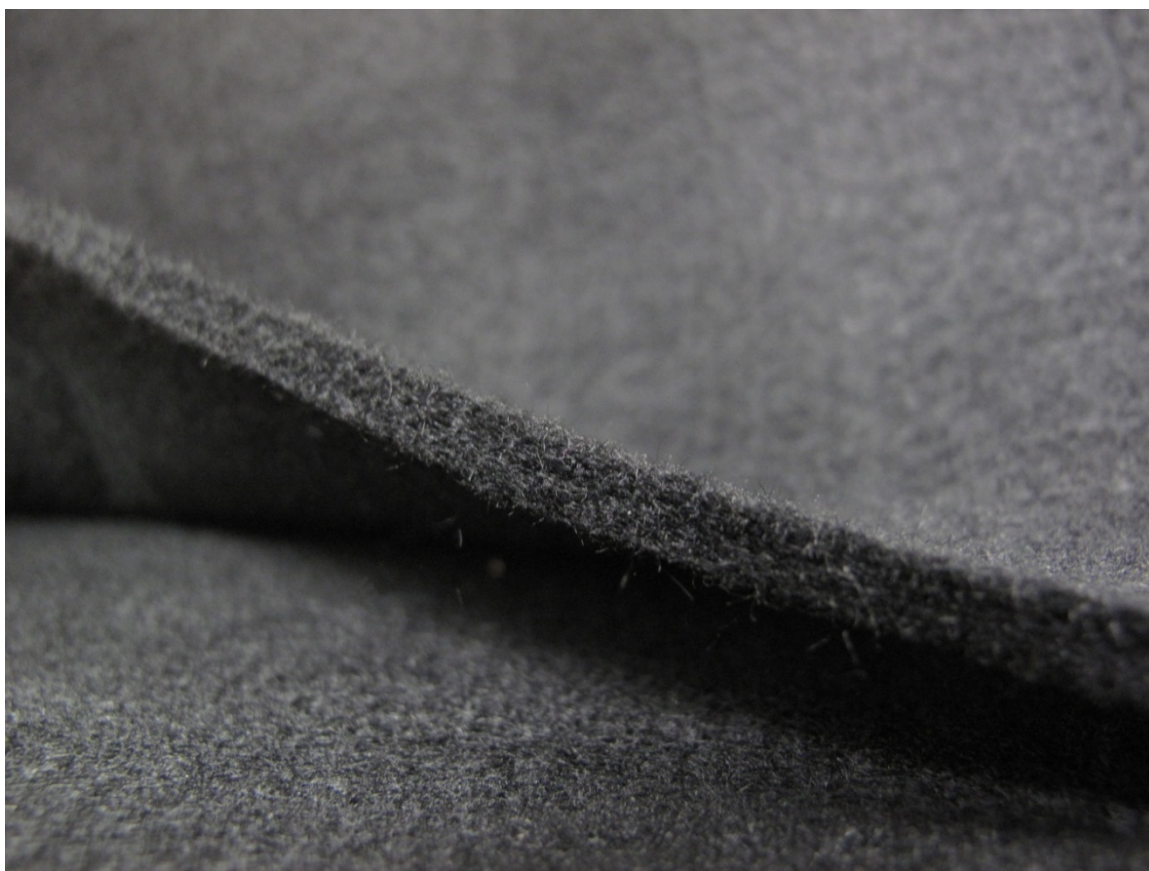


Figure 2.20. Close-up photograph of the polyacrylonitrile (PAN) sample materials used to measure burner performance.

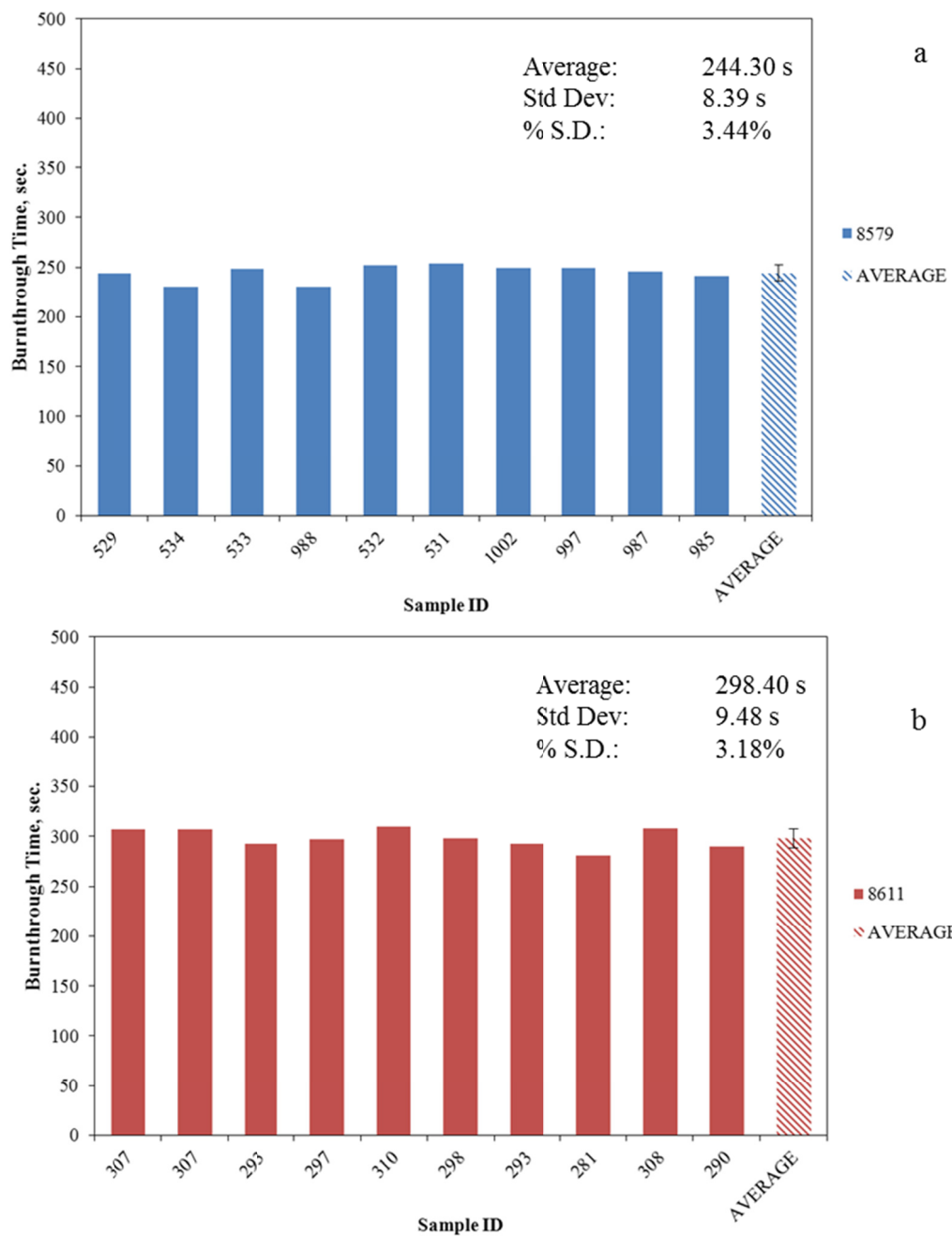


Figure 2.21. Baseline burnthrough times for PAN-8579 (a) and PAN-8611 (b) samples. The individual sample identification numbers are listed on the horizontal axis with the overall average. The material burnthrough time, in seconds, is displayed on the vertical axis. The average, standard deviation, and relative standard deviation (%) are displayed on the plot.

3 Analysis of Burner Parameters

This chapter presents results obtained from the PIV measurements, flame temperature measurements, and material burnthrough tests on the FAA NexGen burner. The intent is to correlate the measured flow fields with the standard burner performance metrics of flame temperature and burnthrough time that are performed when using the burner for certification of aircraft materials. A solid understanding of the fundamental flow properties created by various burner configurations is crucial to developing an updated standardized burner configuration for use around the world for aircraft materials fire testing and airplane certification. It is desired that the burner be simple to construct, calibrate, and use; therefore the configuration of the burner components should be simplified as much as possible in order to reduce errors during construction and set up.

The initial testing was focused on studying the internal burner air flow, starting with an empty burner tube, and then adding components one at a time to understand each component's effect on the basic flow. The burner was then configured for thermal/acoustic insulation burnthrough testing as per [18] to study the airflow produced when the burner is in its operational configuration. The fuel spray pattern was studied to

determine the size, shape, and circumferential symmetry. Lastly, the external burner flow was studied by examining the burner cone exit flow and the flow field around and entrained into the burner air flow.

3.1 Internal Burner Flow

3.1.1 Airflow

Measurements on Draft Tube. The initial PIV measurements were focused on determining the flow field exiting the draft tube. The baseline configuration is the draft tube with no fuel pipe, stator, or turbulator inside in order to assess the flow exiting the choke-muffler assembly and flowing into the draft tube. Single-camera 2D PIV was used for these measurements as the flow is assumed to be similar to pipe flow and relatively symmetric. Figure 3.1 displays the burner configuration and PIV measurement plane (x - y plane). The standard coordinate axes for this work are also displayed. The x -axis is aligned with the draft tube and fuel pipe axis, the y -axis is the vertical axis normal to the burner axis, and the z -axis is the transverse axis normal to the burner axis. The measured mean in-plane velocity field exiting the draft tube is shown in Figure 3.2(a) against the non-dimensionalized x - and y - axes, normalized by the burner draft tube inner diameter d of 101.6 millimeters. The contour plot represents the velocity magnitude while the vectors represent the magnitude and direction of the in-plane velocity field. The in-plane velocity field is similar to that of jet flow near the nozzle exit, with a clear potential core region just downstream of the nozzle exit with a slight increase in the jet width. The

velocity profile near the draft tube exit ($x/d=0.2$) is displayed in Figure 3.3 (blue). The profile is nearly flat, and asymmetry can be found about the draft tube axis. The asymmetry is speculated to be caused by slight misalignment of the pipe nipple or the back plate welded to the back section of the burner housing.

The burner was next configured with a 90-degree pipe elbow inserted between the muffler and the pipe nipple mounted to the back of the burner, as shown in Figure 3.1 bottom. This was done to decrease the overall burner length as a shorter burner would be beneficial for some laboratories with limited space. The PIV measurements were made in the same plane as the previous configuration. Figure 3.2(b) displays the measured mean in-plane velocity field against the non-dimensionalized x - and y - axes normalized by the draft tube inner diameter for the 90-degree elbow configuration. The contour plot represents the velocity magnitude while the vectors represent the magnitude and direction of the in-plane velocity field. The in-plane velocity field is similar to that from the previous configuration, both in magnitude and direction. Figure 3.3 displays the mean axial velocity profiles at one pipe diameter downstream from the draft tube exit for both configurations. The horizontal axis represents the radial position normalized by the draft tube inner diameter while the vertical axis represents the measured mean axial velocity U in meters per second. It is evident that the velocity profiles are similar, both having an asymmetric shape with higher velocities found below the burner axis and a similar peak velocity value. The 90-degree elbow can be considered to provide an equivalent velocity profile to that of the straight sonic choke-muffler assembly.

Measurements on Draft Tube with Fuel Pipe. The fuel pipe was then installed into the empty burner tube as shown in Figure 3.4. The fuel pipe is aligned with the axis of the draft tube in the front half of the burner, while in the back half a dogleg pipe bend allows the pipe to exit the back of the burner 38 millimeters below the air inlet, which is aligned with the burner axis. Figure 3.5 displays the measured mean in-plane velocity field at the draft tube exit for the draft tube with fuel pipe configuration, plotted against the non-dimensionalized x - and y - axes normalized by the draft tube inner diameter. The contour plot represents the velocity magnitude while the vectors represent the magnitude and direction of the in-plane velocity field. It can be seen that the in-plane velocity field is asymmetric about the axis with a higher velocity region in the upper portion of the flow field. This is due to the dogleg bend, which deflects the incoming air upwards. Figure 3.6 compares the velocity profile at one diameter downstream for the fuel pipe, 90-degree elbow, and straight configurations. The horizontal axis represents the radial position normalized by the draft tube inner diameter while the vertical axis represents the measured mean axial velocity U . It is evident that the fuel pipe influences the velocity profile significantly when compared to the two empty burner tube configurations.

Measurements on Draft Tube with Stator. The fuel pipe was removed and the stator was placed in the tube as shown in Figure 3.7. The holes for the igniters and the central fuel pipe hole were covered with aluminum tape for these measurements to simulate the blockage normally created by the fuel pipe and igniters. The face of the stator was

recessed from the end of the draft tube by $x/d=.25$, $.75$, and 1.25 to study the effect of axial positioning of the stator on the airflow. The stator was oriented such that the vertical centerline between the two igniter-holding vanes was aligned with the y -axis. Figure 3.8 shows the measured mean in-plane velocity field at the burner exit for the three different axial positions of the stator, plotted against the non-dimensionalized x - and y - axes normalized by the draft tube inner diameter. The contour plot represents the velocity magnitude while the vectors represent the magnitude and direction of the in-plane velocity field. Comparison of Figure 3.8 (a-c) shows similar in-plane velocity fields characterized a hollow air flow pattern exiting the draft tube. Though this measurement is only of the in-plane velocity, evidence of a swirling flow field can be seen. The flow is symmetric about the axis, a hollow core exists with low and reverse flow, and increased jet growth is observed when compared to the empty burner tube configuration. It can be seen for the axial position of the stator at $x/d=.25$ (c) reverse flow is observed near the draft tube exit. The jets all flare outward to varying degrees depending on the axial position of the stator in the draft tube, and the overall jet width at an axial location one diameter downstream varies from $0.6d$ for $x/d=.25$ to about $1.2d$ for $x/d=.75$ and 1.25 , as displayed in Figure 3.9. The axial position of the stator is found to influence the magnitude of the draft tube exit flow and the growth rate of the jet.

Turbulator on Empty Draft Tube. To determine the effect of the turbulator on the basic flow field it was installed on to the end of an empty draft tube, as displayed in Figure 3.10. Figure 3.11 displays the measured mean in-plane velocity field of the burner

configured with an empty draft tube and the turbulator placed on the end of the draft tube, plotted against the non-dimensionalized x - and y - axes normalized by the draft tube inner diameter d . The contour plot represents the velocity magnitude while the vectors represent the magnitude and direction of the in-plane velocity field. Figure 3.12 shows the comparison of the mean axial velocity profile at $x/d=1$ with the empty draft tube configuration. The horizontal axis represents the radial position normalized by the draft tube inner diameter while the vertical axis represents the measured mean axial velocity U . The diameter of the turbulator exit is $.68d$, therefore the area contraction results in an increase in the exit velocity, with the maximum velocity being about 2.5 times greater with the turbulator installed. By examining Figure 3.11 it can be seen that the jet width slightly increases further downstream.

Measurements on Fully Configured Burner. The burner was then configured as it would be during testing, with the stator positioned one diameter upstream of the draft tube exit, the turbulator placed on the end of the draft tube, and the fuel rail, nozzle, and igniters all configured according to [18]. The test configuration and measurement plane are displayed in Figure 3.13. Figure 3.14 displays the measured mean in-plane velocity field for this configuration, plotted against the non-dimensionalized x - and y - axes normalized by the draft tube inner diameter d . The contour plot represents the velocity magnitude while the vectors represent the magnitude and direction of the in-plane velocity field. The flow field is more jet-like with peak velocity near the center of the flow field and growth typical of a turbulent jet. The influence of the turbulator is seen to

restrict the outward growth of the swirling flow when compared to the growth observed when only the stator was installed. In order to determine how the turbulator vanes influence the flow field, the vanes were filled in with putty so that only the effect of the area contraction of the turbulator can be observed, as displayed in Figure 3.16. It should be noted that this configuration would not be used during testing; it is only an experiment to determine the effect of the vanes on the flow field. The measured mean in-plane velocity field, displayed in Figure 3.16, is plotted against the non-dimensionalized x - and y - axes normalized by the draft tube inner diameter d . The contour plot represents the velocity magnitude while the vectors represent the magnitude and direction of the in-plane velocity field. Here it can be seen that the flow does still flare outwards in the top portion of the flow field, indicating that the turbulator vanes and not the area contraction are responsible for restricting the outward growth of the flow. The turbulator vanes can be seen to even out the irregular flow caused by the non-uniformity of the internal burner components, i.e. asymmetric stator, igniters, and fuel pipe, and reduce the spread rate of the swirling flow field, concentrating the air flow near the burner axis.

To complement the data displayed in Figure 3.14, additional measurement planes were acquired for the standard burner configuration. The measurement planes are sketched relative to the turbulator exit plane in Figure 3.17. The planes were at $z = -0.16d$, $-0.08d$, 0 , $0.08d$, and $0.16d$. The mean measured in-plane velocity fields are displayed in Figure 3.18. By comparing the figures, it can be seen that although the center plane flow is dominant in the axial direction, the neighboring planes have greater vertical velocities.

Figure 3.19 (a-e) displays the same data in a three-dimensional view to show velocity profiles from all 5 measurement planes at streamwise locations of $x/d=0.2, 0.5, 1.0, 1.5,$ and 1.8 . The upward and downward velocity in the outer measurement planes is indicative of swirling flow in the counter-clockwise (positive) direction when looking into the burner. As the flow moves further downstream, the vertical component of the velocity vectors decay and the flow becomes nearly axial indicating the decay of the swirling flow further downstream.

To investigate the swirling flow further, stereoscopic PIV was used to visualize the three-component velocity field at 12 planes downstream from the burner from $x/d=0.05$ to 3.0 as sketched in Figure 3.20. Figure 3.21 displays the mean image from the first frames of camera 1 at $x/d=.05$. The mean image clearly shows the effect of the turbulator vanes on the exit flow field, as there are eight distinct regions where the seeding is concentrated, corresponding with the eight turbulator vanes. Figure 3.22 (a-1) displays the measured mean velocity field for the three-component velocity measurements at 12 downstream axial measurement planes. The range of measurement planes was chosen as this is the length of the burner extension cone, 304.8 millimeters, or about 3 pipe diameters, and it was desired to study the evolution of the unconfined swirling airflow pattern in this region. The field of view for these measurements was approximately 1.1 diameters high by 1.45 diameters wide. The flow field at the turbulator exit is displayed in Figure 3.22 (a) at an axial distance of .05 diameters from the exit plane. The horizontal axis represents the z -axis while the vertical axis represents the y -axis, both normalized by the

draft tube inner diameter d . The contour plot represents the magnitude of the out-of-plane (U) axial velocity, while the vector map represents the in-plane horizontal (W) and vertical (V) components. The counter-clockwise rotation of the swirling flow is evident as is the entrainment of surrounding flow into the centralized rotating region. The U velocity is seen to initialize as four distinct high velocity jets emerging from the four spaces between the stator vanes with a peak velocity of around 18 m/s (a). As the flow moves downstream the four high velocity jets (a-b) merge into two high velocity regions in the upper-left and lower-right quadrants of the flow (c-g), and the two regions converge into one (h). The flow field begins to assume a round jet like shape from $x/d=1.5$ on. The center of rotation is found to migrate slightly from the axis at around $x/d=1.75$. The peak axial velocity at each measurement plane was plotted against the axial position in Figure 3.23 to show the axial velocity decay. A curve fit of the experimental data yields the relation $U(x) = 31.739x^{-0.308}$.

The swirling effect of the stator can be seen in the 3D measurements of the flow field. The swirl number S is often useful to describe swirling flows. It is defined as the axial flux of the tangential momentum divided by the axial flux of axial momentum times the nozzle radius [54]:

$$S = \frac{\int_0^R U W r^2 dr}{R \int_0^R U^2 r dr} \cong \frac{2}{3} \tan \phi \quad (3.1)$$

where U , W are the mean axial and circumferential velocities, respectively, r is the radial coordinate and R is the tube radius. For the stator in this study, the vane angle is

approximately 60° , resulting in a swirl number of 1.15. According to [38], flows with swirl number $S \sim 0.4$ are considered to have weak swirl. The low degree of swirl results in increased width of a free or confined jet flow, and the jet growth, entrainment, and decay are enhanced as the swirl number increases. Flows with higher swirl $S > \sim 0.6$ have strong radial and axial pressure gradients set up near the nozzle exit, resulting in axial recirculation in a central region along the jet axis. With a swirl number of 1.15, the stator alone can be considered to cause strong swirl, as evidenced by the central recirculation region in Figure 3.8 (c), though the axial position of the stator is found to influence the degree of recirculation. The swirling flow in the complete burner, however, is found to be significantly altered by the addition of the turbulator, as shown in Figure 3.22, where no reverse flow exists and jet growth is reduced due to the influence of the turbulator.

3.1.2 Fuel Spray

This section discusses the measurements made on the standard fuel spray nozzle that is currently accepted for use in the NexGen burner. Nozzle M has been used for decades as it was the nozzle that was supplied with the Park oil burners that fire test methods were originally based on. The nozzle is rated at 142 mL/min flow rate when provided with fuel oil at 7.9 bar (100 psig), but is operated at 6.5 bar to achieve 126 mL/min. The spray pattern is a solid cone with a spray angle of 80° . The 126 mL/min flow rate is required for the seat cushion, cargo liner, and powerplant component test methods, while the 378 mL/min flow rate is used for insulation burnthrough. The 126 mL/min flow rate was

chosen for this study due to the lower flow rate and wider use of 126 mL/min vs. 378 mL/min nozzles. The measurements were made of the spray only; the burner air was not flowing with the spray.

Water was used as the working fluid rather than jet fuel due to the high volatility and explosion hazard of atomized jet fuel in a confined chamber while using a high power laser for PIV measurements. The use of water in place of jet fuel does not reflect a direct analogy; rather water is used to show a qualitative difference in the spray pattern. Previous research in [55] described a global sizing velocimetry (GSV) measurement of fuel oil and water in a commercial oil burner spray nozzle with a flow rating of 31.5 mL/min and pressure 6 bar. Droplet size was measured with GSV near the nozzle exit. It was found for water that larger drops with diameter 45 μm were generated in the spray sheet area, and smaller drops with diameter 15 μm in the recirculation zone. Fuel oil in the same nozzle at the same pressure resulted in a different distribution of drop sizes with a greater concentration of 15 μm drops and a shifted peak droplet size of around 25 μm in the spray sheet area. These measurements show that it can be expected that water sprays will generally produce larger droplet sizes than a fuel oil spray.

The purpose of these measurements is to investigate the spray pattern and to determine the influence of the spray pattern on flame temperature measurements and material burnthrough tests. Though it is known that droplet size will also have an effect on burner

performance, for the purpose of this study the drop size distribution is assumed to be constant, as no variables are being altered that would affect the drop size.

The measurement plane for these measurements is displayed in Figure 3.24. Figure 3.25 displays the mean measured in-plane velocity field of the spray produced by nozzle M. The contour plot represents the magnitude of the in-plane velocity while the vector plot represents the magnitude and direction of the x - and y -component velocity vectors. The horizontal axis represents the axial distance from the nozzle tip while the vertical axis represents the radial distance from the nozzle tip, both normalized by the draft tube inner diameter. Immediately apparent is the asymmetric spray pattern (a) exiting the nozzle, with a higher velocity and longer penetration depth found on the bottom half of the spray cone than the top half. Also, the velocity of the droplets is seen to quickly decelerate by around 75% within $0.5d$. The asymmetry of the flow field continues further downstream, though it is not as pronounced as it is initially. To determine if this asymmetry was in fact a result of the nozzle construction, the nozzle was physically rotated 180° on the fuel pipe and the measurement was repeated. Figure 3.25 (b) displays the mean measured in-plane velocity field of the spray produced by nozzle M after being rotated 180° on the fuel pipe. It is apparent that the high velocity region has been rotated 180° with the nozzle, and is now in the upper portion of the plot. Figure 3.26 displays the measured mean axial (U) velocity profiles near the spray nozzle exit at $x/d=0.37$. The horizontal axis represents the radial distance from the axis normalized by the draft tube inner diameter while the vertical axis represents the axial (U) velocity in meters per second.

The blue data series represents the baseline 0° configuration while the red data series represents the 180° rotated configuration. Comparison of the two data sets shows the near-symmetry about the x -axis, indicating that rotating the nozzle results in a rotation of the spray pattern. These measurements indicate that though a nozzle may provide the desired fuel flow rate and spray angle, the circumferential consistency of the spray pattern may be skewed.

To determine the effect that this spray asymmetry has on burner performance, flame temperature measurements were made with a nozzle of similar construction on a NexGen burner configured to perform the seat cushion flammability test method. The nozzle was rotated in 20° increments between flame temperature measurements over a full revolution. Figure 3.27 shows the measured flame temperature in degrees Celsius at each measurement location averaged over thirty seconds at a sample rate of one sample per second. Each data series represents a single thermocouple measurement location in the flame. The horizontal axis represents the angle of rotation of the nozzle, and the vertical axis represents the measured flame temperature in degrees Celsius. Significant changes in the measured flame temperature are observed over the full rotation of the nozzle. Thermocouple 1 experiences the greatest fluctuation in flame temperature from 872°C at 140° rotation to 979°C at 80° rotation. Thermocouple 4, which is located in the center of the flame, is least affected by the nozzle rotation, varying from 960°C at 140° rotation to 984°C at 60° rotation. The fact that the outer thermocouple is most influenced by nozzle rotation while the inner thermocouple is not can be verified by reexamining Figure 3.26.

The velocity in the center of the spray is nearly constant when rotating 180°, but the velocity near the edges of the spray cone varies significantly when rotating 180°. This circumferential spray pattern asymmetry results in a flame that has spatially non-uniform measured flame temperature. The PIV measurements displayed in Figure 3.25 demonstrate the dependency of the flame temperature profile at the standard measurement location on the spray pattern symmetry. This conclusion has been suspected during initial NexGen burner development as it was known that in order to achieve the desired temperature range of $1037 \pm 37^\circ\text{C}$ without modifying the air or fuel flow rates or internal burner geometry, rotating the nozzle incrementally could bring low-measuring thermocouples into range.

3.2 External Burner Flow

3.2.1 Cone Exit Flow

The air flow field exiting the burner cone was measured with PIV to determine how the previously analyzed flow exiting the draft tube translates to the flow field exiting the cone. Nine measurement planes were created perpendicular to the cone exit plane; one on the cone centerline and four on each side of the centerline, $.25d$ apart as displayed in Figure 3.28. The field of view of each measurement plane was 170 by 170 millimeters, allowing for measurement from the cone exit to $1.67d$ downstream. Figure 3.29 (a-e) displays an isometric view of the burner cone exit plane projected on to the three dimensional measurement axes. The axis normal to the burner exit plane represents the

x -axis with the origin at the draft tube exit plane. The vertical axis represents the y -axis with the origin at the burner axis, and the transverse axis represents the z -axis with the origin at the burner axis. All axes are normalized by the draft tube inner diameter d . The outline of the cone exit plane is drawn in the y - z plane, as are the flame temperature measurement locations, with vertical lines and dots representing the thermocouple probes. It can be seen that the flow exiting the burner cone is irregular in both magnitude and direction across the entire exit plane. The flow is largely axial in direction and is significantly greater in magnitude in the center-right region, while in the center-left the flow is very low and negative towards the edge, indicating reverse flow back in to the cone. As the flow progresses in the axial direction similar observation can be made, though the profiles begin to spread out, but at one diameter downstream, where the flame temperature is measured and where test samples are typically placed, the flow is still unevenly distributed and significantly greater in magnitude on the right side, while the left side is still very low. These measurements quantify the strong asymmetry in the cone exit flow which affects burnthrough test uniformity and results.

Figure 3.30 displays a photograph taken immediately after the burner was shut down after taking a flame temperature measurement. The heavy soot that collected on thermocouple #1 resulted in an unusually low flame temperature reading due to the soot insulating the thermocouple and shielding it from the flame heat. It is now speculated that the soot formation is due to the low velocity region found near thermocouple #1. Soot formation is a complex process, but is known to be dependent upon residence time and local flame

temperature [55]. As was seen in the previous section, the fuel spray nozzle can provide an asymmetric spray pattern, and the combination of a high velocity spray jet and a low velocity air flow region results in an overly rich region and increased soot formation, which collects on the thermocouple probe. The nozzle can be rotated to align the low velocity fuel spray with the low velocity air flow to reduce the soot creation in that region and vary the location of soot formation, thereby providing a flame temperature measurement within specification. This procedure has been recommended by the FAA when a laboratory is attempting to achieve the required flame temperature range if a thermocouple is reading an unusually low temperature relative to the neighboring thermocouples.

Stereoscopic PIV was used to further investigate the cone exit plane flow field. Since the exit plane is larger than can be obtained with a single measurement plane, the exit plane was divided into four areas to visualize the complete flow field as displayed in Figure 3.31. Each area had a field of view of 135 by 95 millimeters, with a combined measurement plane of 274 by 171 millimeters. Figure 3.32 (a) displays the combined three-component mean velocity field at the cone exit plane. The horizontal axis represents the transverse direction z , while the vertical axis represents the radial direction y , both normalized by the draft tube inner diameter d . The contour plot represents the magnitude of the axial velocity U , while the vector plot represents the direction and magnitude of the in-plane velocity V and W . The irregularity of the flow distribution in the cone exit plane is apparent, with a high axial velocity region in the top right section

and reverse axial flow found in the bottom left section. This corresponds with the previous measurements displayed in Figure 3.29 at the cone exit plane, which also shows a high velocity region in the top right section and reverse flow in the bottom left section. Figure 3.32 (b) displays the stereoscopic PIV data from Figure 3.22 plotted on the same axes with the black line representing the shape of the burner cone exit plane. Comparison of the two figures shows that the unconfined swirling flow evolves axially as a fairly symmetric round swirling jet at $x/d=3$, whereas when the flow is confined by the burner cone the flow distribution at $x/d=3$ becomes highly irregular and asymmetric. Also, the magnitude and shape of the high axial velocity region is more spread out for the confined flow.

The results found here are similar to those found in [56], where swirling flows in circular-to-rectangular transition ducts were studied for applications to exhaust nozzle technology for combat aircraft. The NexGen burner can be considered analogous to the circular-to-rectangular transition duct, with the draft tube being the circular duct, the burner cone the rectangular (ellipsoidal) duct, and the stator-turbulator combination acting as the swirler. It was determined in [56] from flow visualization that a skewed velocity field is found at the rectangular duct exit when a counter-clockwise rotating swirling flow is introduced upstream of the transition duct. The flow transformation is attributed to cross-streamwise pressure gradients in the corners of the transition duct. Pressure measurements made on the inside walls of the transition duct reveal asymmetric pressure readings with respect to the transition duct axes when compared to the case with a non-swirling flow, indicating

that the swirling flow structure impinges upon the walls, resulting in a skewed structure with asymmetric streamwise velocity distribution at the duct exit plane. These conclusions can be applied to the current measurements at the burner cone exit plane to understand that the observed irregular exit plane velocity distribution is a result of the swirling airflow confined by the varying internal geometry of a circular to ellipsoidal transition.

3.2.2 Flow Field External to Burner Cone

The flow field around the burner cone exit was investigated to determine the interaction between the still laboratory air and the cone exit flow. Figure 3.33 displays a schematic of the measurement plane for this series of testing. The measurement plane was centered on the vertical cone centerline. The chamber was filled with seed particles prior to testing to see the air around the cone. Figure 3.34 displays a typical raw PIV image from these measurements. The top portion of the cone can be seen as the blacked-out area in the lower left region, as the cone was masked out for PIV analysis. The mean measured in-plane velocity field is displayed in Figure 3.35 (a) plotted against the x - and y -axes, both normalized by the draft tube inner diameter d . The contour plot represents the magnitude of the in-plane velocity field while the vector plot represents the magnitude and direction of the in-plane velocity field. Immediately evident is the cone exit flow field, which can be seen to be slightly expanding in the y -direction. The magnitude of the cone exit flow corresponds with the measurements displayed in Figure 3.32 of the stereoscopic PIV measurements made at the cone exit plane. Entrainment of the

surrounding air can be seen near the cone exit flow-ambient air boundary, while the surrounding air further from the cone is nearly still. The flow streamlines are plotted over the in-plane velocity field magnitude contour plot in Figure 3.35 (b). The streamlines help to visualize the mean flow path of the surrounding air being entrained into the cone exit flow, showing strong entrainment of surrounding air far from the cone exit plane. Figure 3.36 (a) displays the scalar mean of the vorticity plotted against the normalized x - and y -axes. Red contours indicate positive counter-clockwise rotation while blue contours indicate negative, clockwise rotation. The shear layer is evident on the top portion of the cone exit flow, indicating mixing between the cone exit flow and the surrounding air. The vorticity can also be seen to decay in the streamwise direction. The growth of the exit flow field can be seen as a result of the entrainment of the surrounding air into the exit flow.

Though the mean in-plane velocity field does indicate the overall direction and magnitude of the flow, the instantaneous flow field can give more information on the typical vortex size, interaction between the cone exit flow and the surrounding air. Figure 3.36 (b) displays a typical calculated instantaneous vorticity field for the cone exit flow. The horizontal axis represents the x -axis while the vertical axis represents the y -axis, both normalized by the draft tube inner diameter d . The contour plot represents the instantaneous vorticity while the vector plot represents the instantaneous in-plane velocity field. Vortical structures are evident in the figure resulting from the irregular, swirling flow exiting from the cone and the shear layer between the exit flow and the still

ambient air. The structures can be seen to decay in strength as they progress away from the cone exit in the axial direction. The vorticity at the cone exit plane indicates high turbulence and mixing with the surrounding air.

3.3 Chapter 3 Summary

The following statements summarize the results presented in Chapter 3.

- The basic flow field exiting the empty draft tube is similar to the potential core region of a turbulent jet at the nozzle exit with a slight increase in the jet width and a nearly flat velocity profile.
- Inserting a 90° pipe elbow upstream between the muffler and the burner inlet has little effect on the measured draft tube exit velocity. The velocity profile at the draft tube exit is nearly similar to the straight muffler-burner configuration.
- The fuel pipe was found to influence the draft tube exit flow field. The velocity profile at the draft tube exit was found to be skewed towards the top portion of the draft tube, indicating that the dogleg bend in the fuel pipe diverts the incoming flow upwards.
- The stator by itself was found to create a draft tube exit flow field characterized by two jets issuing from the draft tube above and below the burner axis with a central core region of low velocity. The magnitude and shape of the flow field was found to be dependent upon the axial position of the stator face relative to the draft tube exit plane. As the stator was moved closer to the draft tube exit plane,

the magnitude of the velocity increased, as did the strength of the reverse flow on the burner axis. The measured flow fields are typical of high swirl ($S \approx 1.15$) axial vane swirlers, with a central recirculation region and increased jet width growth.

- The turbulator by itself was found to increase the magnitude of the draft tube exit flow due to exit area contraction. The exit flow field was found to be very straight and only slightly increase in width downstream.
- The fully configured burner exit flow field appears jet-like with peak velocity near the center of the flow field and growth typical of a turbulent jet. The influence of the turbulator is seen to restrict the outward growth of the swirling flow and even out non-uniform flow caused by the asymmetric internal components.
- The effects of turbulator exit area contraction and vanes were disassociated by filling in the vanes with putty, thereby only allowing the area contraction to influence the exit flow field. It was found that the flow flares outward as it did when only the stator was installed in the draft tube, indicating that the turbulator vanes are responsible for restricting the outward growth of the swirling flow field.
- Measurement of the fully configured NexGen burner exit flow field in four additional cross-streamwise planes showed that although the center plane was largely axial, the neighboring planes have more off-axis velocity, indicating the direction of the counter-clockwise swirling flow exiting from the turbulator.
- Three-component velocity fields were obtained at 12 axial measurement planes from $x/d = .05$ to 3. The resulting plots showed the evolution of the swirling

burner exit flow characterized by four distinct high velocity jets issuing from the stator vanes with strong centralized counterclockwise flow. As the flow progresses axially, the four jets combine first into two distinct regions of high velocity, then finally into a single, round jet shape. The in-plane rotational flow is found to increase in size and decrease in magnitude as the flow progresses. The axial velocity was found to decrease to approximately one third its initial value over the range of three pipe diameters downstream.

- In-plane measurements on the centerline of the standard spray nozzle “M” reveal a strongly asymmetric hollow in-plane velocity field despite the nozzle being rated as a solid spray cone type nozzle. The velocity profile at the nozzle shows nearly seven times greater velocity on one side of the cone compared to the other. Rotation of the nozzle 180° resulted in a near mirror image of the initial velocity profile, revealing circumferential asymmetry of the spray pattern.
- Flame temperature measurements of nozzle “M” rotated over 360° in increments of 20° indicate that the flame temperature profile is dependent upon the alignment of the high and low velocity regions of the spray cone. A single measurement location had a maximum variation of 11% over the range of rotation.
- Cone exit plane measurements show that the flow exiting the burner cone is irregular in both magnitude and direction across the entire exit plane and up to one draft tube diameter downstream. Overall there is higher velocity in the top right and lower and reverse flow found in the bottom left of the cone exit plane. The low velocity region coincides with the measurement location for

thermocouple #1, which can become shrouded in soot during a temperature measurement, resulting in abnormally low temperature readings. The combination of low air flow with high fuel flow can result in an overly fuel rich region near thermocouple #1 causing soot to form on the thermocouple sheath.

- The swirling burner airflow is altered significantly when confined with the burner cone as evidenced by the cone exit plane measurements. Comparison of the unconfined burner air flow measurements with the cone exit plane measurements show drastically different flow distributions and magnitudes at the same axial location. Previous studies on swirling flow in circular-to-round transition ducts have also found that the shape of the transition results in a skewed velocity distribution due to the flow impinging on the top and bottom surfaces of the duct.
- The measurements made on the exterior of the cone indicate entrainment of the surrounding ambient air into the cone exit flow. Instantaneous and mean vorticity data show vortical structures exiting the burner cone. The entrainment and mixing of surrounding air is evidenced by the counter-rotating structures and by the decay of the mean vorticity and growth of the cone exit flow field.

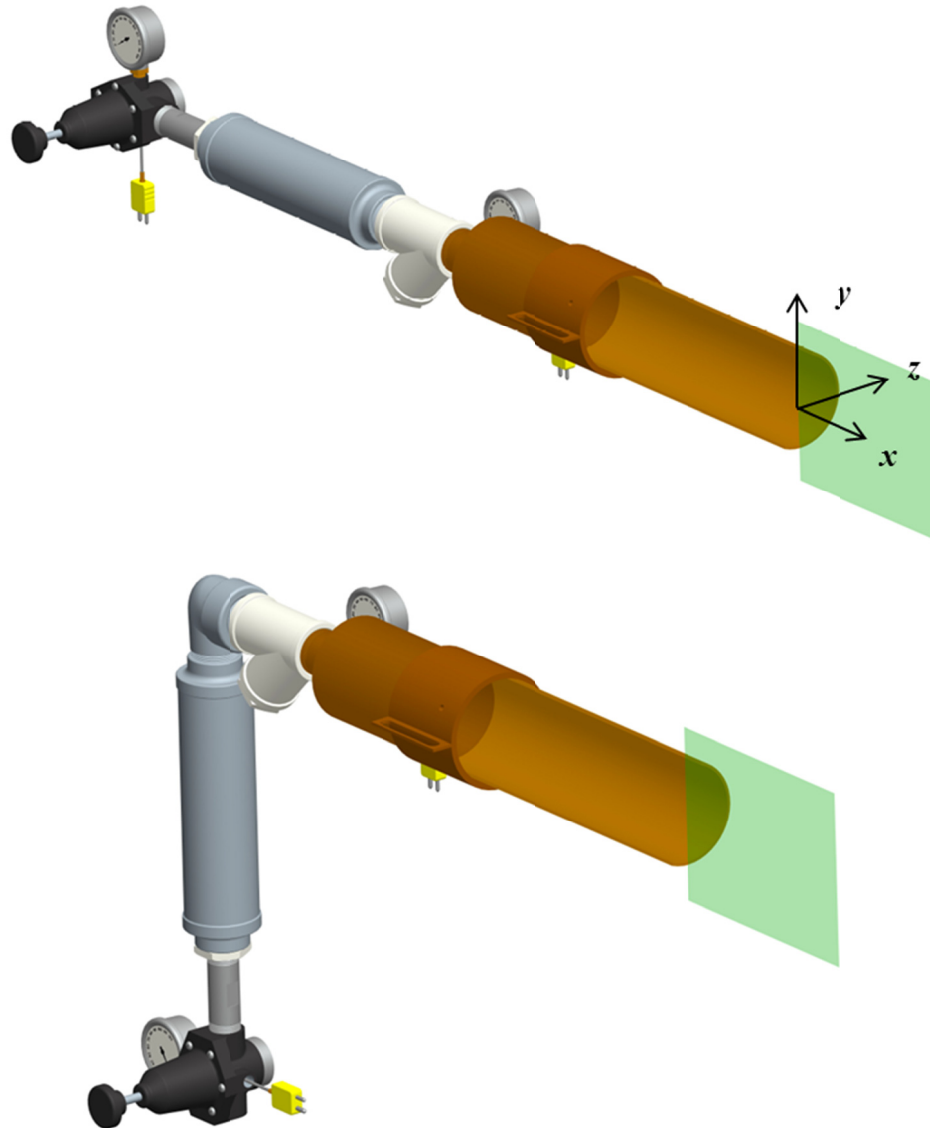


Figure 3.1. Burner configurations for empty tube baseline tests. The measurement plane is aligned with the vertical axis of the draft tube. The standard coordinate axes for this work are shown in the measurement plane. Straight configuration (top) and 90° elbow configuration (bottom).

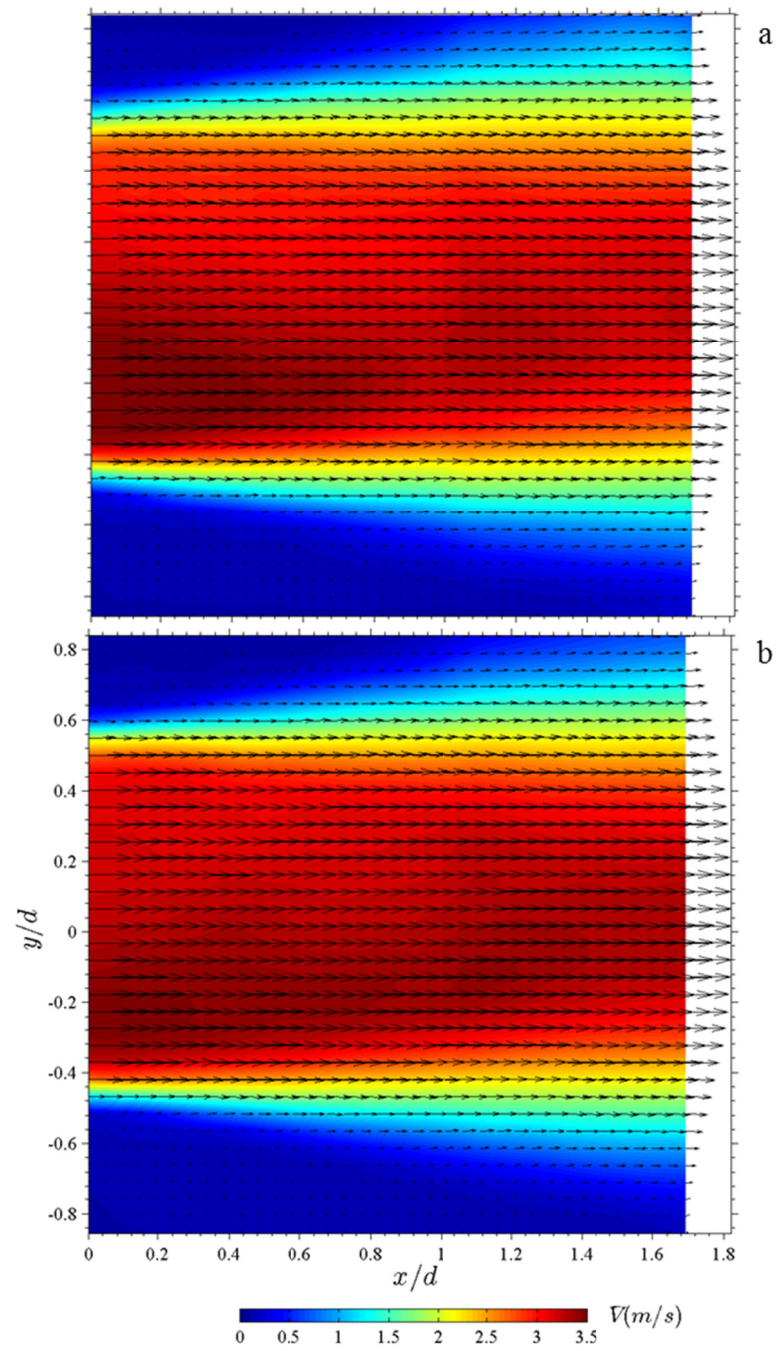


Figure 3.2. Contour and vector plot showing measured mean in-plane velocity field exiting the empty draft tube from $x/d=0-1.8$. Comparison of the straight air inlet configuration (top) and the 90-degree inlet configuration (bottom).

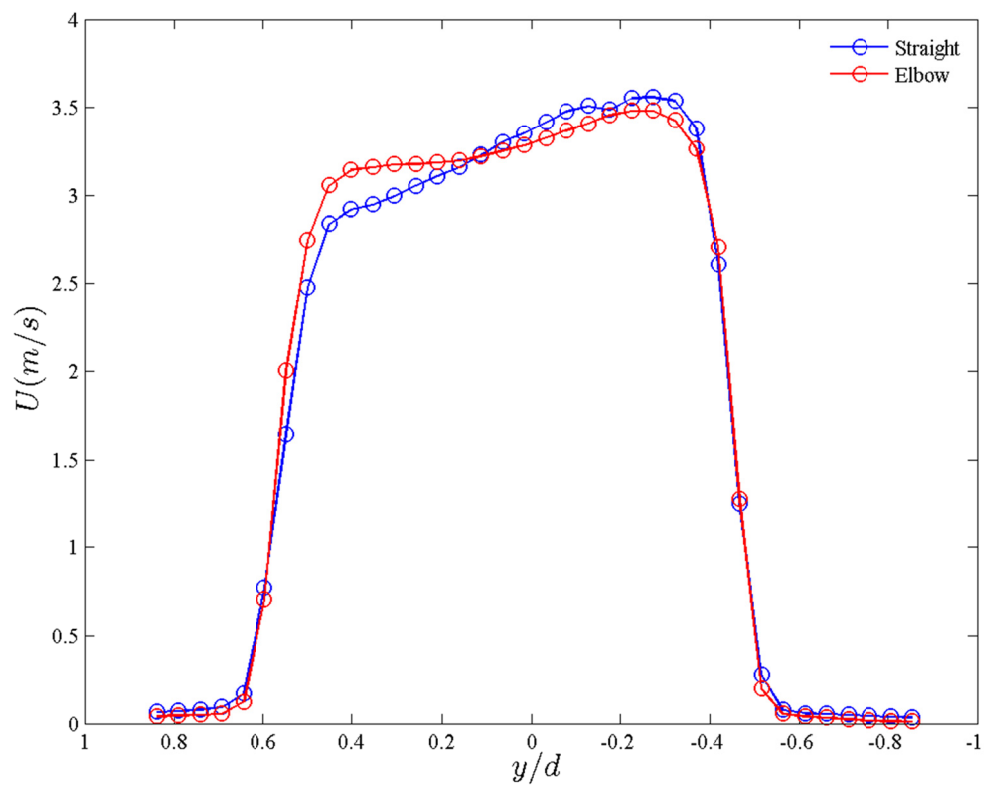


Figure 3.3. Velocity profiles at the draft tube exit ($x/d=0.2$). Comparison of two different upstream muffler configurations shows asymmetry about the burner axis and nearly similar velocity profile shapes for both configurations.

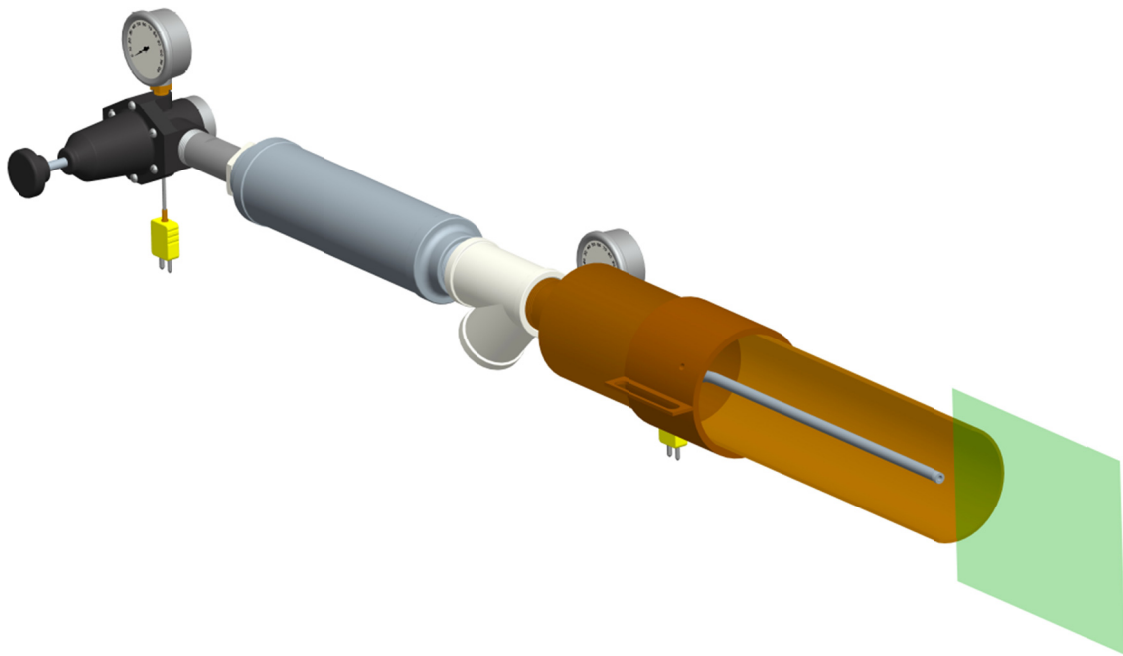


Figure 3.4. Schematic of the fuel pipe in the burner tube and PIV measurement plane.

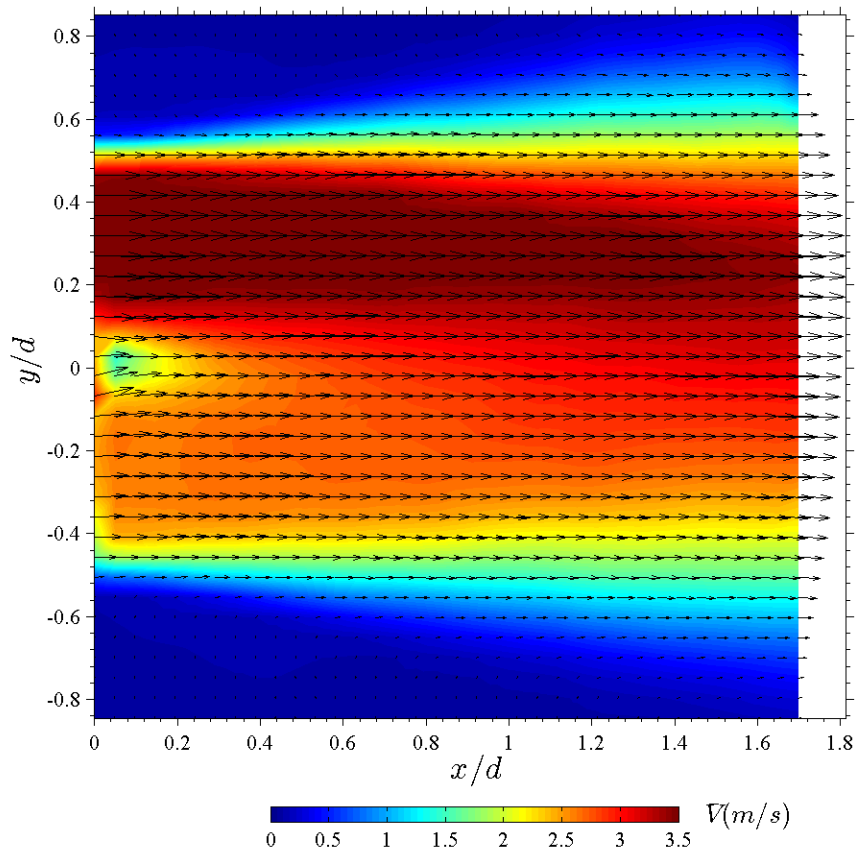


Figure 3.5. Contour and vector plot showing measured mean in-plane velocity field exiting the draft tube from $x/d=0-1.8$. The fuel pipe was installed in the burner and is aligned with the burner axis.

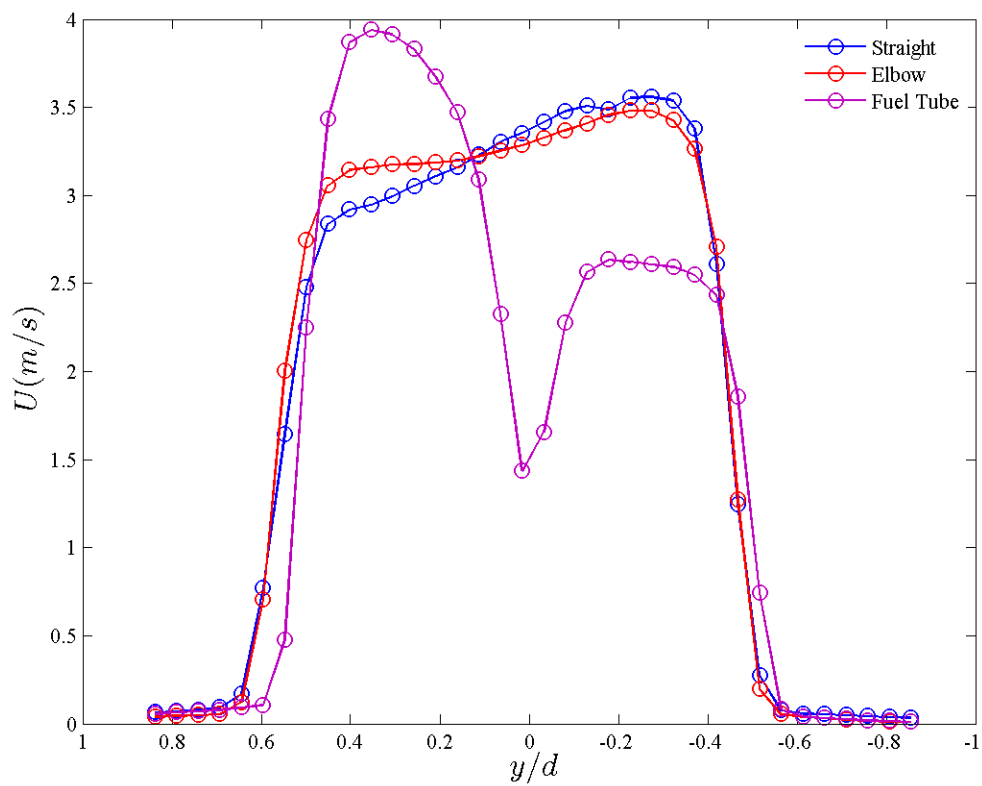


Figure 3.6. Velocity profiles at the draft tube exit. Comparison of two different upstream muffler configurations and the effect of the fuel pipe in the draft tube.

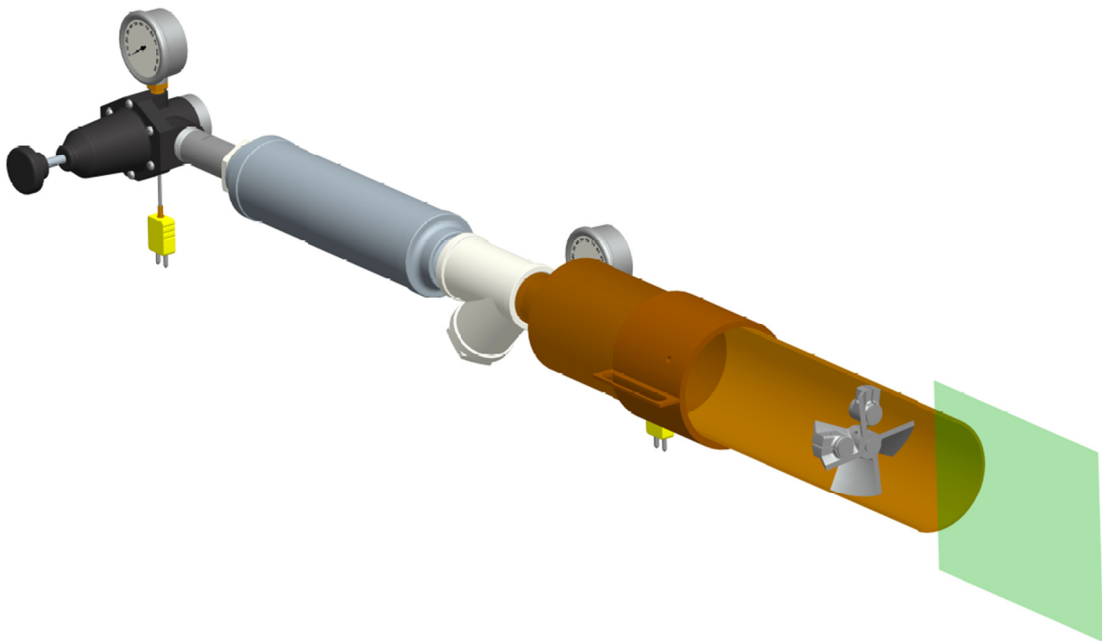


Figure 3.7. Schematic of the stator in the draft tube and PIV measurement plane. The holes on the stator were blocked with aluminum tape for these measurements.

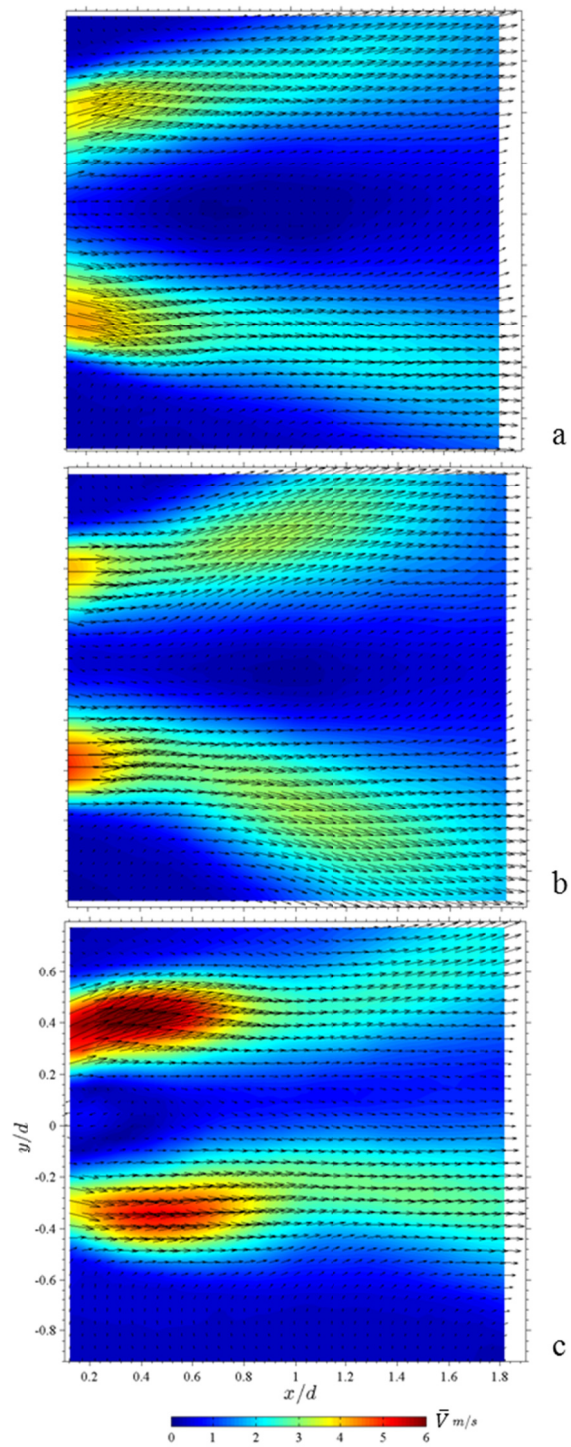


Figure 3.8. Contour and vector plot showing measured mean in-plane velocity field exiting the draft tube from $x/d=0.1-1.8$. The stator was inserted into the draft tube and recessed 127 mm (a), 76.2 mm (b), and 25.4 mm (c) from the draft tube exit plane. The magnitude of the exit velocity and the jet growth are seen to vary with stator location in the draft tube.

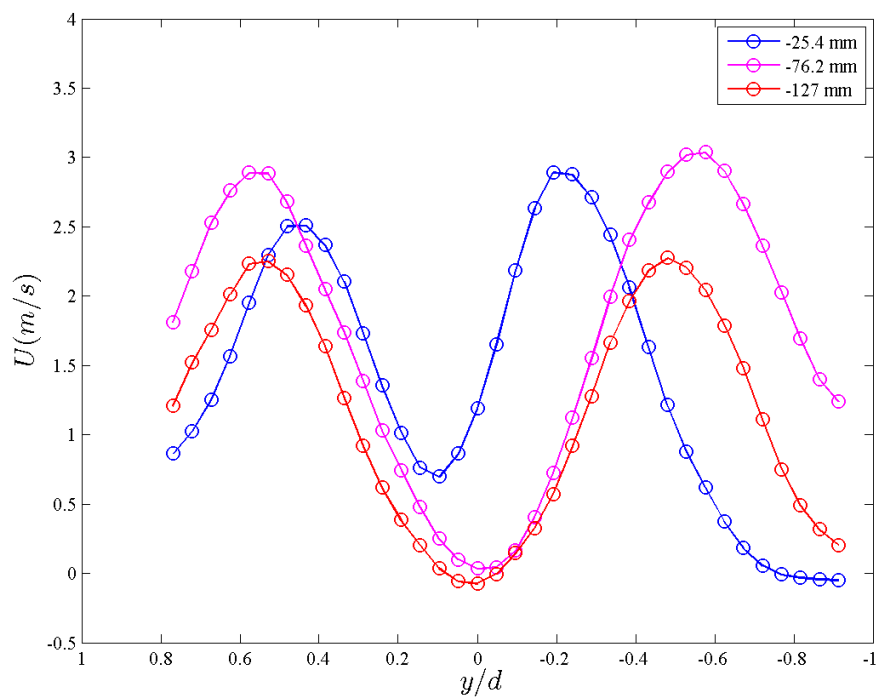


Figure 3.9. Comparison of measured mean velocity profiles for the three stator positions at $x/d=1$.

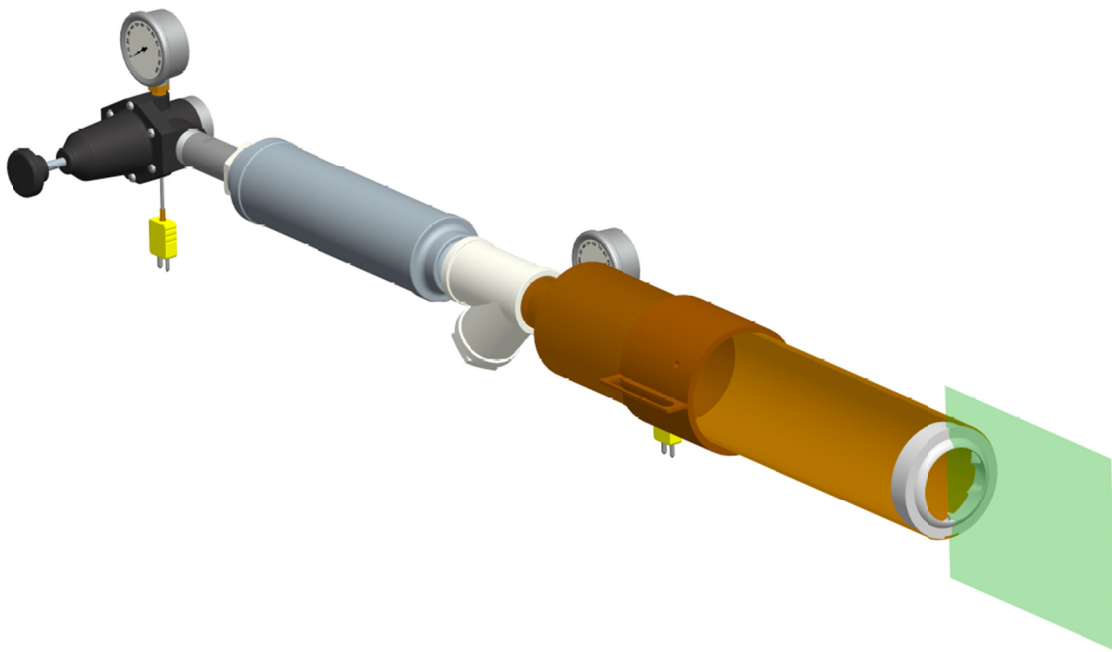


Figure 3.10. Schematic of the turbulator on the end of the empty draft tube and PIV measurement plane.

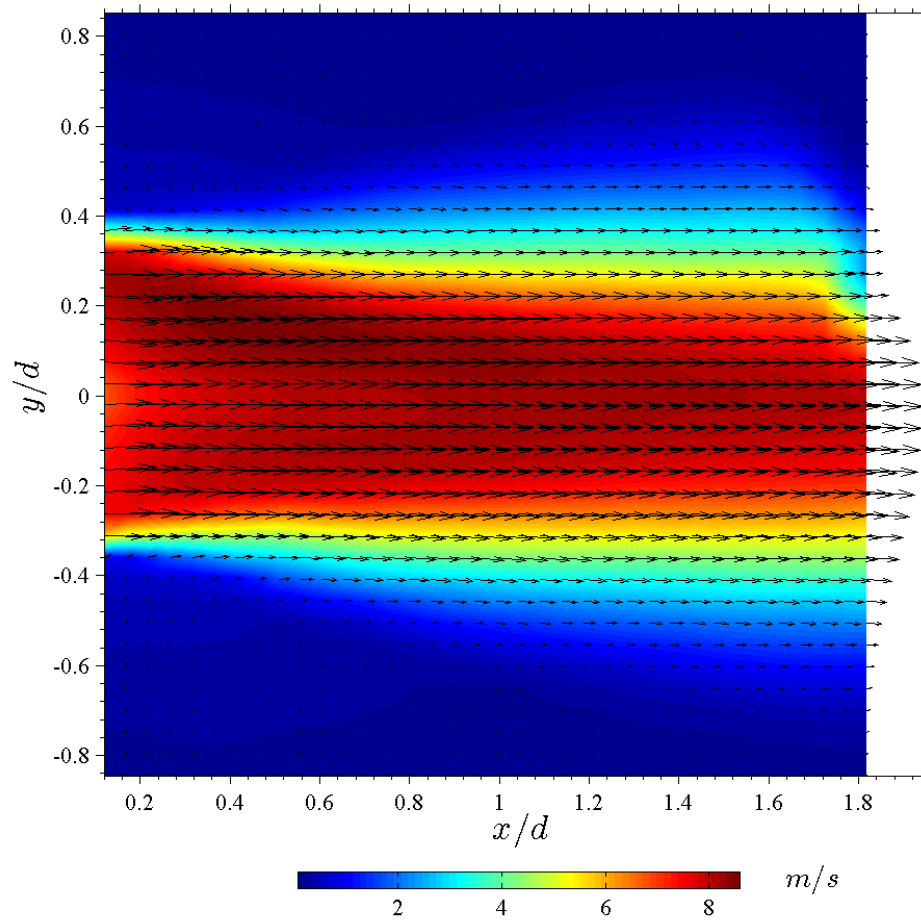


Figure 3.11. Contour and vector plot showing measured mean in-plane velocity field exiting the draft tube from $x/d=0.1-1.8$. The turbulator was installed on the end of the empty draft tube.

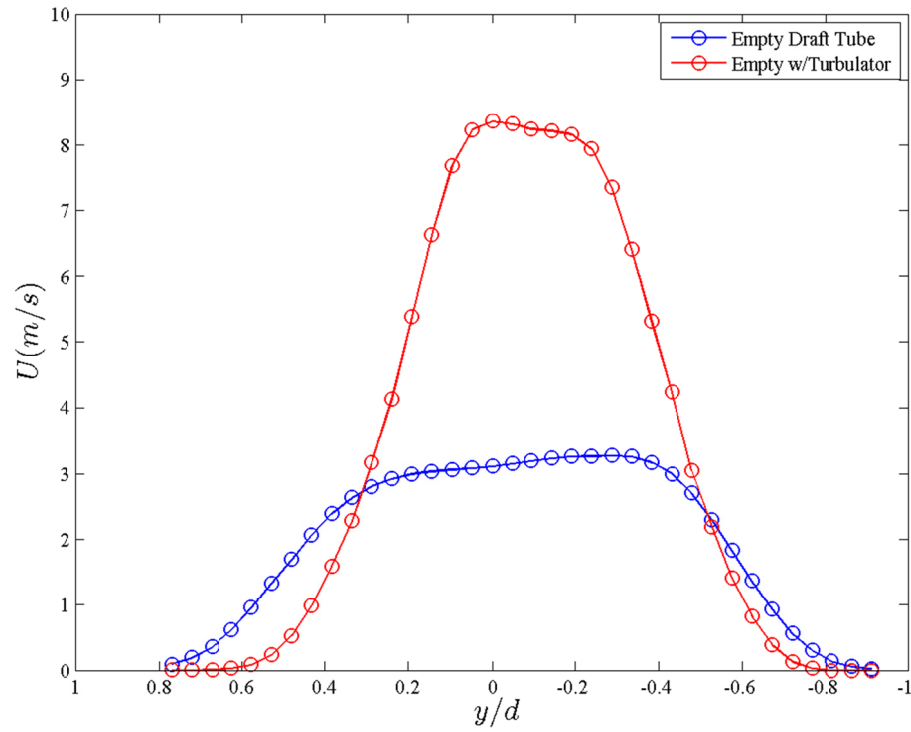


Figure 3.12. Measured mean axial velocity profiles at $x/d=1$, comparison between the empty draft tube configuration and the addition of the turbulator on the end of the draft tube.

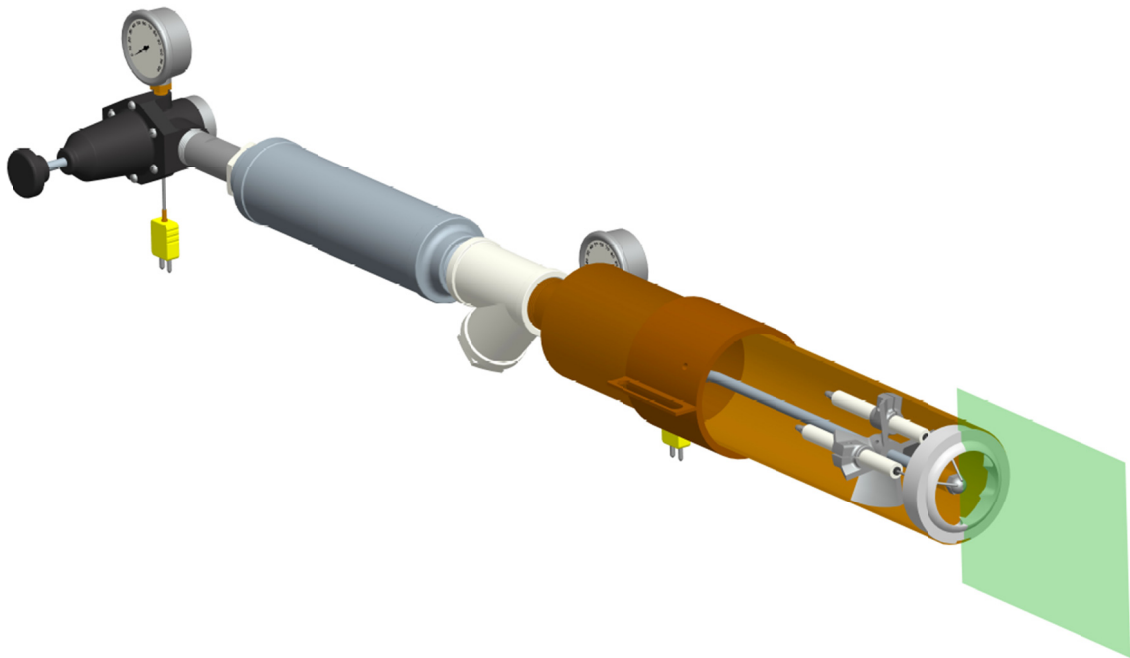


Figure 3.13. Schematic of the fully configured NexGen burner and PIV measurement plane.

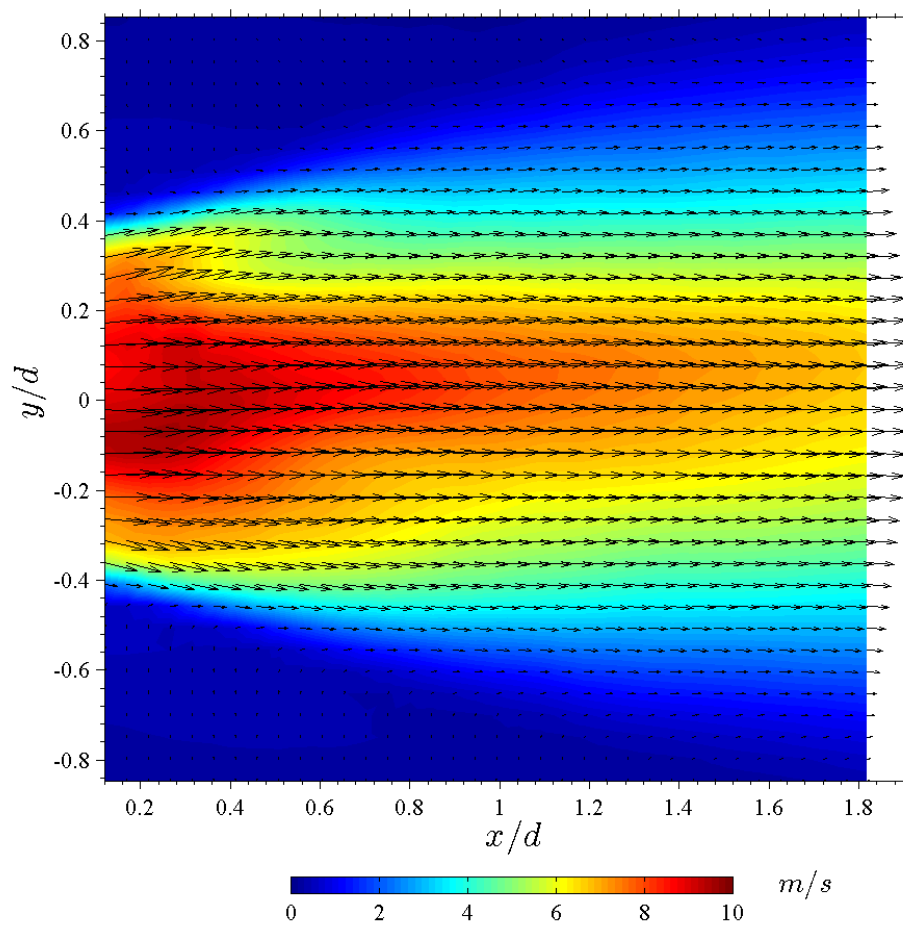


Figure 3.14. Contour and vector plot showing measured mean in-plane velocity field exiting the draft tube from $x/d=0.1-1.8$ for the fully configured NexGen burner.

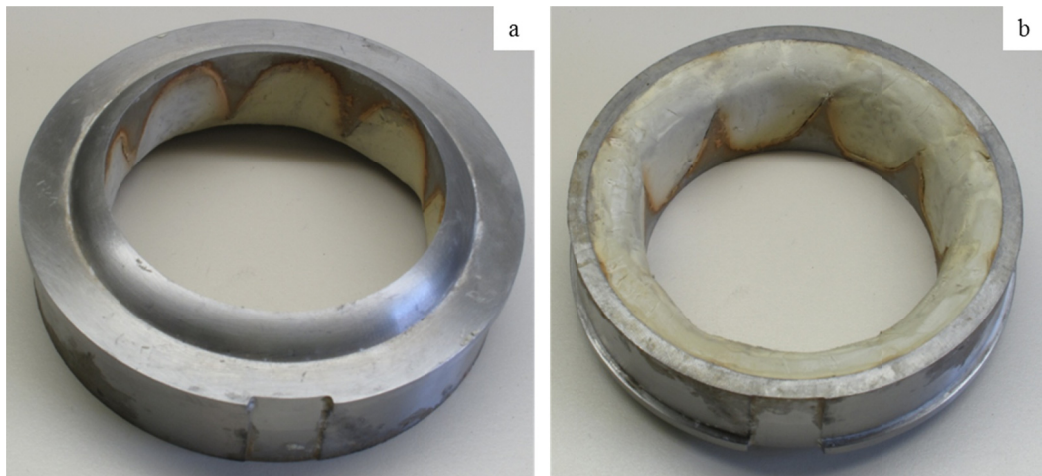


Figure 3.15. Front (a) and back (b) view of the turbulator with filled-in vanes.

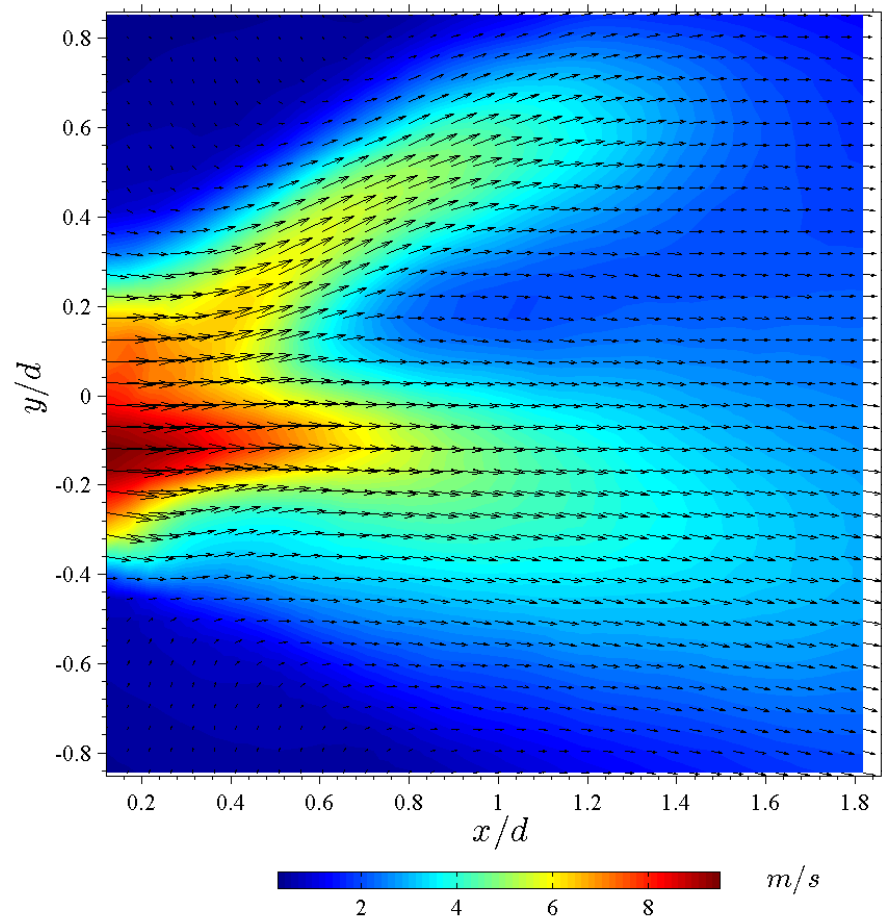


Figure 3.16. Contour and vector plot showing measured mean in-plane velocity field exiting the draft tube from $x/d=0.1-1.8$. The turbulator vanes were filled in with putty to eliminate the effect of the vanes on the flow while still maintaining the exit plane area reduction of the turbulator; comparison to Figure 3.14 shows that the turbulator vanes limit jet growth and even out the flow, creating symmetry.

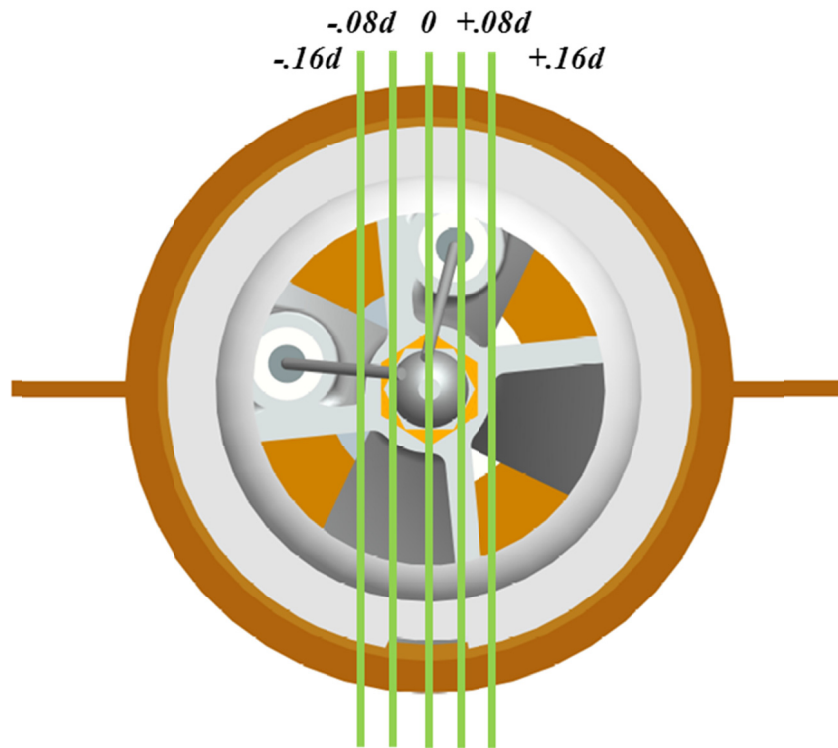
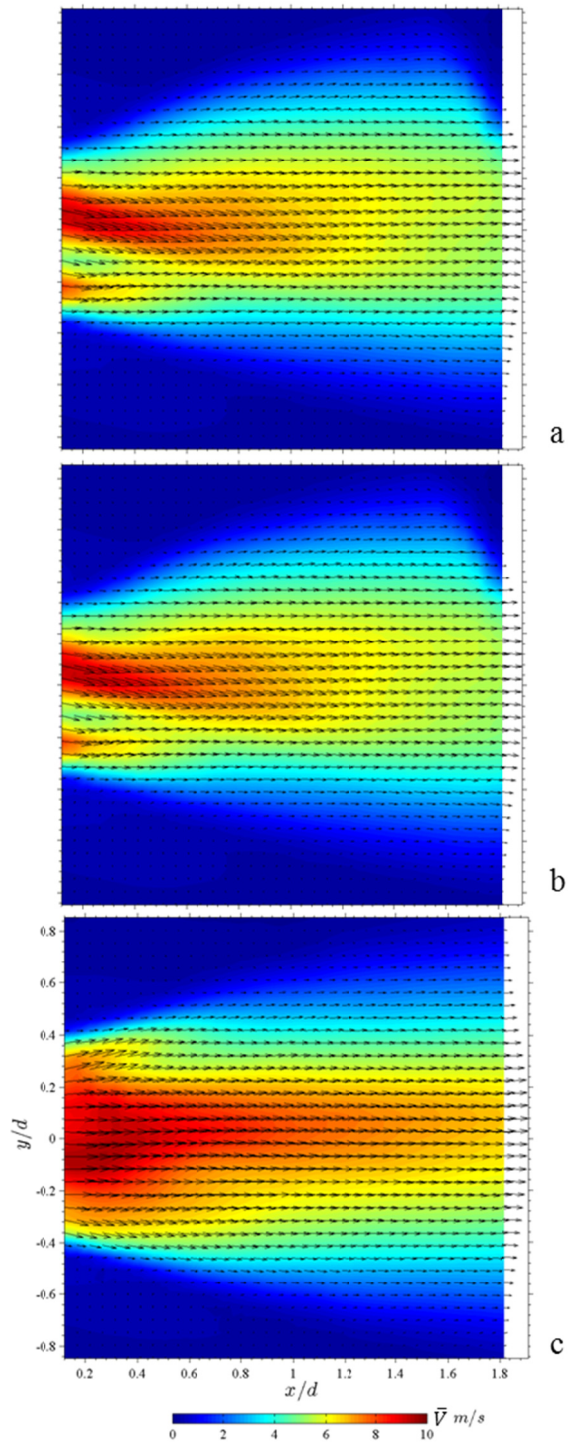


Figure 3.17. Front view of the turbulator exit plane showing the five measurement planes adjacent to the vertical centerline plane.



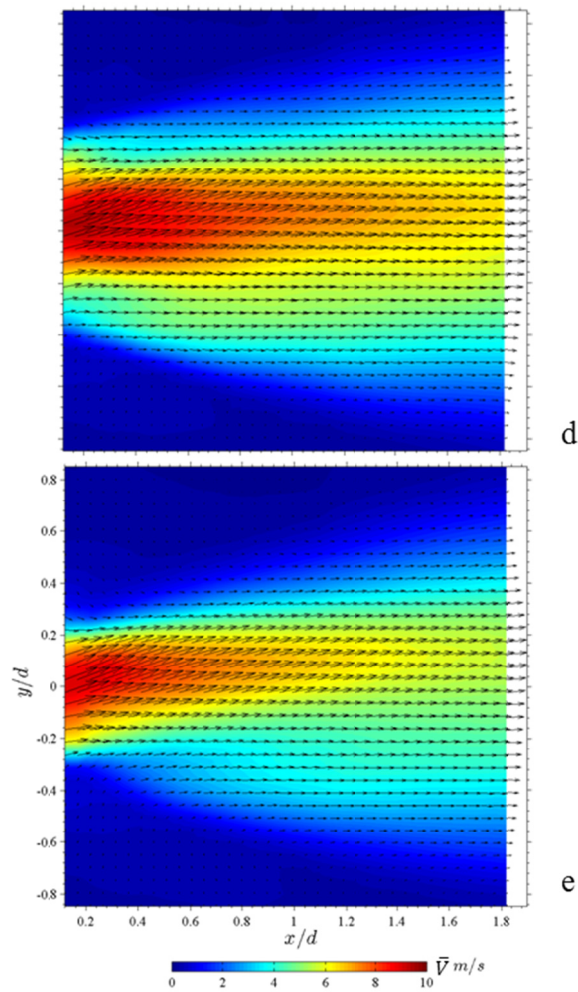
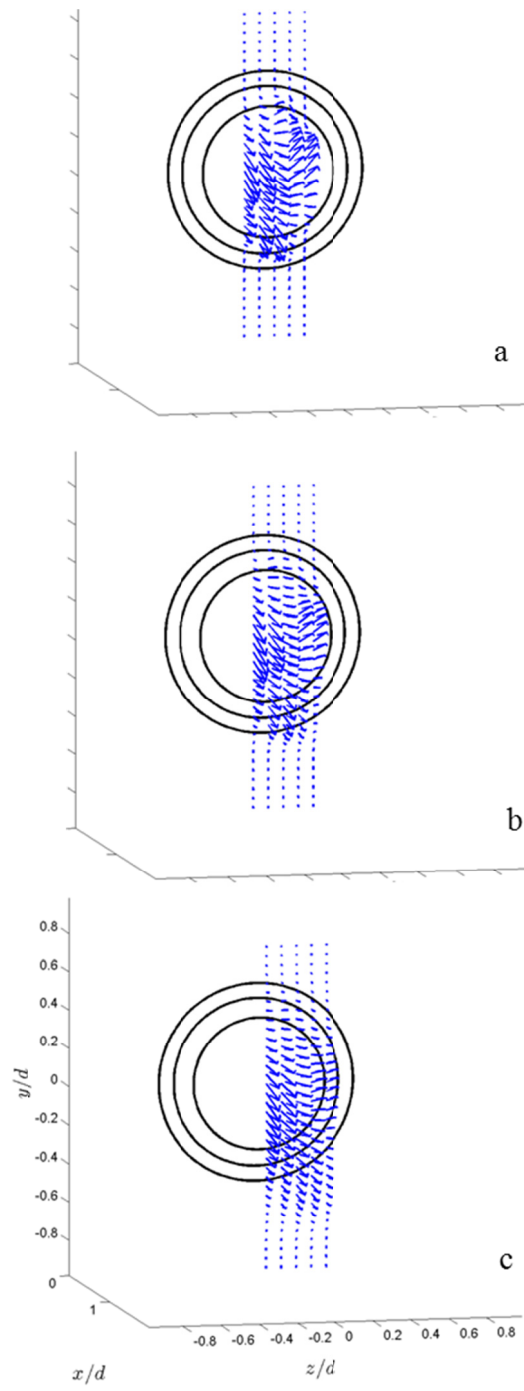


Figure 3.18. Contour and vector plots showing measured mean in-plane velocity field exiting the draft tube from $x/d=0.1-1.8$, $z/d = -0.16d$ (a), $-0.08d$ (b), 0 (c), $0.08d$ (d), $0.16d$ (e).



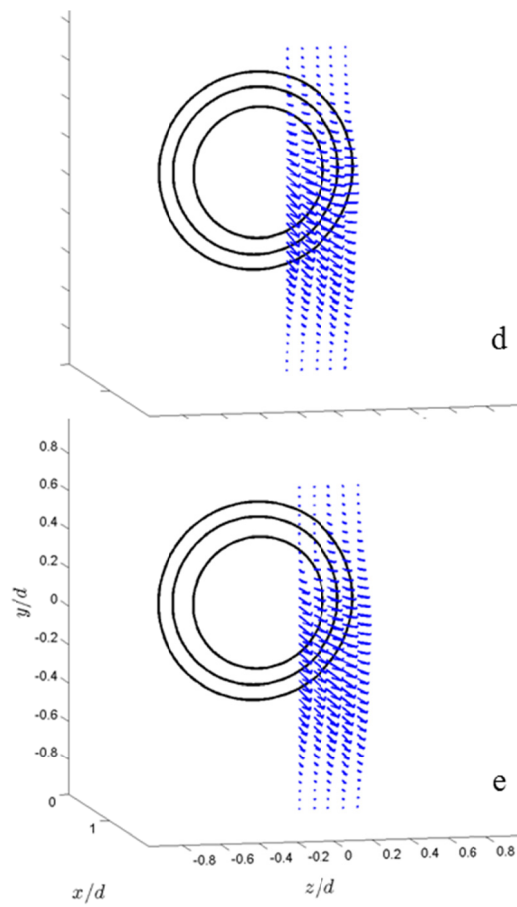


Figure 3.19. Measured mean velocity profiles exiting the turbulator at 5 cross streamwise planes at $x/d=0.2$ (a), 0.5 (b), 1.0 (c), 1.5 (d), and 1.8 (e).

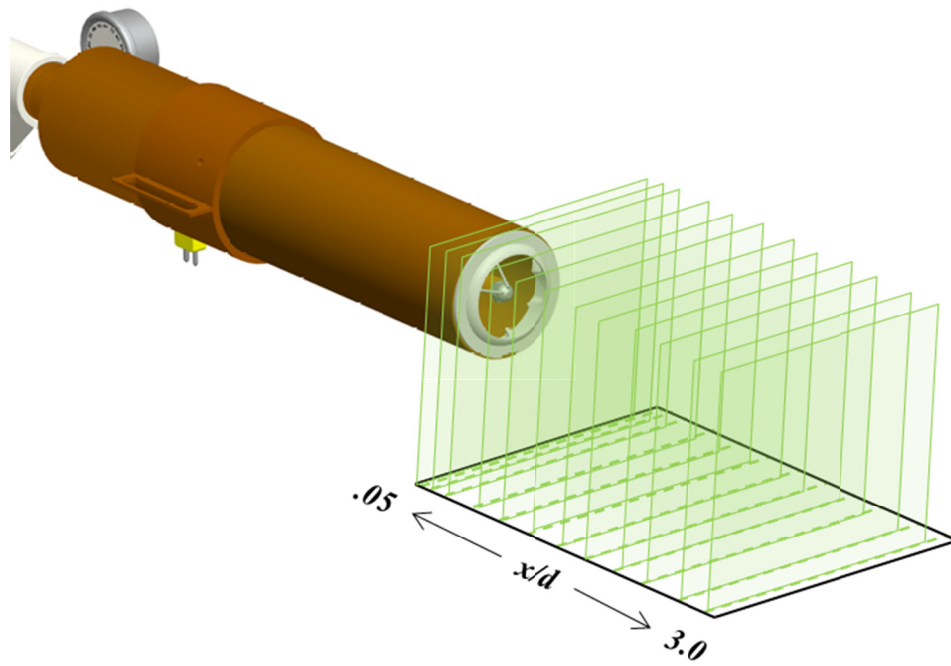


Figure 3.20. PIV measurement plane locations for stereoscopic measurements of unconfined swirling jet emerging from the turbulator exit.

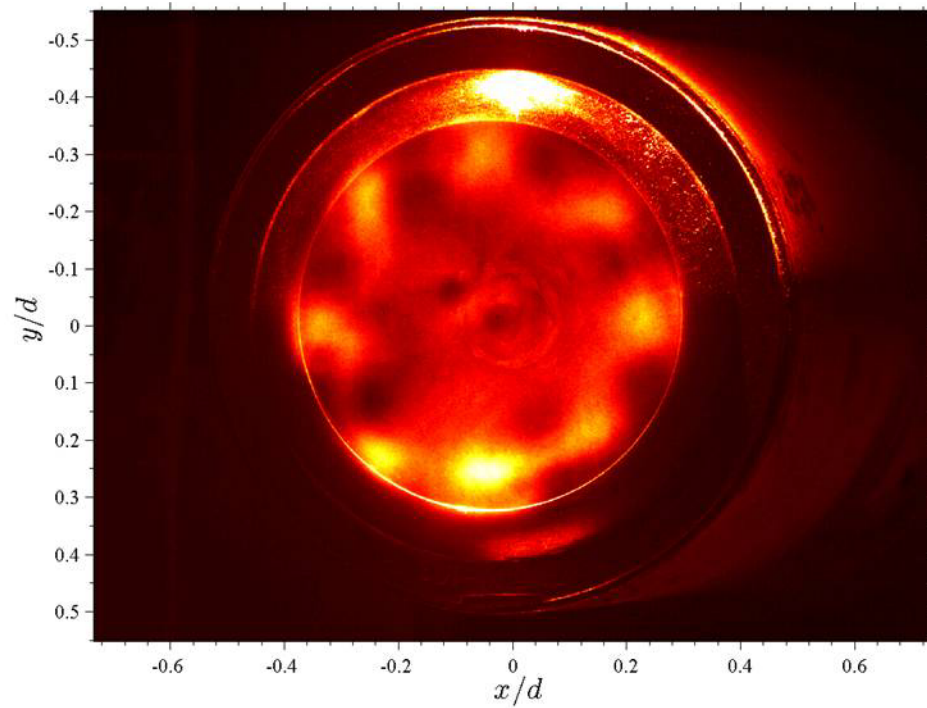
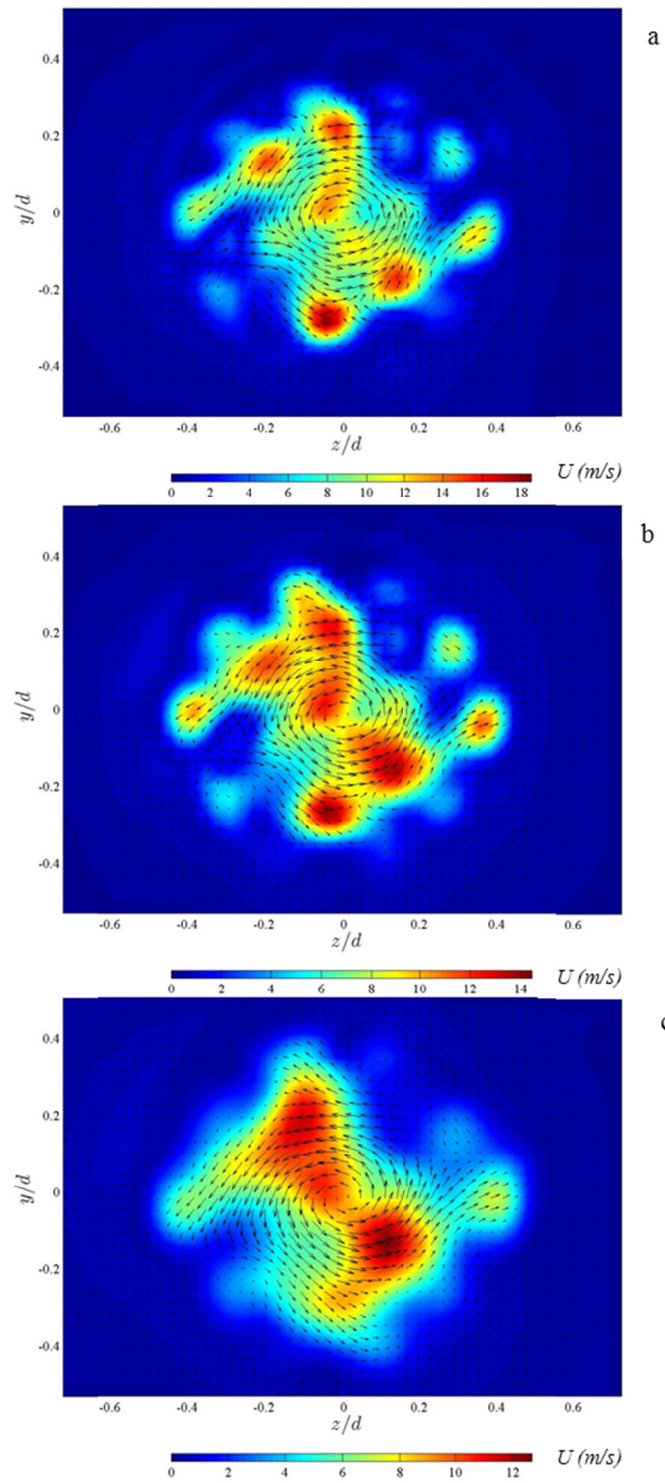
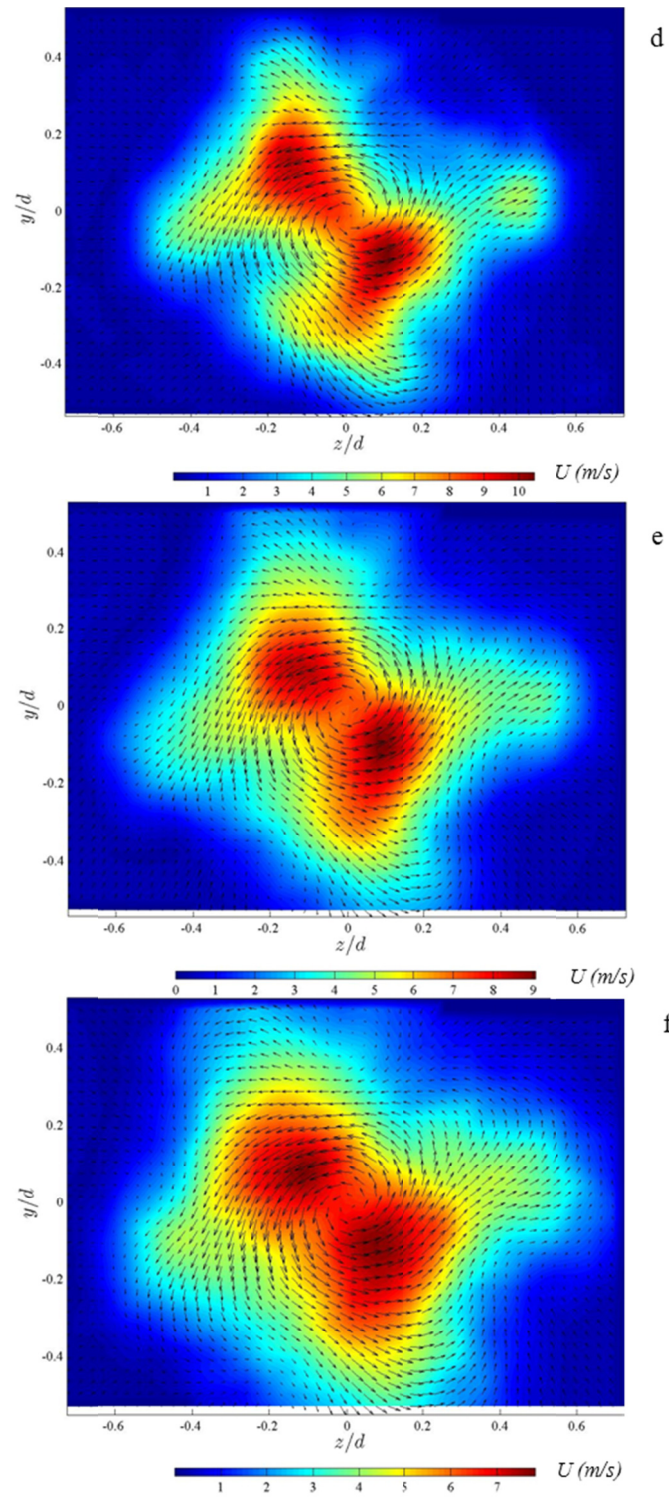
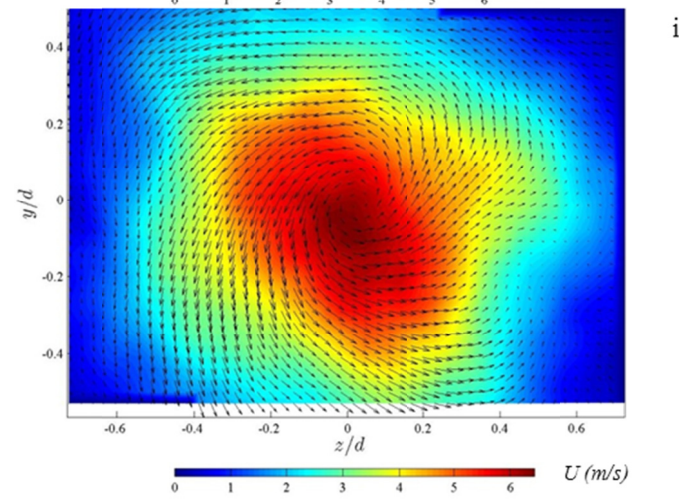
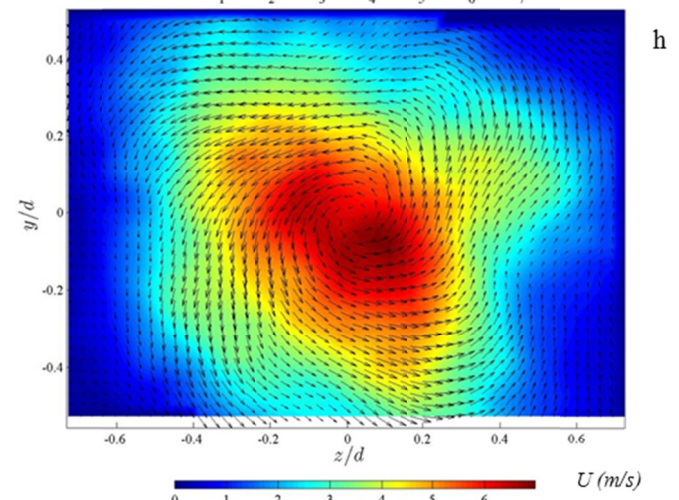
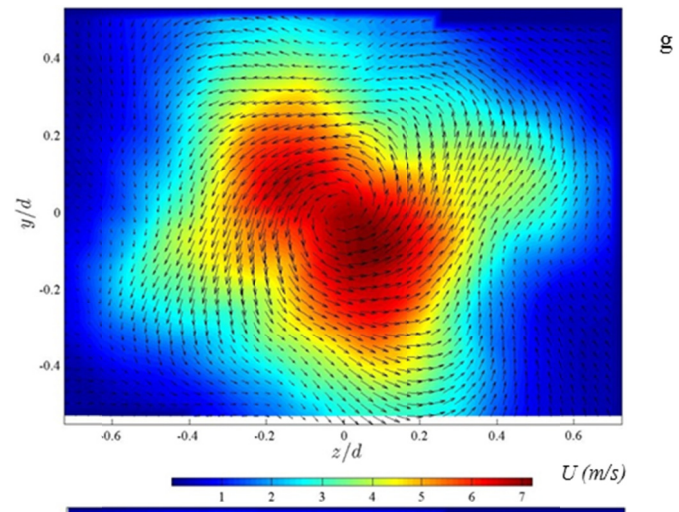


Figure 3.21. Mean image of instantaneous raw data images for stereoscopic PIV measurements of the unconfined swirling jet emerging from the turbulator exit. The seed particles are seen to be concentrated in eight locations around the turbulator circumference, coincident with the location of the eight turbulator vanes.







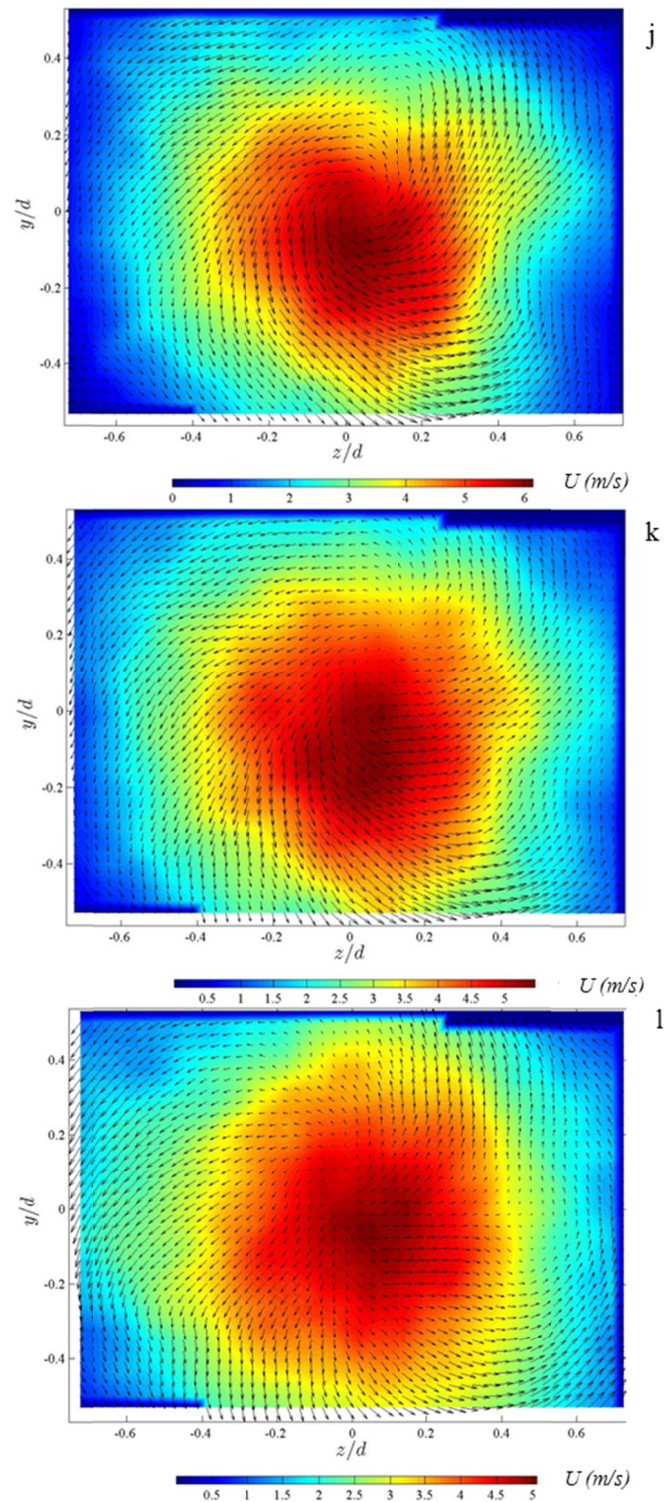


Figure 3.22. Contour and vector plots showing measured three-component mean velocity field exiting the draft tube at $x/d=0.05$ (a), 0.1 (b), 0.25 (c), 0.5 (d), 0.75 (e), 1.0 (f), 1.25 (g), 1.5 (h), 1.75 (i), 2.0 (j), 2.5 (k), and 3.0 (l).

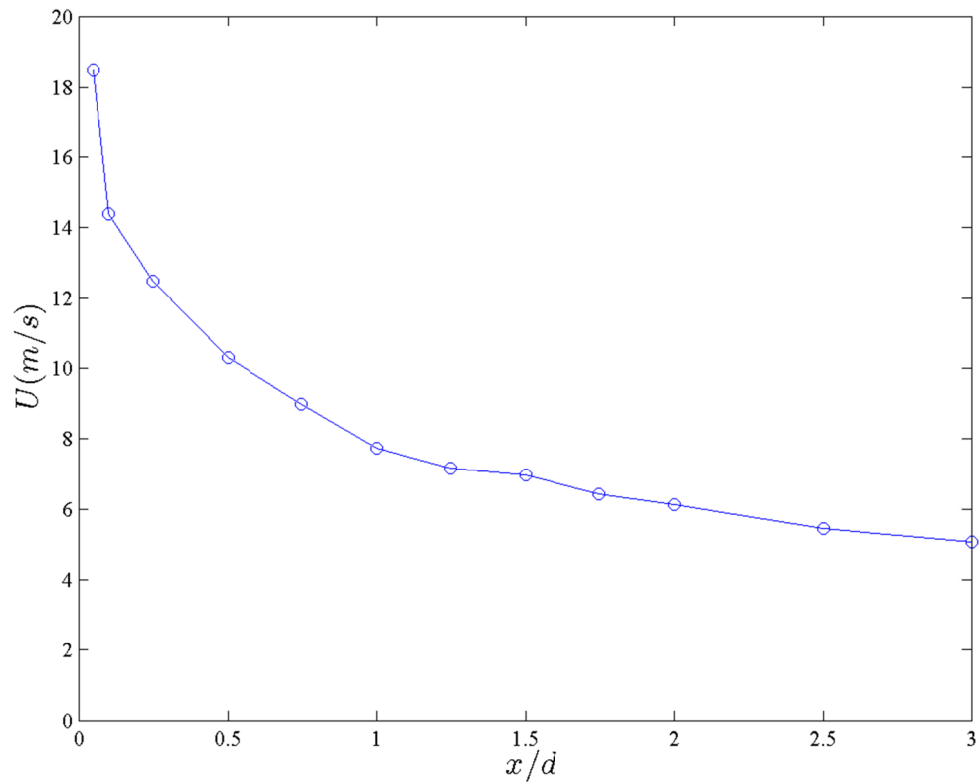


Figure 3.23. Peak mean U -component velocity in each axial measurement plane from $x/d=0.05$ to 3 indicating the axial velocity decay as a function of the axial position.

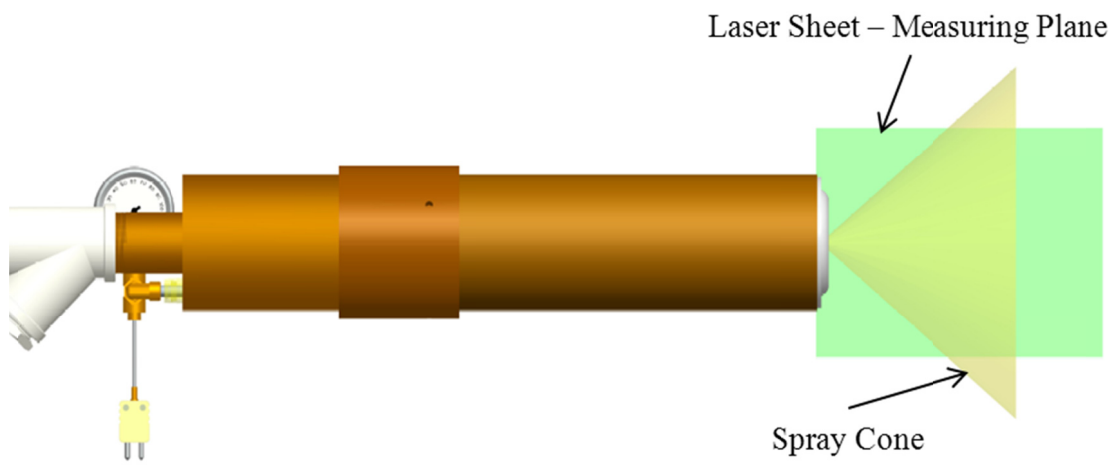


Figure 3.24. Measurement plane location for spray nozzle PIV measurements.

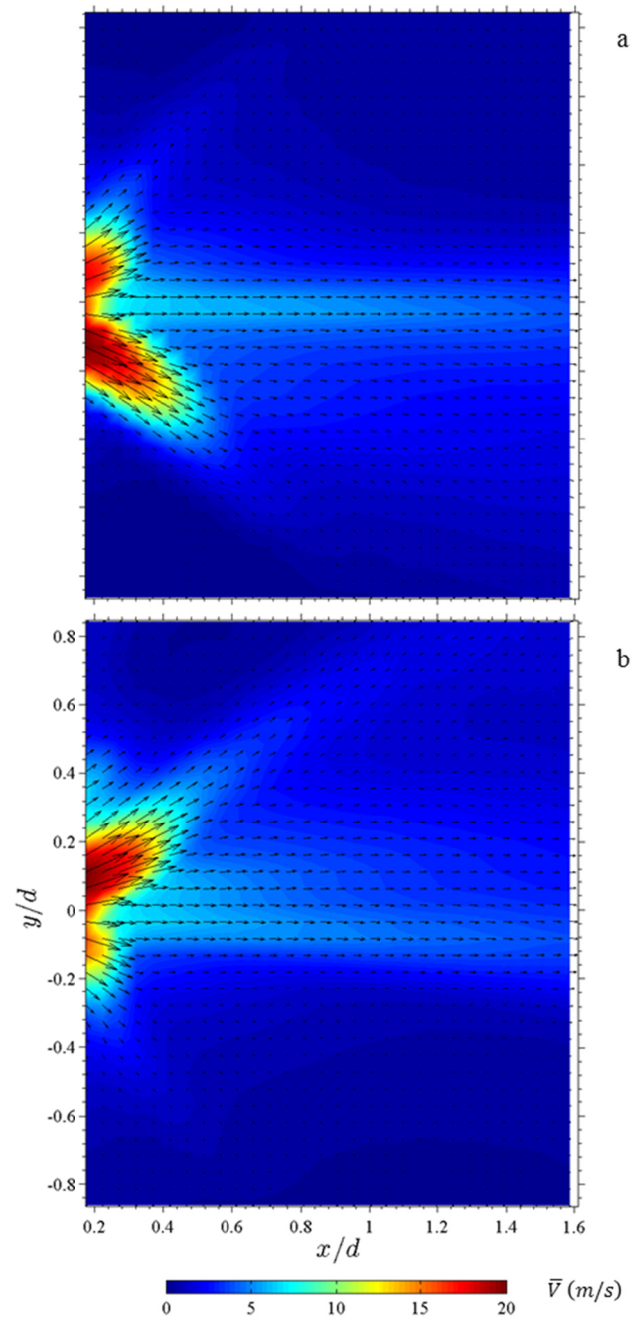


Figure 3.25. Contour and vector plots showing measured in-plane velocity field of the spray produced by Nozzle M, 2.25 gph-rated at 100 psig at 0° (a) and 180° (b) rotation.

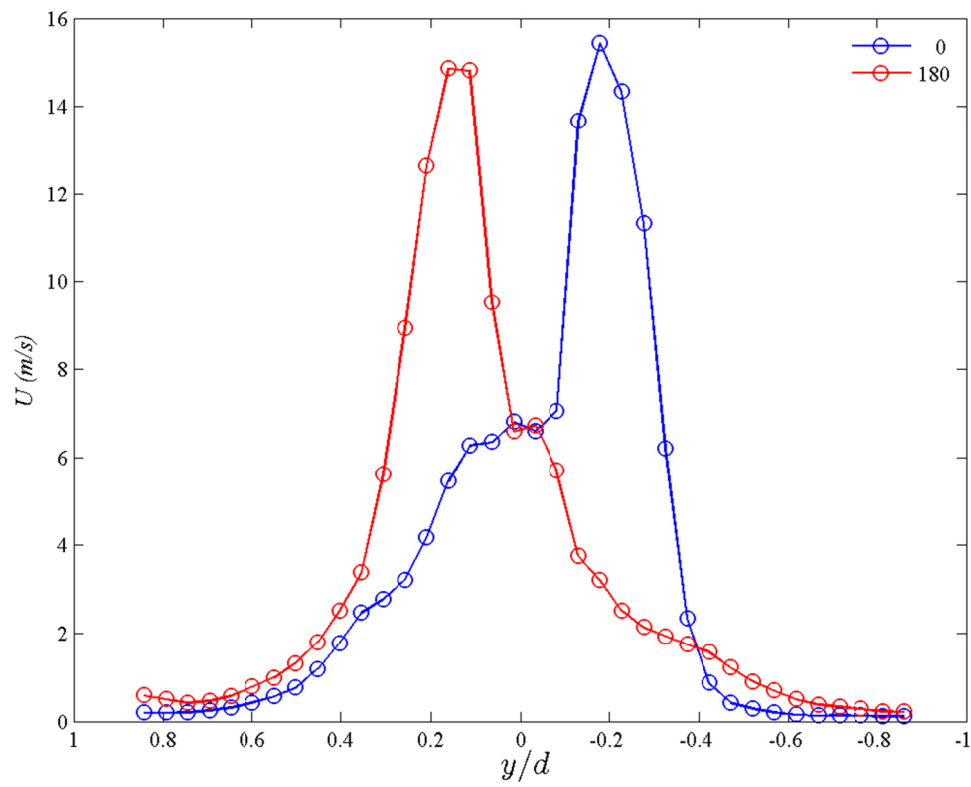


Figure 3.26. Comparison of the mean axial velocity profiles at the spray nozzle exit ($x/d=0.37$) for nozzle M at 0° and 180° .

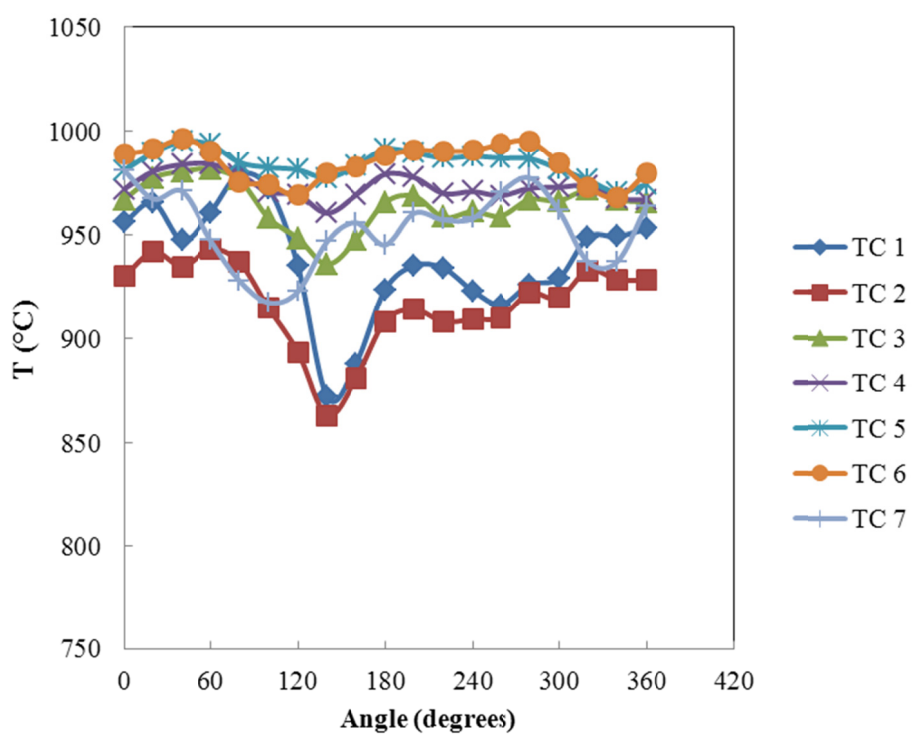


Figure 3.27. Average measured flame temperature at seven thermocouple (TC) locations plotted against the nozzle rotation angle for nozzle M.

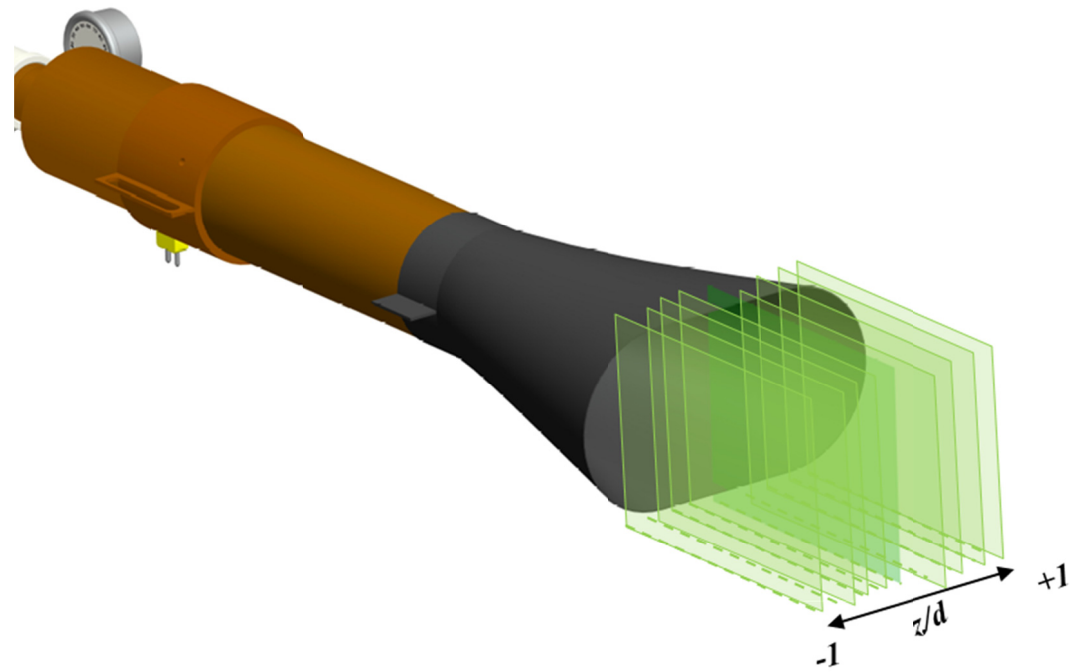
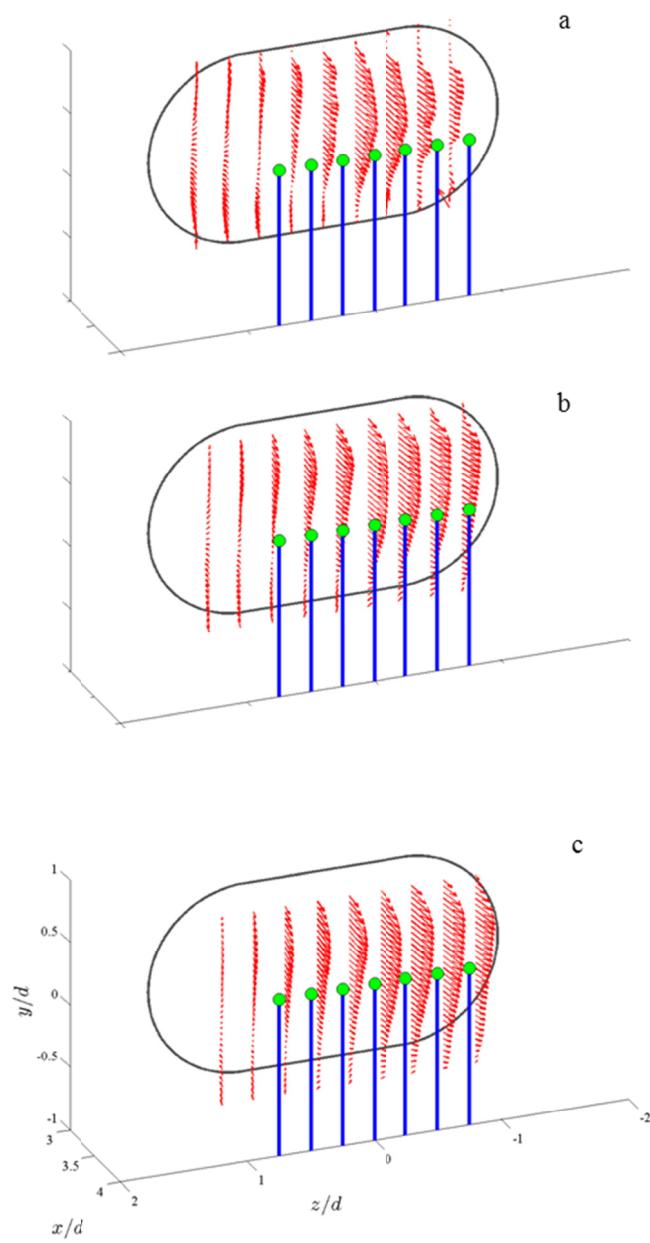


Figure 3.28. Location of 9 cone exit flow measurement planes $0.25d$ apart from $-1d$ to $1d$.



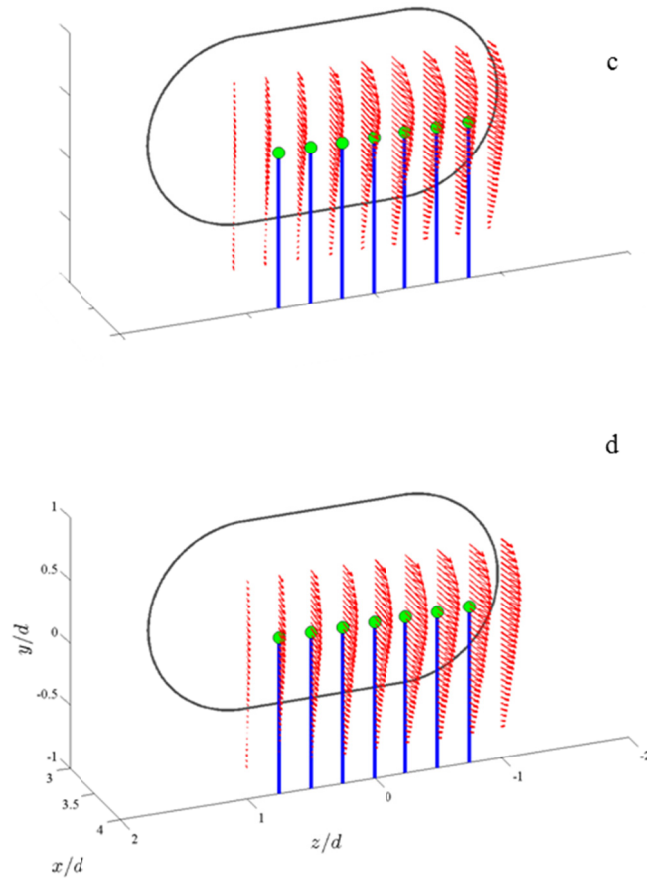


Figure 3.29. Measured mean in-plane velocity profiles exiting the burner cone at 9 cross-streamwise planes from $-1 < z/d < 1$ at axial distance $x/d=3$ (a), $x/d=3.25$ (b), $x/d=3.5$ (c), $x/d=3.75$ (d), and $x/d=4.0$ (e) from the turbulator exit plane. The flame temperature measurement locations are indicated by the green points.

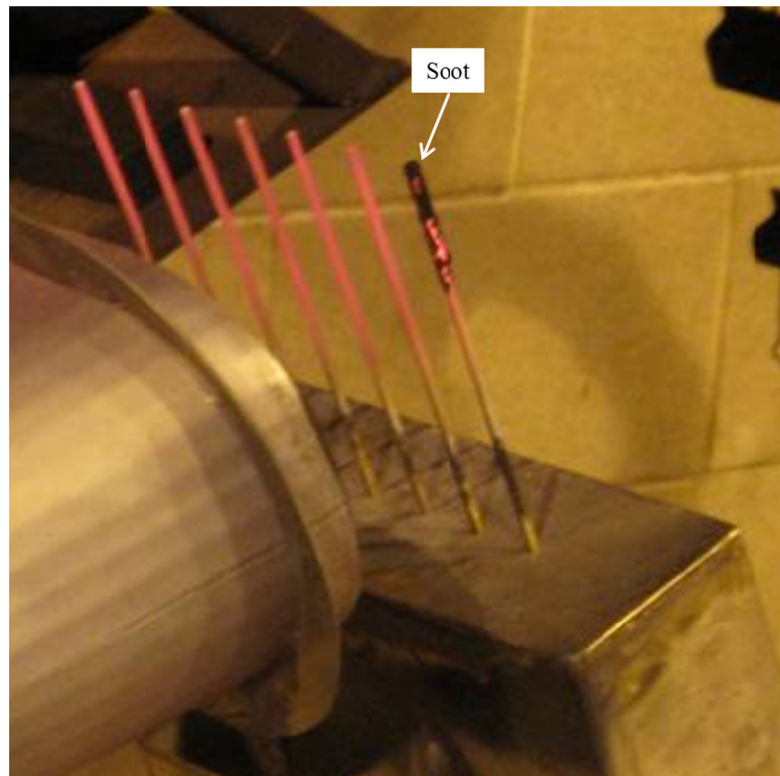


Figure 3.30. Flame temperature thermocouples immediately after a measurement. Note the heavy soot coating on thermocouple #1. This thermocouple location coincides with the low velocity region found in the cone exit plane measurements.

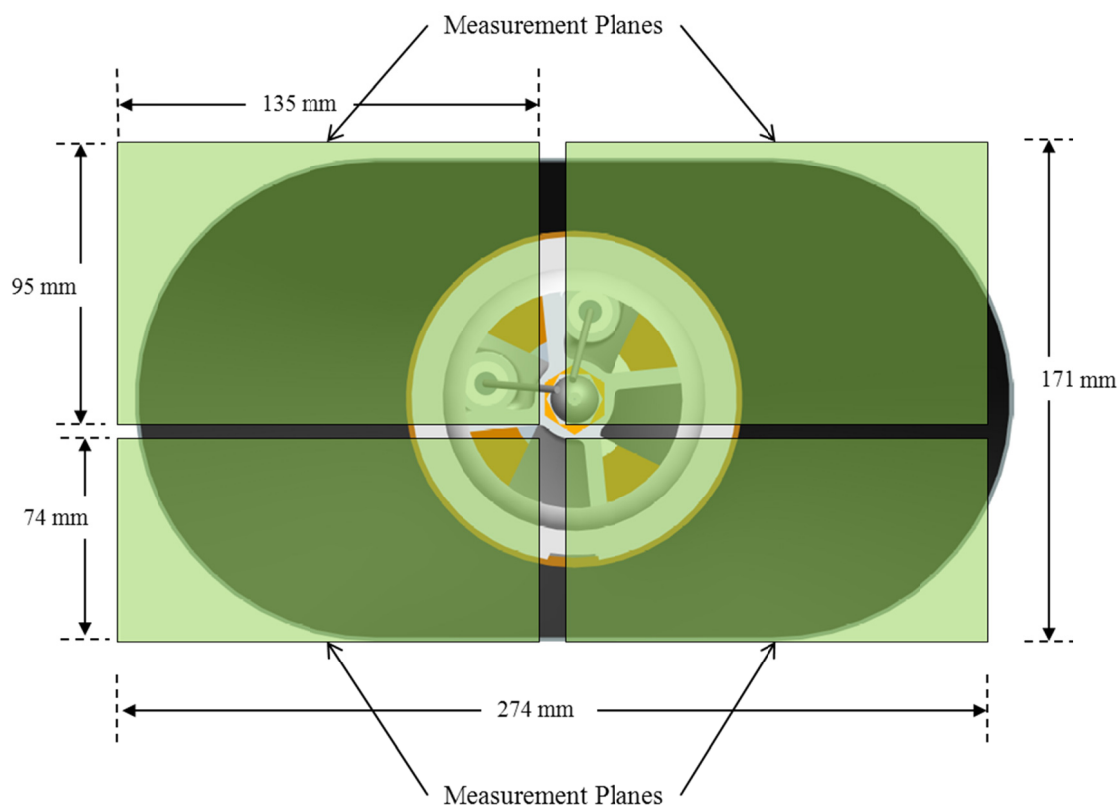


Figure 3.31. Measurement plane locations at the burner cone exit plane for stereoscopic PIV measurements of the cone exit flow.

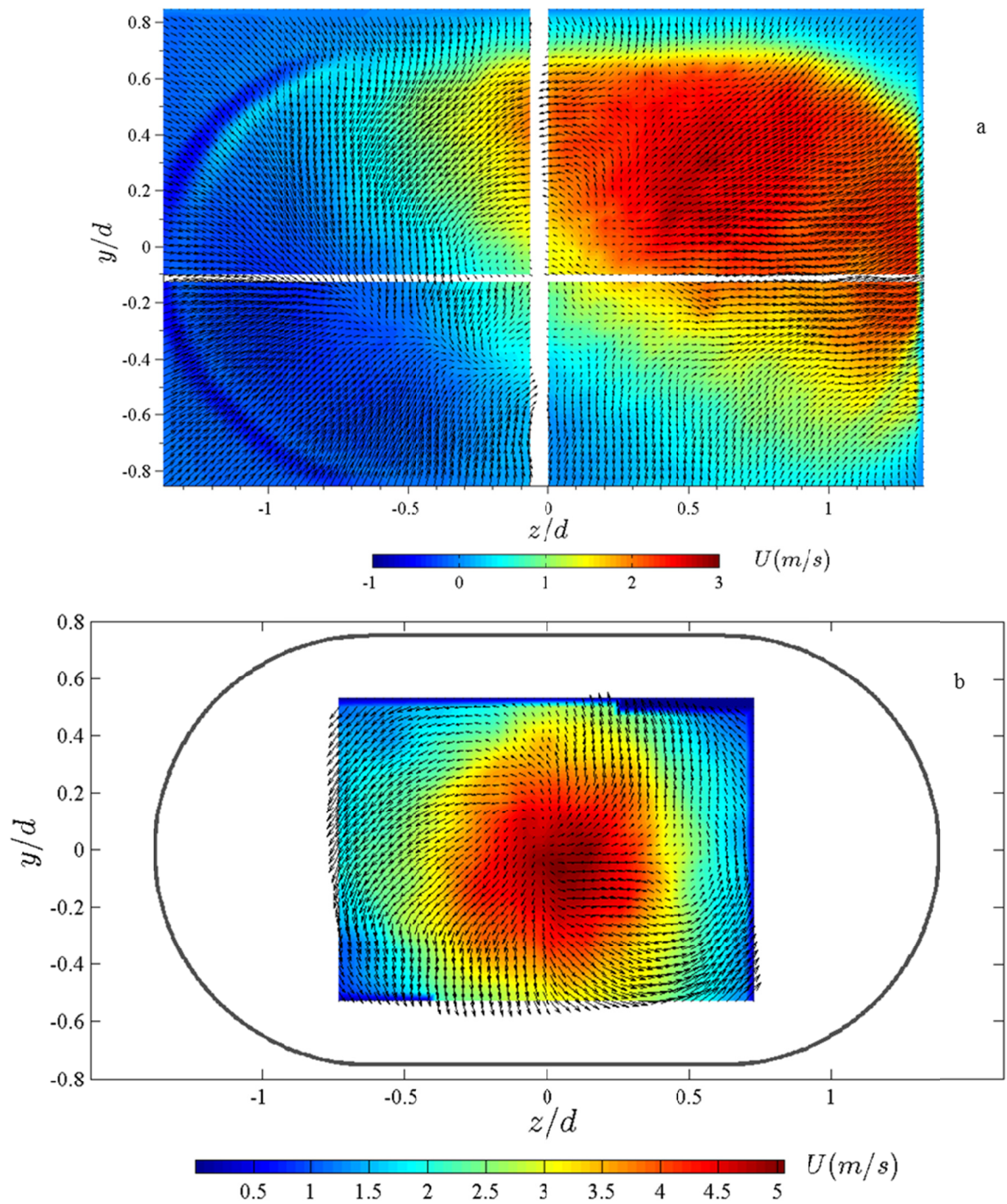


Figure 3.32. Contour and vector plots showing measured three component velocity field at the burner cone exit plane formed by combining four individual measurement planes (a) and comparison with the unconfined swirling jet emerging from the turbulator (b).

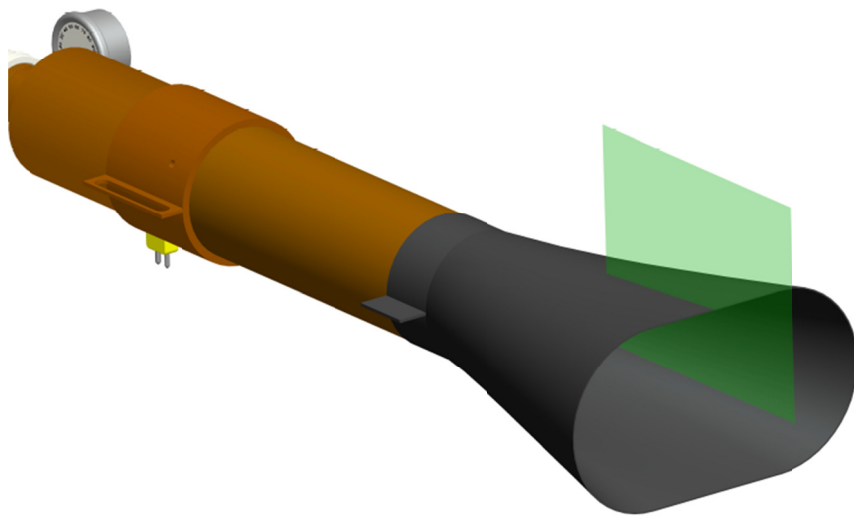


Figure 3.33. Location of the external cone flow field measurement plane.

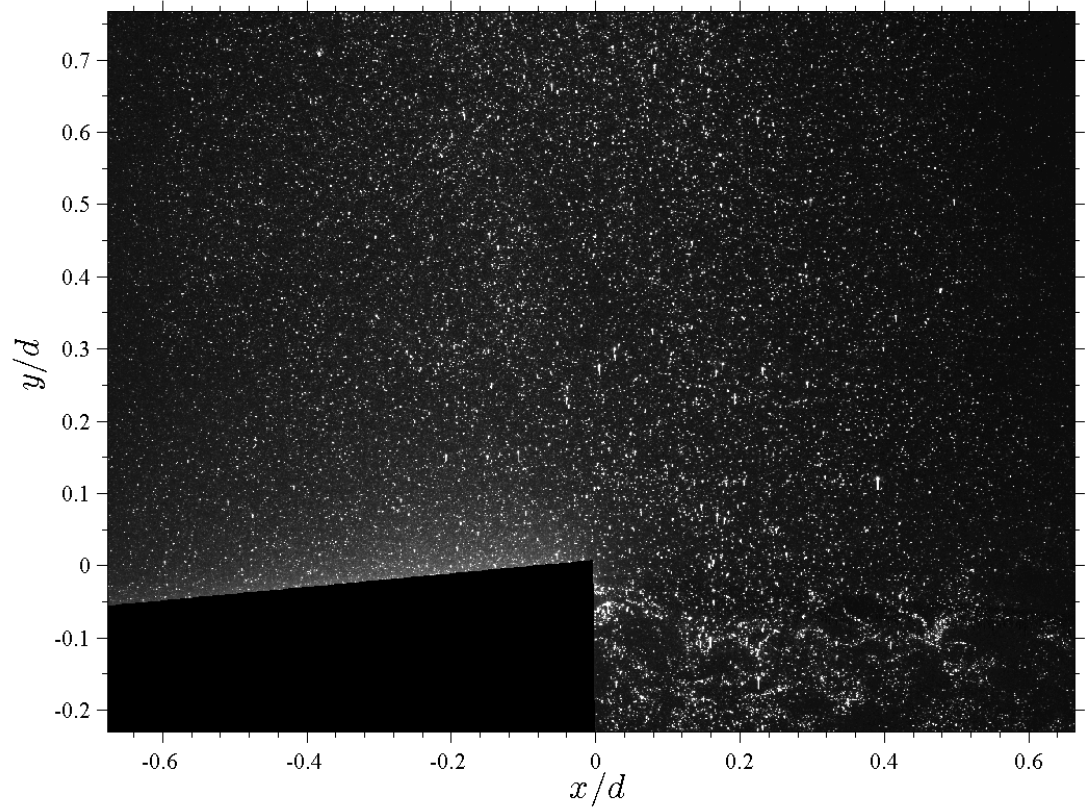


Figure 3.34. Typical raw PIV image of the cone centerline plane, external flow field. The blacked-out area is the top portion of the cone, which was masked out for analysis.

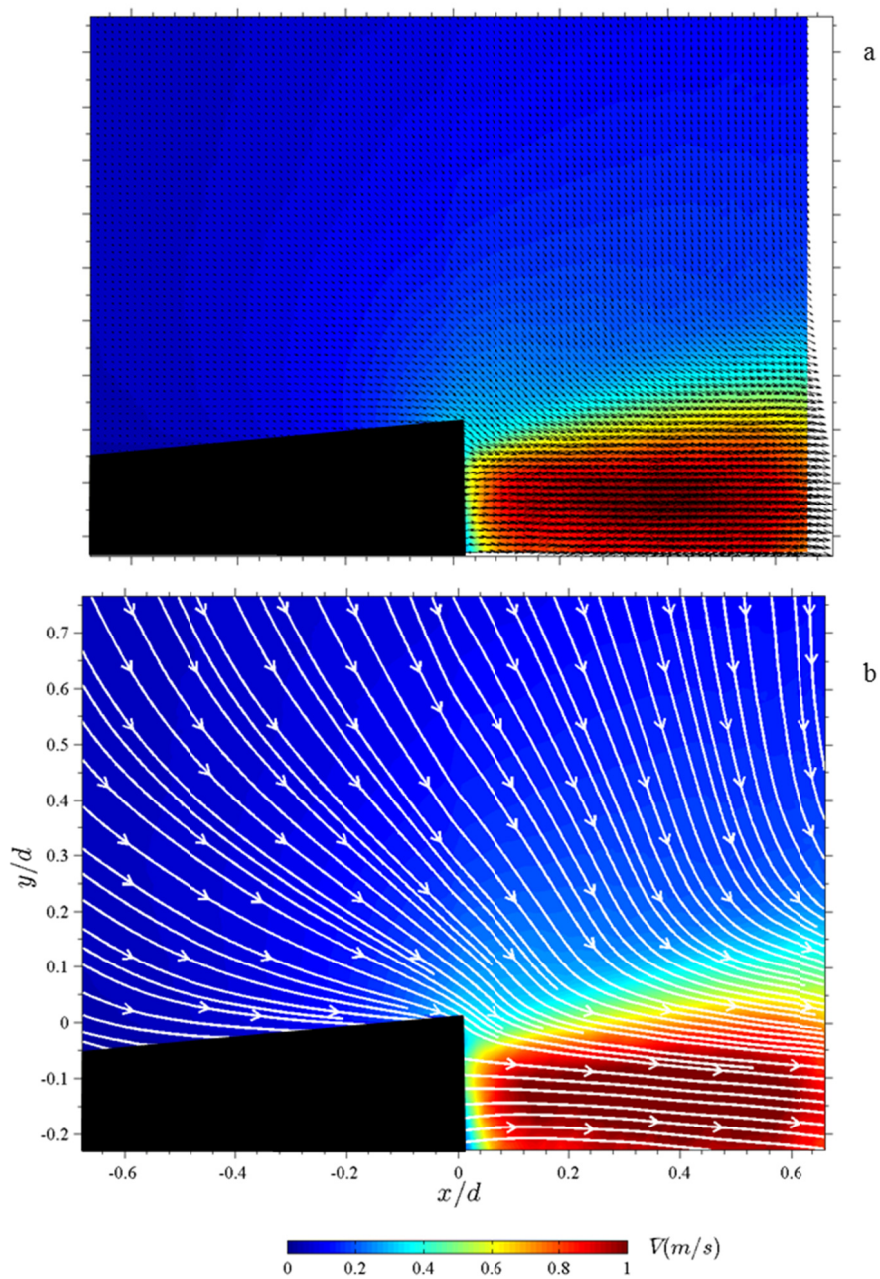


Figure 3.35. Contour and vector plots showing measured in-plane velocity field (a) and calculated streamlines (b) of the burner cone external flow field.

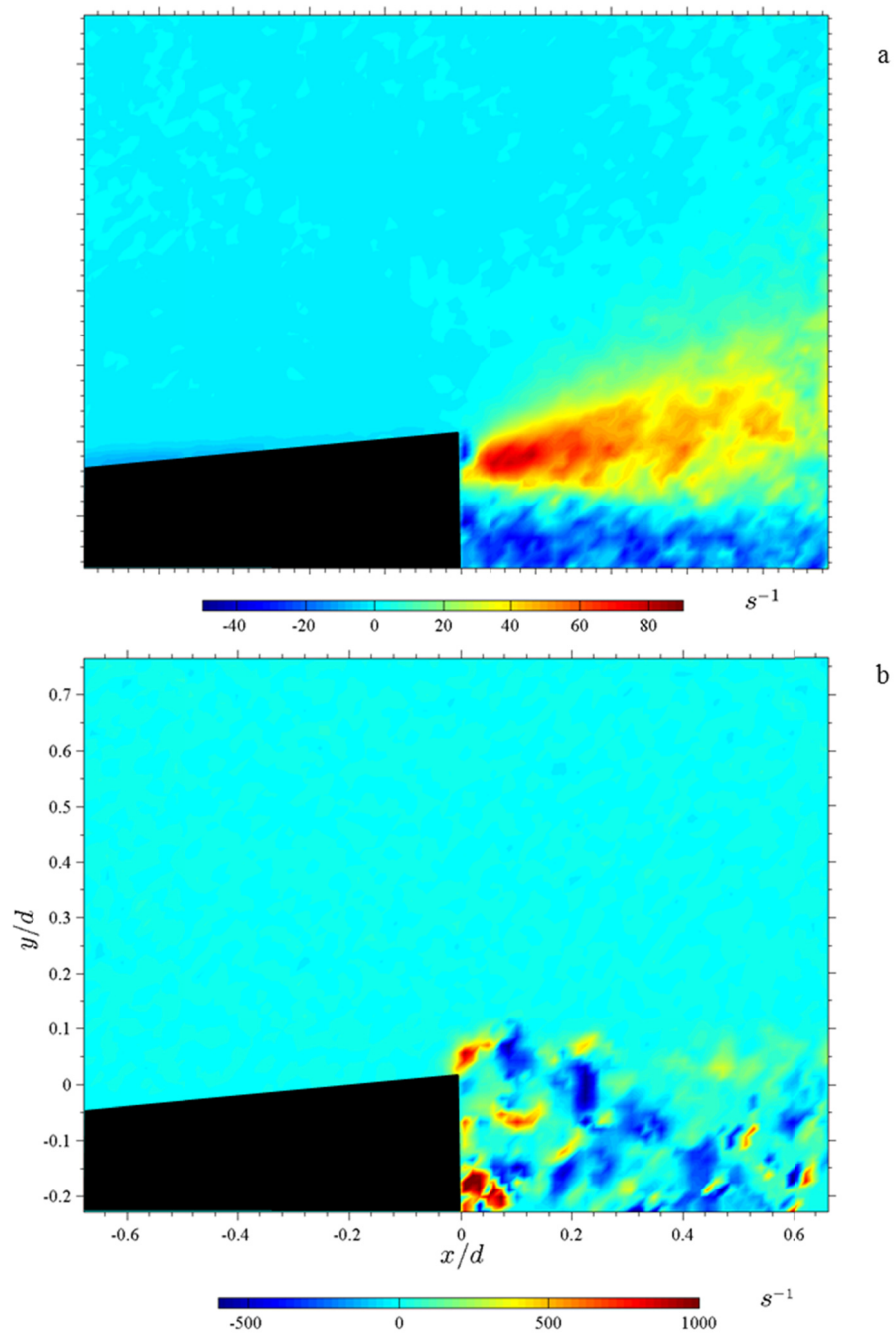


Figure 3.36. Contour plots showing the scalar mean of the vorticity (a) and typical instantaneous vorticity (b) from the cone exit flow on the cone centerline.

4 Analysis of Potential Design Improvements

This chapter presents results obtained from the PIV measurements of the non-reacting flow, flame temperature measurements, and material burnthrough tests on selected design improvements for the FAA NexGen burner. The results presented in the previous chapter reveal that several of the burner components provide asymmetric flow patterns, which translate into uneven distribution of the flame when performing a temperature measurement or material fire test.

4.1 Internal Burner Flow Improvements

4.1.1 Symmetric Stator

The first design improvement was to replace the original stator with one that is completely symmetric by removing the igniter holders from the stator. This was done by drawing the stator in 3D computer aided drafting (CAD) software, removing the igniter holders, and sending the digital model to a computer numerical control (CNC) machine shop. The final part is shown in Figure 4.1 to the right of the original stator. It has been assumed for some time that the asymmetry of the stator causes irregular flow, and by removing the igniters and igniter wires the flow would be more uniform. The resulting

configuration is without an ignition source, so an alternative method of burner ignition was needed to perform tests. A handheld propane torch was found to safely and easily ignite the fuel air mixture, as shown in Figure 4.2. The symmetric stator was evaluated with three methods: PIV measurement of the exit flow field, flame temperature measurements on the insulation burner, and material burnthrough times. The results of all three are compared to the original stator to show the difference in performance.

The configuration of the symmetric stator for the PIV measurements is shown in Figure 4.3. The symmetric stator was placed in the same axial and rotational configuration that the original stator would be during testing – one pipe diameter upstream from the turbulator exit plane and the vertical centerline between two stator vanes oriented 30° counterclockwise from the vertical centerline of the burner tube. The measurement plane, also shown in Figure 4.3, was aligned on the vertical draft tube centerline and placed at the turbulator exit plane. An example of typical PIV image data is displayed in Figure 4.4. The field of view was 246 x 185 millimeters. Identical measurements were made with the original stator in order to have a direct comparison of original vs. symmetric stator.

Figure 4.5 (a) displays the measured mean in-plane velocity field exiting the turbulator exit plane for the baseline symmetric stator configuration. The horizontal axis represents the axial distance from the turbulator exit plane while the vertical axis represents the radial distance from the burner axis. The contour plot represents the magnitude of the

mean in-plane velocity field while the vector plot represents the magnitude and direction of the in-plane velocity field. The in-plane velocity field again resembles typical exit flow for a turbulent jet with noticeable growth of the jet due to entrainment. The same measurements were repeated with the original stator at the same axial and rotational position on the fuel pipe, and at the same sonic choke inlet pressure. Figure 4.5 (b) displays the measured mean in-plane velocity field for the original stator. Figure 4.6 displays the mean axial velocity profiles for both stators at the turbulator exit, $x/d=0.3$ (a) and $x/d=1$ (b). The horizontal axis represents the radial distance from the burner axis normalized by the draft tube inner diameter d while the vertical axis represents the axial velocity magnitude in meters per second. The blue data series represents the original stator and the red data series represents the symmetric stator. The axial velocity profile at the turbulator exit is symmetric, with a peak axial velocity of approximately 11.5 meters per second. At one diameter downstream the profile is seen to spread out, and the peak velocity has reduced to about 8 meters per second. The peak is also seen to move slightly off axis. The mean axial velocity profile for the original stator at the turbulator exit is not as symmetric as the profile from the symmetric stator, and the peak axial velocity is lower for the original stator. Further downstream, however, the profile for the original stator becomes more symmetric, and the peak axial velocity remains around 10 meters per second. The original stator results in a narrower profile with a higher peak velocity which further supports the fact that the symmetric stator provides a broader swirling jet with more evenly distributed velocity than the original stator.

The angle of the symmetric stator vanes is identical to the original stator, yet the PIV measurements indicate increased jet growth over the original stator as seen in the velocity profiles at $x/d=1$. The swirl number assessment for axial vane swirlers assumes a symmetric swirler; therefore the presence of the igniter holders in the original stator alters the “perfect” swirler assumption, reducing the actual swirl number of the flow. Velocity measurements were made at the draft tube exit for the configuration with only the symmetric stator in the draft tube to compare to the measurements in section 3.1.1 with the original stator in the draft tube. Figure 4.7 displays the measured mean in-plane velocity field at the draft tube exit with the symmetric stator recessed 50.8 (a) and 101.6 (b) millimeters, respectively, plotted against the non-dimensionalized x - and y - axes normalized by the draft tube inner diameter. The contour plot represents the velocity magnitude while the vectors represent the magnitude and direction of the in-plane velocity field. The in-plane velocity fields are similar to the original stator measurements, with two diverging jets exiting the draft tube and a central region of recirculation. The axial velocity profiles at one diameter downstream are displayed in Figure 4.8 for both symmetric stator positions. Comparison with the profiles in Figure 3.9 show greater jet width and recirculation for the symmetric stator measurements, both attributes of a higher swirl number swirler.

The flame temperature was measured on the insulation burnthrough burner to determine how the characteristics of the flow created by the symmetric stator influences the flame temperature profile. Figure 4.9 displays the measured flame temperature averaged over

thirty seconds at each measurement location and the overall flame temperature average. The horizontal axis represents the thermocouple probe and the vertical axis represents the measured flame temperature in degrees Celsius. The measured flame temperature for the symmetric stator is represented by the blue bars while the original stator is represented by the red bars. The symmetric stator provides a nearly uniform and symmetric flame temperature profile with a minimum to maximum difference of only 30°C. The original stator has a non-uniform but nearly symmetric profile with a spread of 93°C. The overall average flame temperature for the symmetric stator is greater than for the original stator by 35°C. It can also be seen that the symmetric stator, when oriented in the same manner as the original stator, does not result in low temperature readings on thermocouple #1 like the original stator does, perhaps due to the greater spread rate and wider velocity profile.

Thus far the symmetric stator has proven to provide a more uniform and symmetric velocity and temperature profile and an overall higher flame temperature over the original stator. The next test series was focused on determining how these attributes affect burner performance in an actual material fire test. Both stator configurations were set up in the insulation burnthrough burner, and the picture frame blanket holder was used to evaluate the burnthrough time of the standard polyacrylonitrile (PAN) materials. Figure 4.10 presents the material burnthrough times recorded during testing for the PAN-8579 (a) and the PAN-8611 (b) material. A set of four samples were run for the symmetric stator to compare to the NexGen burner baseline data set of ten samples. It can be seen that the symmetric stator baseline configuration results in a longer average burnthrough time for

both materials, 16.45 seconds longer on the PAN-8579 and 33.6 seconds longer on the PAN-8611, or in terms of the standard deviations of the NexGen burner baseline data set, almost 2 standard deviations for PAN-8579 and 3.5 standard deviations for the PAN-8611. Despite having a higher average measured flame temperature and more uniform temperature distribution, the symmetric stator provided longer burnthrough times than the original stator. The symmetric stator did have lower relative standard deviations for both materials compared to the original stator, indicating that it may provide a slightly more repeatable flame.

The symmetric stator was then run through a series of rotations and axial translations on the fuel pipe to determine if a burnthrough time equivalent to the original stator could be found. Only flame temperature measurements were made for this test series. A series of seven rotations in 15° increments from 0° to 90° were made at the standard axial position of 1 pipe diameter upstream of the turbulator exit, followed by a series of translations in 25.4 millimeter increments from 152.4 to 50.8 millimeters. The flame temperature spread, $\Delta T = T_{\text{Max}} - T_{\text{Min}}$, was used to find the most uniform flame temperature distribution while also seeking the highest overall average flame temperature. Figure 4.11 (a) displays the average measured flame temperatures at the standard measurement locations over the series of rotations and axial translations. Each thermocouple is represented by a different color and shaped data series. The horizontal axis represents the rotational angle and axial position of the symmetric stator. The vertical axis represents the measured flame temperature in degrees Celsius. Thermocouple #1 reads the lowest of all

thermocouples, though through the series of rotations and translations the reading on thermocouple #1 eventually reaches temperatures similar to the other thermocouples. Figure 4.11 (b) displays the flame temperature spread (blue) and average flame temperature (red) against the rotational and axial position of the symmetric stator. The flame temperature spread corresponds to the left vertical axis (ΔT , °C) while the average flame temperature corresponds to the right vertical axis (°C). The flame temperature spread is found to vary with rotation angle and axial position of the symmetric stator, with the lowest flame temperature spread and hence the most uniform flame temperature distribution at 0° rotation and 50.8 millimeters recessed from the turbulator exit plane. The overall average flame temperature is also found to vary with the symmetric stator rotational angle and axial position, with the highest average flame temperature found at 0° rotation and 50.8 millimeters recessed from the turbulator exit plane. This stator position was also tested with the original stator for a direct comparison. Figure 4.12 displays the average measured flame temperatures for each thermocouple for the symmetric stator (blue) and original stator (red) at the baseline position (solid) and at 0° 50.8 millimeters (dashed). It can be seen that the symmetric stator has an overall higher flame temperature at the new position, while the measured flame temperature for the original stator has changed little over all thermocouples.

A series of PAN burnthrough tests was performed to determine the effect of stator position on material burnthrough time. Four tests of PAN-8579 and four tests of PAN-8611 were run for both the original stator and the symmetric stator at 0° 50.8 millimeters.

Figure 4.13 displays the results from the PAN-8579 (a) tests and PAN-8611 (b) tests. The original stator is displayed as blue bars while the symmetric stator is red. The average burnthrough times from the baseline tests are shown as solid bars, and the individual and average burnthrough results from the current test series are displayed as dashed bars. The horizontal axis displays the test sample number or indicates average burnthrough, while the vertical axis represents the burnthrough time in seconds. Despite achieving an average flame temperature higher than any other configuration tested and the most uniform flame temperature distribution, the symmetric stator at 0° 50.8 millimeters provided the longest burnthrough for both the PAN-8579 and PAN-8611 materials. The original stator at 0° 50.8 millimeters provided the fastest burnthrough times for both materials despite having a flame temperature that is similar to the baseline configuration and significantly less than the symmetric stator at 0° 50.8 millimeters. These tests indicate that the flame temperature is not an accurate measure of burner performance, and a different parameter must have a greater influence on material burnthrough.

PIV measurements were made on the airflow exiting the draft tube for both stators at the position of 0° 50.8 millimeters. The measurement plane was the same as was described for the previous symmetric stator measurements and displayed in Figure 4.3. The mean measured in-plane velocity field is shown in Figure 4.14 (a) for the symmetric stator and (b) for the original stator at 0° 50.8 millimeters. The shape of the profiles differs slightly, with the symmetric stator resulting in a wider jet downstream than the original stator.

The velocity profiles at the turbulator exit plane and one diameter downstream are shown in Figure 4.15 (a-b). It can be seen that although the symmetric stator has a slightly higher initial peak velocity than the original stator, the axial velocity is again seen to decay more rapidly than the original stator. The velocity profile is also seen to be wider for the symmetric stator than for the original stator, indicating that the symmetric stator produces an airflow that grows faster, resulting in a more uniformly distributed air flow pattern than for the original stator.

The flame temperature measurements, material burnthrough tests, and PIV analysis all indicate that the symmetric stator is not equivalent to the original stator. Though it does provide an overall higher measured flame temperature and more uniform temperature distribution, the material burnthrough tests indicate that this uniformity produces a flame that is less severe than the original stator. From a safety perspective, the symmetric stator, when used in place of the original stator, would allow for materials to pass a material burnthrough test that the original stator would have otherwise failed, possibly allowing materials on to an aircraft that do not meet the safety standard developed on the NexGen burner with original stator. Also, using the symmetric stator in place of the original stator does not eliminate the complexity of describing the configuration of the internal components.

4.1.2 Flame Retention Heads

The next test series focused on an alternative method of providing an air flow pattern similar to the original stator-turbulator combination with fewer components and a less complicated set up procedure. The flame retention head is a relatively modern commercially available oil burner component that attaches to the end of the draft tube, replacing the stator and turbulator. Figure 4.16 displays the three different flame retention heads used in this work. The head consists of three openings: center opening, primary slots, and secondary slots. The center opening allows for room for the spray nozzle to protrude and spray fuel into the air flow. The primary slots are tangential slits acting as an axial swirler, mixing the swirling air with the fuel spray droplets. The vane angle of the primary slots is approximately 56° , and according to [54] the estimated swirl number is 1.01, similar to the estimated swirl number of the stator, 1.15. The secondary slots create an axial co-flow to envelop the swirling flow, concentrating the flame towards the center, and allow more air to be used by the flame. The three flame retention heads tested, F12, F22, and F31, have identical center openings and primary slots; the only difference is the width of the secondary slots. The F12 has slots that are 4.75 millimeters wide, the F22 has slots that are 8.8 millimeters wide, and the F31 has slots that are 14.4 millimeters wide. The exit plane area for the flame retention heads was calculated and compared to the exit plane area of the turbulator, as displayed in Table 4.1. The exit area of the turbulator falls between that of the F22 and the F31.

Flame temperature measurements were made for all three flame retention heads. Figure 4.17 displays the average measured flame temperatures for the three flame retention heads: F12 in blue, F22 in red, and F31 in green. The horizontal axis represents the measurement location and overall average. The vertical axis represents the measured flame temperature in degrees Celsius. It is apparent that all three flame retention heads provide different flame temperature profiles, and the shape of the profile can be linked to the size of the secondary openings for each flame retention head. The average flame temperatures are all in the same range of the previous original stator and symmetric stator tests.

Material burnthrough tests were performed to determine how the flame retention heads would perform in actual fire testing. Figure 4.18 presents the average burnthrough times for the PAN-8579 and PAN-8611 materials. The F12 is represented by the blue bars, the F22 by the red bars, the F31 by the green bars, and the original stator baseline is represented by the blue dashed bars. A wide range of burnthrough times is found in this test series. The F12 consistently provides the fastest burnthrough while the F31 provides the longest burnthrough, with the F22 in the middle. The average measured flame temperatures for the flame retention heads do correlate with the burnthrough times, with the F12 having the highest flame temperature and fastest burnthrough time and the F31 having the lowest flame temperature and longest burnthrough time, though the difference in temperature between the F12 and the F31 is only 35°C. The F22 is found to be nearest

to the original stator baseline configuration with burnthrough times on average 24 seconds faster.

Lastly, the flame retention heads were analyzed using PIV to study the draft tube exit flow. The measurement plane was the same as was described for the previous stator measurements. The mean measured in-plane velocity fields for the flame retention heads are displayed in Figure 4.19 for the F12 (a), F22 (b), and F31 (c). Comparison of the figures shows that the shape of the in-plane velocity field is a result of the size of the secondary slots. The F12 has the smallest secondary slots; therefore the exit area is the smallest so the exit velocity is the greatest. The F31 has the largest secondary slots and the lowest exit velocity and a higher velocity exiting the secondary slots than the center hole. The mean axial velocity profiles at the draft tube exit and one diameter downstream are shown in Figure 4.20 (a-b). At the draft tube exit the three profiles are similar in shape but vary in magnitude. The flows exiting the center hole and secondary slots are evident and are nearly equivalent for each head. At one diameter downstream the flow is more evenly distributed, with the center hole flow still evident for the F12 and F22, while the F31 has a greater velocity near the edges due to the large secondary slot size. Comparison of the velocity profiles with those from the original stator in the previous section shows that the F22 is most similar to the original stator in magnitude at one diameter downstream.

The analysis of the flame retention heads indicates that the flame temperature measurements and material burnthrough times are dependent upon the shape and magnitude of the in-plane velocity field. The high axial flow created by the F12 head resulted in high flame temperatures in the center of the measurement rake and low flame temperatures near the edges. The F12 also had the fastest burnthrough time, on average two times as fast as the original stator baseline, due to the strength of the flame and the concentrated area of impingement on the material. Conversely, the F31 had the lowest overall flame temperature but most uniformly distributed temperature profile, and the longest burnthrough time, on average 1.4 times longer than the original stator baseline. The flame created by the F31 was more uniformly distributed with no high velocity regions; therefore the material was not as forcefully impinged upon. The F22 had a flame temperature profile most similar to the original stator baseline with higher temperatures found on the outer thermocouples and a low temperature trough in the center. The material burnthrough times were the most similar to the original stator baseline, on average only 1.1 times faster. The magnitude of the peak velocity at one diameter downstream was most similar to the original stator baseline as well. As a replacement for the stator-turbulator combination, the F22 provides the most similar flame temperature profile, material burnthrough time, and in-plane velocity field to the baseline configuration, with fewer components and a greatly simplified set up arrangement.

4.1.3 Correlation of Burnthrough Data with Velocity Data

Sufficient data has been collected to this point to make a general correlation between material burnthrough time and burner exit velocity as measured with PIV. Peak axial velocity values at a downstream distance of $x/d=1$ from the draft tube exit were extracted from the in-plane velocity field measurements for each configuration tested. These values were used to correlate PAN-8579 and PAN-8611 material burnthrough time to burner exit velocity, as displayed in Figure 4.21. The horizontal axis represents the measured peak axial velocity at $x/d=1$ while the vertical axis represents the material burnthrough time in seconds. Each data series represents a different burner configuration. The figures clearly show an inverse relationship between burnthrough and peak axial velocity; as peak axial velocity increases, material burnthrough times decrease. The same burnthrough data for PAN-8579 and PAN-8611 was plotted against the corresponding average measured flame temperature in Figure 4.22. The correlation between material burnthrough time and average flame temperature is not strong, as the configuration with the highest average flame temperature had one of the longest material burnthrough times for both materials. These results indicate that the configuration-dependent burner exit velocity magnitude is more of a critical parameter than measured flame temperature.

4.1.4 Fuel Spray

The velocity measurements of the standard nozzle M revealed an asymmetric spray pattern and the effect it has on flame temperature measurements. The design

improvement chosen for this area is an off-the-shelf oil burner nozzle, referred to here as nozzle D, a 126 mL/min-rated nozzle at 7.9 bar. PIV was used to visualize the spray pattern and determine symmetry. The measurement plane was again taken at the nozzle exit and was aligned on the vertical axis of the draft tube. Again, water was used as the working fluid for these experiments.

A full rotational study was performed on Nozzle D to determine circumferential spray symmetry. Figure 4.23 (a-f) displays the measured mean in-plane velocity field for the spray produced by nozzle D over a series of rotations in increments of 60° completing a full rotation. The contour plot represents the magnitude of the in-plane velocity while the vector plot represents the magnitude and direction of the x - and y -component velocity vectors. The horizontal axis represents the axial distance from the nozzle tip while the vertical axis represents the radial distance from the nozzle tip, both normalized by the draft tube inner diameter. As was observed for nozzle M there is noticeable spray asymmetry that travels with the rotation of the nozzle D. Figure 4.24 displays the measured mean axial velocity profiles near the spray nozzle exit at $x/d=0.37$. The horizontal axis represents the radial distance from the axis normalized by the draft tube inner diameter while the vertical axis represents the axial (U) velocity in meters per second. Each nozzle rotation is represented by a different color data series. It is evident that the high velocity region rotates with the nozzle rotations and that the spray pattern is circumferentially asymmetric. Compared to the measurements of nozzle M in Section 3.1.2, nozzle D has a lower peak axial velocity due to the different nozzle ratings (142

mL/min for nozzle M, 126 mL/min for nozzle D) as a result of different orifice size, producing different droplet sizes with different velocities despite running at the same flow rate.

A nozzle of similar specification to nozzle D was installed in a horizontally-mounted NexGen burner in the same manner as nozzle M was tested in the previous section to acquire flame temperature measurements. The nozzle was rotated in 20° increments between flame temperature measurements over a full revolution. Figure 4.25 displays the measured flame temperature in degrees Celsius at each measurement location averaged over thirty seconds at a sample rate of one sample per second. Each data series represents a single thermocouple measurement location in the flame. The horizontal axis represents the angle of rotation of the nozzle, and the vertical axis represents the measured flame temperature in degrees Celsius. The temperature range on the vertical axis is identical to the temperature range for the temperature measurement of nozzle M. Compared to nozzle M, it can be seen that the flame temperature measurements recorded for nozzle D are less sensitive to nozzle rotation, as the level of fluctuation is significantly less than was found for nozzle M. Nozzle D did however provide overall lower measured flame temperatures compared to nozzle M.

Material burnthrough tests were performed with a 378 mL/min nozzle D of similar spray pattern to compare with the PAN baseline tests that were run with nozzle M. Figure 4.26 displays the average burnthrough times for the PAN materials from the baseline tests

with nozzle M in blue and the tests with nozzle D in red. The blue bars represent an average of 10 tests, while the red bars represent an average of 4 tests. The horizontal axis lists the PAN material type and the vertical axis represents the burnthrough time in seconds. All burner parameters were held constant between the two test series; the only change was the swapping of nozzle M for nozzle D. Good agreement of the measured burnthrough times is found between nozzle D and nozzle M despite the circumferential spray asymmetry found with both types of nozzle. It appears that the burnthrough test is less sensitive to directional spray differences, as the entire flame is impinging upon the flat sheet of test sample. In other NexGen burner test methods where the flame does not impinge upon a flat sample, such as the seat cushion flammability test, the directional differences are more influential on test sample burning since a high velocity region from the burner could either impinge upon or entirely avoid the seat cushion sample.

4.2 External Burner Improvement

4.2.1 Reinforced Cone

Often times a fire test lab that performs dozens of NexGen burner tests in a single day must replace the burner cone on a regular basis due to exit plane warpage. There is no specified tolerance for the exit plane dimensions, though many labs use their best judgment when it comes time to replace the cone. The cost for the cones can be high as they are custom fabricated parts, and many labs look for alternative methods to prolong the life of the burner cone. One common method is to weld a steel ring around the exit

plane, as displayed in Figure 4.27, to force the exit plane to retain its shape through many heating cycles. The influence of the ring on test results has been questioned for some time, whether the ring has an effect on the airflow around the cone or a radiative effect on the test sample. Here, the external flow field is measured and compared to the original cone to determine any similarities or differences in flow fields.

The measurement plane for this test series was the same as displayed in the previous chapter for the external cone measurements. The plane was centered on the vertical cone centerline. Figure 4.28 displays sample PIV data from these measurements. The top portion of the cone, as well as the ring, can be seen as the blacked out area in the lower left of the image. The mean measured in-plane velocity field is displayed in Figure 4.29 (a) plotted against the x - and y -axes, both normalized by the draft tube inner diameter d . The contour plot represents the magnitude of the in-plane velocity field while the vector plot represents the magnitude and direction of the in-plane velocity field. The cone exit flow field can be seen in the bottom portion of the figure, and is largely axial in direction. The flow streamlines are plotted over the in-plane velocity field magnitude contour plot in Figure 4.29 (b). The influence of the reinforcement ring can be seen in the direction of the streamlines. Comparison with the streamline plot from the original cone shows that the reinforcement ring does interrupt the surrounding air from being entrained into the exit flow. The ring is seen to block incoming air from being entrained in the exit flow. For the reacting flow case, this could affect cooler air from reaching the flame or the test sample, influencing test results. The scalar mean of the vorticity is displayed in Figure

4.30 (a). The shear layer is evident on the top portion of the cone exit flow, indicating mixing between the cone exit flow and the surrounding air. The vorticity can also be seen to decay in the streamwise direction. The reinforcing ring is seen to create a region of negative vorticity immediately downstream. Figure 4.30 (b) displays a typical instantaneous vorticity field for the reinforced cone measurements. The horizontal axis represents the x -axis while the vertical axis represents the y -axis, both normalized by the draft tube inner diameter d . The contour plot represents the instantaneous vorticity while the vector plot represents the instantaneous in-plane velocity field. Vortical structures can be seen in the cone exit flow, and the reinforcing ring is seen to create a recirculation zone immediately downstream.

Two nearly identical burner cones that have not been exposed to fire were installed on the insulation burnthrough NexGen burner to determine the effect of the ring on flame temperature measurements and material burnthrough. The cones differ only in the fact that one cone, called the ring cone, has a 1.22 millimeter thick, 25.4 millimeter high ring welded to the outer surface at the cone exit plane. Both cones were manufactured from 1.22 millimeter thick 310 stainless steel by the same machinist, and for this test series both experienced the same amount of heat exposure, so differences cone heat loss are assumed to be negligible in the comparison. Figure 4.31 displays the average measured flame temperatures for the standard cone in blue and the ring cone in red. The horizontal axis represents the measurement location and overall average. The vertical axis represents the measured flame temperature in degrees Celsius. Comparison of the two

data series reveal only slight differences in the magnitude of the measured temperatures and the temperature profile, with the ring cone measuring lower on all but one thermocouple, and having a lower overall average. Material burnthrough test results are displayed in Figure 4.32 for the PAN-8579 material (a) and the PAN-8611 material (b). It can be seen that the ring cone has faster overall burnthrough times on both material types, indicating the ring cone provides a more severe burner configuration for material burnthrough tests. Though the PIV measurements alone cannot substantiate the exact nature of the increased severity, it is speculated that the ring could create higher turbulence downstream, increasing mechanical stressing of flexible materials during testing, or the ring serves to interfere with cooler surrounding air from being entrained into the burner flame, increasing flame severity.

4.3 Summary

The following statements summarize the results presented in chapter 5.

- A new symmetric stator was designed and constructed without igniter holders. Measurement of the exit flow field and comparison to the original stator show increased growth of the swirling jet downstream of the exit and lower peak axial velocity. Flame temperature measurements show more symmetric and uniform temperatures and an overall higher average flame temperature. Material burnthrough tests reveal longer burnthrough times for the symmetric stator than the original stator.

- A series of axial and rotational movements were made with the symmetric stator to find a more comparable material burnthrough time to the original stator. Flame temperature measurements indicate the highest overall flame temperature and most uniform temperature profile was found at an axial distance of 50.8 millimeters from the stator face to the turbulator exit plane and the vertical centerline between vanes aligned with the vertical centerline of the draft tube. The original stator, when placed at the same position, yielded flame temperatures only slightly higher than its baseline configuration. Material burnthrough tests with both stators at the same location show that the original stator at this position has faster burnthrough times than the baseline while the symmetric stator has even longer burnthrough times than all cases tested. PIV measurements reveal higher velocity magnitude and narrower jet width for the original stator over the symmetric stator. These tests indicate that although a higher and more uniform flame temperature may be measured, the material burnthrough is more directly dependent upon the magnitude of the flow velocity.
- A set of three flame retention heads were used to replace the stator and turbulator combination. The heads had identical center hole and tangential primary slot sizes and only differed in the size of the coflowing secondary slots; F12 had the smallest coflow, F31 the largest. Flame temperature measurements indicate generally higher temperatures for the FRH vs. the stator-turbulator combination, and the temperature profile is influenced by the shape of the flow field. Material burnthrough times reveal that the F12 yielded the fastest burnthrough time while

the F31 yielded the longest, with the F22 being most comparable to the NexGen burner baseline. PIV measurements reveal similarly shaped axial velocity profiles at the draft tube exit, though significant variation in magnitude. The material burnthrough times can be directly correlated to the magnitude of the peak velocity for the flame retention heads.

- An oil burner fuel spray nozzle from a different manufacturer was analyzed with PIV to determine spray pattern consistency. A series of 6 rotations of the nozzle reveal spray pattern asymmetry in each plane similar to the standard NexGen nozzle. Flame temperature measurements reveal less rotational sensitivity to spray asymmetry than the standard nozzle, and material burnthrough testing indicates burnthrough times similar to the standard nozzle, indicating less dependence of material burnthrough on spray pattern when impinging upon a large, flat test sample.
- The addition of a reinforcement ring around the cone exit plane is used by some laboratories to maintain cone exit plane shape during repeated hot-cold cycling. PIV measurements of the area above the cone top surface indicate the ring prevents surrounding air from being entrained into the cone exit flow. The ring is also found to create large scale vortices just downstream. Flame temperature measurements from a new standard cone and a new ring cone reveal only slight differences in temperature magnitude and profile. Material burnthrough tests indicate the ring cone provides a more severe configuration as burnthrough times were faster than the standard cone for both materials.

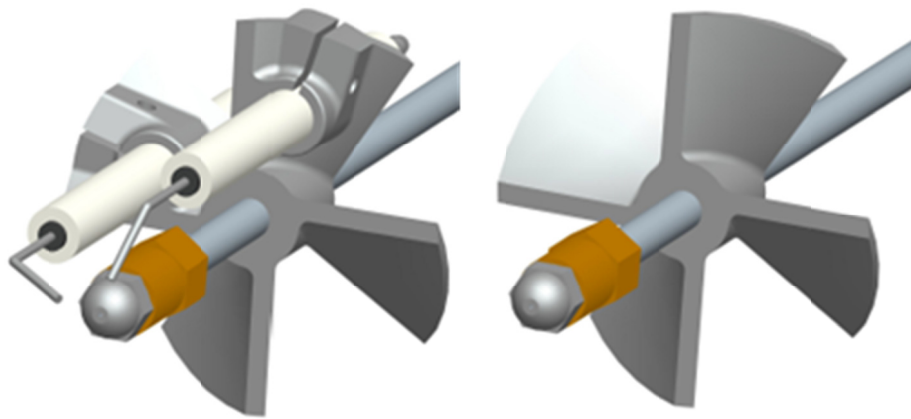


Figure 4.1. Original stator (left) and symmetric stator (right) on the fuel pipe with fuel nozzle.

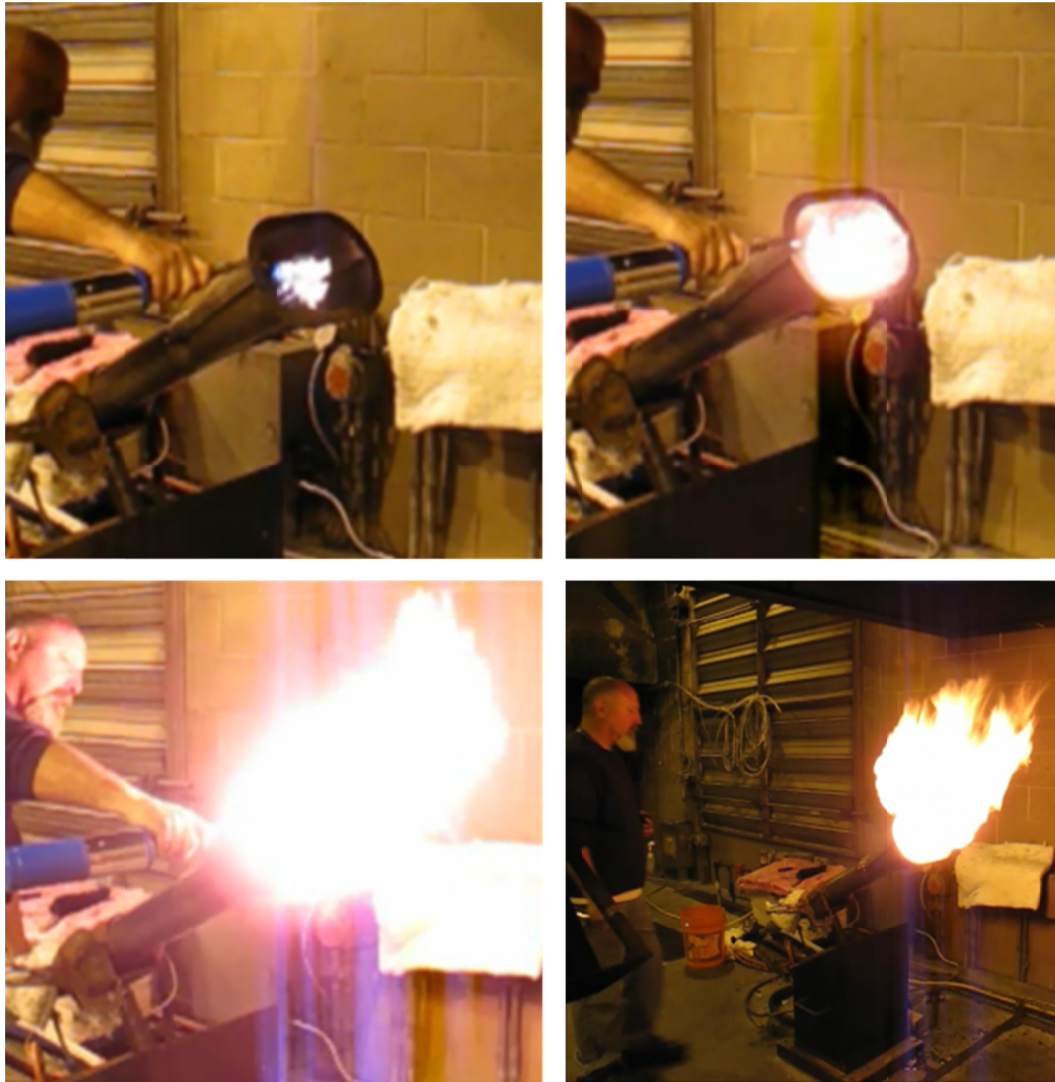


Figure 4.2. Ignition of the NexGen burner with a handheld propane torch. The use of an igniter-less stator requires an external ignition source.

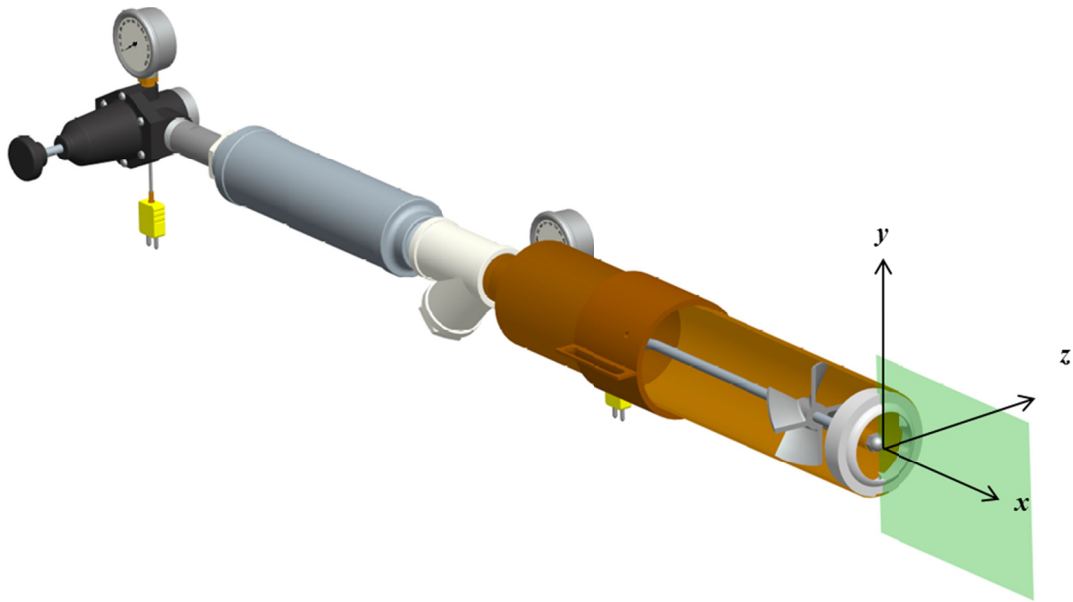


Figure 4.3. Schematic of the test configuration for the symmetric stator PIV measurements. The draft tube is cut away to show the internal components. The measurement plane is approximated by the green rectangle.

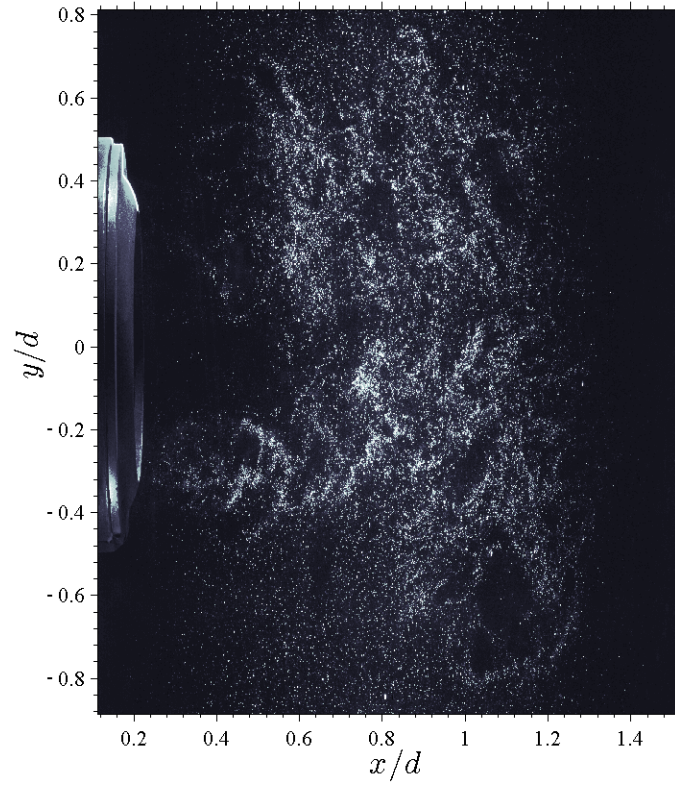


Figure 4.4. Typical PIV image data for the symmetric stator tests.

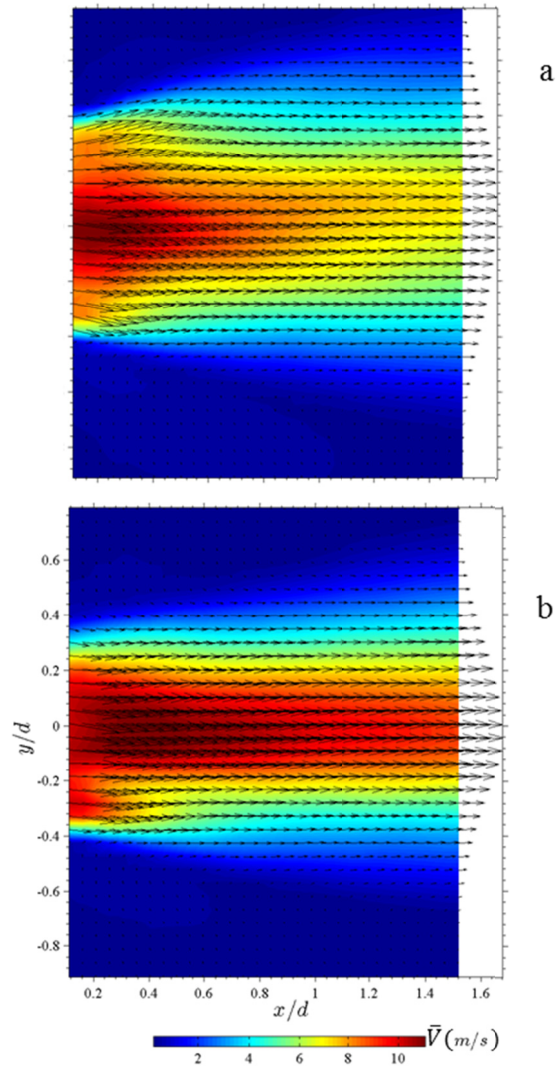


Figure 4.5. Contour and vector plots showing measured mean in-plane velocity field exiting the turbulator for the symmetric stator baseline configuration (a) and the original stator baseline configuration (b).

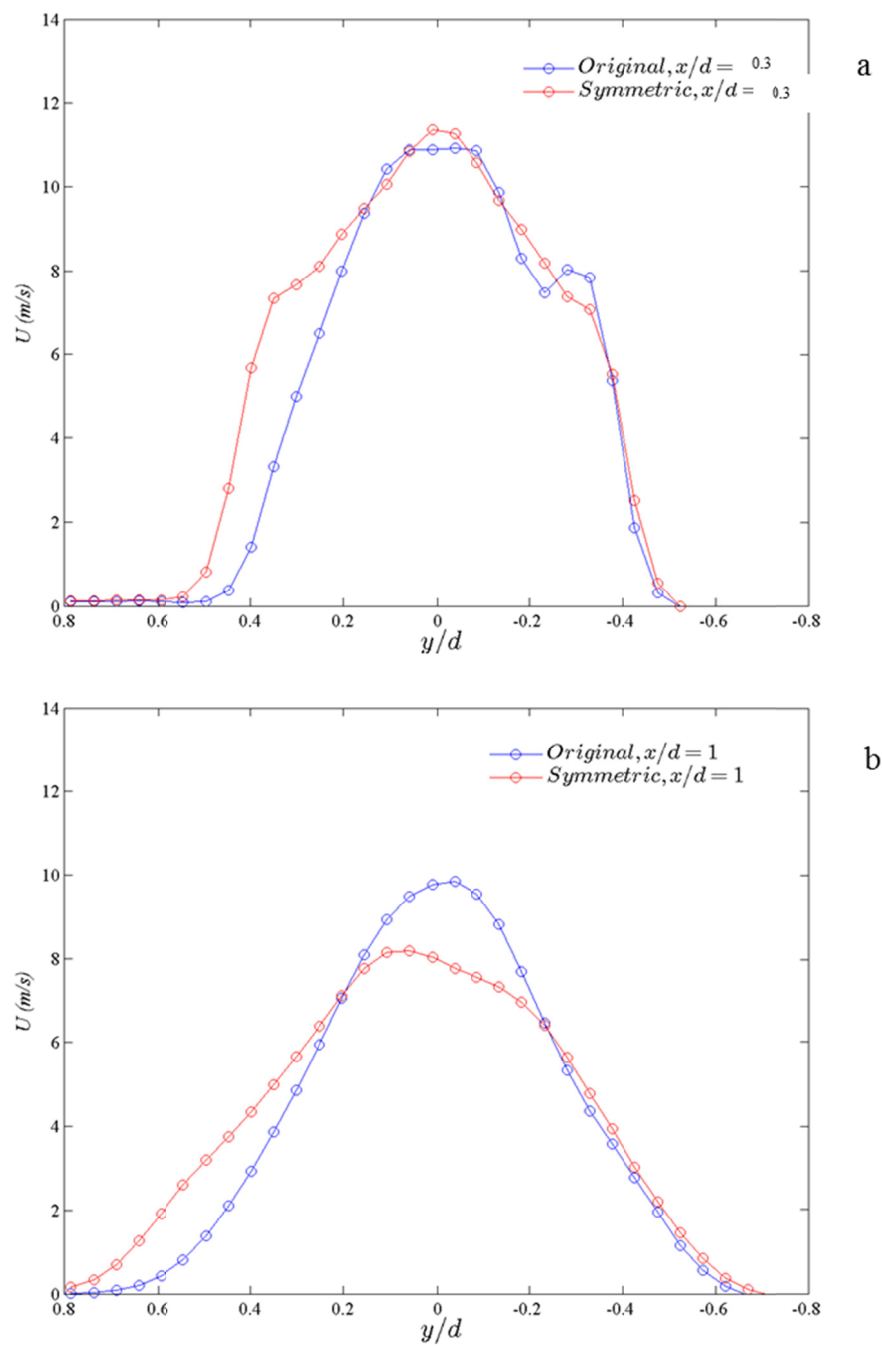


Figure 4.6. Comparison of mean axial velocity profiles at the turbulator exit, $x/d=0.3$ (a) and one diameter downstream $x/d=1$ (b), for the original stator (blue) and symmetric stator (red) configurations.

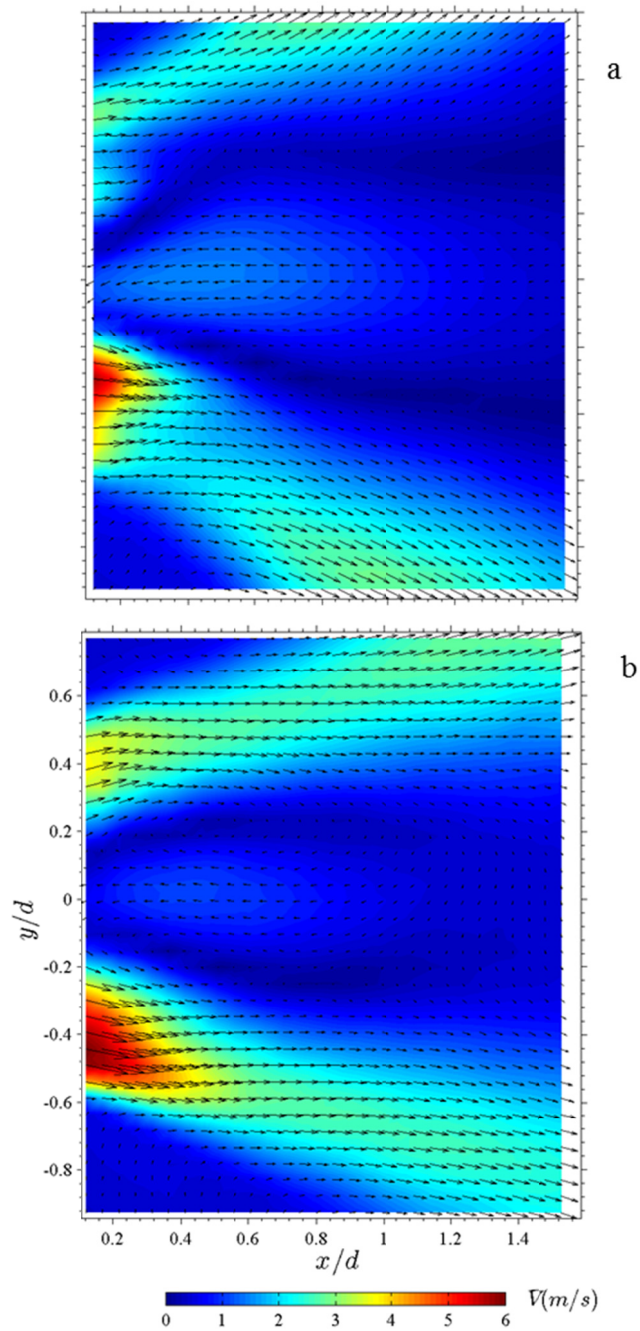


Figure 4.7. Contour and vector plots showing measured mean in-plane velocity field exiting the draft tube. All internal components except the symmetric stator were removed from the draft tube. The symmetric stator vertical centerline was aligned with the draft tube vertical centerline, and recessed 50.8 mm (a) 101.6 mm (b) from the draft tube exit plane.

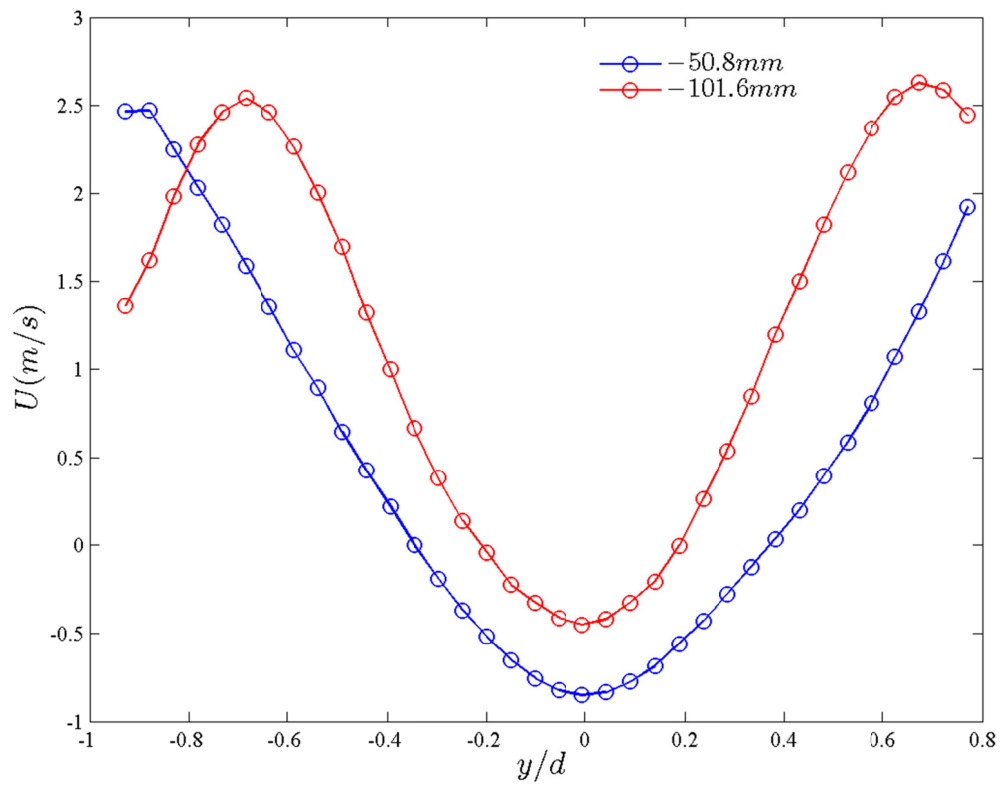


Figure 4.8. Measured mean velocity profiles for the two symmetric stator positions at $x/d=1$. Comparison with Figure 3.9 shows greater jet growth for the symmetric stator.

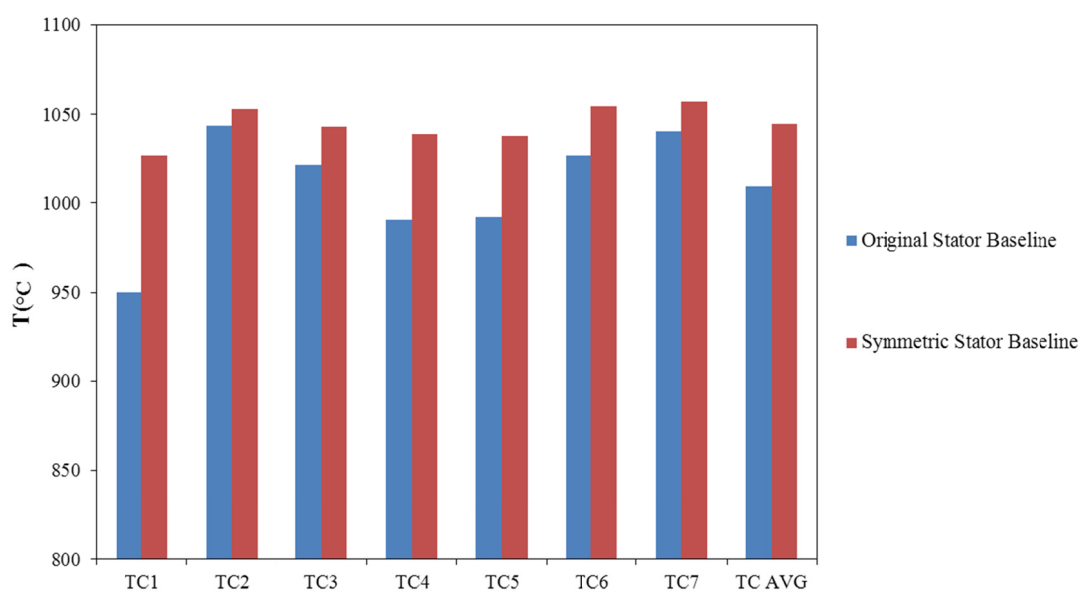


Figure 4.9. Average measured flame temperatures at each thermocouple measurement location (TC) for the original stator baseline (blue) and the baseline symmetric stator (red).

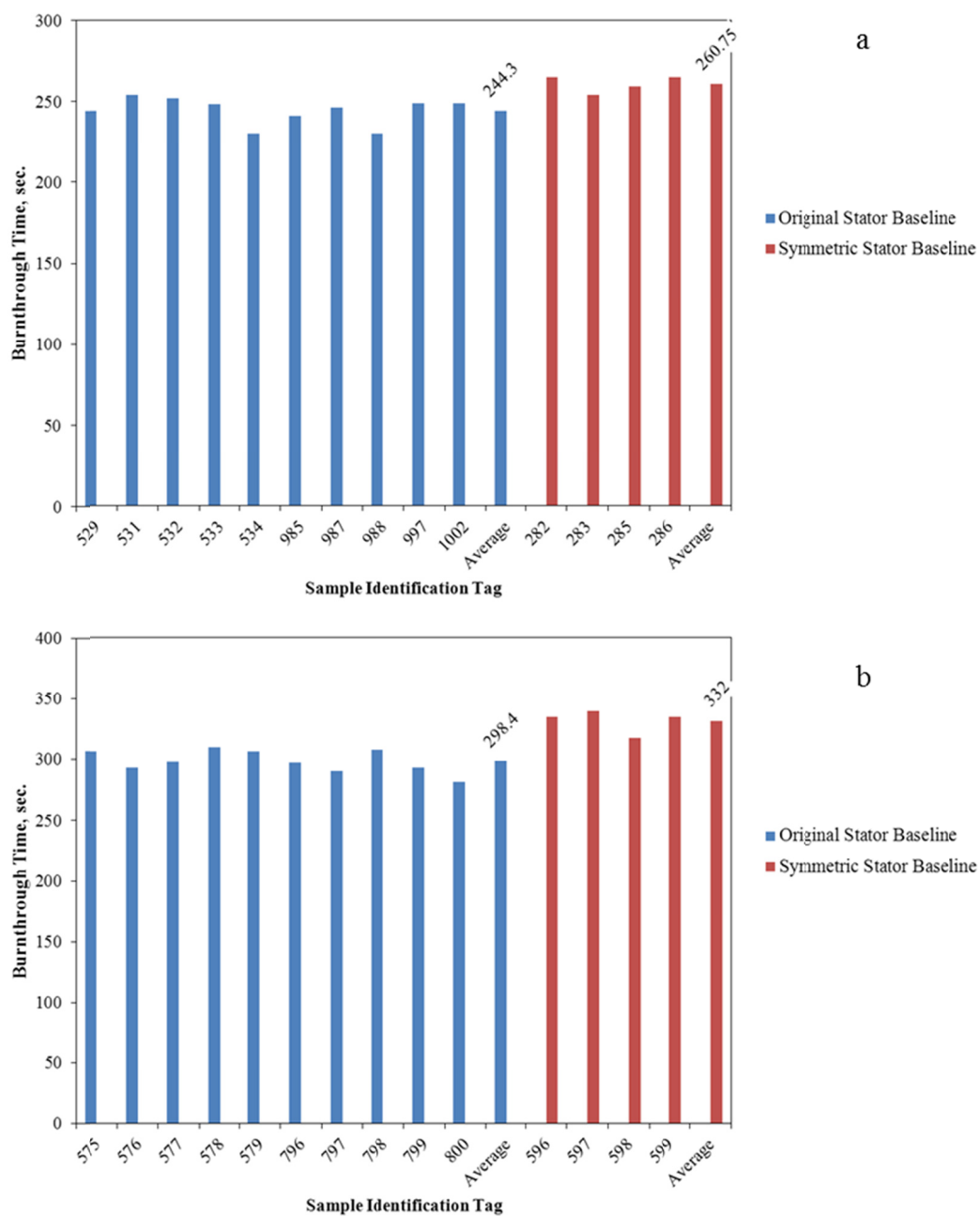


Figure 4.10. Burnthrough times for PAN 8579 (a) and PAN-8611 (b) material. Comparison of original stator baseline (blue) vs. symmetric stator baseline (red).

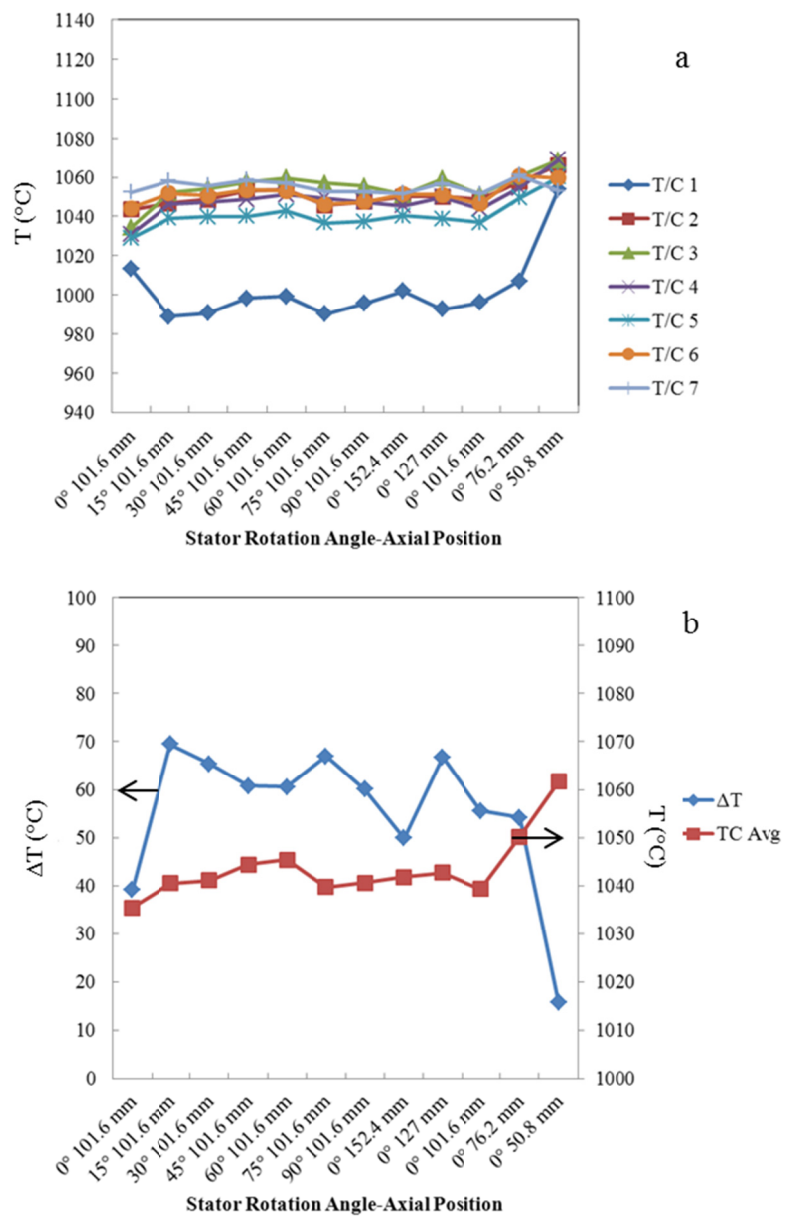


Figure 4.11. Average measured flame temperature for the symmetric stator at various axial and radial locations (a) and flame temperature spread (ΔT , blue) and overall average flame temperature (TC AVG, red), for the symmetric stator at various axial and radial locations (b).

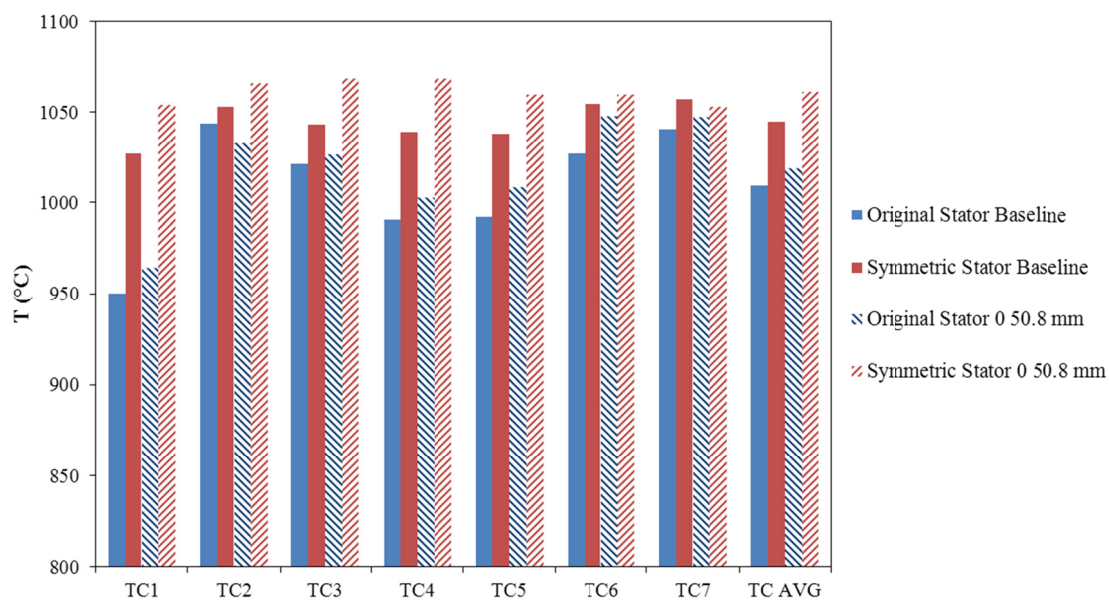


Figure 4.12. Average measured flame temperatures at each thermocouple location (TC) for the symmetric stator (blue) and the original stator baseline (red) at the baseline position (solid) and at 0° 50.8 millimeters (dashed).

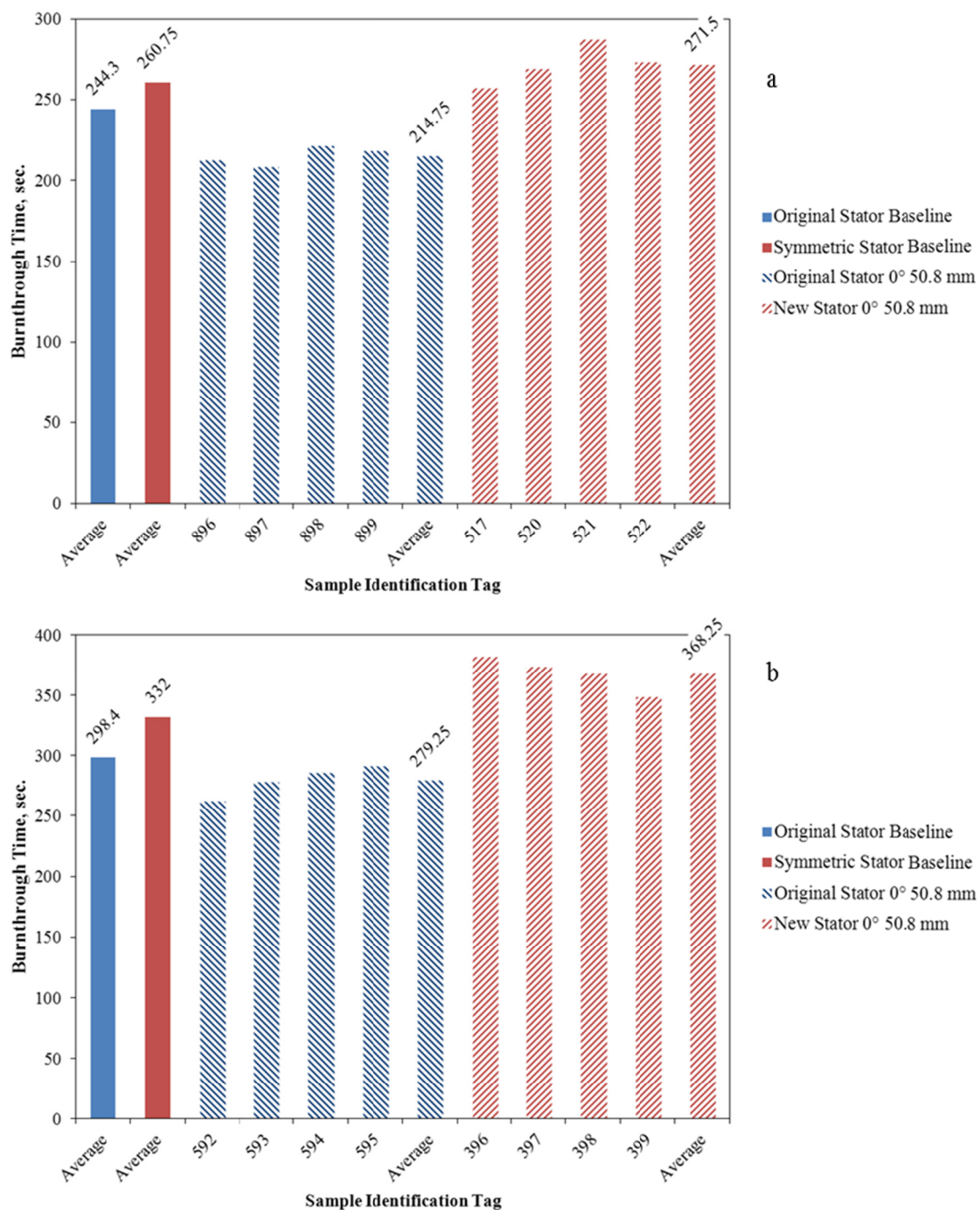


Figure 4.13. Burnthrough times for PAN-8579 material (a) and PAN-8611 material (b). The average burnthrough time of baseline stator position (solid) is compared with the new stator position (dashed) for the original stator (blue) and the symmetric stator (red).

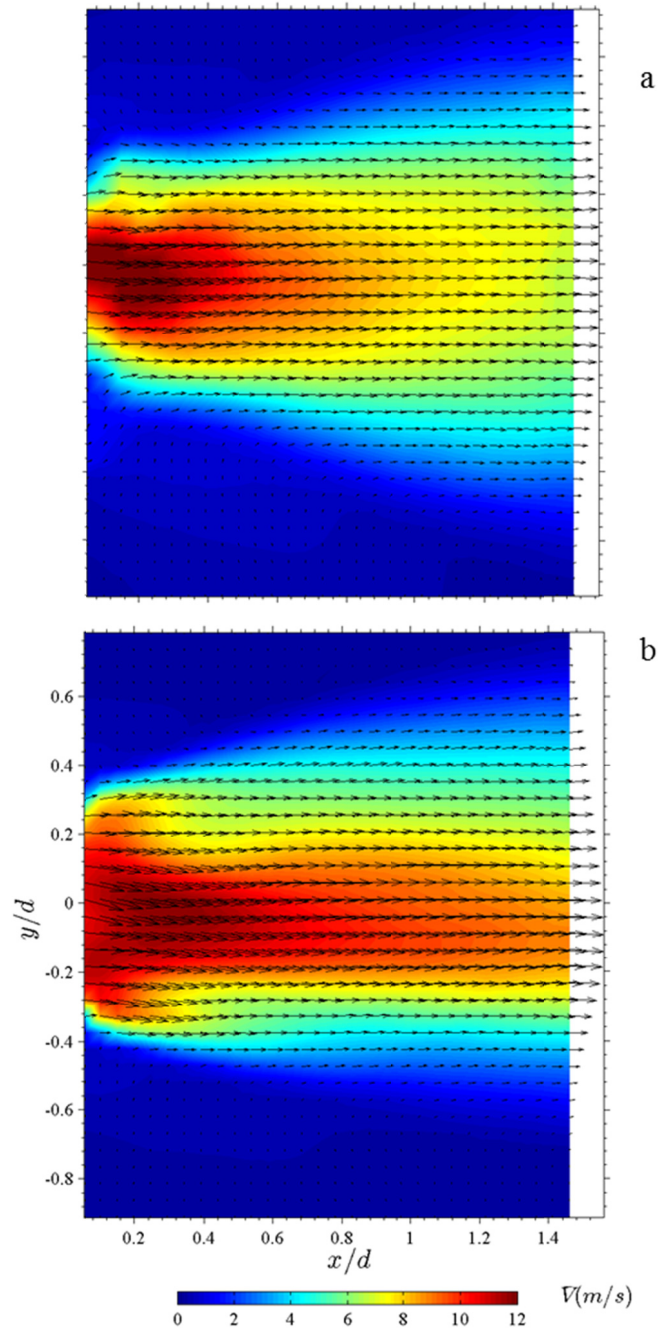


Figure 4.14. Contour and vector plots showing measured mean in-plane velocity field exiting the turbulator for the symmetric stator at 0° 50.8 millimeters (a) and the original stator at 0° 50.8 millimeters (b).

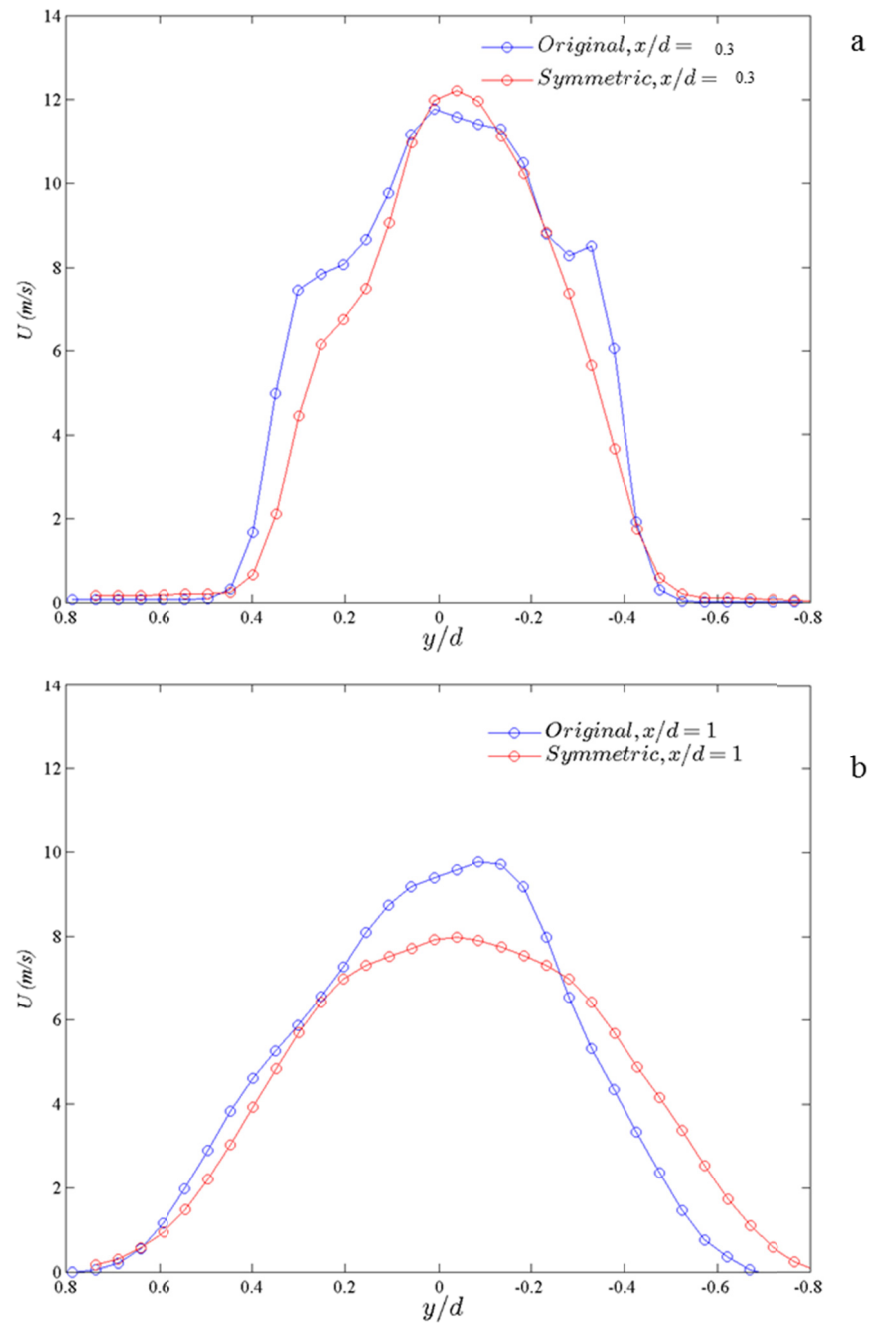


Figure 4.15. Comparison of mean axial velocity profiles at the turbulator exit for the original stator (blue) and symmetric stator (red) at 0° 50.8 millimeters at $x/d=0.3$ (a), and $x/d=1.0$ (b).

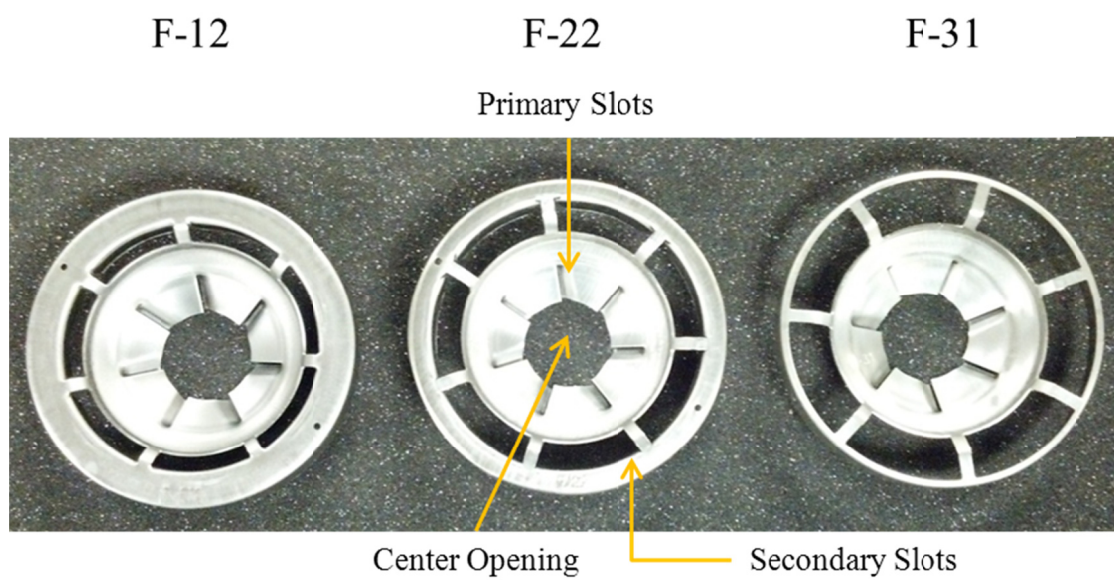


Figure 4.16. Photograph of three flame retention heads tested in this work showing the locations of the center opening, primary slots, and secondary slots.

	Units	F12	F22	F31	Turbulator
Center Hole Area	mm ²	660.52	660.52	660.52	3739.28
Primary Slots Area	mm ²	260.17	260.17	260.17	
Secondary Slots Area	mm ²	903.85	1697.61	3206.29	
Total Area	mm ²	1824.54	2618.30	4126.98	3739.28

Table 4.1. Measured exit plane area for the flame retention heads compared to the turbulator.

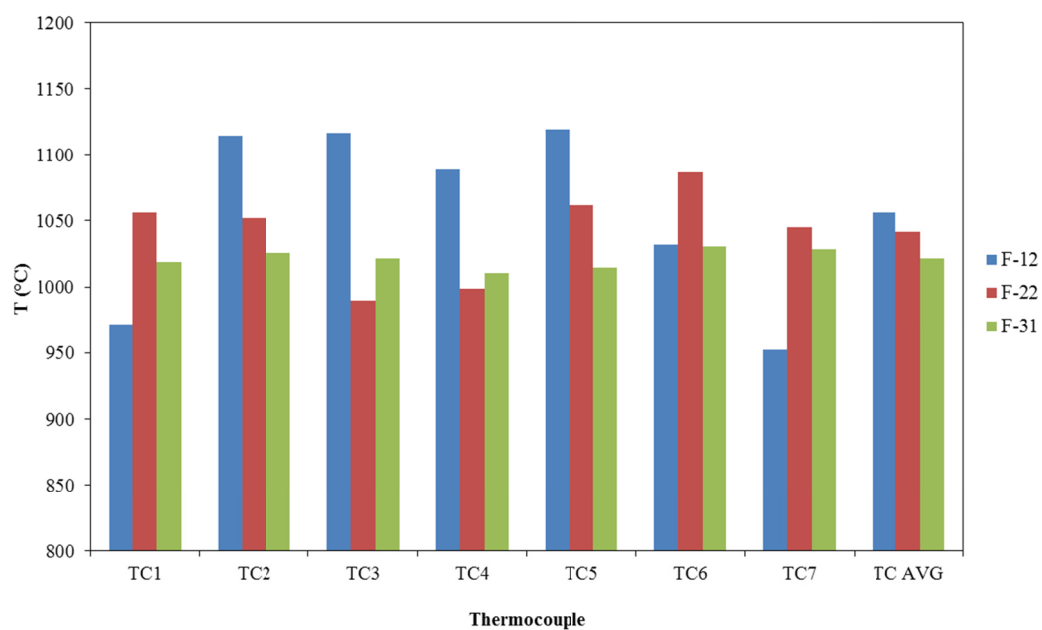


Figure 4.17. Average measured flame temperatures for the three flame retention heads, F12 (blue), F22 (red), and F31 (green).

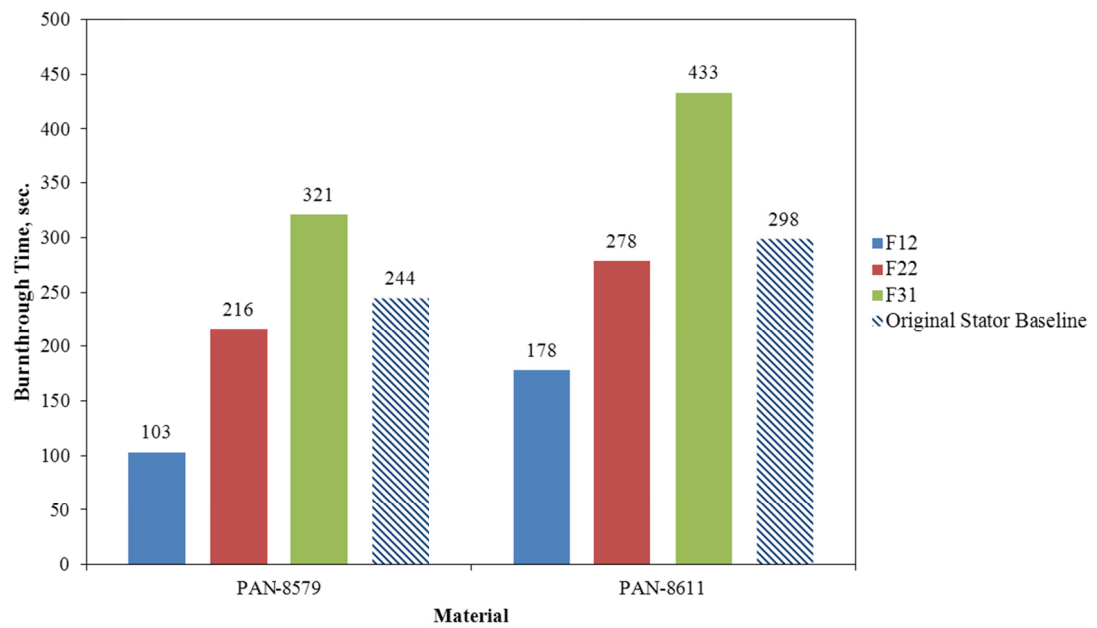


Figure 4.18. Average burnthrough times for PAN-8579 and PAN-8611 materials for the three flame retention heads tested: F12 (blue), F22 (red), F31 (green), and original stator baseline (blue/white).

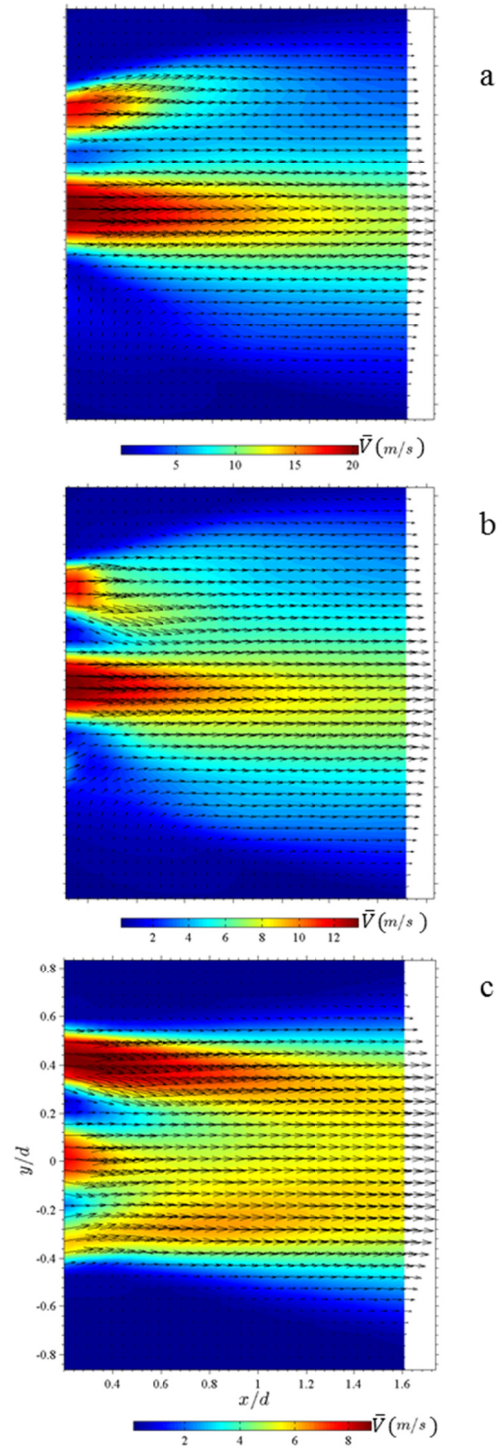


Figure 4.19. Contour and vector plots showing measured mean in-plane velocity field exiting the flame retention heads for the F12 (a), F22 (b), and F31 (c).

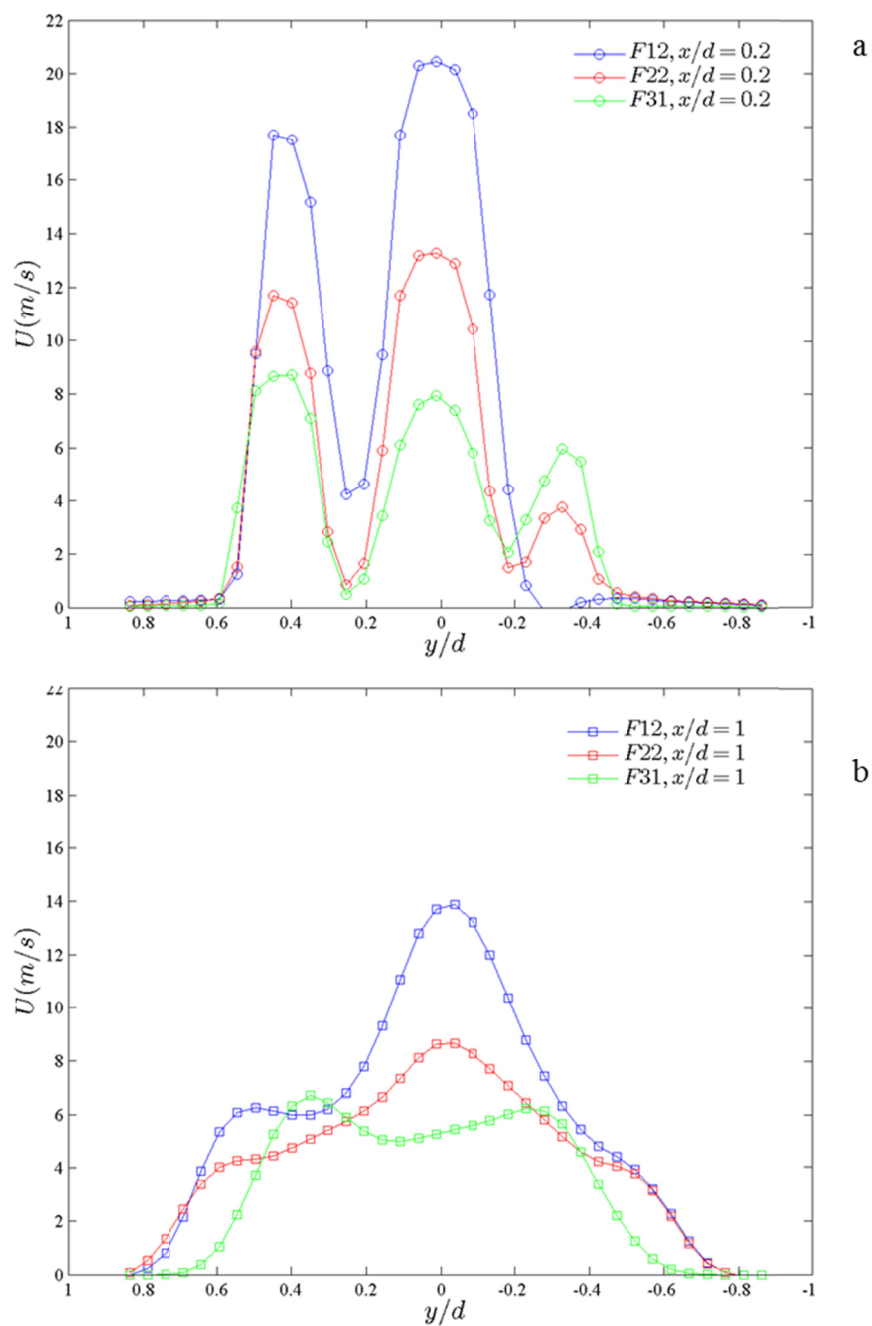


Figure 4.20. Comparison of the mean axial velocity profiles for each flame retention head at the draft tube exit $x/d=0.2$ (a) and $x/d=1.0$ (b).

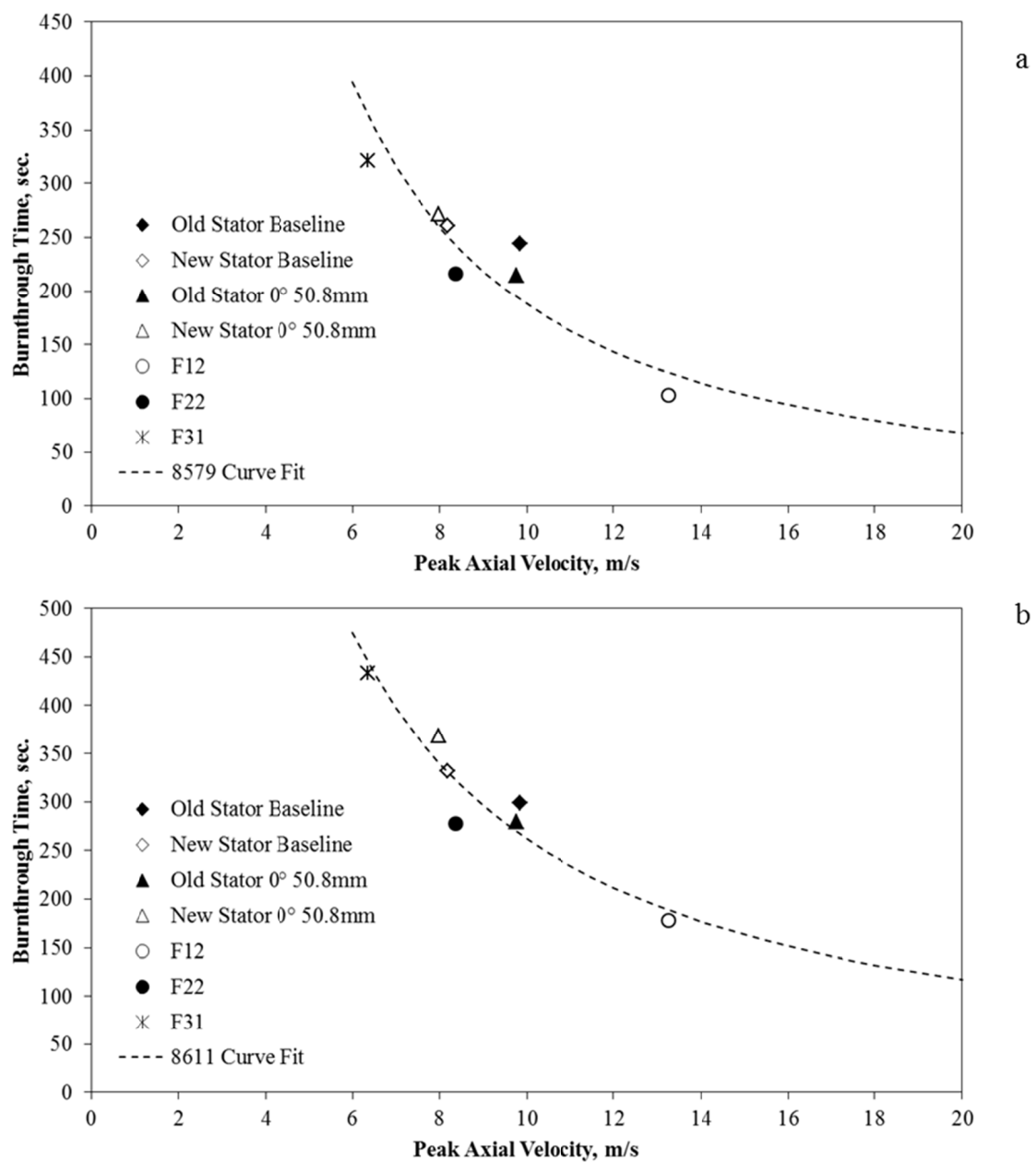


Figure 4.21. Average material burnthrough time as a function of measured peak axial velocity at $x/d=1$ for PAN-8579 (a) and PAN-8611 (b).

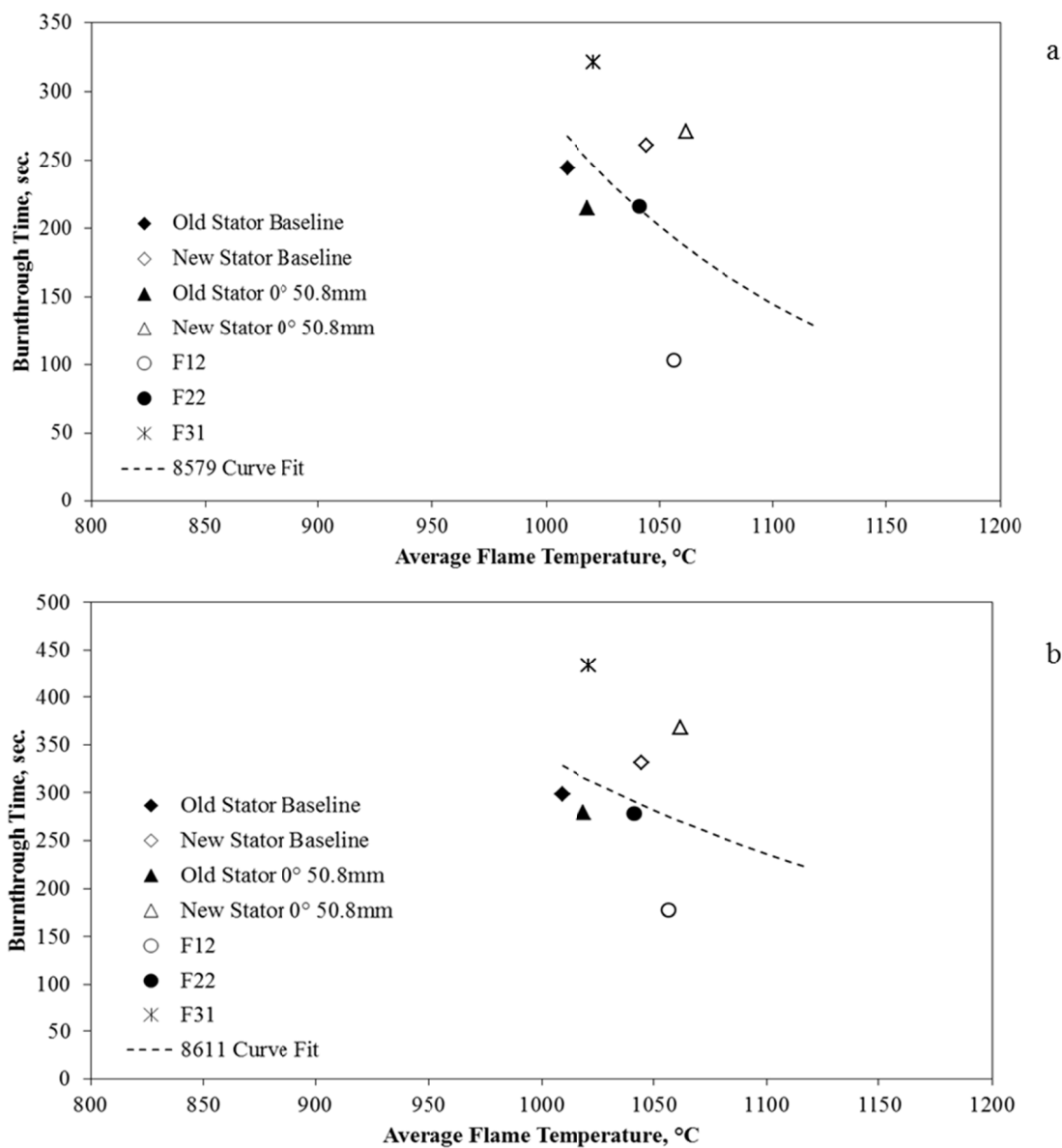
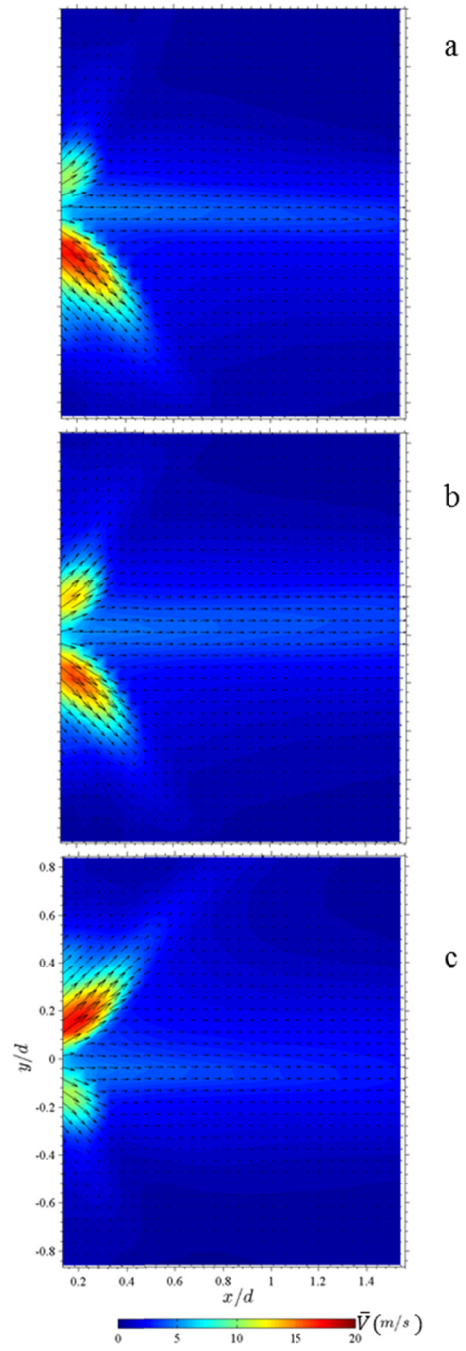


Figure 4.22. Average material burnthrough time as a function of measured average flame temperature for PAN-8579 (a) and PAN-8611 (b).



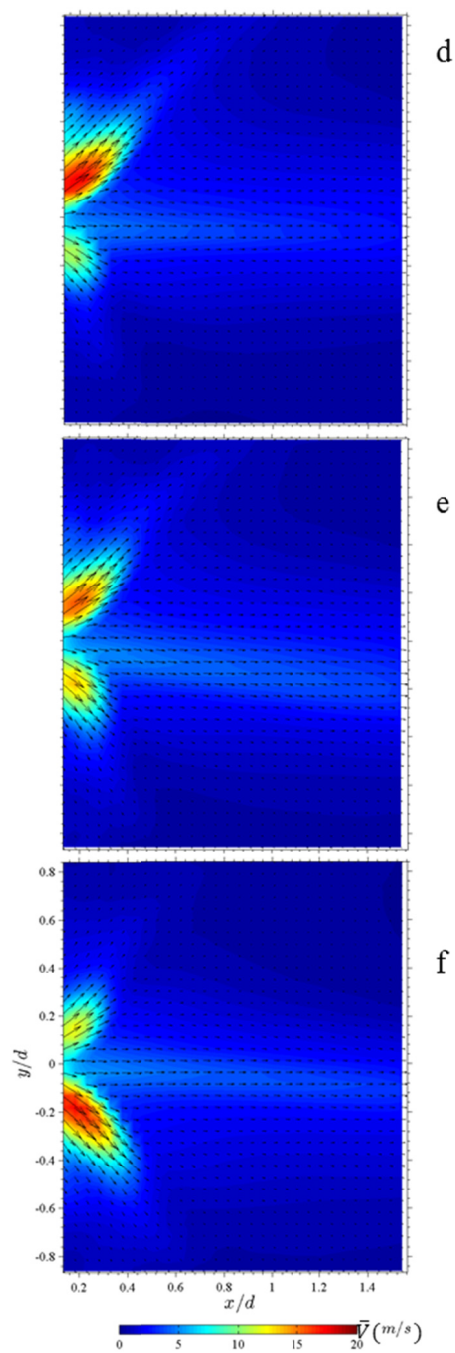


Figure 4.23. Contour and vector plots showing measured in-plane velocity field of the spray produced by Nozzle D, 126 mL/min (2.0 gph)-rated at 6.87 bar (85 psig). The nozzle was rotated in 60-degree increments resulting in 6 nozzle rotations (a-f).

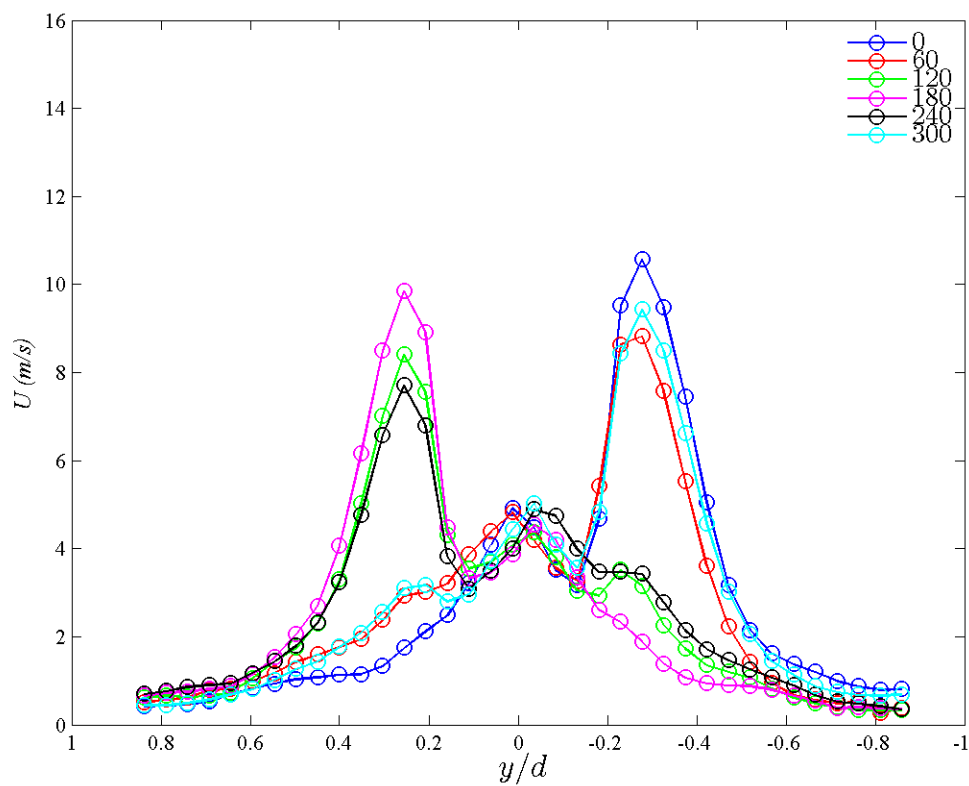


Figure 4.24. Comparison of the mean axial velocity profiles at the spray nozzle exit ($x/d=0.37$) for nozzle D at 60° increments.

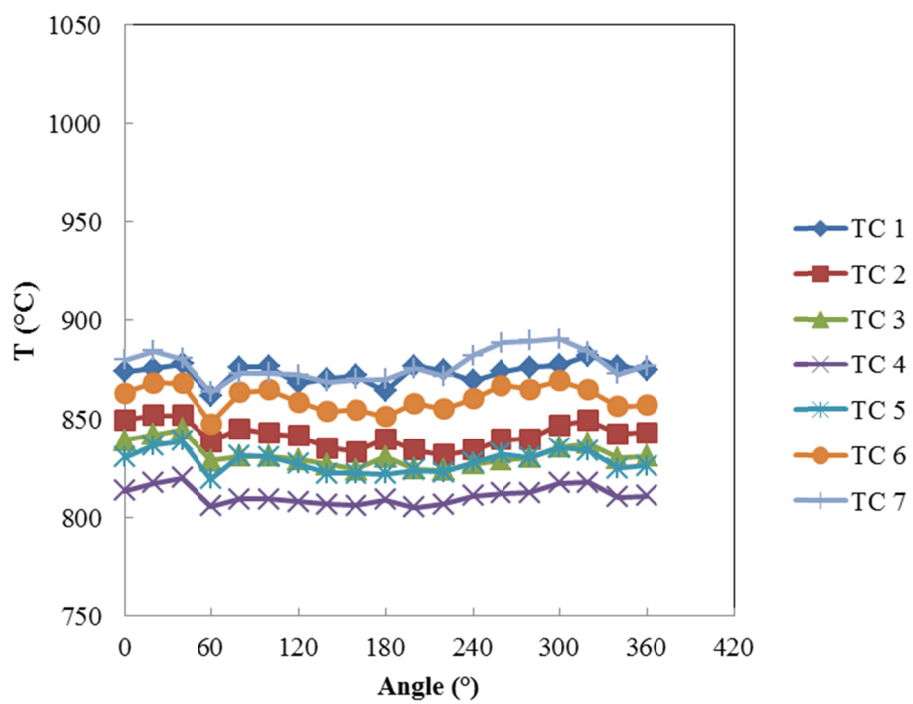


Figure 4.25. Average measured flame temperature at seven measurement locations plotted against the nozzle rotation angle for nozzle D.

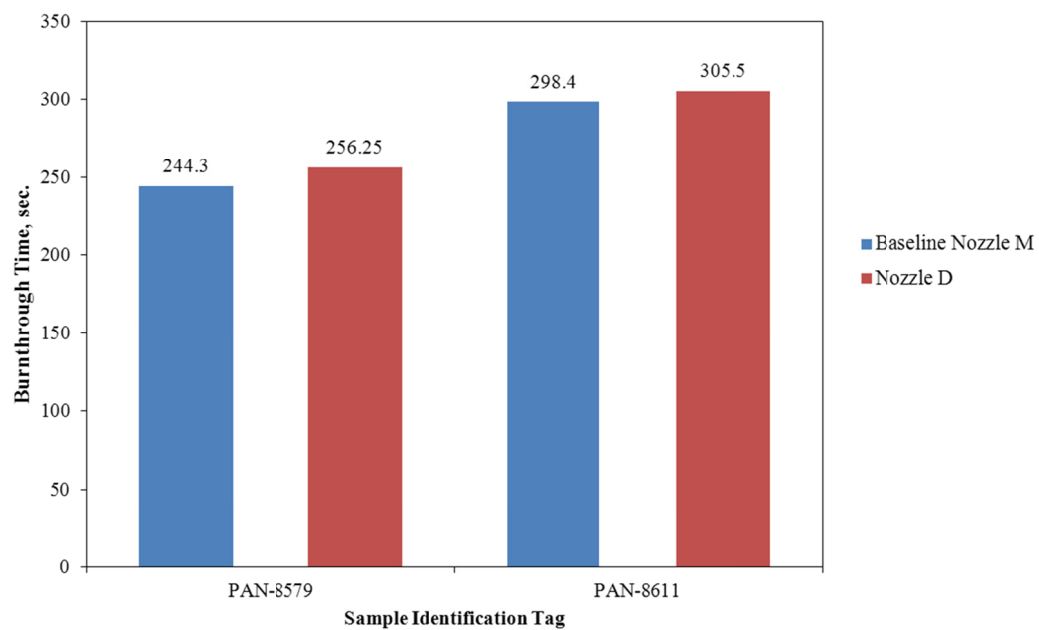


Figure 4.26. Average burnthrough times for PAN materials from nozzle M (blue) and nozzle D (red).



Figure 4.27. Photograph of a reinforced burner cone.

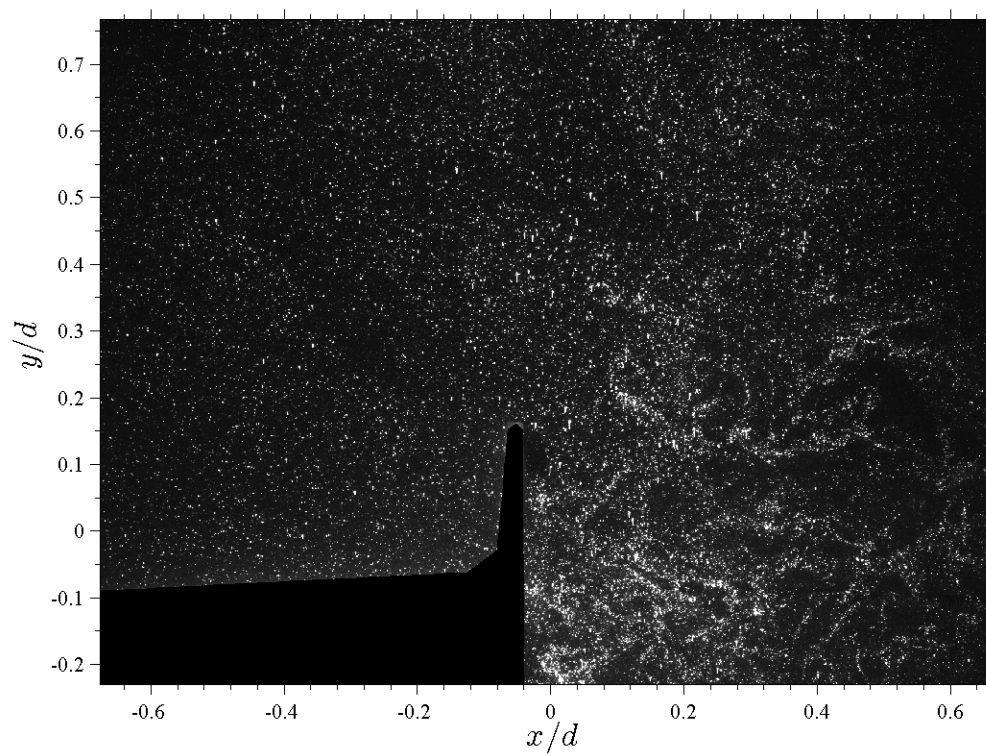


Figure 4.28. Sample PIV image of the reinforced cone centerline plane, external flow field. The blacked-out area is the top portion of the cone, which was masked out for analysis.

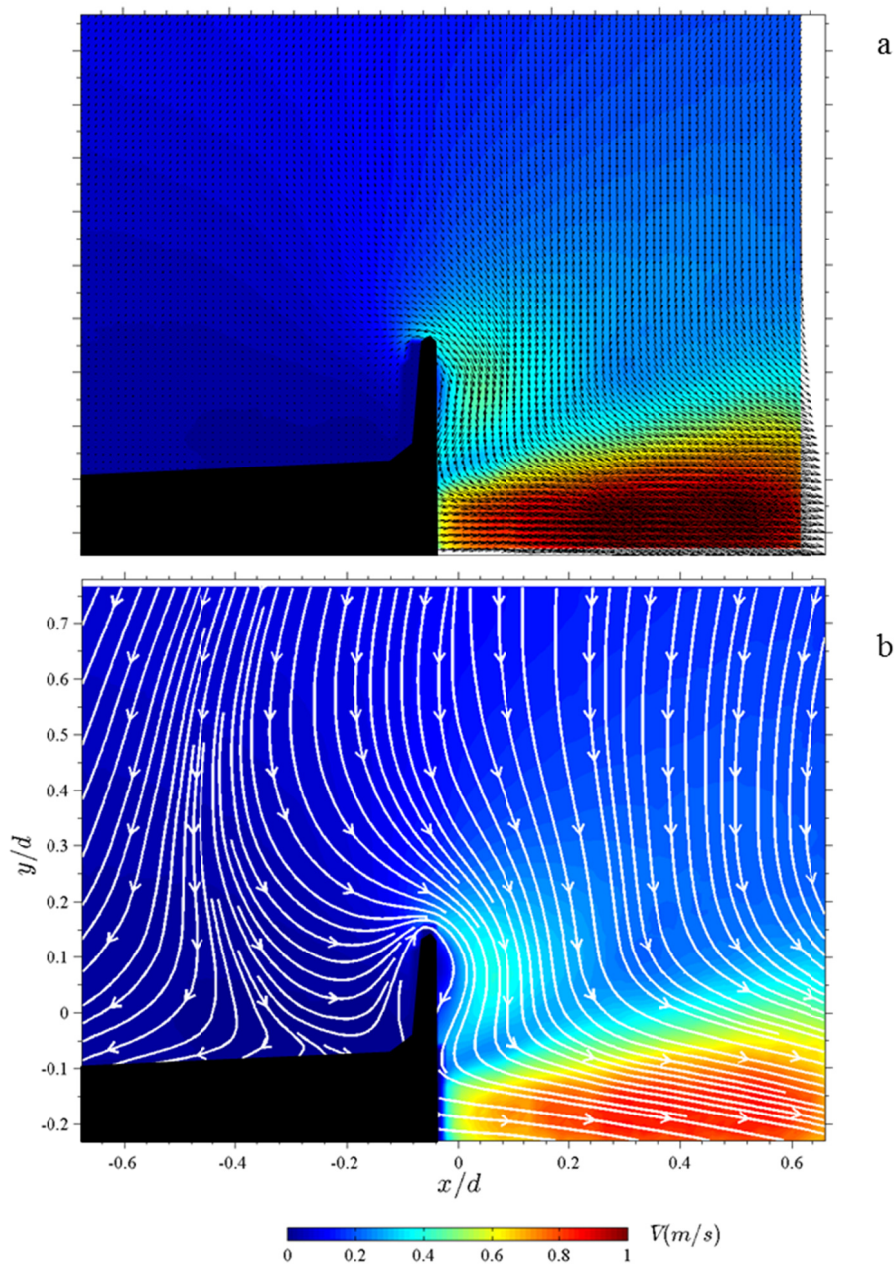


Figure 4.29. Contour and vector plots showing measured in-plane velocity field (a) and calculated streamlines (b) of the reinforcement ring burner cone external flow field.

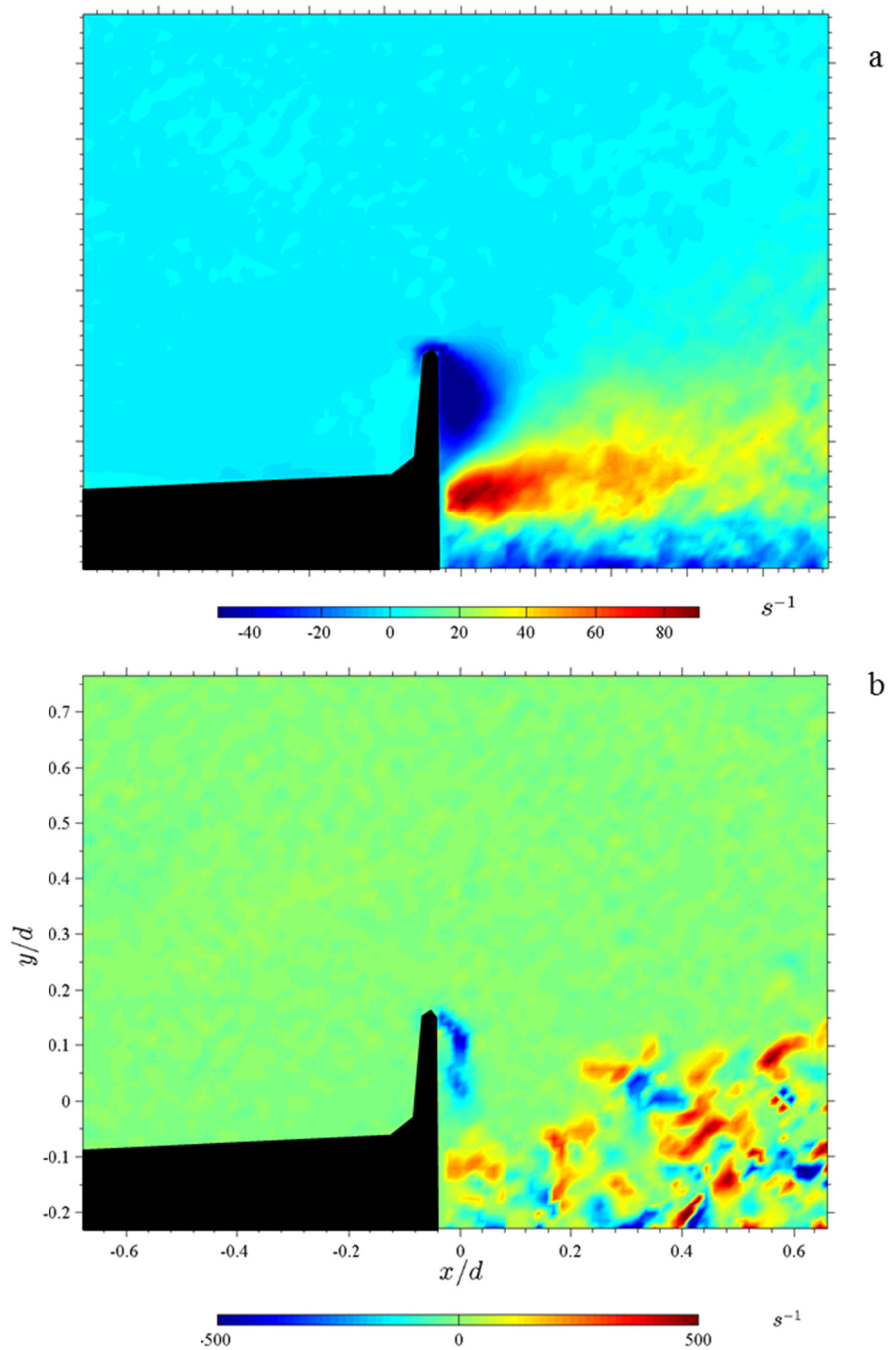


Figure 4.30. Contour plots showing the scalar mean of the vorticity (a) and typical instantaneous vorticity (b) from the reinforcement ring cone exit flow on the cone centerline.

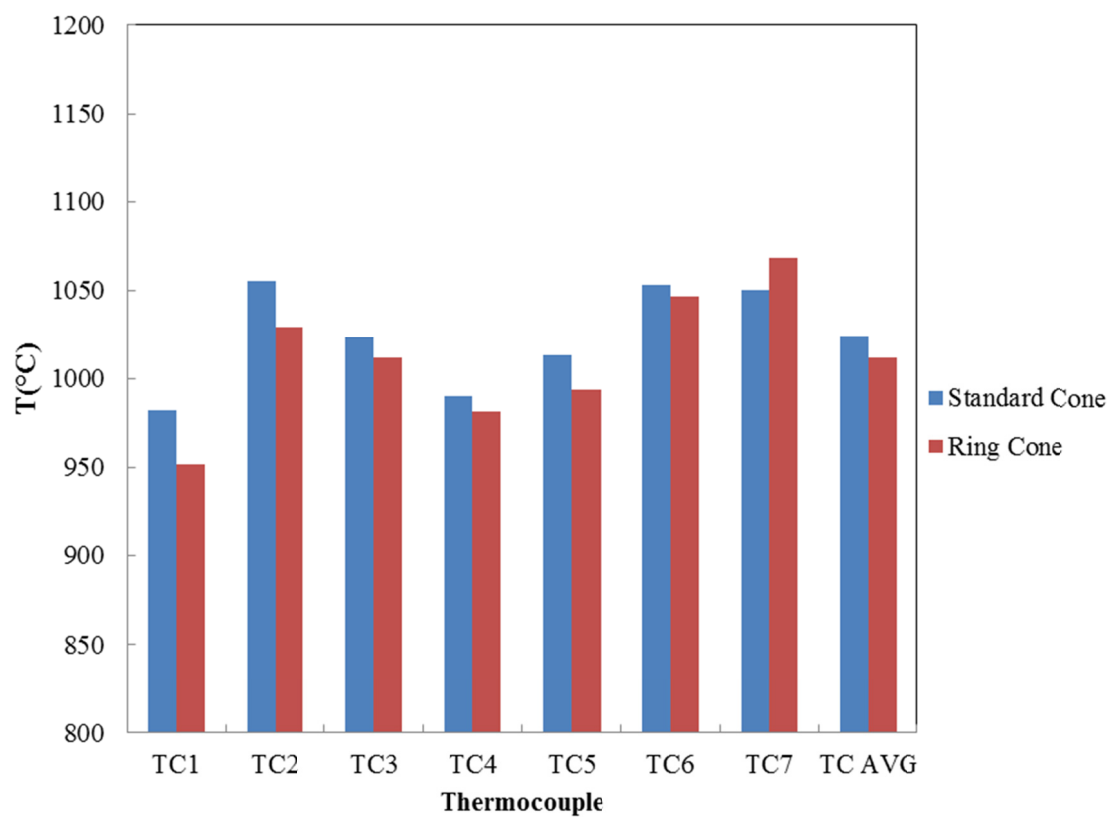


Figure 4.31. Average measured flame temperatures for the standard cone (blue) and the ring cone (red).

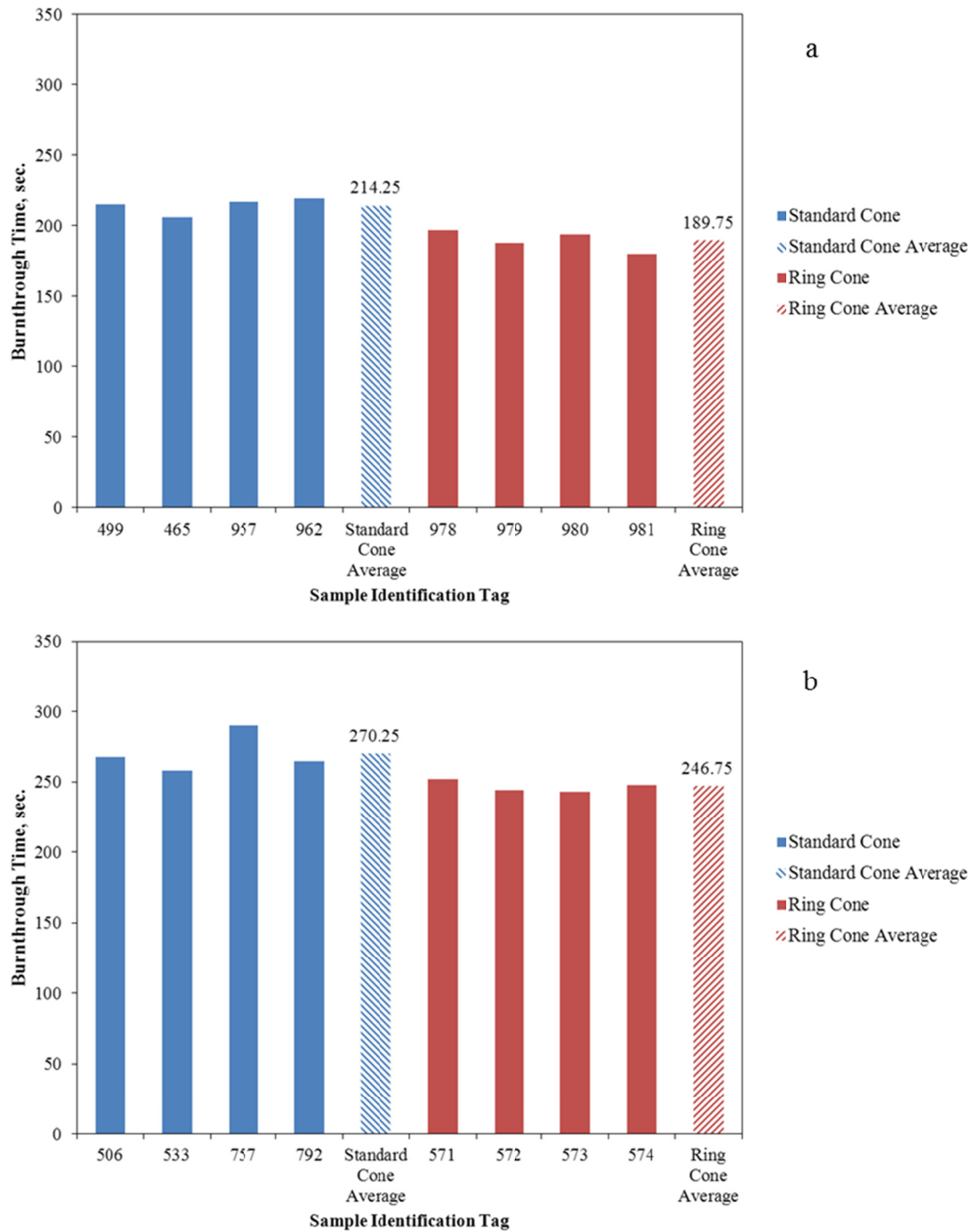


Figure 4.32. Burnthrough times for PAN-8579 material (a) and PAN-8611 material (b). Comparison of the standard cone design (blue) and the reinforcement ring cone design (red).

5 Concluding Remarks

The Federal Aviation Administration makes use of threat-based fire test methods and certification requirements for aircraft materials to enhance the level of safety in the event of an in-flight or post-crash fire on a transport airplane. The global nature of the aviation industry results in these test methods being performed at hundreds of laboratories around the world; in some cases testing identical materials at multiple labs but yielding different results. The test methods have evolved from simple Bunsen burner material tests to larger, more complicated apparatuses, requiring greater understanding of the most influential parameters on apparatus performance. The FAA Next Generation (NexGen) fire test burner was analyzed with Particle Image Velocimetry (PIV) to determine how the various burner components and configurations affect the flow field and performance.

Burner exit air flow was revealed as the most critical parameter for material burnthrough testing, as the magnitude and shape of the velocity profiles exiting the draft tube heavily influence material failure times. This finding reveals the necessity for a simple and repeatable method of configuring the burner such that all laboratories will have identical

configurations, resulting in identical exit air flow fields and comparable material burnthrough times. Measured flame temperatures did not show a direct correlation to material burnthrough times – high average flame temperatures do not necessarily dictate fast burnthrough times. However, flame temperature measurements are useful for indicating day to day burner consistency, and a drastic change in the flame temperature profile could indicate misaligned burner components.

The configuration of the stator and turbulator was found to have an effect on the exit in-plane velocity field, measured flame temperatures, and material burnthrough times. Replacing the stator with a perfectly symmetric stator was found to increase uniformity in both velocity and temperature profiles, but significantly increase material burnthrough time. Also, the symmetric stator would need to be specified at a set axial and rotational position, requiring similar detailed set up and maintenance procedures to the original stator. The use of flame retention heads would greatly simplify the burner specification and provides more uniform flame temperatures and burnthrough times similar to the current baseline configuration.

The current fuel spray nozzle was found to provide a circumferentially asymmetric spray pattern, directly affecting the measured flame temperature profile. Nozzles from a different manufacturer yielded similar asymmetry in both spray pattern and flame temperature, but yielding material burnthrough results similar to the baseline configuration. The dependence of burner performance on nozzle spray pattern is most

likely test-method dependent; the insulation and cargo liner burnthrough tests are large, flat samples directly impinged upon by the whole burner flame. Other test methods, including the seat cushion test, have test specimens only partially immersed in the flame, and depending on the direction of the asymmetric spray pattern, test results could be affected.

The flow exiting the burner cone was found to be highly asymmetric, due to the growth of the swirling air flow confined in a circular-to-ellipsoidal burner cone. The low velocity region coincides with a temperature measurement location often known to result in low temperatures due to soot collecting on the thermocouple. Alteration of the cone shape to a circular exit plane could eliminate this asymmetry, though the test methods are designed around the ellipsoidal shape of the burner exit plane relative to the specimen size and shape. The addition of a reinforcement ring around the burner cone exit plane was found to alter the flow field around the cone, create turbulence and rotation downstream in the cone exit flow, and decrease material burnthrough times when compared to an identical cone without a ring.

The results of this investigation provide a basis for future modifications to the NexGen burner in order to simplify the burner specification and increase worldwide reproducibility of test results while maintaining the severity of the threat-based requirements. This investigation was successful in identifying critical parameters of the NexGen burner with the use of flow visualization and material burnthrough tests.

Recommendations for future measurements on the NexGen burner would be correlating reacting and non-reacting flow fields and investigation of the reacting flow field impinging on the various test samples in different burner orientations.

6 References

- [1] J. Gardlin, "A Threat-Based Approach to Part 25 Flammability Regulations," in *Proceedings from the Sixth Triennial International Fire and Cabin Safety Research Conference*, Atlantic City, NJ, 2010.
- [2] United States of America Civil Aeronautics Board, *Fire Prevention in Carrier Aircraft CAR Part 4 Amendment 1*, Washington, D.C., November 1 1946.
- [3] Code of Federal Regulations Title 14 Aeronautics and Space, *Appendix F Part I - Test Criteria and Procedures for Showing Compliance with Sec. 25.853 or Sec. 25.855*, Washington, D.C., 2003.
- [4] C. Sarkos, R. Hill and W. Howell, "Full-Scale Wide-Body Test Article Employed to Study Post Crash Fuel Fires," *ICAO Bulletin*, pp. 30-39, October 1982.
- [5] Special Aviation Fire and Explosion Reduction (SAFER) Advisory Committee, "Final Report Volume I," Office of Aviation Safety, Washington, D.C., 1980.
- [6] Federal Aviation Administration Transport Directorate ANM-100, "Lessons Learned from Transport Airplane Accidents," Federal Aviation Administration, 27 January 2012. [Online]. Available: <http://accidents-ll.faa.gov/index.cfm>.
- [7] Federal Aviation Administration, "Fire Protection Requirements for Cargo or Baggage Compartments," in *Federal Register*, Washington, D.C., May 16, 1986.
- [8] Federal Aviation Administration, "Flammability Requirements for Aircraft Seat Cushions," in *Federal Register*, Washington, D.C., October 26, 1984.
- [9] Federal Aviation Administration, "Materials Working Group," Fire Safety Branch, 19 March 2013. [Online]. Available: <http://www.fire.tc.faa.gov/materials.asp>.
- [10] J. E. Demaree, "Reevaluation of Burner Characteristics for Fire Resistance Tests," Federal Aviation Administration, Washington, D.C., 1977.
- [11] R. Gardon, "An Instrument for the Direct Measurement of Intense Thermal

- Radiation," *The Review of Scientific Instruments*, vol. 24, no. 5, pp. 366-370, 1953.
- [12] A. V. Murthy, B. K. Tsai and R. D. Saunders, "Radiative Calibration of Heat-Flux Sensors at NIST: Facilities and Techniques," *Journal of Research of the National Institute of Standards and Technology*, vol. 105, no. 2, pp. 293-305, 2000.
- [13] P. Cahill, "Evaluation of the Reproducibility of the FAA Oil Burner Fire Test for Aircraft Seat Cushions," Federal Aviation Administration, Washington, D.C., 2007.
- [14] T. Marker, "Discussion of Burnthrough Test Method for Aircraft Thermal Acoustic Insulation Blankets," in *International Aircraft Materials Fire Test Working Group*, Atlantic City, NJ, March 2005.
- [15] Federal Aviation Administration, "Fire Penetration Resistance of Thermal/Acoustic Insulation Installed on Transport Category Airplanes," *Federal Register*, pp. 1438-1442, 12 January 2007.
- [16] R. Ochs, "Development of a Next-Generation Burner for Use in Testing Thermal Acoustic Insulation Burnthrough Resistance," May 2009.
- [17] "Next Generation Fire Test Burner: Plans and Information," FAA Fire Safety, 18 September 2012. [Online]. Available: http://www.fire.tc.faa.gov/pdf/materials/NexGenPlans_9_2012.pdf.
- [18] Advisory Circular 25.856-2A Installation of Thermal/Acoustic Insulation for Burnthrough Protection, Federal Aviation Administration, 2008.
- [19] C. H. Kuo and A. K. Kulkarni, "Analysis of Heat Flux Measurement by Circular Foil Gages in a Mixed Convection/Radiation Environment," *Journal of Heat Transfer*, vol. 113, pp. 1038-1040, 1991.
- [20] J. T. Nakos, "Uncertainty Analysis of Steady State Incident Heat Flux Measurements in Hydrocarbon Fuel Fires," Sandia National Laboratories, Albuquerque, New Mexico, 2005.
- [21] M. Raffel, C. Willert, S. Werely and J. Kompenhans, *Particle Image Velocimetry: A Practical Guide*, 2nd Edition, Berlin: Springer-Verlag, 2007.
- [22] J. M. Beer and N. A. Chigier, *Combustion Aerodynamics*, New York: John Wiley &

Sons, Inc., 1972.

- [23] L. Muniz, "Particle Image Velocimetry Studies of Turbulent Nonpremixed Flames (Doctoral Dissertation)," Stanford University, 2002.
- [24] F. J. Diez and W. J. A. Dahm, "Effects of heat release on turbulent jet shear flows. Part 3. Buoyancy effects due to heat release in jets and plumes," *Journal of Fluid Mechanics*, vol. 575, pp. 221-255, 2007.
- [25] P. N. Papanicolaou and J. List, "Investigations of Round Vertical Turbulent Buoyant Jets," *Journal of Fluid Mechanics*, vol. 195, pp. 341-391, 1988.
- [26] S. Corrsin, "Investigation of flow in an axially symmetrical heated jet of air," NACA, 1943.
- [27] S. Corrsin and M. S. Uberoi, "Further experiments of the flow and heat transfer in a heated jet," NACA, 1950.
- [28] S. Corrsin and M. S. Uberoi, "Spectra and diffusion in a round turbulent jet," NACA, 1951.
- [29] I. Wygnanski and H. E. Fiedler, "Some measurements in the self-preserving jet," *Journal of Fluid Mechanics*, vol. 38, pp. 577-612, 1969.
- [30] H. J. Hussein, S. P. Capp and W. K. George, "Velocity measurements in a high-Reynolds-number, momentum-conserving, axisymmetric, turbulent jet," *Journal of Fluid Mechanics*, vol. 258, pp. 31-75, 1994.
- [31] C. Fukushima, L. Aanen and J. Westerweel, "Investigation of the Mixing Process in an Axisymmetric Turbulent Jet using PIV and PLIF," in *10th International Symposium on Applications of Laser Techniques to Fluid Mechanics*, Lisbon, Portugal, July 2000.
- [32] B. Boersma, G. Brethouwer and F. T. M. Nieuwstadt, "A Numerical Investigation on the Effect of the Inflow Conditions on the Self-Similar Region of a Round Jet," *Physics of Fluids*, vol. 10, no. 4, pp. 899-909, 1998.
- [33] J. -L. Boreau, D. Huilier and H. Burnage, "On the effect of a co-flowing stream on the structure of an axisymmetric turbulent jet," *Experimental Thermal and Fluid*

- Science*, vol. 17, pp. 10-17, 1998.
- [34] C. Willert and M. Jarius, "Planar Flow Field Measurements in Atmospheric and Pressurized Combustion Chambers," *Experiments in Fluids*, vol. 33, pp. 931-939, 2002.
- [35] C. Willert, C. Hassa, G. Stockhausen, M. Jarius, M. Voges and J. Klinner, "Combined PIV and DGV applied to a pressurized gas turbine combustion facility," *Measurement Science and Technology*, vol. 7, pp. 1670-1679, 2006.
- [36] V. Palero and Y. Ikeda, "3D Imaging of Evaporation Fuel Droplets by Stereoscopic PIV," *Journal of Visualization*, vol. 5, no. 3, pp. 285-292, 2002.
- [37] N. Yamada, Y. Ikeda and T. Nakajima, "Multi-Intensity-Layer PIV Application to a Practical Burner," in *10th International Symposium on the Application of Laser Techniques to Fluid Mechanics*, Lisbon, Portugal, July 2000.
- [38] D. G. Lilley, "Swirl Flows in Combustion: A Review," *AIAA Journal*, vol. 15, no. 8, pp. 1063-1078, August 1977.
- [39] S. Bernero, A. Glauser and M. Zajadatz, "Cold Flow and Spray Visualization Experiments Applied to the Development of ALSTOM Dual Fuel Gas Turbine Burners," in *13th International Symposium on Applications of Laser Techniques to Fluid Mechanics*, Lisbon, Portugal, June 2006.
- [40] L. K. Su, O. S. Sun and M. G. Mungal, "Experimental investigation of stabilization mechanisms in turbulent, lifted jet diffusion flames," *Combustion and Flame*, vol. 144, pp. 494-512, 2006.
- [41] M. Legrand, J. Nogueira, A. Lecuona, S. Nauri and P. A. Rogriguez, "Atmospheric low swirl burner flow characterization with stereo PIV," *Experiments in Fluids*, vol. 48, no. 5, pp. 901-913, 2010.
- [42] S. Pfadler, M. Loffler, F. Dinkelacker and A. Leipertz, "Measurement of the conditioned turbulence and temperature field of a premixed Bunsen burner by planar laser Rayleigh scattering and stereo particle image velocimetry," *Experiments in Fluids*, vol. 39, no. 2, pp. 375-384, 2005.
- [43] V. R. Palero and Y. Ikeda, "Droplet-size-classified stereoscopic PIV for spray characterization," *Measurement Science and Technology*, vol. 13, pp. 1050-1057,

2002.

- [44] H. C. V. d. Hulst, *Light Scattering by Small Particles*, New York: Dover, 1957.
- [45] A. Melling, "Tracer particles and seeding for particle image velocimetry," *Measurement Science Technology*, vol. 8, pp. 1406-1416, 1997.
- [46] Y. Cheng, "A Study of the Fine-Scale Three-Dimensional Flow Structures in Turbulence Using Time-Resolved Stereoscopic Scanning Particle Image Velocimetry," Thesis (Ph. D.) - Rutgers, The State University of New Jersey, Mechanical and Aerospace Engineering, 2011.
- [47] J. Mullin, "A Study of Velocity Gradient Fields at the Intermediate and Small Scales of Turbulent Shear Flows via Dual-Plane Stereo Particle Image Velocimetry," Ph. D. Dissertation, The University of Michigan, Ann Arbor, Michigan, 2004.
- [48] "Oil Burner Test for Seat Cushions," in *Aircraft Materials Fire Test Handbook Chapter 7*, 2008.
- [49] E. M. Moffatt, "Methods of Minimizing Errors in the Measurement of High Temperature Gases," *Instruments*, vol. 22, no. 2, pp. 122-132, 1949.
- [50] R. J. Moffat, "Gas Temperature Measurement," in *Temperature: Its Measurement and Control in Science and Industry*, New York, Reinhold, 1962, pp. 553-571.
- [51] D. C. Collis and M. J. Williams, "Two-Dimensional convection from Heated Wires at Low Reynolds Numbers," *Journal of Fluid Mechanics*, vol. 6, no. 4, pp. 357-384, 1959.
- [52] W. M. Pitts, E. Braun, R. D. Peacock, H. E. Mitler, E. L. Johnsson, P. A. Reneke and L. G. Blevins, "Temperature Uncertainties for Bare-Bead and Aspirated Thermocouple Measurements in Fire Environments," in *Thermal Measurements: The Foundation of Fire Standards*, West Conshohocken, PA, ASTM International, 2002.
- [53] L. G. Blevins, "Behavior of Bare and Aspirated Thermocouples in Compartment Fires," in *Proceedings of the 33rd National Heat Transfer Conference*, Albuquerque, New Mexico, August 15-17, 1999.

- [54] R. M. C. So, S. A. Ahmed and H. C. Mongia, "Jet Characteristics in Confined Swirling Flow," *Experiments in Fluids*, vol. 3, pp. 221-230, 1985.
- [55] TSI Incorporated, "Application of Global Sizing Velocimetry (GSV) to Gasoline Direct Injection (G-DI) Sprays," TSI, 2006.
- [56] I. Glassman, *Combustion*, 3rd Edition, San Diego, CA: Academic Press, 1996.
- [57] J. J. Miao, E. C. Lin, Q. S. Chen, J. H. Chou, D. Pan and C. K. Lin, "Swirling Flows in Circular-to-Rectangular Transition Ducts," *Experiments in Fluids*, vol. 20, pp. 401-409, 1996.
- [58] I. L. Roberts, J. E. R. Coney and B. M. Gibbs, "Estimation of Radiation Losses from Sheathed Thermocouples," *Applied Thermal Engineering*, vol. 31, no. 14-15, 2011.
- [59] R. M. C. So, S. A. Ahmed and H. C. Mongia, "Jet characteristics in confined swirling flow," *Experiments in Fluids*, vol. 3, pp. 221-230, 1985.